The Analysis and Removal of Systematic Trends in STEREO's HI-1A Photometry and a Search for Planetary Transits

by

Gemma Nicole Whittaker

A thesis submitted to
The University of Birmingham
for the degree of
DOCTOR OF PHILOSOPHY

Astrophysics and Space Research Group
School of Physics and Astronomy
The University of Birmingham
December 2013

Abstract

STEREO'S wide-field imager, HI-1A, offers the opportunity to investigate astrophysical phenomena. This camera continually monitors stars within a magnitude range of $4 \leq R \leq 12$, for up to 20 days, without interruptions from the Earth's atmosphere or the diurnal cycle. From this data, light curves for more than 50,000 targets have been produced. These have the photometric potential to make a significant contribution to surveys for transiting planets, which currently lack continuous, space-based observations, for bright stars ($R < 9$) in particular. Hence a transit survey, using the HI-1A light curves, presents a worthy challenge. If it is successful in finding new planets then it will help to fill a current observational gap and provide bright targets, which are ideal for further ground-based study.

The original HI-1A light curves were found to possess a wide range of systematic and observational influences, including vignetting, tracking errors and contamination from the Sun. To counteract these effects and increase the potential yield of a transit search, the HI-1A trend removal pipeline (TRP) was constructed. This pipeline draws on various resources and techniques, including a non-linear iterative filter, to create an effective noise reduction process, with negligible effect on transit-like signals.

A noise analysis was conducted which shows that the TRP reduces the point-to-point scatter by up to 50 % for the brightest targets ($R \leq 6$) and 25 % for the faintest ($R \geq 9$). The correlated (systematic) noise on transit timescales was found to be negligible for the majority of the targets and only 20 % of the total noise for the brightest stars, which amount to < 3 % of the sample.

A number of transit-like signals were detected in an automated search for planet candidates. These were then put through a series of tests, to ascertain the planet-likelihood of each signal detected. While no candidate passed every test, the detection of a signal with a depth of < 1 % and a high signal-to-noise ratio, implies that a transit survey with the HI-1A light curves is more than capable of detecting planets. However solar flux and CMEs, which feature in the majority of the observations, are likely to be the main causes for the lack veritable planet candidates. Therefore it is crucial that these sources of noise be more effectively treated, to improve the outcome of subsequent transit searches.

Dedication:

To my dad, who would have loved this.

To my mum, for being with me all the way.

To Mr Wakefield, the most inspirational physics teacher there ever was.

Acknowledgements

Thank you to the following people and organisations, without whom I would either still be trying to figure this out, or have packed it all in long ago to pursue a career on the Great British Bake Off.

First and foremost thank you to my supervisor, Ian Stevens, for your patience and understanding and above all, for giving me the time to develop my own ideas, while providing gentle encouragement.

A huge thank you to Bill Chaplin, for taking me under your wing at a crucial time and saving my sanity. Thank you for your time spent proof-reading my chapters, which were always late, sorry! Also thanks for all your advice and for making me see things from a different perspective. You were a huge support when I needed it most and I am truly thankful to have had you on my side these last few months.

I am indebted to the IT legend that is David Stops. I don't think any amount of my (attempted) cakes could repay you for your unwaivering support with my many many computer issues. From backups to continuous IDL issues and beyond, you fixed it all. I really think you are magic.

Thank you also to the following people, who made the PhD journey better, whether or not they know it: Mark Burke (fellow office worker), for your useful tips and advice throughout the years; Chiara Mingarelli (my partner in yoga), although we never got to share an office, you were always there to listen to my rantings (you know what I'm talking about); Chris Eyles for taking the time to discuss anomalies in the data with me one day; Lucy Collinson (postgraduate support), you really were most supportive!

A special thanks to Vino Sangarlingam, for being so patient with me and for providing endless help and advice from my first day on the job. You are an inspiration to me.

I would also like to thank Suzanne Aigrain, Frédéric Pont, Danielle Bewsher and Chris Eyles, for publishing their ideas and methods so that it could benefit others like myself. Their work has been the backbone of many of the ideas and methods in this thesis and I am very grateful to them for it.

Thank you to the people at the Rutherford Appleton Laboratory, STEREO and BlueBEAR, whose services were used at various times throughout this work.

More personally, thank you to Tim Cox, for being great and for stepping up to the plate. Thanks for all the cooking, cleaning, and general house-husbandry. Also thanks to your family and particularly Mick and Linda for begin so kind, supportive and always there for me should I need them.

To my Mum and brother Liam. Thank you for all the proof reading, Mum I'm pretty sure you could do your own PhD in Astrophysics by now! You are both great and I love you. Liam, I'll see your Dr Whittaker.

Finally I would like to thank Carole Haswell and Ilya Mandel for their time spent reading the thesis and for their evaluation of my work. Your comments and suggestions for the thesis were highly valued and I thank you for helping me to see my strengths as well as my weaknesses.

Statement of originality

I hereby declare that this thesis presents original work undertaken at the University of Birmingham, from October 2009 to April 2013. During this time the work carried out has been entirely my own, under the supervision of Dr Ian Stevens.

Where there are methods and ideas from the literature which have been used in this work, these are referenced accordingly. A summary is given below:

- Chapter 1: This gives an introduction to the field of Exoplanets and describes the theory which is relevant detecting transiting planets. The information made available in the Exoplanet Database has been made use of, to illustrate key results in the field. Figure 1.5 is taken from Winn (2010) and is referenced as such.

- Chapter 2: This introduces STEREO and the HI-1A in detail. The available documentation has been used when providing details and specifications of this instrument. Figures 2.1, 2.2, 2.4 and 2.5 are from the associated publications and are referenced as such.

- Chapter 3: This chapter describes the process of obtaining the light curves. The HI-1A images were downloaded from the Rutherford Appleton Laboratory (RAL). The key IDL programs used to extract the light curves were designed by Danielle Bewsher (RAL), Daniel Brown (Aberystwyth University), Vino Sangaralingam and Steve Spreckley (both at the University of Birmingham). Some modifications were made to the original programs in this work. Figure 3.3 was taken from the literature and has been referenced as such.

- Chapters 4, 5 and 6: These chapters have formed the basis of the recently published paper:
  STEREO trend removal pipeline and planet detection possibilities (Whittaker et al., 2013).
  Chapter 5, which describes the trend removal pipeline (TRP) developed for the HI-1A, makes use of the methods and ideas presented in Aigrain and Irwin (2004) and Aigrain et al. (2009). In particular, the non-linear iterative filter (NLF) described in Section 5.3.5 is based on that which was formulated for CoRoT data. The noise analysis presented in Chapter 6 is also based on that

applied to CoRoT data in Aigrain et al. (2009), but uses the theory and techniques outlined in Pont et al. (2006). The methods presented in this paper are now widely used when analysing light curves both prior to and following transit searches.

- Chapter 8: This presents the analysis of the HI-1A planet candidates. The Exoplanet Diagnostic test, presented in Tingley and Sackett (2005) is summarised and used to help identity false-positive detections, as it has been used by other surveys before. The contamination test, set out in Section 8.3.4 was developed in collaboration with my supervisor, Dr Ian Stevens.

Contents

List of Figures

List of Tables

Chapter 1

Introduction

1.1 Extra Solar Planets

The field of "Exoplanets" began in 1992, with the first discovery of a planetary system orbiting another star, in this case the pulsar PSR1237+12 (Wolszczan and Frail, 1992). A pulsar is the rapidly rotating remnant of a massive star ($M_\star > 8\ M_\odot$), which has exhausted its fuel and ended its life in a supernova. It is therefore not a main-sequence (M-S) star like the Sun. The presence of nearby planets was revealed by observing the small (microsecond) variations in the arrival times of radio emission from the millisecond pulsar, which would otherwise be strictly regular. These variations, too small to be attributed to a stellar body, were later found to be due to three planets, with a combined mass of < 9 Earth-masses ($M_\oplus$) and all within 0.5 AU of their host star. Pulsar timing variations are just one of many measurable quantities which can convey the presence of a planet, via its influence on the host star. Therefore this constitutes just one method which can be used to detect planets. Other methods include astrometry, the radial velocity (RV) technique, the transit method, gravitational microlensing, transit timing variations (TTVs) and imaging, the later being the only method to directly observe planets rather than their host stars. A summary of these methods is presented in Table 1.1[1] whilst, due to its use in this work, the transit method is described in more detail in Section 1.2.

Following the first planetary detections, the next significant milestone was discovery 51 Peg b orbiting the main-sequence star 51 Pegasi, a G2-type star which is in the same evolutionary phase as our Sun. This famous discovery belongs to Mayor and Queloz (1995). They used the RV technique, which measures variations in the radial velocity of a star (along our line-of-sight) as it moves around its centre of mass. The discovered planet was found to have a minimum mass of 0.5 $M_{\rm J}$ (Jupiter masses) and be in orbit at

[1] Acronyms used to denote the surveys are as follows: High Accuracy Radial velocity Planetary Search (HARPS), Anglo-Australian Planet Search Program (AAPSP), California & Carnegie Planet Search (CCPS), Super-Wide Angle Search for Planets (SuperWASP), Hungarian Automated Telescope (HATNet), COnvection ROtation and planetary Transits (CoRoT), Optical Gravitational Lensing Experiment (OGLE), Very Large Telescope/Nasmyth Adaptive Optics System (VLT/NACO), Wide-field Infrared Survey Explorer (WISE).

a distance of just 0.05 AU from its host star. In this case (and with all RV detections), only a minimum mass could be established because of the unknown inclination angle, i, of the planetary orbit with respect to its star.

The discovery of 51 Peg b confirmed the existence of planets around stars like our own, but more than this, it contradicted the current theories describing planet formation and evolution. Until then these were based on the nine planets in our Solar system (Pluto still regarded as one), with the small rocky planets residing near to the Sun and the gas-giants much further away. However, 51 Peg b is a massive planet, orbiting extremely close to its host star, with an orbital period of just 4.2 days – a "Hot-Jupiter". This is now a category that describes all planets which are similar to Jupiter in mass and size, but only a short distance from their stars, such that their surface temperatures are extremely high. The high mass, short distance planets induce the biggest influence on their host stars so it is no surprise that the early detections were biased to Hot-Jupiters, as they were easier to detect by most methods.

Since the early discoveries, the field has flourished, with the rate of planet detections increasing each year, as shown in Figure 1.1. At this time[2] a total of 861 planets have been confirmed in 677 systems, of which 128 are multiple planet systems. In addition, there are thousands of potential candidates, awaiting follow-up observation to confirmation their nature.

The increasing rate of detection, indicated by Figure 1.1, owes itself to the large number of surveys which have joined the hunt for planets. Three of the major ground-based surveys are HARPS[3], SuperWASP[3] and OGLE[3], which use the RV, transit and lensing methods respectively to consistently discover and characterise new systems (e.g. Lo Curto et al. (2013a); Triaud et al. (2013); Han et al. (2013)). There are also two dedicated space-based missions, CoRoT and *Kepler*, which were launched in 2007 and 2009 respectively, bringing the field into a new era. These satellites have the advantage of escaping the effects of the Earths atmosphere, which limit the detectability of planets in ground-based observations. The absence of this source of noise in space, coupled with superior photometric precision, are the reason why CoRoT and *Kepler* currently provide the most planetary candidates from transit observations. This is conveyed in Figure 1.2, which shows a substantial increase in the detections of transiting planets, since these two missions began.

[2]Information accurate as of 1st April 2013, www.exoplanet.eu (Schneider, 1995).

[3]See footnote 1 on previous page.

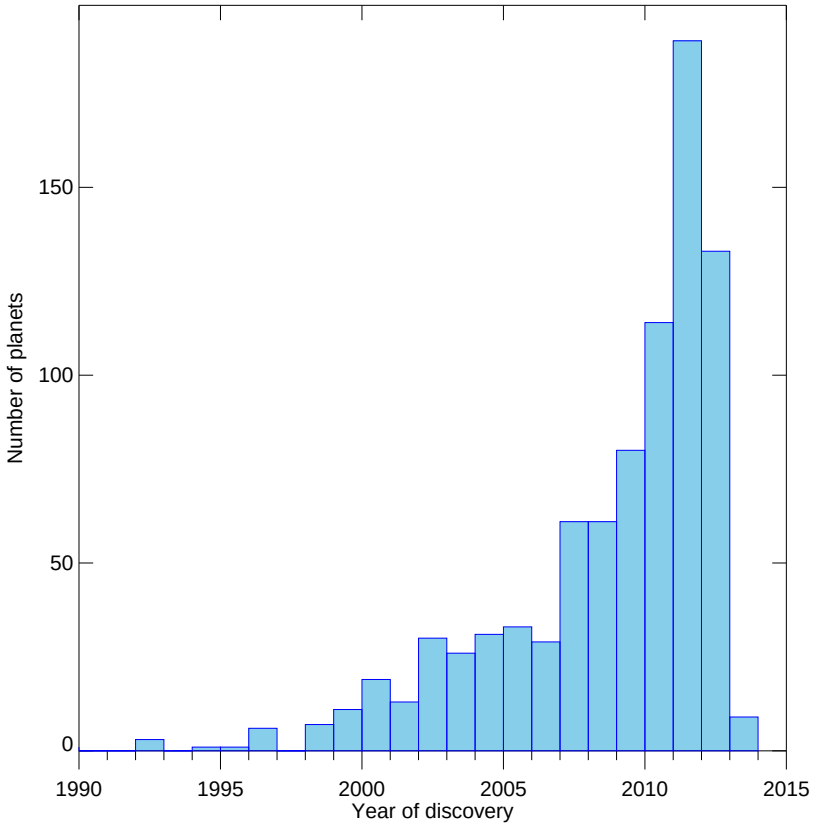

Figure 1.1: A histogram showing the number of planet detections made each year, following the first discovery made by Wolszczan and Frail (1992). This highlights the expansion of the field, owing to the increasingly sophisticated methods and instruments which are being developed in the field. The information is accurate as of 1st April 2012, from the Extrasolar Planet Database (Schneider, 1995).

1.2 Detecting transiting planets

The transit method is used to detect planets by measuring the fractional drop in stellar brightness as a planet passes across the disk of a star in our line-of-sight. It achieves this with a photometer, which exposes a Charged Coupled Device (CCD) to the incoming radiation from a star. The light arriving at the CCD is measured at regular intervals, producing a series of data points which constitute a light curve. If a transit occurs while a star is being observed, the planet will block a fraction of the star's light, proportional to the ratio of their sizes, as given by:

$$\delta = \left(\frac{R_{\rm P}}{R_\star}\right)^2 . \tag{1.1}$$

Here $R_{\rm P}$ and $R_\star$ are the radii of the planet and star respectively and δ is referred to as the signal depth. It follows from this equation that for a given $R_\star$, a larger planet is more easily detected than a smaller one.

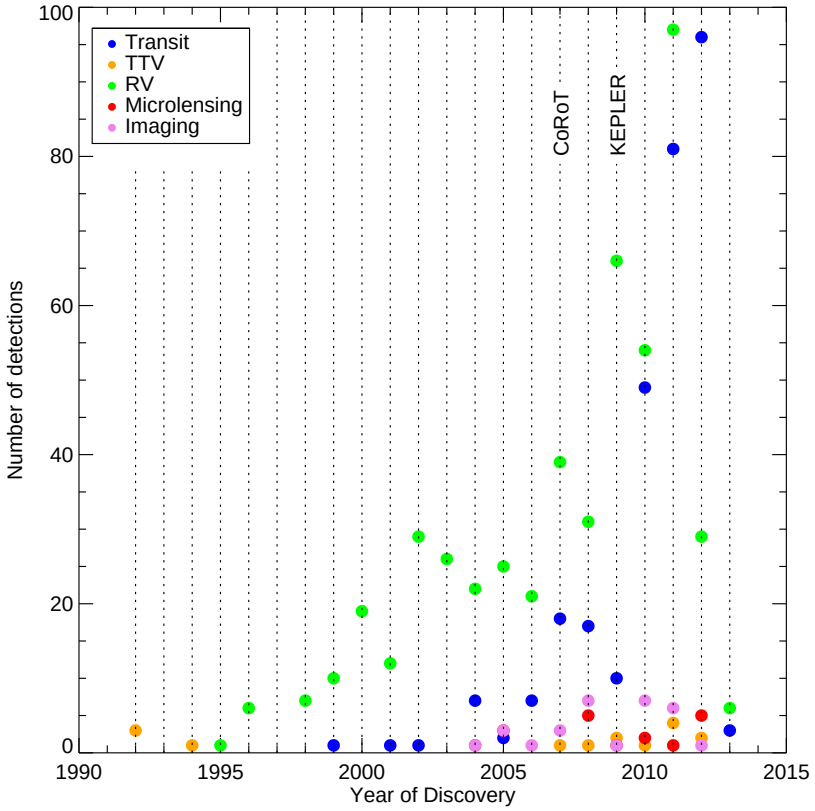

Figure 1.2: The number of planets detected each year, with respect to their method of discovery. This shows that the RV and transit methods have had the most success with regards to detection rate. It also conveys the rapid advancement in the field, following the launch of CoRoT and *Kepler*. The information is accurate as of 1st April 2012, from the Extrasolar Planet Database (Schneider, 1995).

For example, the Earth produces a signal depth of ~ 0.01 % when it transits the Sun, whereas Jupiter creates a larger, but still relatively small 1 % drop in flux. Figure 1.3 shows an example of a transit signal detected in a *Kepler* light curve[4]. This transit is from the recently discovered *Kepler*-68 b (Gilliland et al., 2013), which has a radius of 0.2 $R_{\rm J}$ and orbits a solar-sized star, producing a signal depth of 0.04 %.

One limitation of the transit method is that it can only be used to discover the subset of planets whose orbital planes are are aligned with our line-of-sight. The probability of this alignment is given by the equation below, where $R_\star$ is the stellar radius and a is the semi-major axis (the distance between the star and planet).

$$\mathcal{P}_{\rm tr} = \frac{R_\star}{a}. \tag{1.2}$$

This equation means that planets which are orbiting close to their host stars have a higher probability of

[4]Data courtesy of the NASA Exoplanet Archive – http://exoplanetarchive.ipac.caltech.edu.

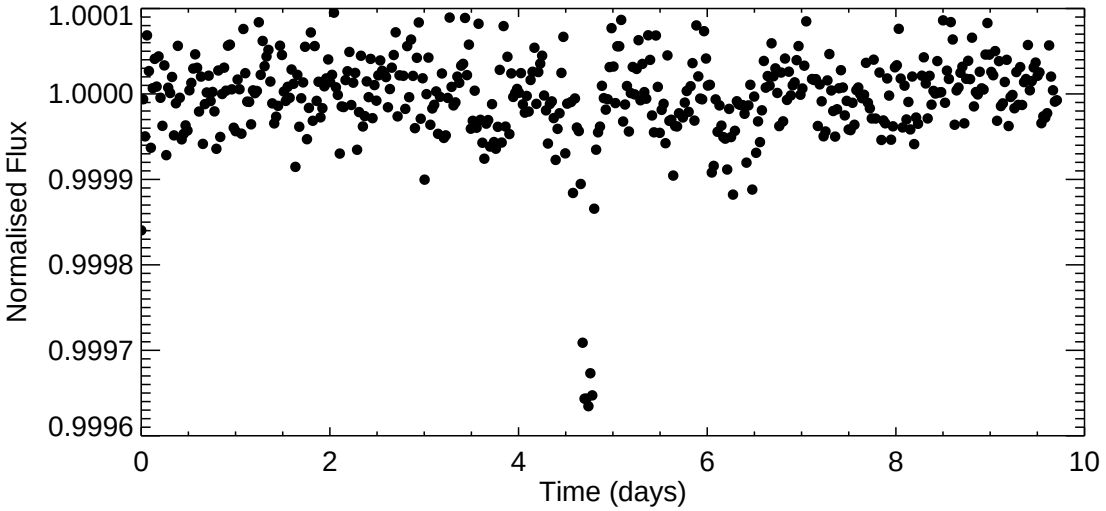

Figure 1.3: A part of the light curve obtained with *Kepler* for TYC 3551-189-1 (*Kepler* 68), which has V = 10. The transit is from *Kepler*-68 b (Gilliland et al., 2013), a planet with $R_{\rm P}$ = 0.2 $R_{\rm J}$ and a semi-major axis of 0.06 AU.

detection than those which are far away. As an example, for an observer outside the Solar system, the probability of an Earth-Sun transit is $\sim$ 0.5 %, while for Jupiter it is $\sim$ 0.01 %. However, if Jupiter was much closer to the Sun and a Hot-Jupiter like 51 Peg b, the probability for a transit increases to $\sim$ 10 %. This further explains the high detection rate of Hot-Jupiters, as indicated by Figure 1.4. This is a plot of planet radii versus semi-major axes for all transiting planets detected to date[5].

With regards to detecting transits, the probability of alignment must be considered together with the frequency of planets around other stars. Statistical studies such as Wright et al. (2012) find that the frequency of Hot-Jupiters around solar-type stars (spectral types F to K) is $\sim$ 1 %. This means that the probability of finding one that transits such a star is $\sim$ 1/1000. For this reason, most transit surveys have to be wide or deep-field to enable them to observe enough solar-like stars for a planet detection.

1.2.1 Transit characteristics

Depending on the characteristics of the detector, a light curve may have many points in a given time interval, or relatively few. This corresponds to the cadence of the observations, i.e. the time between consecutive data points. If the cadence is high, then a transit should have a relatively flat bottom and sloping sides, which correspond to the ingress and egress of the transit. An idealised transit shape is

[5]Information accurate as of 1st April 2013, www.exoplanet.eu (Schneider, 1995).

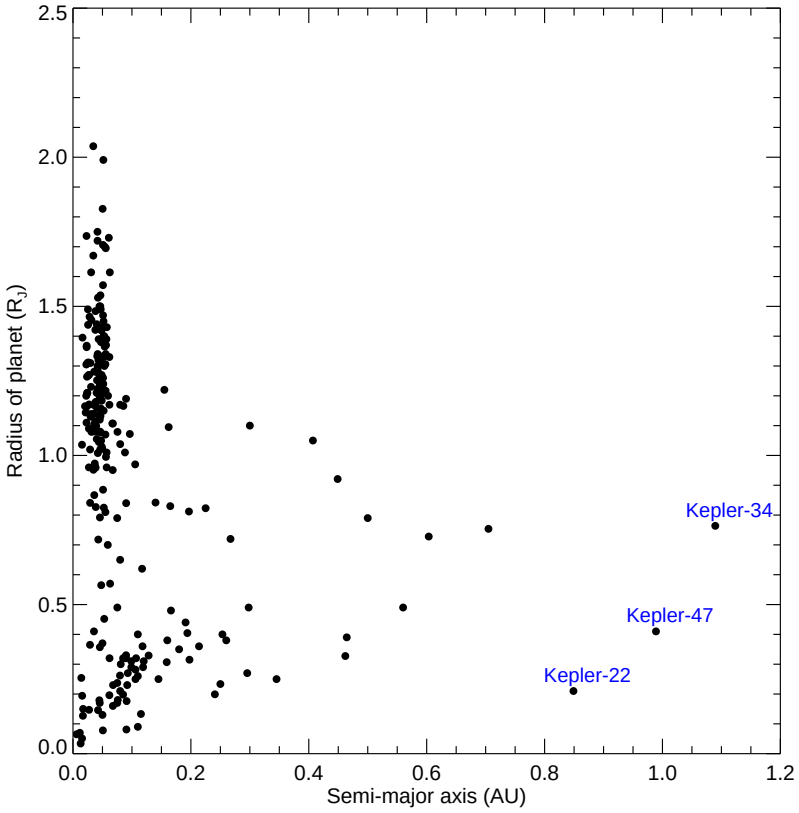

Figure 1.4: A plot of planet radius (in units of Jupiter radii) versus semi-major axis (in units of AU), for all transiting planets detected to date. The bias towards Hot-Jupiters is explained by their higher probability of detection and past limitations in photometric sensitivities and observing durations. This is changing now that CoRoT and *Kepler*, which observe continuously, are able to detect planets on wider orbits with periods of $\sim$ 1 year. The information is accurate as of 1st April 2012, from the Extrasolar Planet Database (Schneider, 1995).

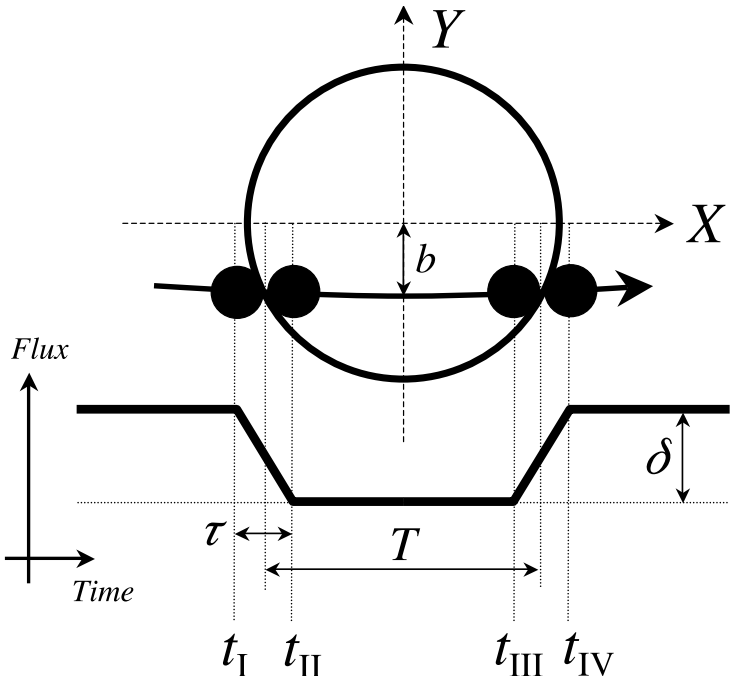

Figure 1.5: A schematic showing a planet's passage across a star, which gives to the characteristic transit shape shown above (Winn, 2010). The impact parameter, labeled as b on the diagram is the projected distance between a transit and the equator of the star. The ingress and egress are defined between four points of contact, $t_{\rm I} - t_{\rm II}$ and $t_{\rm III} - t_{\rm IV}$, respectively.

illustrated in Figure 1.5 (Winn, 2010). This also shows the different phases associated with a planet's passage across a star. The ingress and egress occur when a planet is entering and leaving the transit respectively. During these phases, marked between $t_{\rm I} - t_{\rm II}$ and $t_{\rm III} - t_{\rm IV}$ in the figure, the fraction of observed light gradually decreases and then increases, with respect to the proportion of the planet's disk blocking the star. The actual amount of blocked light is also dependent on the temperature of the star and the gradient of opacity in its atmosphere, also known as stellar limb darkening. In data with a high cadence, these two effects may be visible in the light curve, similar to the example shown in Figure 1.5. However, as the ingress and egress phases occur over a short duration, these features are only detectable in high cadence data. In light curves with a low cadence this information will be masked by the long integration time and transits of a few hours may appear more V-shaped than the typical U-shape.

The full formulation for calculating the transit duration is a function of many parameters. These include the host star's mass and radius, $M_\star$ and $R_\star$; the semi-major axis, a; the impact parameter, b (see Figure 1.5), which relates to the orbital inclination, i, by $bR_\star = a\cos i$. For a circular orbit with zero eccentricity,

the transit duration can be approximated as:

$$T_{\rm dur} = 1.8\sqrt{(1-b^2)}\frac{R_\star P^{1/3}}{M_\star^{1/3}}(hours), \tag{1.3}$$

where P is the orbital period (in days) and the other parameters are described before. This equation is equivalent to Equation 3 in Moutou et al. (2005) and is one of the many approximations which can be used to estimate transit duration. It is particularly suited to short-period planets, which are close enough to their stars to circularise their orbits due to tidal effects. Conversely, planets at greater distances from their host star may have more eccentric orbits, for example due to planet-planet scattering. This will affect the observed duration and hence the equation for $T_{\rm dur}$ should also account for this. It follows from Equation 1.3, and from observation, that most planets with periods < 10 days will have transit durations of a few hours, as shown in Figure 1.6. This is a plot of $T_{\rm dur}$ versus orbital period for transit detections to date[6], where the transit durations have been calculated with Equation 1.3 and therefore zero eccentricity is assumed.

The consequences of the orbital geometries described above imply the following list of requirements for any transit survey to have a successful outcome:

- The cadence of the observations must be shorter than the duration of the transit, so that the signal is not lost in the data.
- The total duration of the observations must be long enough, so that enough transits can be observed to be attributed to a positive detection.
- The noise, from atmospheric, instrumental and stellar effects (see Section 4.2), must not be greater than the depth of the expected signal (typically ≤ 3 %).
- A large number of stars must be observed, to counteract the low probability of a detection.

Aside from these factors, transit surveys have a separate issue to contend with – false-positives (FPs). These are pseudo transit detections, caused by different scenarios mimicking a transit signal (see Section 8.2). They can be extremely difficult to distinguish from genuine detections and so the transit method often relies on follow-up observations, conducted by RV surveys, to confirm planetary candidates. Conversely, transit detections are also beneficial to RV surveys, as they provide the inclination angle i, which cannot be measured from RV observations. Hence transit detections enable the planet's mass to be measured, as well as provide the size of the planet from the transit depth.

[6]Information accurate as of 1st April 2013, www.exoplanet.eu (Schneider, 1995).

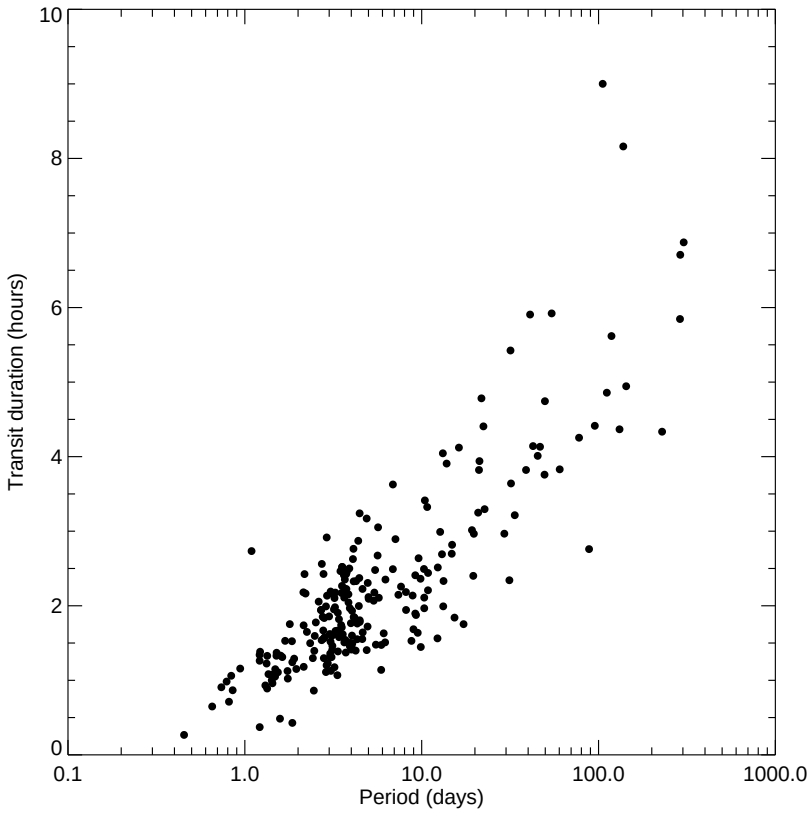

Figure 1.6: A plot of transit duration (in hours) versus period (in days) for all transiting planets detected to date. The transit durations were estimated with Equation 1.3, using the measured orbital parameters. The information is accurate as of 1st April 2012, from the Extrasolar Planet Database (Schneider, 1995).

1.3 Current motivations

The accelerating rate of discovery is a testament to the advancements being made in this field. However, Figures 1.1 and 1.2 do not convey the full extent of these developments with regards to the instrumentation, methods of detection and noise reduction techniques, which together determine the detectability of planets.

In the exoplanet community, studies are now being published on a daily basis with the results of newly confirmed planets as well as statistical analyses such as Fang and Margot (2012) and Fressin et al. (2013), which are based on a much wider range of planetary detections. In the past, planetary systems were expected to be found with similar characteristics to the solar system, i.e. with nearly coplanar, almost circular orbits, in a prograde direction. These features were explained by formation theories (e.g. Goldreich and Ward (1973)) which were based on the premise that all planets form within a proto-planetary disk, such that dense, rocky planets coalesce near to a star, while inflated gas-giants form further out. As of 2013, planets have been found in highly eccentric orbits, e.g. HD 98649 b (Mayor et al., 2011), or tilted with respect to to the spin-axis of their system, such as for XO-3 (Winn et al., 2009). Some planets have even been observed to orbit in a retrograde motion, which is in the opposite direction to the spin of the star, e.g. WASP-8b (Queloz et al., 2010). Each new discovery is an addition to growing census of planets, whether in agreement with existing observations or challenging the current theory. Ultimately, this census will help us to understand the physical processes that govern the formation of planetary systems, enabling us to predict their evolution.

Aside from an ongoing quest to discover all types of planetary system and refine current theories, the motivations which are currently driving the exoplanet community can be summarised as follows:

- Discover Earth-analogs, which are potentially habitable and possibly sustaining life.
- Survey more planets around bright stars, which provide high signal-to-noise ratios and enable more accurate determinations of the measurable quantities. Bright stars also require less observing time with regards to ground-based spectroscopic follow-up. Therefore these can be more easily confirmed from the determination of their masses.
- Detect more planets in binary systems, such as Kepler 16 (Doyle et al., 2011) and Kepler 47 (Orosz et al., 2012). It is suggested that at least 50% of G-type dwarfs (Raghavan et al., 2010) and 30% of M-type dwarfs (Fischer and Marcy, 1992) reside in binary systems. Therefore, discovering more

planets around either close or widely separated binary stars, will lead to a better understanding of the formation and stability of planetary systems.

- Continue to develop detection methods and noise removal techniques, which are an important determinant in the detectability of planets. This will reduce the detection bias towards giant, short-period planets, which produce the most detectable signals in RV and transit surveys. Hence more Earth-analogs and other interesting systems should be found.

1.4 What can STEREO offer transit surveys?

The purpose of this thesis is to present an analysis of the photometric data from STEREO's HI-1A. From an early assessment of the raw data, it was predicted that with careful noise-reduction techniques, this detector could make a valuable contribution to the current transit surveys. For example Figure 1.7 illustrates a current observational gap for transiting planets around bright stars ($V < 8$). In this figure, which uses cross symbols to represent transit detections and grey circles to represent detections by other methods, the apparent V-magnitudes are shown, of all currently confirmed host stars[7]. Whereas CoRoT and *Kepler* are limited to observing stars no brighter than V=11 and V=9 respectively[8], STEREO's HI-1A will be able to probe the brighter magnitude regime, with continuous (20-days) and repeated observations (yearly).

A comparison between the main strengths and limitations of ground and space-based observations are listed in Table 1.2. The purpose of this table is to show that, whereas CoRoT and *Kepler* have superior photometric precision, ground-based surveys are able to observe stars which space-based surveys currently cannot and therefore they are complementary to each other.

The recently approved[9] space-based mission TESS (Transiting Exoplanet Survey Satellite) will also make a valuable new addition to family of transit surveys. This mission, which is scheduled to be launched in 2017, is to be an all-sky survey which monitors stars with $5 \leq \mathrm{V} \leq 12$, meaning that it will observe stars out with the scope of CoRoT and *Kepler*, but with a similar photometric precision. However, as TESS won't be operational for a few years, there is still much that can be accomplished by a survey with STEREO's HI-1A camera, which offers the following benefits:

[7] Information accurate as of 1st April 2013, www.exoplanet.eu (Schneider, 1995).

[8] NASA Exoplanet Archive, http://exoplanetarchive.ipac.caltech.edu/.

[9] NASA official news release regarding TESS approval can be found at: http://www.nasa.gov/home/hqnews/2013/apr/HQ_13-088_Astro_Explorer_Mission_.html.

- A substantial field-of-view (FOV), covering $\sim$ 20 % of the sky (see Figure 1.8).
- An intermediate range of magnitudes (with respect to current ground and space-based surveys): $4 < V < 12$.
- It avoids atmospheric effects and therefore is not limited by seeing, etc.
- The HI-1A instrument has uninterrupted observations, providing up to 20 days of continuous data per year, for each target.
- The observations are repeated annually, allowing long-term studies to be conducted. This is useful for monitoring the effects of long-term stellar variability and spots on the detections of transit signals.
- The ability to learn from the effects of space-based systematic noise in photometry, so that valid detrending methods may be developed.

These factors, together with Figures 1.7 and 1.8, suggest that a transit survey with STEREO's HI-1A could make a valuable addition to the field. Therefore, the production of light curves, an analysis of the data and work to optimise it for a transit search, are worthy challenges, all which form the basis of this thesis.

1.5 Thesis outline

As follows:

- Chapter 2 gives an introduction to the STEREO mission and a description of the HI-1A instrument, which has provided the photometric data used in this work. A summary of the calibration pipeline, SECCHI-PREP, is also included. This is the standard reduction routine for the HI data, which includes flat-field and background corrections, among others.
- Chapter 3 describes the methods for producing the stellar light curves from the HI-1A images. This task required the use of the BlueBEAR computer cluster, at Birmingham University, for processing and storing the substantial amount of data. In total, light curves for $\sim$ 74,000 targets were obtained.

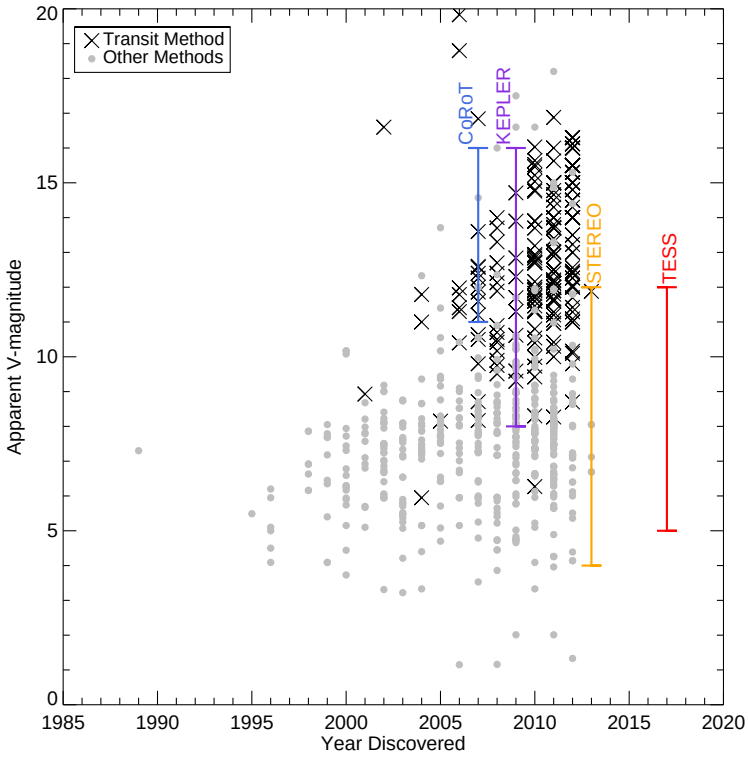

Figure 1.7: The apparent V-magnitudes of host stars, with respect to detection date. This highlights the observational bias in transit surveys towards fainter stars and therefore the need for new space-based missions, e.g. STEREO and TESS, which can bridge the observational gap. The information is accurate as of 1st April 2012, from the Extrasolar Planet Database (Schneider, 1995).

- The original HI-1A light curves were found to possess a variety of systematic and observational influences, including vignetting, tracking errors and solar flux. These are presented in Chapter 4, with examples to illustrate their impact on the data. This chapter closes with a summary of the main systematic trends, which could limit the outcome of a transit survey.

- Chapter 5 describes the HI-1A trend removal pipeline (TRP), which was constructed to counteract the effects of the main sources of noise. This pipeline draws on various resources and techniques, including a non-linear iterative filter (NLF), to create an effective noise reduction process with negligible impact on transit-type signals. These results are shown for three light curves with short-duration eclipses. Two examples of anomalous results are also discussed.

- Chapter 6 presents the noise analysis. This was based on a method for estimating the correlated noise (from the systematics) on a two hour timescale, which is the approximate duration for a detectable transit in the HI-1A light curves. This chapter includes an evaluation of the detection

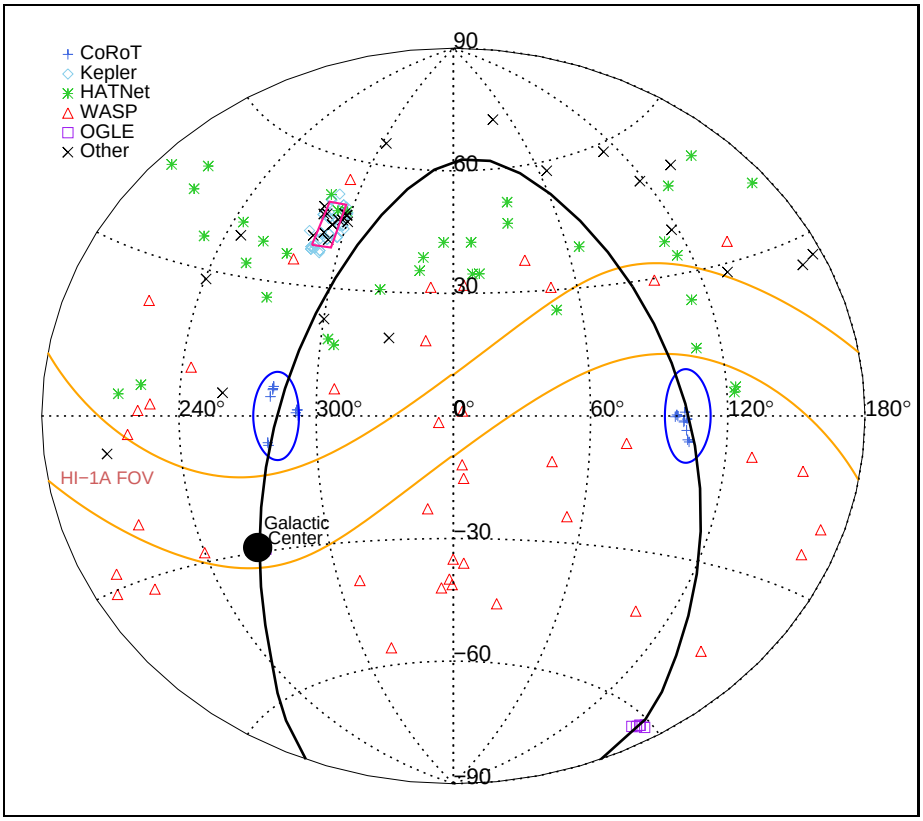

Figure 1.8: An all-sky map illustrating the HI-1A FOV in the context of other transit surveys, in the equatorial coordinate system. The *Kepler* FOV is indicated by the hot pink rectangle at [290.5°, 44.5°] and the CoRoT fields are shown as blue ellipses at [282.5°, 0°] and [102.5°, 0°]. The HI-1A views the 20°-wide region within the orange lines. All host stars found by the main transit surveys are plotted according to the key, where 'Other' refers to the Qatar and XO projects, among others. The Galactic Plane is shown as the thick black line with the Galactic Centre labeled for reference.

threshold for a transit survey, with regards to the signal-to-noise ratio of the detrended data.

- Chapter 7 contains the details of the transit search, which was performed with strict detection criteria to avoid an overwhelming number of false-positive detections from other astrophysical sources, e.g. eclipsing binaries. A sample of model light curves, based on the HI-1A data, were constructed to determine an appropriate threshold to be used by the transit detection algorithm.

- Chapter 8 presents the analysis of candidates from the transit search, which involved a series of vetting tests to establish the planet-likelihood the detected signals. These tests include statistical tools from the literature, in addition to custom methods, such as a test for contamination using available catalogue data.

- Chapter 9 discusses the results of the HI-1A transit survey and future improvements that could be made to increase the likelihood of planet detection in subsequent transit searches.

	Measurement	Number of Detections	Measured parameters	Biased towards	Used by
Radial Velocity (RV)	• The velocity semiampltiude of the host star ($K_\star$); proportional to the planets mass (M_p) and semi-major axis (a). • $K_\star \sim 10$ m s^{-1} for Jupiter-Sun orbit. • $K_\star \sim 10$ cm s^{-1} for Earth-Sun orbit.	• **504**, e.g. HD 159868 c (Wittenmyer et al., 2012), BD-061339 b (Lo Curto et al., 2013b).	• Period, P. • Semi-major axis, a. • Lower mass limit, $M_\mathrm{p}\mathrm{sin}i$, where i is the inclination.	• Massive planets. • Small semi-major axes.	• HARPS • AAPSP • CCPS
Transit	• The fractional drop, δ, in a star's flux as a planet passes across it, where $\delta = (R_\mathrm{P}/R_\star)^2$. • $\delta \sim 1$ % for Jupiter-Sun transit. • $\delta \sim 0.01$ % for Earth-Sun transit.	• **294**, e.g. WASP-80 b (Triaud et al., 2013), HAT-P-34 b (Bakos et al., 2012).	• Period, P. • Radius ratio, $R_\mathrm{P}/R_\star$. • Scaled semi-major axis, $a/R_\star$.	• Giant planets. • Small semi-major axes.	• SuperWASP • HATNet • CoRoT • *Kepler*
Transit timing variations (TTVs)	• The variations in the times of transits, caused by non-transiting planets. • Minute timescales for Earths. • Hour timescales for giants.	• **15**, e.g. Kepler-9d (Holman et al., 2010), KOI-872 c (Nesvorný et al., 2012).	• Period, P. • Semi-major-axis, a. • Mass, M_P.	• All planets, so long as they are in resonance.	• MOST • *Kepler*
Gravitiational microlensing	• The perturbation of light from distant stars, by a planet's gravitational field. • Timescale of perturbation on the scale of 1 day.	• **18**, e.g. OGLE-2006-BLG-109L (Gaudi et al., 2008), OGLE-2007-BLG-368L b (Sumi et al., 2010).	• Mass ratio, $M_\mathrm{P}/M_\star$ • Semi-major axis.	• All planets. • Large semi-major axes.	• OGLE • VLT/NACO
Direct imaging	• The direct visible/thermal emission from a planet, using adaptive optics or nulling interferometry.	• **30**, e.g. Fomalhaut b (Kalas et al., 2005), HR 8799 b,c,d (Marois et al., 2008).	• Mass, M_P. • Semi-major axis.	• Giant planets, with faint host stars. • Large semi-major axes.	• Spitzer • WISE • Subaru

Table 1.1: A summary of the main methods used to detect planets. All acronyms are given in the footnote on page 1.

	Ground-based	Space-based
Strengths	• Observe a wide range of stellar magnitudes, e.g. HATNet covers $V = 2.8 - 17.8$. • All-sky, i.e. not confined to a single field-of-view (FOV) (see Figure 1.8). • The bright candidates can be easily confirmed with follow-up RV observations.	• Superior photometric precision: *Kepler* ~ 0.01 % $\rightarrow$ Earths. CoRoT ~ 0.04 % $\rightarrow$ Super-Earths. • Long-baseline, uninterrupted observations $\rightarrow$ detect long-period planets (Earth-analogs). • Avoids atmospheric effects.
Weaknesses	• Atmospheric conditions limits the photometric precision to ~ 1 %. • Observations interrupted by diurnal cycle, which affects the detectability of transit signals. • Observations are subject to weather and time constraints; it is not feasable to monitor the same FOV for long durations (i.e. short-baseline).	• Magnitude limited: $9 < V <16$ – *Kepler*. $11 < V <16$ – CoRoT. • Only observe a small fraction of stars in the sky: *Kepler* FOV = 115 degrees^2. CoRoT – two FOVs = $\sim$ 78 degrees^2 each.

Table 1.2: The main strengths and limitations of the current ground and space-based transit surveys. This shows that ground-based surveys are complementary to CoRoT and *Kepler* and vice versa. It also conveys the need for more surveys with the ability to study bright stars with uninterrupted observations, such as STEREO and TESS. The values given here are provided by the NASA Exoplanet Archive (http://exoplanetarchive.ipac.caltech.edu).

Chapter 2

Introducing STEREO and the HI instrument

2.1 Introduction

The NASA Solar TErrestrial RElations Observatory (STEREO) was designed to make observations of solar phenomena in 3D by positioning two spacecraft on either side of the Sun. Since their launch in October 2006, these identical satellites have enabled the study of solar activity and coronal mass ejections (CMEs) in unprecedented detail by offering a 360° view of the Sun. So far the mission has made significant advances in solar studies, such as obtaining the first complete image of the far side of the Sun[1] and observing the fastest CME on record[2], at $\sim$ 2000 miles s^{-1}. The images and information provided by STEREO are enabling a better understanding of solar activity, the space weather this creates and the effect that this has on the Earth. But by an unexpected coincidence, it is also very well suited to wide-field stellar studies using the photometry of the background stars, which are abundant.

The orbits of each satellite are illustrated in Figure 2.1, in red (A) and blue (B). The twin satellites travel in heliocentric orbits at 0.97 and 1.07 AU respectively. In this configuration STEREO-A advances while STEREO-B recedes from the Earth by $\sim 22°$ each year.

Onboard each satellite is a multi-instrument suite called SECCHI (Sun-Earth Connection Coronal and Heliospheric Investigation). This includes an extreme UV imager (EUVI), a pair of white-light coronographs (COR-1 and COR-1) and a pair of Heliospheric Imagers (HI-1 and HI-2). SECCHI is located on the front of the satellites, as shown in Figure 2.2. Included in the diagram are the locations of the other instrument packages, which all monitor different different aspects of solar activity. Details of these can be found on the main STEREO website[3].

The Heliospheric Imagers are used primarily to observe the propagation of CMEs along the Sun-Earth

[1]The corresponding news article can be viewed at http://www.nasa.gov/mission_pages/stereo/news/farside-060111.html.
[2]The corresponding news article can be viewed at http://www.nasa.gov/mission_pages/stereo/news/fast-cme.html.
[3]The details of the STEREO instruments can be found here: http://stereo.gsfc.nasa.gov/instruments/instruments.shtml.

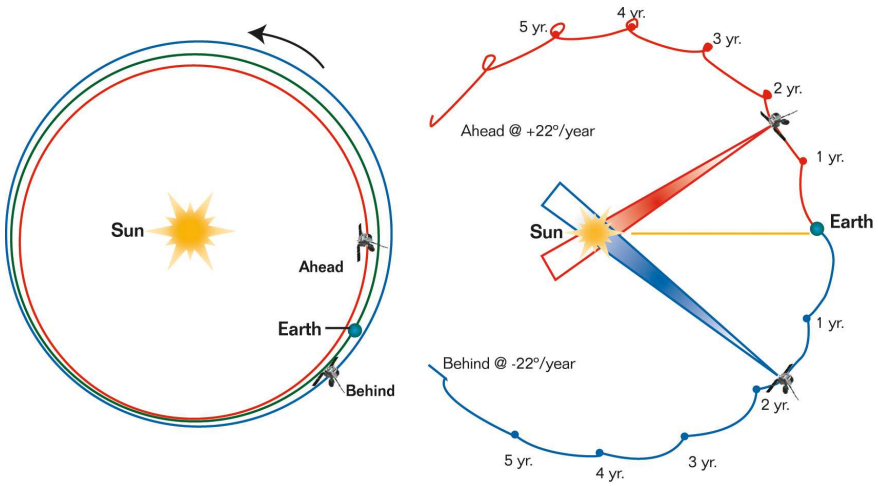

Figure 2.1: The heliocentric trajectories of the STEREO satellites. STEREO-A moves ahead of the Earth at a rate of $\sim 22^{\circ}$ year^{-1} while STEREO-B recedes from the Earth at the same rate (Image courtesy of NASA/Johns Hopkins University Applied Physics Laboratory).

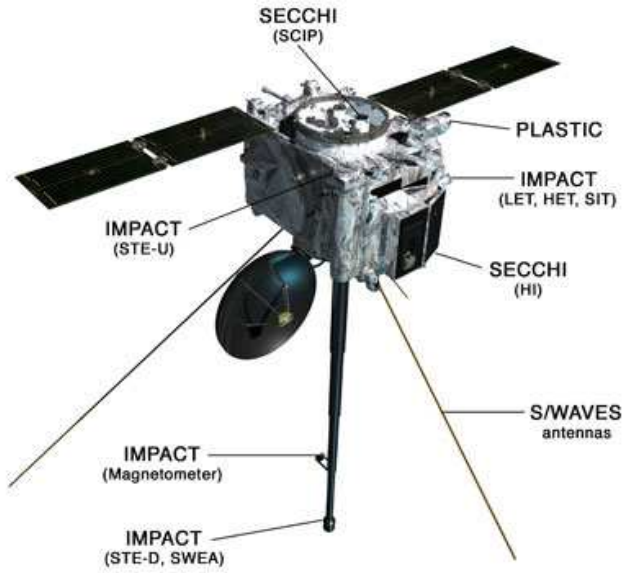

Figure 2.2: A schematic of one of the STEREO satellites showing the location of each instrument package and the HI, which is directed toward the Sun (Image courtesy of NASA/Johns Hopkins University Applied Physics Laboratory).

plane. While monitoring this region, they also observe an abundance of diverse background stars, providing a wealth of photometric data for stellar studies.

The work presented in this thesis is based primarily on the observations of the HI-1 detector onboard STEREO-A. The key features of this instrument are presented in the next section, followed by a description of SECCHI-PREP, the standard calibration pipeline for all SECCHI instruments.

2.2 The HI-1

The HI-1 and HI-2 are mounted on the front of the STEREO spacecraft, as shown in Figure 2.2. A complex baffle system surrounds the cameras, which helps to shield the detectors from direct and scattered Sun light. The later refers to the F and K-coronas, which are due to dust particles and free electrons respectively. Their combined brightness is $\sim 10^{-9}$ - 10^{-12} $B_{\odot}$ (where $B_{\odot}$ is the intensity of the solar disk); this is at least an order of magnitude above that of a typical CME and comparable to that of the background stars, which range between 10^{-9} - 10^{-11} $B_{\odot}$. Despite the baffle system, solar contamination remains a major issue, but efforts to reduce it are implemented by the calibration routine (Section 2.3).

The HI-1 and HI-2 cameras have a field-of-view (FOV) measuring $20^{\circ} \times 20^{\circ}$ and $70^{\circ} \times 70^{\circ}$ respectively. Ideally, both cameras would be used for a planet search, giving a larger FOV and hence increasing the likelihood of discovering a planet. However, the CCD on the HI-2 camera has a relatively larger pixel size and point-spread-function (PSF) than HI-1, resulting in a lower angular resolution. This means that the light curves from the HI-2 camera are noisier and have insufficient photometric precision for transit surveys. For this reason, only the higher quality, HI-1 data are considered.

For ease of reference, the HI-1 specifications are listed in Table 2.1. This CCD is a visible light detector with 2048×2048 pixels, having angular dimensions of 35.15×35.15 arcsec. For comparison, this is approximately 10-times greater than the pixel size of the *Kepler* and CoRoT detectors, meaning that the STEREO light curves will be much more prone to contamination from stars which are nearby on the CCD.

The optical axis of the camera is aligned with the ecliptic plane and its centre is directed $\sim 14^{\circ}$ from the Sun. This places the Sun just 4° from the right and left-hand edges of the HI-1A and 1B images respectively. A schematic of the HI-1A detector is shown in Figure 2.3. This illustrates the spread of solar contamination in the images, particularly from CMEs. The shaded parts of the diagram are the areas affected by vignetting, where there is a reduced response in the pixels. This occurs because the

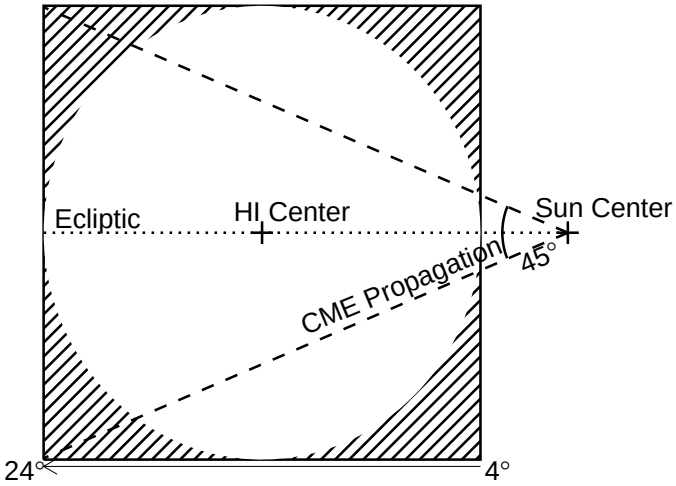

Figure 2.3: Diagram of the HI-1A detector. This illustrates the areas affected by vignetting (shaded regions) and also the range of typical CMEs, which are expected to remain within a cone of 45° extending out from the Sun in the ecliptic plane (Socker et al., 2000).

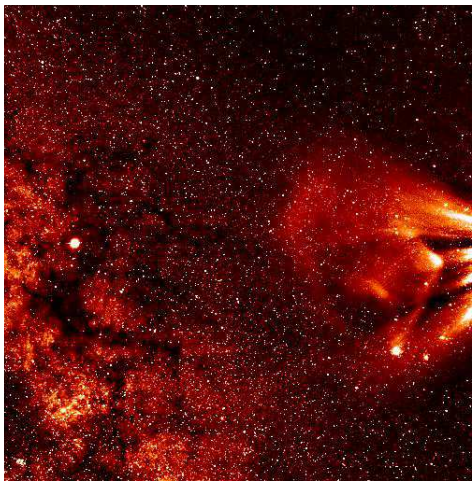

Figure 2.4: A reduced image from HI-1A, showing a CME on the right-hand side as well as scattered light covering most of the field. Despite this, the background stars are still very prominent. (Image courtesy of stereo.rl.ac.uk.)

CCD is a square design, whereas the optics are circular and so the corner pixels receive less photons than those in the circle shown on the diagram. Although the flat-field has been optimised to reduce this effect (Bewsher et al., 2010), it is still an issue for many light curves, as shown in Chapter 4. The adjacent image in Figure 2.4 was taken by the HI-1A camera and has been calibrated with SECCHI-PREP (described in the next section). This observation shows scattered light across the whole FOV and a bright CME on the right-hand side.

The CCD is back-illuminated, meaning that the incoming photons have a direct path to the semi-conductor material without being absorbed by the electrodes. This gives a quantum efficiency of 93 % at $\sim$ 550 nm. A standard anti-reflective (AR) coating has been used which provides optimum spectral coverage in the range of 430 nm $-$ 730 nm (closest to the R-bandpass), but there is reduced transmission down to 400 nm and up to 950 nm.

Each image from the HI-1 consists of 30 exposures of 40 seconds each. This avoids saturation while achieving the required signal-to-noise ratio (SNR) in the observations. This also benefits the removal

Centre of Field of View from the Sun	13.98°
Angular Field of View	20°
Image Array (2x2 binning)	1024×1024
Image Pixel Size	70.3 arcsec
Average PSF (FWHM)	111 arcsec
Spectral Bandpass	630-730 nm
Exposure time	40 seconds
Nominal Exposures Per Image	30
Image Cadence	40 min
Brightness Sensitivity	3×10^{-15} $B_\odot$

Table 2.1: HI-1A instrument specifications ($B_\odot$ is the intensity of the solar disk).

of cosmic ray effects, which have an impact rate of 45 pixels s^{-1}. Cosmic rays and other high-energy particles are eliminated during on-board processing by comparing each 40 s exposure to the preceding one on a pixel-by-pixel basis. If the value in a given pixel exceeds a 5-σ threshold (where σ is the expected photon noise), it is replaced with the value from the previous image.

As a consequence of both telemetry restrictions and the timescales of CME propagation, the total image cadence is 40 minutes. This means that in each image, light from the star has been recorded for only 50% of the time, giving an effective duty cycle of 50% over the total duration of the observation (up to 20 days).

The original observations are binned up, 2×2, producing binned images with 1024 × 1024 pixels, having angular dimensions of 70.3 × 70.3 arcsec. In these images, the source point-spread function (PSF) has a full width at half maximum (FWHM) value of ∼1.5 image pixels in the x and y directions (Bewsher et al., 2010). This means that the majority of the flux from a point source should reside in a circle with a diameter of 1.5 pixels, equating to an angular area of ∼ 2.4 square arcmin.

The consequence of binning the data is that the PSF is slightly undersampled. This is according to (Howell et al., 1996), who define the sampling parameter, r, as:

$$r = \frac{\mathrm{FWHM}}{p}, \tag{2.1}$$

where the FWHM and pixel size, p, are in the same units. For HI-1A data, the above equation gives

r =1.5, which is considered to be only marginally sampled ($r \leq 1.5$ is undersampled). The effect of this in light curves is discussed in more detail in Section 4.3.1.

When the instrument is performing optimally, a total of 36 image frames are produced per day. This provides up to 720 photometric measurements in 20 days, which is the time average taken for each star to pass over the FOV. However, telemetry errors and momentum dumps (which are both frequent) produce gaps in the data and missed data points.

It is found that large gaps in the time series can adversely affect the performance of transit detection algorithms (Section 7.2) and lead to false results. However, the trend removal pipeline (Chapter 5), includes a stage to avoid this outcome in the subsequent transit search, by bridging large data gaps with artificial data.

2.3 Initial calibrations with SECCHI-PREP

All HI images are available from the UK Solar System Data Center[4]. There are three levels of data with different stages of calibration applied: Level 0 is raw (uncalibrated), Level 1 has undergone basic processing (described below) and Level 2 has an additional background correction applied (described in Section 2.3.1).

SECCHI-PREP is the standard data reduction routine for all SECCHI instruments[5]. It is designed to remove various instrumental effects which occur during data acquisition and accomplishes this with the following pipeline:

1. **Identify and remove saturated columns.** HI-1A has a pixel full well capacity of $\gtrsim$ 200,000 e^-. When this capacity if exceeded, for instance when a particularly bright object such as a planet is observed, saturation occurs. This causes excess charge to "bleed" into adjacent pixels in the same column. Bleeding is prohibited along rows due to physical barriers in the CCD. Saturated pixels invalidate the shutter-less readout correction (described below) so the entire column must be removed and the pixel values replaced with 'NaN' values. Further the consequences of saturation in the light curves are discussed in Section 4.4.

2. **Identify missing data and replace with zero values.** Telemetry "drop-outs" and bi-monthly momentum dumps are two of the main causes of missing data. While the latter is anticipated and

[4]UKSSDC: www.ukssdc.rl.ac.uk/solar/stereo/data.html.

[5]SECCHI-PREP is an IDL routine from the SolarSoftWare distribution (Freeland and Handy, 1998).

usually last for a few hours ($\sim 7 - 8$ images), the former occurs at random times and can affect either a single or many consecutive images.

3. **Shutter-less readout correction.** This compensates for the absence of shutters on the instrument, which is due to mechanical constraints.

   Following an exposure, each line of pixels is read out horizontally and the counts from each pixel are recorded. The CCD is then cleared of residual charge in the vertical direction, ready for the next observation. In HI-1A, the readout time of each line, $T_{\rm read}$, is ~ 2.3 ms and the clear time of each column, $T_{\rm clear}$, is ~ 0.1 ms. As there are m rows of pixels, where m goes from 0 to 2048 (pixels), each row will be exposed to incoming radiation for an additional time of $m \times T_{\rm read}$. This causes objects in the image to appear smeared vertically upwards. The clearing sequence causes smearing in the opposite direction, but as $T_{\rm clear} \ll T_{\rm read}$, this effect is much more subtle.

   The shutter-less readout correction involves calculating, for each pixel at (x, y), a total response time $R_{\rm time}$, which is obtained by the following matix multiplication,

$$R_{\rm time}(x, y) = T(x, y)\, I(x, y), \tag{2.2}$$

   where I is the count rate for a given pixel in the original image. The T in the equation is a matix with 2048 $\times$ 2048 elements, filled with $T_{\rm exposure}$ along the diagonal, $T_{\rm read}$ above the diagonal and $T_{\rm clear}$ below it. Therefore the original (smeared) image may be corrected for the effects of shutter-less readout by multiplying $R_{\rm time}$ by the T^{-1}, i.e.

$$I_{corrected} = R_{\rm time}\, T^{-1}, \tag{2.3}$$

   At this stage the pixel values would usually be summed over each exposure to give a total count. However, as the total readout time for the CCD is ~ 4.8 seconds, which is a significant fraction of the observation time, rather than converting the measurements to a total signal in DN (data counts), units of count rate are used instead, i.e. DN s^{-1}.

4. **Large-scale flat-field correction.** An update to the standard flat-field correction was developed by Bewsher et al. (2010), to account for the reduced response in the corners of the detector (see Figure 2.3). The original version, which was calibrated pre-flight using a light source, wrongly assumed axial symmetry around the central line and therefore failed to correct for the effects of vignetting.

The method for the updated calibration use a sample of stars, observed from 2007 – 2008, to determine the ratio of measured to predicted intensity across the CCD, i.e:

$$R = \frac{I_{\rm meas}}{I_{\rm pred}}. \tag{2.4}$$

For the calculation, $I_{\rm meas}$ is the measured flux from the star and $I_{\rm pred}$ is estimated from one of the following methods:

(a) For stars with a known spectral type and where their spectrum is available in the Pickles library of stellar spectra (Pickles, 1998), $I_{\rm pred}$ can be found by folding the spectrum through the instrument response function. This means taking the component of the spectrum that corresponds to the wavelength range of the detector, converting it to units of photons, then multiplying this by the instrument response and integrating over the total wavelength range.

(b) If a star's spectral type is unknown, then instead its B, V and R magnitudes can be used to find $I_{\rm pred}$, by mapping these colours to the HI magnitude scale (calculated from the spectral folding).

Once a value for R has been obtained, the new flat-field correction is given by the following equation,

$$f = \frac{1}{R}. \tag{2.5}$$

This corrects for large-scale difference in the response of the detector, but does not account for pixel-to-pixel variations. For the latter, a small-scale flat-field correction is required, however this has not been developed at this time.

5. **Update pointing parameters.** The pre-flight header values for the spacecraft attitude are replaced with updated values, called the attitude solutions. These are calculated on an image-by-image basis, using up to 80 known stars in the field-of-view (FOV). Starting with an estimate for the pointing, the stars are identified and their positions are measured. These positions are then compared with the catalogue positions to derive an optimized attitude solution for the whole image frame. Following this, the average error on the position of a star is less than 1 image pixel, which is equivalent to 70.3 arcsec. This is used as the margin of error to identify the targets in the images (see Section 3.4).

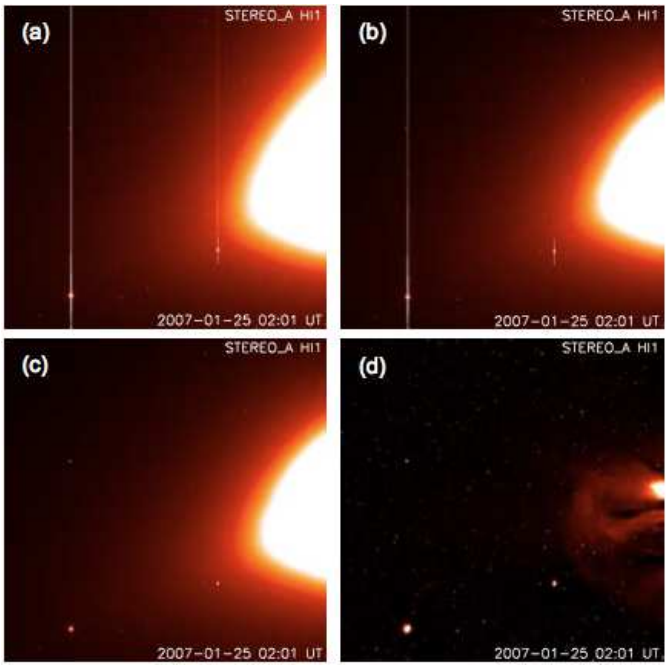

Figure 2.5: SECCHI_PREP results for an image from HI-1A, taken on January 25 2007. This shows, a) The original image; b) After shutter-less and flat-field corrections have been applied; c) After removing saturated columns, due to Venus and Mercury; and d) After background subtraction.

2.3.1 Background removal

Background removal takes the images from Level 1 to Level 2 by removing the F-corona with a one-day-minimum-map. This is essentially a matrix containing the minimum values in each pixel, over a sequence of 36 images. It is effective in removing the F-corona because this component is slowly evolving compared to the drift of the stars across the FOV ($\sim$ 2.5 arcmin hour^{-1}). Other sources of background light, such as CMEs and solar flux, can occur on shorter and longer timescales, therefore not all components of background light are removed by this process.

Figure 2.5 shows the results of the various stages of SECCHI_PREP for an image taken with HI-1A. Panel (a) contains the original (Level 0) image and (b) shows it after the shutter-less readout and flat-field corrections have been applied. In (c) the saturated columns, which were due to Venus and Mercury, have been removed and lastly, panel (d) shows the effect of the background removal. As seen by the final image, a CME is still clearly visible on the right-hand-side, which is a source of contamination in the light curves, when the stars enter this region.

The next chapter describes the process of selecting and tracking the targets in the Level 2 images and the production of their light curves using aperture photometry.

Chapter 3

From Images to Light Curves

3.1 Introduction

This chapter describes how the stellar light curves were produced from the Level 2 images, i.e. Figure 3.1. In total, light curves for over 70,000 stars were extracted from the images, for the period of April 2007 to November 2011.

The Level 2 data were downloaded from the UK Solar System Data Center (UKSSDC)[1] at the Rutherford Appleton Laboratory (RAL), using the rsync facility. This unix utility copies the data from the remote server at RAL to the local destination (here) via a secure connection. It is more suited for syncing a large number of files in a complex directory tree, than ssh for example.

Initially, the aim was to use the images from both HI-1A and HI-1B, to increase the data set for each star. By using both detectors, each target could have 40 days of data per year, instead of the 20 days possible with a single camera. Hence, the images from both detectors, totaling to $\sim$ 120,000 files for these five years, were downloaded and processed in the following manner. The file size for this complete set of data is $\sim$ 533 GB.

3.2 BlueBEAR processing

The BlueBEAR computer cluster (Birmingham Environment for Academic Research) is a substantial facility for large-scale processing. This service is available to registered users and provides access to additional memory and storage, such were the requirements here. In total, the cluster has 848 cores running at 2.2 GHz. Through BlueBEAR, the IDL[2] virtual machine can be accessed. This offers a restricted version of IDL where there is no command line, meaning that all necessary programs must be

[1] All levels of HI data can be downloaded from http://www.ukssdc.ac.uk/solar/stereo/data.html.

[2] IDL (Interactive Data Language) is a powerful computer language which is useful for the analysis and visualisation of a wide range of scientific data.

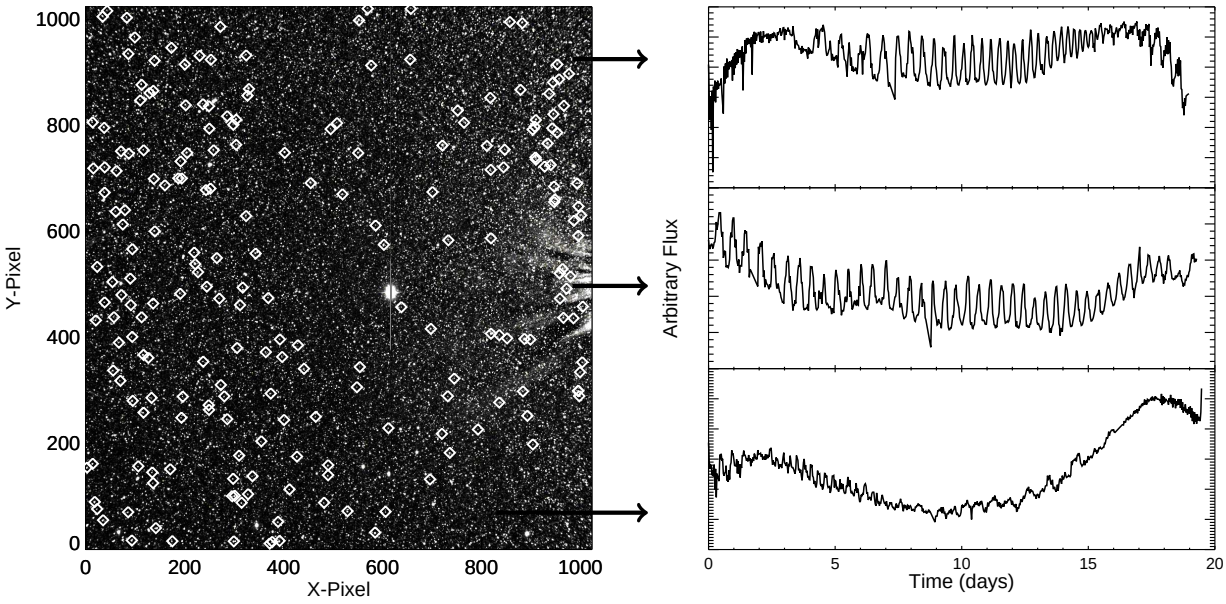

Figure 3.1: On the left is an image from HI-1A. The white diamonds highlight a selection of bright targets, which have been identified from the input catalogue. On the right are the light curves from three stars. These have been produced with the procedures described in this chapter.

compiled on a local machine and built into a single source file. This is then run on BlueBEAR via a logon node. Access to a node is established via "job submission", which requires details of the requested time and memory resources so that the job can be added to the appropriate queue, until a node becomes available.

To use BlueBEAR efficiently (i.e. to complete the processing in as little time as possible) requires a great deal of organisation and planning to ensure that the time on the cluster is used to its maximum potential. This is because queue times for nodes can vary from a few minutes to longer than a day, but when a node is assigned the processing must be started manually from a local machine. The program then runs until all files have been processed or the job time has run out, in which case it terminates immediately. It was useful to plan the time needed to process each set of files, to avoid wasting node-time or having a program terminated before all the files were processed.

As the maximum storage available to each user is 250 GB, it was also necessary to set up a file transfer program to copy files to BlueBEAR and then back to the local machine. This way, the possibility of reaching the maximum storage capacity was reduced and so the processing could continue.

3.3 Input catalogue

The positions for approximately 600,000 stars, with R-magnitudes between 4 and 12, are contained in the input catalogue. This information comes from NOMAD[3], which is a compendium of Hipparcos, Tycho-2, UCAC-2 and USNO-B1 catalogues, as well as 2MASS photometric data. The NOMAD database lists over 1 billion stars and provides extensive sky-coverage, making it the best resource for this study. Each star has a single entry in NOMAD, so if it has been observed in more than one survey, then only the results attributed with the lowest uncertainty are provided. The reliability of the entries can vary considerably depending on the magnitude and systematic errors associated with a particular observation, but in the majority of cases the measurements are fairly precise.

The histograms in Figures 3.2 (a) and (b) illustrate the distributions of the catalogue stars in Right ascension (RA, J2000) and R-magnitude, respectively. In the former, the densely populated region at $\sim 260^{\circ}$ corresponds to the Galactic centre, while another highly populated region at $\sim 100^{\circ}$ corresponds to the Galactic Plane (also see Figure 1.8). The light curves from these regions are far more likely to suffer contamination from nearby sources on the CCD, than those from outside these densely populated areas.

3.4 Identifying target stars

The pointing solutions contained in the image headers are used to convert the coordinates of catalogue stars into pixel locations on the CCD. These positions are then matched up with peaks in the data, which are defined in pixels with an intensity greater than 1.5 times the average background, in an area of 5×5 pixels. If a peak is located within 1 image pixel of a catalogue position then a match is made, i.e. a target is identified. This margin of error is chosen since the pointing solutions should recover the correct target positions to within 1 image pixel (Brown et al., 2009). However, there are occasions when the pointing may be inaccurate, for instance if an image does not contain enough stars to obtain a good fit for the solution, or if a telemetry drop-out has caused missing blocks of data. These instances are identified from a parameter in the image header, $ravg$, which has a value close to zero to denote accurate pointing, or close to one if there was a problem with the solution.

Target identification is restricted to the brightest stars by a factor of 1.5 in their neighbourhood, which is an area with a radius of 6 pixels centred on the target. This helps to reduce the risk of a light curve being

[3] http://www.nofs.navy.mil/data/fchpix/

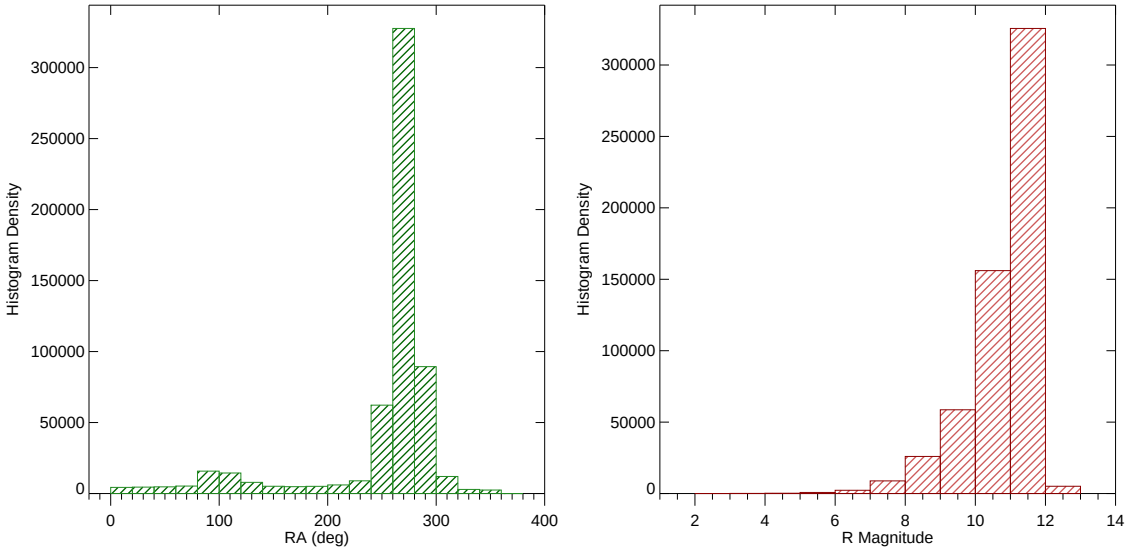

(a) RA (J2000) **(b)** R Magnitude

Figure 3.2: The input catalogue contains $\sim$ 600,000 stars with $4 \leq R \leq 12$. On the left, the distribution of these stars is illustrated with respect to their RA. This shows the high proportion of stars located in the Galactic Plane and from which many of the light curves will be blended with the light from nearby stars. On the right, the histogram shows the distributions of stars with respect to their R-magnitudes.

disproportionately blended with another star. Therefore, if two stars are located within 6 pixels of each other on the CCD and their magnitudes differ by less than 1.5, then neither star will be selected, however if the difference in R-mag is greater than this, then the brightest star will be selected and the fainter star will be ignored.

3.5 Aperture photometry

The measurements of the stellar and background flux and their corresponding errors are obtained by performing aperture photometry, with the IDL *aper* function. This method requires a precise location for each target in the image, which is found using a centroid to pin-point the position of a target on the sub-pixel level. The centroid fits a 2-D Gaussian profile to the PSF and determines the centre of the peak. However the accuracy of the centroid can depend on the degree to which the PSF is sampled on the image, as well as the SNR for a particular source, as is shown in Section 4.3.1.

Using aperture photometry, a star's flux is measured from the image by summing the data counts in a user-defined region, centred on the target. As the targets are point-sources and the PSF on the HI-1

detectors are roughly symmetric, a circular aperture is used. The size of photometric aperture is typically chosen to be 2-3 times the size of the PSF, ensuring that it encompasses 100% of the stellar photons. However, the PSF on HI-1A covers a large angular area on the sky ($\sim$ 3.3 square arcmin), which means that the measurement of the flux through an aperture is subject to a high level of background noise, as well as possible contamination from stars which are nearby on the CCD. Furthermore, for faint stars, which constitute the largest proportion of the targets, having a large aperture area may decrease the SNR, by increasing the noise from background, scattered and solar photons. For these reasons, it was useful to collect multiple sets of data using a range of aperture radii and then select the dataset which provided the highest SNR (lowest point-to-point scatter), for the majority of the light curves. An aperture radius of 2.5 pixels was found to be the optimal choice for the HI-1A light curves. A measurement of the background (sky) radiation is made by summing the pixel counts in an annulus of 6 to 10 pixels around a target. This value is then subtracted from the aperture measurements to obtain a final value, called the sky-subtracted flux.

The accuracy of the background and hence of the final flux measurement, will be subject to certain factors. Primarily, the density of stars in the vicinity of the target will be a factor, since in crowded fields, the light from nearby stars may fall into the sky-annulus, the source aperture, or both. In the case where the contaminating flux is measured in the annulus and not in the aperture, the background may be significantly overestimated with respect to the source. This will result in a decrease in the SNR, as source photons (the signal) may be removed when the "sky"-background is subtracted from the aperture measurement. The extent of this effect will be different for each star depending on the level of overcrowding and on the magnitude of the star, i.e. an overestimated background will have less effect on the light curve of a bright star than a fainter one.

Small-scale variations in the background light may also affect the sky-estimate. This is because the background correction (Section 2.3.1) uses 1-day minimum map to filter out effects from the F-corona, which does not account for background radiation varying on shorter timescales. Therefore these sources, which include solar flux and CMEs, will also compromise the final flux measurements.

The image in Figure 3.3 illustrates aperture photometry performed on an HI-1A image. Over each selected target there has been placed an inner aperture for measuring the flux (solid circle) and an annulus for estimating the background (between the two dotted circles). Whereas this field is not significantly crowded, it can be seen that for some of the targets, the estimate of the background will also include

flux from neighbouring stars. In most cases this will lead to an over-estimation of the background, which, when subtracted from the source flux, will result in an increase in the scatter in the light curve. Contamination in the light curves will be discussed further in Chapters 4, 6 and 8.

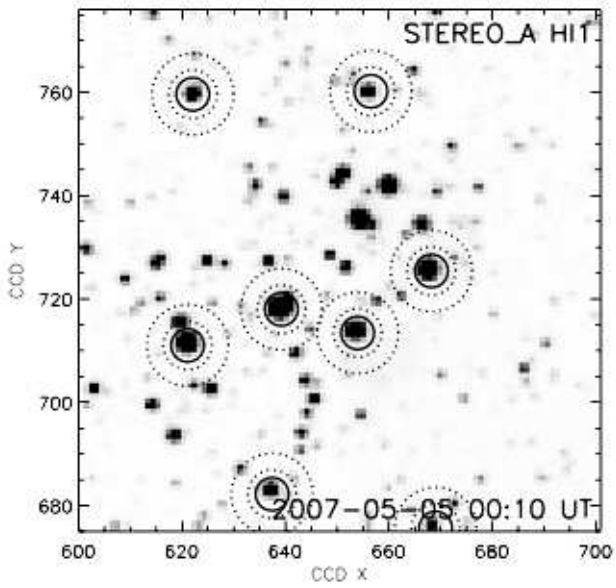

Figure 3.3: An example of aperture photometry on an image from HI-1A (Bewsher et al., 2010). The solid circles around selected targets are the apertures within which the source flux is measured. The background is taken from the sky-annulus, which is between the dotted, concentric circles. This estimate is then removed from the source measurement to give a value for the sky-subtracted flux.

3.6 Flux units and magnitudes

As mentioned in Section 2.3, the substantial readout time of the image with respect to the integration time means that the flux is given units of DN s^{-1} as opposed to total count rate. Unless a comparison is to be drawn with the results from other studies, the choice of units is arbitrary. However, it may sometimes be useful to convert the flux into an apparent magnitude for the system, $m_{\rm HI}$. If this is the case, the equation below can be used to calculate $m_{\rm HI}$ directly from the measured flux, F.

$$m_{\rm HI} = -2.5 \log_{10} \left(\frac{F}{\mu F_0} \right). \tag{3.1}$$

Here F_0 is the flux of the reference star Vega[4], which would provide a data count of 103, 968 DN s^{-1} in an HI-1A observation (Bewsher et al., 2010). The factor μ in the equation takes a value of 0.93, which

[4]Being one of the brightest stars in the sky, Vega is often used to calibrate photometric observations as it is defined as having zero magnitude at all wavelengths.

is equivalent to the quantum efficiency of the detector, i.e. the proportion of photons which fail to be detected. These "lost" photons are either absorbed by the instrument optics or pass directly through the CCD, without reacting with the silicon lattice.

3.7 Flux uncertainty

The uncertainty in the flux for the HI-1A light curves is calculated within the aperture photometry program from the following equation,

$$\delta F = \sqrt{N_\star + \sigma^2_{\rm sky} + \frac{\sigma^2_{\rm sky}}{N_{\rm sky}}} \tag{3.2}$$

where $N_\star$ is the number of source photons; σ_{sky} is the variance of the sky background and N_{sky} is the number of pixels contained within the sky region. Individually, these terms represent the photon noise from the source, the scatter in the sky background and the uncertainty in the mean sky background. Typically, this equation would include factors corresponding to the dark current and to the read noise of the instrument. However, as these have negligible impact on the HI-1A data (see Section 4.2), they may essentially be ignored in this case, i.e. set to zero. Therefore the only significant contributions to the uncertainty are from photon counting and from the variance in the sky-background, which are further described in Section 4.2.

3.8 Light curves

Several months of processing more than 4 years of data, cumulated in the production of $>$ 600,000 light curves for $\sim$ 80,000 targets in the FOV.

In the light curves, the time corresponding to each data point is the time stamp from the start of each exposure, converted to Julian date (JD). Units of JD are frequently used to describe the times of astronomical observations, serving as a standard point of reference since the start of the Julian calendar (on 1st January 4713 BC). The Julian dates for the resultant light curves have a range of 2454191.5 to 2455892.5 JD, corresponding to midnight April 1st 2007 and midnight November 27th 2011.

The initial inspections of the data found that the photometry from HI-1B was significantly compromised by external factors, making the light curves redundant for the purposes of a transit search. This is likely to be because 1B is facing towards to the direction of travel and therefore it suffers more impacts from

space debris and dust particles, which are believed to offset the pointing. The result is much greater noise in the light curves.

The data from the HI-1A camera is of very good quality and from this camera alone more than 300,000 light curves have been collected for over 70,000 targets. Histograms showing the distributions of these stars, with respect to RA and R-magnitude are shown in Figure 3.4. In comparison with Figure 3.2, these histograms still show a higher proportion of stars in the Galactic Plane and at fainter magntidues, but due to the selection criteria (Section 3.4), the distributions are more even in both RA and R-magnitude.

Note: In the example light curves shown throughout the remainder of this thesis, the majority are plotted with a timescale starting at zero days (for simplicity), as the actual times of the observations are irrelevant for their purposes.

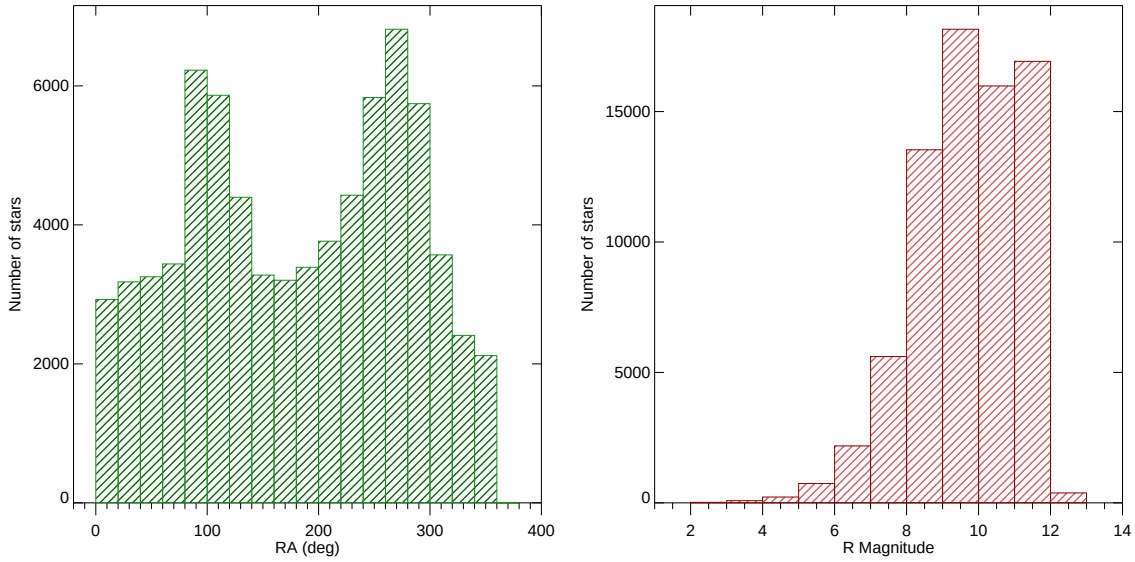

(a) RA (J2000)

(b) R magnitude

Figure 3.4: These histograms show the distributions of the 73,836 targets which were identified from the HI-1A images and tracked throughout the observation period.

Chapter 4

HI-1A DATA CHARACTERISTICS

4.1 Introduction

This chapter describes the common characteristics featuring in the HI-1A light curves. Aside from the basic calibrations with SECCHI-PREP (described in Section 2.3), these light curves have had no further processing and so they are referred to as the raw or original light curves.

The first section is a brief introduction to the noise inherent in CCD observations and in space-based photometry. Each section which follows describes a major component of noise, giving examples to illustrate the extent of its effect in the light curves. Lastly, the overall noise level is discussed.

The purpose of this chapter is to introduce the main sources of noise which reduce the signal-to-noise ratio (SNR) in the data and threaten to compromise a transit search by introducing false-positive or negative results.

4.2 Noise in CCD astromomy

All CCD observations contain noise elements, which arise from a broad range of factors relating to the source (shot noise) and other external sources of light (contamination). Other factors, referred to as systematics, come from the instrument and CCD itself, as well as from the programs and algorithms designed to reduce those instrumental features. The combination of these elements can either completely dominate transit-like signals or else inject unwanted patterns into the time series, which are difficult to disentangle from the data. In a transit search, the former causes false-negative results, where a genuine signal fails to be detected, whereas the latter creates false-positives (FPs), which are transit-like features mimicked by the noise (see Section 7.2). For most transit surveys, FPs are a particular concern (e.g. Almenara et al. (2009); Torres et al. (2011)), as they are caused by a many different circumstances.

These are discussed further in Section 8.2.

The various sources of noise which affect CCD imaging can be grouped into three main categories. The first two are usually referred to as the systematics, these are *instrumental* and *methods* (used to collect and calibrate the data). The third category is *external*, which includes noise sources which depend on the circumstances of the observations. In ground-based imaging, a large proportion of the noise is due to atmospheric effects, whereas in space, scattered light from dust particles and cosmic rays are more prominent. There are also many ways for these categories to combine. For instance if the region being observed has a dense population of stars (*external*) there is risk of contamination in the light curves, but this depends on the size of the PSF (*instrumental*) and the size and shape of the aperture used to measure the flux (*methods*). The key point here is that there is an opportunity for noise to enter the data at any stage in the processing, from the initial observation through to the production of light curves.

The following list summarises the main sources of noise affecting the HI-1A observations. The first group refers to noise sources that are inherent in all CCD-collected data. The second group describes the sources that are specific to the HI-1A instrument and the last group described a number of external factors affecting the data.

General:

- Photon noise - related to the source. This is due to random fluctuations in the arrival time of photons at the detector. In statistics this is referred to as Poisson noise, meaning that it follows a specific, discrete probability distribution. The magnitude of the noise increases as $\sqrt{N_\star}$, where $N_\star$ is the number of photons counted. Hence, observations of fainter stars, which have intrinsically lower $N_\star$ compared to brighter stars, will have a reduced SNR simply due to this property.

  Photon noise is an inherent property of CCD observations and so it sets the lower limit for noise in the light curves.

- Read noise from the instrument. There are two contributing factors which occur during the readout process,

  1. A discrepancy in conversion from an analog to a digital signal, i.e. between the number of electrons counted (e^-) and the assigned data number (DN).
  2. Spurious electrons produced by random fluctuations in the system electronics.

Both these effects combine to produce an average read noise for the CCD, which in the case of HI-1A is approximately 15 e^- pixel^{-1} image^{-1}, equating to 1 DN pixel^{-1} image^{-1}.

- Dark current from the instrument. This is additional electrons produced by heat in the vicinity of CCD. Therefore the amount of dark current is related directly to the temperature of the instrument.

  In HI-1A the CCD is cooled by a passive radiator (facing away from the Sun), to -80°. At this temperature, the dark current is less than 0.1 e^- pixel^{-1} s^{-1}, which is considered to be a negligible effect in the data. However, dark current can also give rise to an anomaly known as hot-pixels, where many electrons are produced locally, i.e. within specific pixels. This usually appears as an upward spike of flux in the light curve.

- Pixel variations. In addition to a large-scale variation over the detector, there is a small-scale variation from pixel-to-pixel, at the level of $2 - 3$ %. This is because each pixel has slightly different sensitivity to incoming photons, either be due to manufacturing errors, or as a result of bombardments from high-energy particles (e.g. cosmic rays). The former can produce low-frequency patterns in the light curves, while the later will temporarily affect the response of a pixel, resulting in downwards spikes in flux. This effect is also present in CoRoT light curves, as shown in Aigrain et al. (2009). In general, space-based telescopes are more prone to impacts from high-energy particles and over time, this can permanently degrade the entire CCD.

- Errors in the flat-field correction. These are due to incorrect assumptions or rounding-off errors in the calculations for determining the flat-field (Section 2.3). For instance the predicted intensities for some stars are obtained from a colour-mixing method, which assumes a linear combination of B, V and R magnitudes. However, as the instrument also has response in the infrared regime, this method may not achieve accurate results for cooler stars, which emit a large proportion of their radiation at longer wavelengths.

STEREO-specific:

- Jitter due to the motion of the satellite. This can reduce the stability of the attitude control, which affects the pointing solutions in the image headers. In turn, this will affect the accuracy of the centroid function and its ability to locate the centre of the target's PSF. CoRoT and *Kepler*, which are also affected by satellite jitter, have made considerable effort to correct for its effects, e.g. Drummond et al. (2006); Stumpe et al. (2012). However, their methods are not applicable to

STEREO, which has tangential as well as line-of-sight motion. Therefore for HI-1A data, this type of noise is considerably difficult to remove.

- Space-debris impacting the satellite. This can affect the stability of the attitude control, but in a more random manner than jitter. Whereas satellite jitter produces low-amplitude noise on long timescales, debris impacts cause sudden changes in the pointing, which are difficult to correct for.

- Telemetry errors, which occur during the data down-link. Although the HI has an allocated telemetry of 2 binned images per hour, often there is a problem during the down-link of the data to the Earth. This can either result in the loss of an entire image, or missing blocks of data within an image. The duration of the missing data can vary from a single missed point to large gaps, extending over a day. In addition to this, STEREO observations are interrupted every 6-8 weeks for momentum dumps. These compensate for the build-up of momentum in the wheels controlling the satellite attitude and usually last for ~ 5 hours (≈ 7 data points).

- Large PSF. As mentioned in Section 2.2, the HI-1A has a considerable pixel size and corresponding PSF. This means that when aperture photometry is used to measure the flux from a target, the light from the neighbouring stars may also be collected due to overlapping PSFs. For any given light curve, the percentage of the flux due to contamination will depend on the relative intensities of the source star and the neighbouring stars and on the fraction of their light which enters the PSF.

- Vignetting, caused by the misalignment of the optics and the detector. This concept was introduced in Section 2.2 with the corresponding diagram in Figure 2.3. It is essentially the reduced response of pixels which are not fully exposed to the incoming light. The large-scale flat-field correction (Section 2.3) is designed to rectify this effect, but as shown in Section 4.3.3, further corrections are needed for some stars.

External:

- Background contamination, from scattered light entering the observation. On Earth, a considerable effort is spent in locating telescopes away from sources of "man-made" light. However, scattered light from the moon, planets and dust particles in the atmosphere are ever present. In space it is equally difficult to avoid external sources of background light and especially for HI-1A as its right-hand edge is just 4° from the centre of the Sun. Whereas SECCHI-PREP reduces background

contamination from the F-corona, direct solar flux and CMEs are prominent in the images and are a great disadvantage to photometric studies of the background stars.

- Cosmic-ray impacts. These highly energetic particles produce multiple electron-hole pairs in the silicon, causing pixels to become saturated. They have an estimated hit rate on the HI detectors of ~ 45 pixels s^{-1} and are removed from the short-duration exposures by a process called cosmic ray scrubbing. However, following a hit, the response in a pixel can be reduced temporarily, therefore affecting subsequent images.

- Solar flares and other transient light sources, producing random spikes in the data. These are common in the STEREO images.

4.3 Data characteristics

This section illustrates the effects of the main sources of noise which are visible in the HI-1A data. Since these components are easily identifiable, methods have be devised to remove/eliminate them from the raw light curves (Section 5.3). However, as is shown, the impact on a particular light curve is dependent on the brightness of the star and its position on the CCD and in the FOV. For instance, an object in the centre of the CCD may suffer different effects to one at the edges and a bright target in a crowded field will be less affected by contamination that a fainter target. Therefore developing an automated pipeline, that will be applicable to all light curves, presents a challenge.

4.3.1 Flux discontinuites

A number of the light curves show discontinuities in the flux at one or multiple times throughout the observation, such as that in Figure 4.1. In this figure the flux measurements are plotted in the upper panel, while the associated y-pixel positions are shown below. These positions should correspond to the centre of the target's PSF on the image (in the y-axis), which is found with the centroid function (Section 3.5). This example illustrates a significant failure in the tracking, where the centroid has failed to accurately locate the target's position on the CCD, resulting in a composite light curve.

This outcome is predominantly related to fainter stars ($R > 9$), particularly if they are located in a crowded region or in an area with high background flux, as this results in a lower SNR. As mentioned in Section 2.2, the PSFs are marginally undersampled in the binned images, meaning that the pixel size is

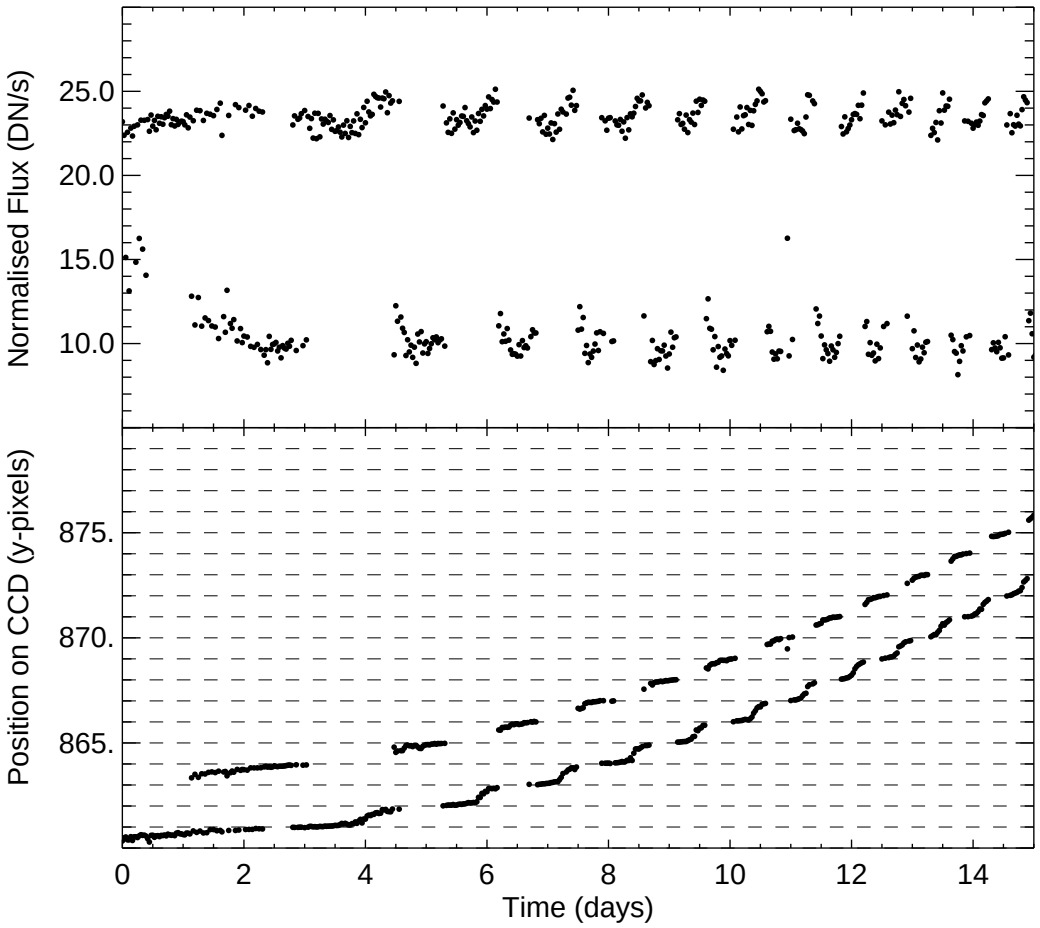

Figure 4.1: An example of a composite light curve, caused by a tracking error. The upper panel shows the flux measurements, which shift periodically between two stars, while the lower panel shows the corresponding y-pixel positions, located by the centroid.

large compared to the PSF. Ideally, the FWHM should be at least 2 image pixels, whereas for the HI-1A, this is 1.5.

The centroid will have a greater accuracy for targets located in the centre or on the edge of a pixel, as this produces a symmetrical distribution of flux in either one or both of the x and y directions. But when a target is between the centre and edge of a pixel, the distribution of flux is asymmetric, making it more difficult to fit with a Gaussian profile. This situation is exaggerated when the SNR is low, as is the case for fainter targets and in areas with high background light. When the PSF cannot be well approximated by a 2-D Gaussian profile, the centroid will fail and jump the next nearest location to which the function can be fit, which is usually a nearby star on the CCD. Hence a composite light curve is created, like that shown in Figure 4.1.

All the light curves affected in this way are not usable for transit surveys, but the majority of cases can be easily identified using statistical methods (see Sections 5.3.2 and 5.3.3).

4.3.2 Solar contamination and CMEs

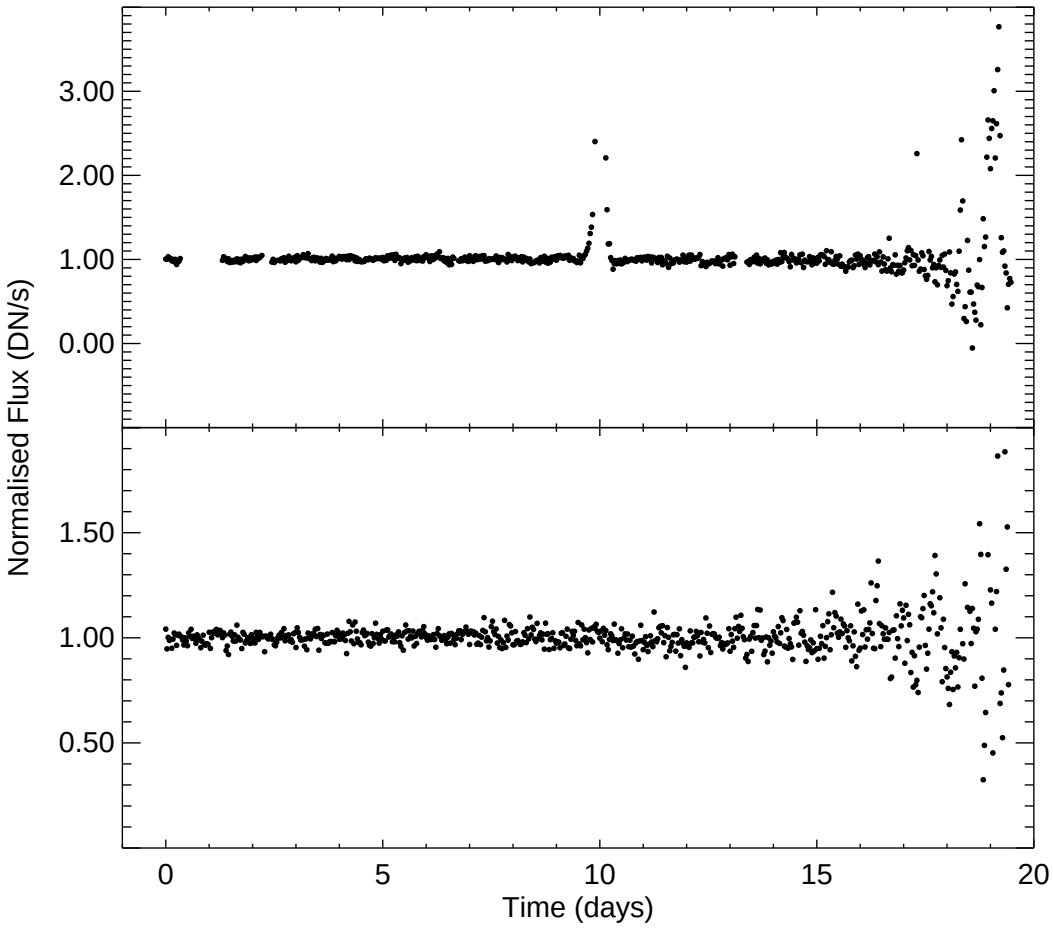

Figure 4.2: These light curves are from stars in the centre of the FOV and are therefore more susceptible to solar contamination. In the upper panel the scatter increases by a factor of 6 at the end of the light curve and there is a prominent solar flare at $\sim$ 10 days. In the lower panel, as the star moves closer to the Sun on the image, the flux increases by 50%, which increases the scatter by a factor of 5.

The Sun's proximity to the FOV means that solar contamination is a concern, especially in the region indicated in Figure 2.3. Solar contamination includes contributions from direct solar flux, flares and CMEs, as well as from scattered light, e.g. the F-corona. Each of these components vary in time and intensity and hence they are extremely difficult to remove from the images, despite the background correction, described in Section 2.3.1.

Both examples presented in Figure 4.2 show an increase in the scatter, by more than a factor of 5, towards the end of each observation and a similar effect is present in the majority of light curves recorded in centre of the CCD. It is clear from the examples shown that the detection of a Jupiter-sized planet around a solar-type star ($\sim 1\%$ depth) would be impeded by this noise and so every effort must be made to remove it from the light curves. This is one of the main objectives of the TRP (Section 5.3).

4.3.3 Reduced/Increased signal at the edges of light curves

A number of light curves exhibit a reduction or increase in flux, either at the start or end of the observation and in some cases both. Examples of this are shown in Figure 4.3. The reduction shown in the upper and middle panels is caused by vignetting which has not been corrected by the flat-field (Section 2.3). Whereas when the flat-field overcompensates, an increase in flux occurs, as is seen in the lower panel on the Figure. Vignetting is one of the many causes of FPs, since a transit-like dip can be mimicked by the drop in flux, when the light curve is folded on certain periods.

4.3.4 Outliers

High and low outliers are common to all light curves and occur at random times throughout the observations, such as those exhibited in Figure 4.4. They can be caused by systematic and observational effects such as tracking glitches and solar flares, respectively.

4.3.5 Data gaps

Very few light curves have complete data sets spanning the entire 20-day period. Most present data gaps which are either due to the removal of saturated columns, telemetry drop-outs or momentum dumps (Section 4.2). Data gaps can affect only a few data points or else substantial sections of the observation, sometimes longer than a day. Significant gaps lasting more than a few data points can be problematic to transit-detection algorithms, e.g. by increasing the noise or introducing a spurious signal into the power spectrum (see Section 7.4). For this reason, methods of introducing artificial data into the gaps may be necessary to aid transit detections.

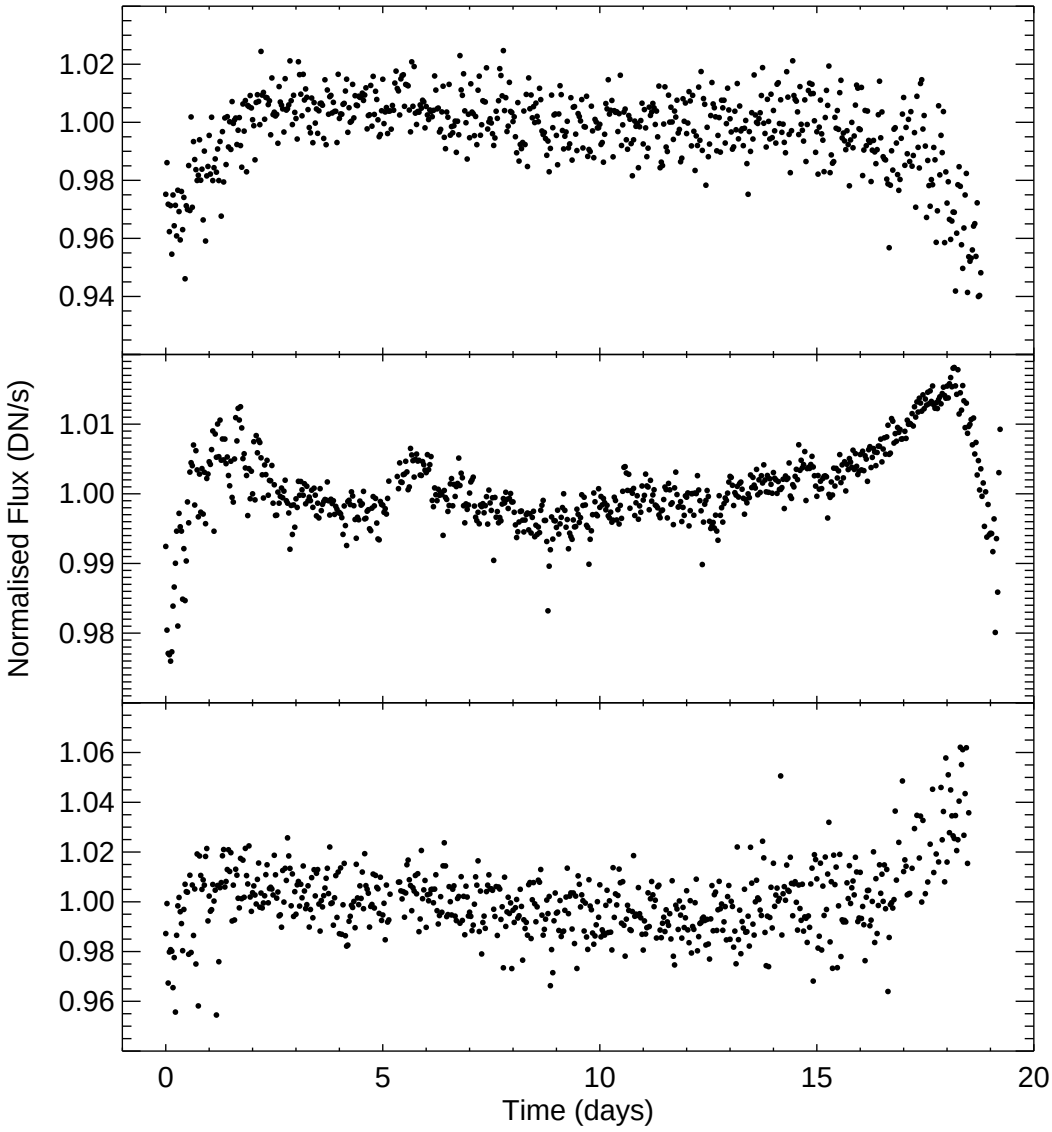

Figure 4.3: Vignetting is a reduction in the response of pixels in the corners of the detector. This usually causes a drop in the flux from stars observed in these regions as seen in the light curves above. The top and middle panel show this effect for a 9th and 5th magnitude star respectively. The bottom panel shows vignetting at the start of the light curve, but an increase in flux at the end. This is due to a flat-field correction overcompensating for the effect.

4.3.6 Stellar variability

Many stars exhibit periodic stellar variability and/or eclipses from binary transits. Three such examples are shown in Figure 4.6. The light curve in the top panel shows a low-amplitude periodic variable

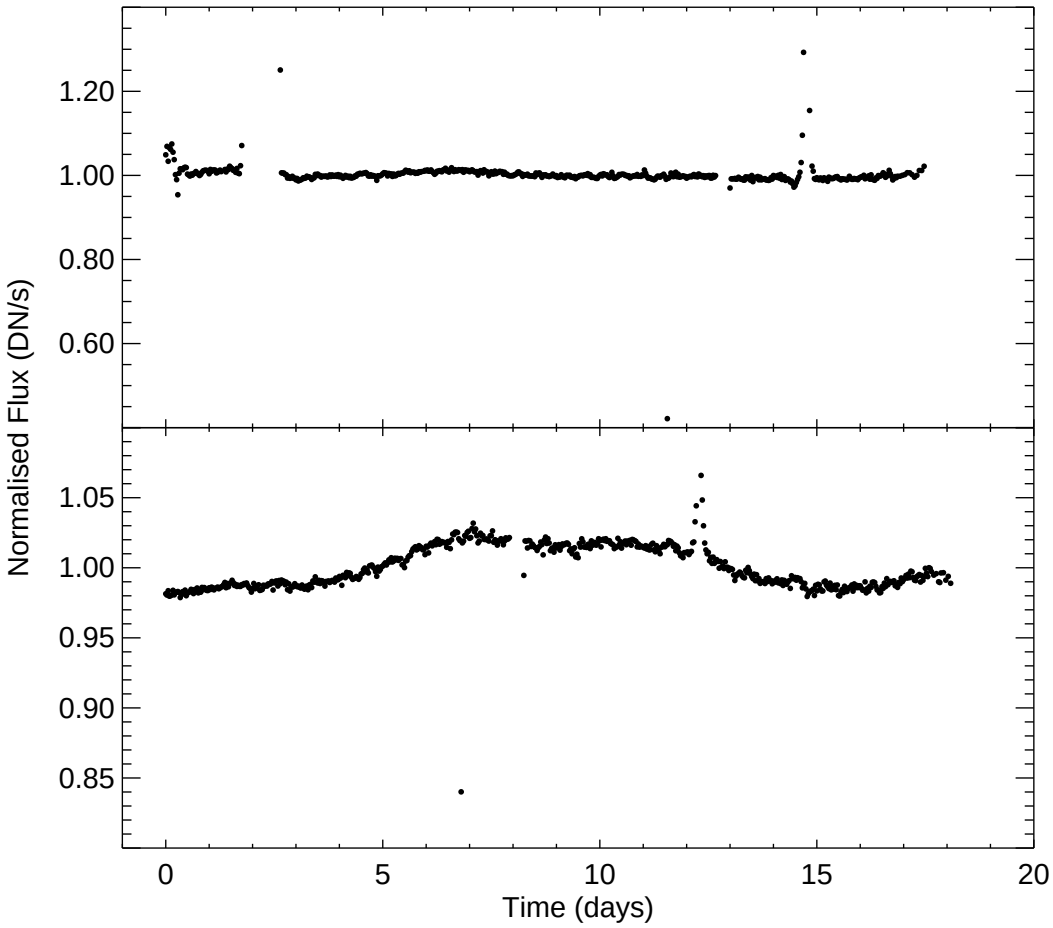

Figure 4.4: Random points of high/low flux (compared with the mean intensity) are called outliers. In the upper panel, two high outliers occur at the start and end of a gap in the light curve, at $\sim$ 2 days. These could be due to an impact on the satellite affecting the pointing and then causing an error in the telemetry. At $\sim$ 15 days a solar flare causes the flux to increase for a few hours. Another flare event is present in the lower light curve at $\sim$ 12 days and there are two points of significantly lower flux at $\sim$ 7 and 8 days. These might also be due to inaccuracies in the pointing.

(HD4965), with a period close to 1 day. The middle panel shows the light curve of an eclipsing binary star (TXLeo), with regular eclipses on a period of just over 2 days. The light curve in the bottom panel is that of a Cepheid variable star (V350 Sgr). Cepheid variables are useful distance indicators as they shows a very strong correlation between pulsation period and luminosity. From the point of view of a transit survey, each of these light curves are problematic, as their periodicities will present a detectable signal to most transit detection algorithms. In particular, low-amplitude variations and shallow binary eclipses are the most problematic.

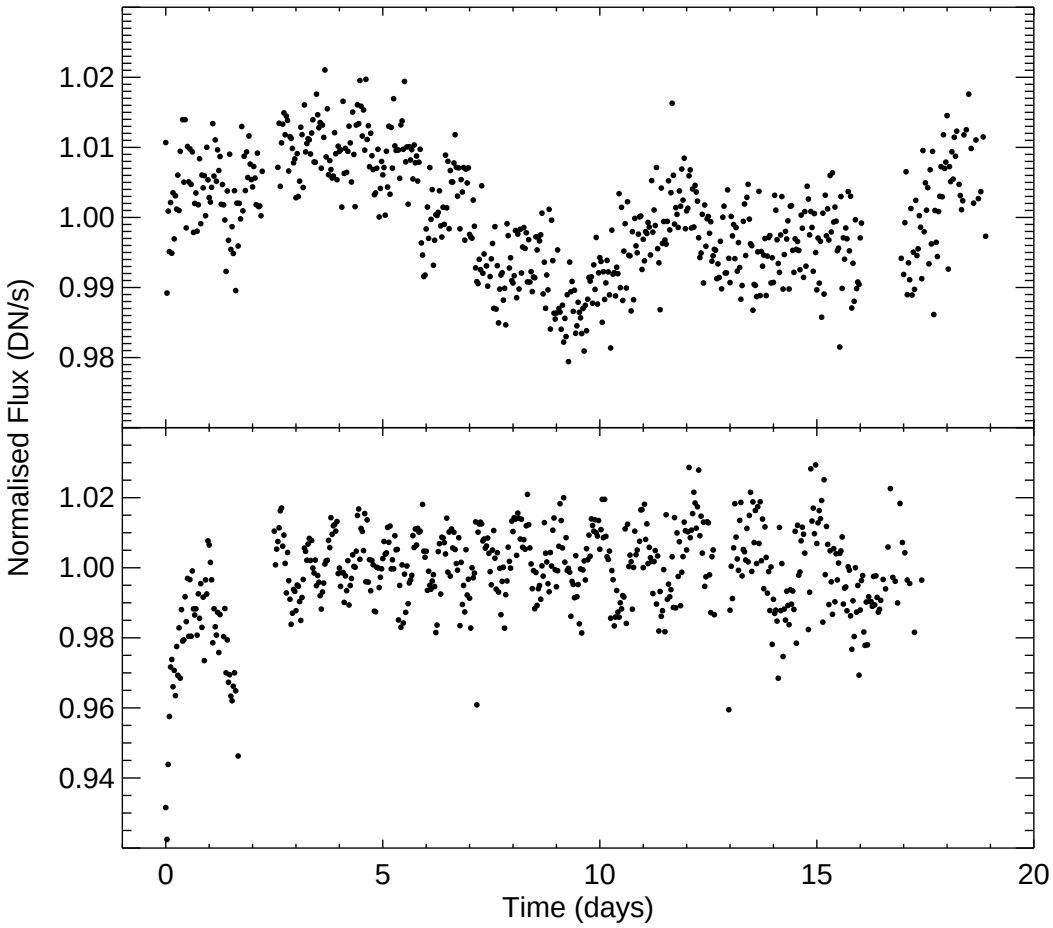

Figure 4.5: The light curves shown above are both affected by multiple gaps in their time-series. The variations in pixel response (upper panel) and stellar variability (lower panel), coupled with this effect, produce spurious peaks in the power spectrum from Fourier analysis. To avoid this scenario, and hence reduce the number of FPs in a transit search, methods are used to artificially pad the data in Section 5.3.7.

4.4 Overall scatter in the raw light curves

The point-to-point scatter in a light curve indicates the overall noise level, from a combination of photon, systematic and intrinsic noise. This value is usually taken as a guideline for determining the size of the signal that can be easily identified in the light curves.

In general, fainter stars are associated with larger scatters than brighter ones, as they have a lower photon count ($N_\star$) and are therefore more susceptible to random fluctuations in the light. This is one of the results shown in Figure 4.7. In the plot the black dots are the estimates of the point-to-point scatter, which have been calculated using *robust_sigma*. This an IDL function that is resistant to outliers, at it

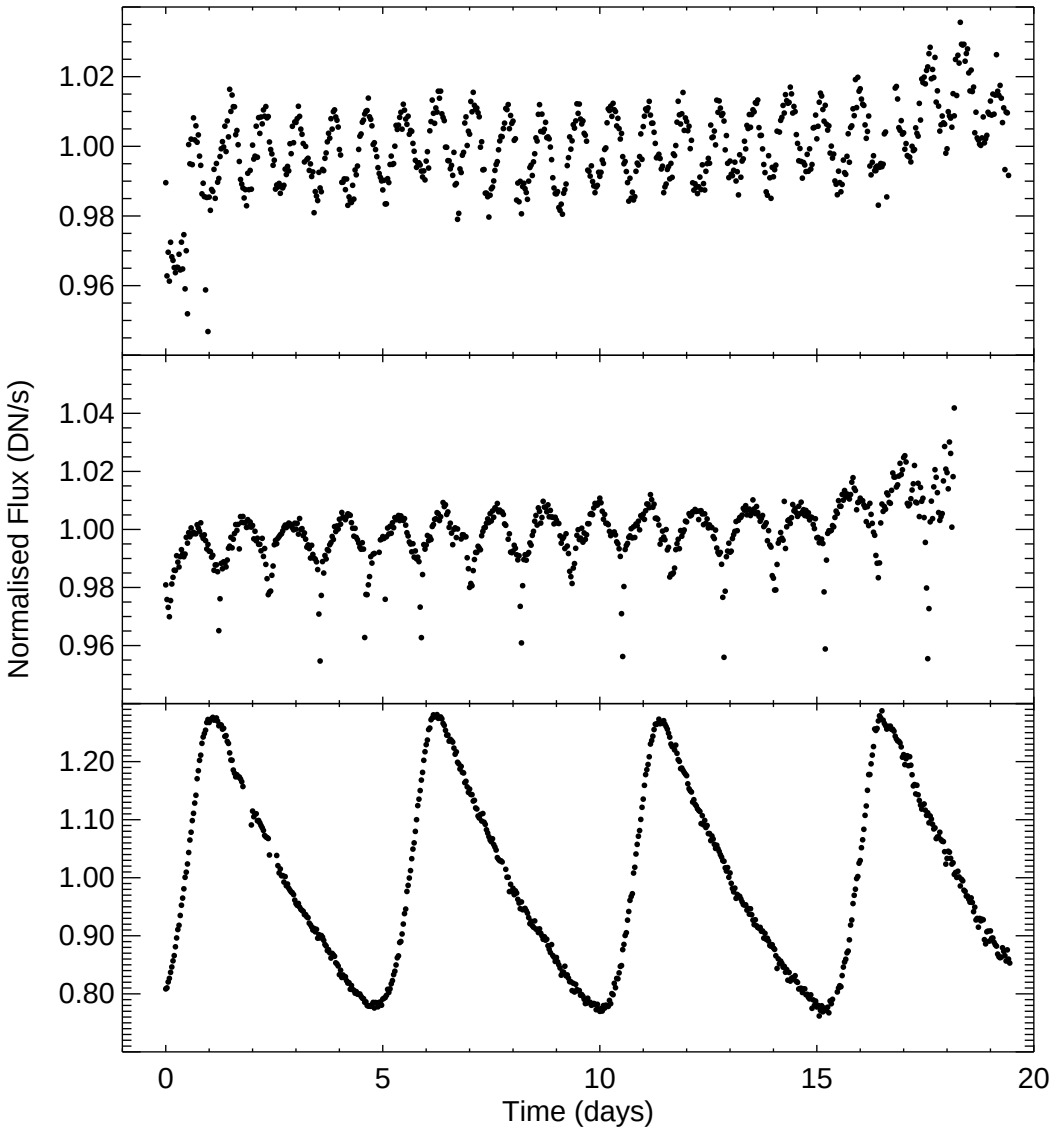

Figure 4.6: Intrinsic stellar variability is present in a high percentage of the light curves. The top panel shows HD4965, a variable, 7th magnitude star, with low-amplitude oscillations and a period of $\sim$ 1 day. The middle panel shows V*TXLeo, a 6th magnitude, binary star with regular eclipse events. The bottom panel is V*V350 Sgr, a 6th magnitude Cepheid variable star.

uses the median absolute deviation (MAD) to calculate σ. The scatter has been plotted on a $\log_{10}$ scale against the catalogue R-magnitudes.

The theoretical photon noise limit is represented by the green dashed line which is calculated from Equation 3.1. This is the formula relating the measured flux, F, to the HI-magnitude scale. Rearranging this into the form of Equation 4.1, will give the predicted flux at each m_{HI}:

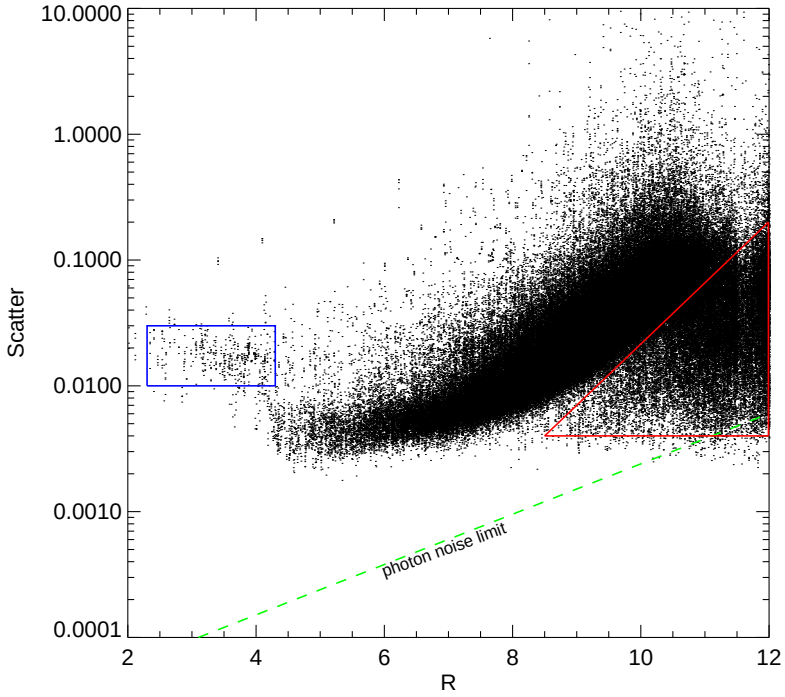

Figure 4.7: The point-to-point scatter for the raw light curves, plotted on a $\log_{10}$ scale, as a function of their catalogue magnitudes. The green dashed line represents the theoretical photon noise for HI-magnitude scale. This is a guideline, since $m_{\rm HI}$ is not equivalent to R for all stars in the sample. The red triangle indicates the light curves which either have incorrect magnitudes, are variables or are contaminated. The blue box highlights the brightest stars in the sample, which appear to have much greater than expected noise. There are also a large number of points above the mean scatter, which are likely to be variables or composite light curves.

$$F = \mu F_0 100^{-m_{\rm HI}/5}. \tag{4.1}$$

F (in DN s^{-1}) in then multiplied by the system gain (15 e^{-1} DN^{-1} (Eyles et al., 2009)) and the length of each exposure sequence (1200 seconds), to give $N_{\rm phot}$, the number of photons per image and finally the predicted scatter, $\sigma_{\rm HI}$ can be calculated from,

$$\sigma_{HI} = \sqrt{N_{\rm phot}}/N_{\rm phot} = \frac{1}{N_{\rm phot}}. \tag{4.2}$$

This is the theoretical photon noise limit.

As explained in Section 3.6, $m_{\rm HI} \approx R$ for most, but not for all, stars in the sample. This is because the spectral response of the instrument is centred on the R passband, but also partially covers and B and

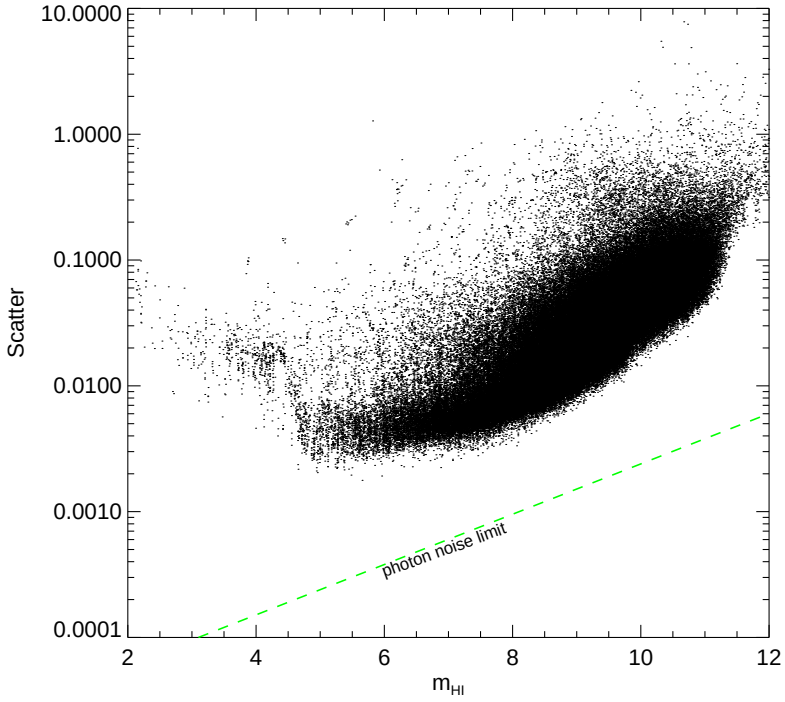

Figure 4.8: The point-to-point scatter for the raw light curves, plotted on a $\log_{10}$ scale, as a function of m_{HI} (calculated directly from the measured flux). The green dashed line here can be directly compared to the scatter, since it is in the same scale. The outliers in the red triangle in Figure 4.7 are absent from this plot, confirming that the measured flux from these light curves is much greater than that anticipated from the catalogue magnitudes. The cluster of bright outliers, seen here and also in Figure 4.7, is likely to be due to a systematic effect.

V spectral passbands. Therefore the instrument is not as sensitive to younger, bluer stars which emit most of their light at shorter wavelengths or to late-type giants, which emit light at infrared wavelengths. Because of this, the photon noise line in Figure 4.7 is included only as guideline, to show the approximate difference between the theoretical and measured noise as a function of R-mag.

On the other hand, these relations are directly comparable in Figure 4.8, which shows the scatter as a function of m_{HI}. In this plot, the magnitudes have been calculated directly from the measured flux values, using equation 3.1.

Both these figures show a general increase in scatter with decreasing brightness, which is expected. However, Figure 4.7 contains a large group of outliers which deviate from this trend, in and around the red triangle. These are associated with light curves all having much lower than expected scatter for their R-magnitudes, some even extending down to the photon noise limit. No such group is seen in Figure

4.8, which is based on the measured, rather than the expected magnitudes.

The main causes for this discrepancy will be one, or a combination, of the following,

1. The target has been incorrectly matched with a catalogue star, i.e. a brighter star has been tracked instead of a fainter one, resulting in a lower then expected scatter. This is a high risk outcome in crowded fields, where the centroid function can struggle to distinguish between points sources (Section 4.3.1).

2. The catalogue magnitude is incorrect (lower than it should be), either as a result of systematic errors or, if the star is a variable it may have been observed during a minimum phase, resulting in a higher magnitude estimate.

3. The light curve is contaminated by the light from nearby stars (in crowded fields), which has increased the signal and therefore reduced the photon scatter.

The other common feature in the figure is the group of stars in the blue box in Figure 4.7. These stars are the brightest in the sample, but they have much greater than expected noise in their light curves. This is due to saturation effects. For HI-1A the full well capacity of each pixel is $\gtrsim$ 200,000 e^- per exposure. This means that saturation starts to become an issue for stars brighter than $\sim$ 4th magnitude, which contribute $\sim$ 1,400,000 e^- per exposure (40 seconds) to their PSF ($\sim$ 7 unbinned pixels). The effect will be greatest for the brightest stars, which saturate more pixels in the area around the PSF.

Saturation effects are dealt with by SECCHI-PREP (Section 2.3), by replacing the data counts (DN) from each pixel in the affected columns with NaN values. However, if there is enough light in the surrounding pixels which are not saturated to constitute a peak (where a peak is defined as 1.5 times the background flux), then this peak will be matched to the closest catalogue star and its flux measured with aperture photometry (see Section 3.5). This will result in a greater than expected scatter in the light curve due to two effects:

1. There will be less flux in the aperture (i.e. photons) and hence greater scatter, due to photon counting (Equation 4.2).

2. Since at least one column has been removed, the centroid will not accurately locate the centre of the source and hence background light from outside the stars PSF will contaminate the aperture.

Figure 4.9 shows the catalogue magnitudes versus the m_{HI} (from measured photometry) for the brightest stars in the sample. Since $m_{\mathrm{HI}} \approx R$ for the majority of stars, this plot indicates that the measured flux

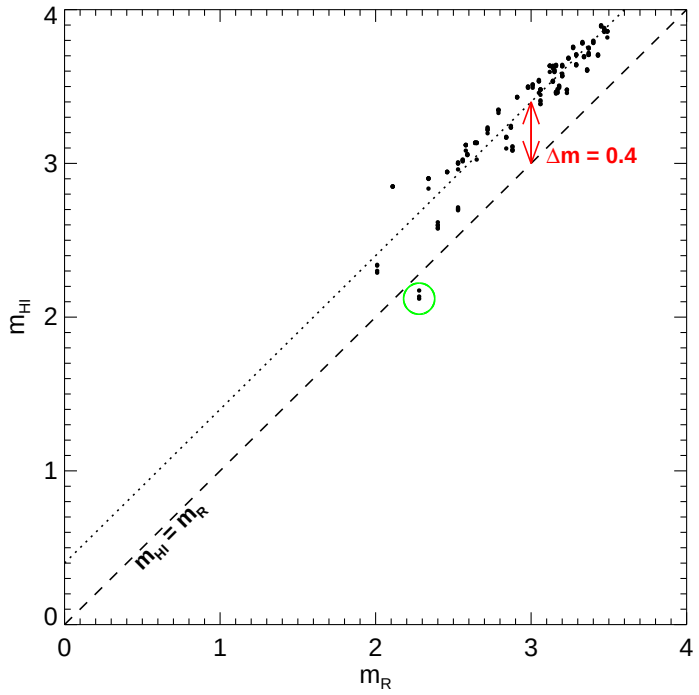

Figure 4.9: This shows the difference between the catalogue magnitudes (R) and $m_{\rm HI}$ for the brightest stars, (blue box in Figure 4.7). On average, these stars lie 0.4 magnitudes above the equality (dashed) line. This difference in magnitude corresponds to a reduction in the measured flux of 30 %, which is due to the effects of saturation. The result is a higher scatter in associated light curves, as shown in Figures 4.7 and 4.8. The few light curves which, instead, appear brighter than expected (in the green circle), match with a star in a double/multiple system having many bright stars, hence this target is likely to have been misidentified.

is significantly lower than expected. For this group of stars, the average difference in magnitudes is 0.4, corresponding to a reduction in the flux of 30 %. In other words, only 70 % of the light emitted from these stars has been recorded in the aperture.

4.5 Large-scale trends in the raw light curves

The mean scatter of the light curves in relation to their positions on the detector and in the sky are shown in Figures 4.10 and 4.11 respectively. These highlight the significant impact that the sources of noise presented in Section 4.3 have on the light curves.

In Figure 4.10, for each group of 50 consecutive pixels in the y-axis of the detector, the mean scatter of the associated light curves has been plotted. This conveys the general trend of the noise as a function of

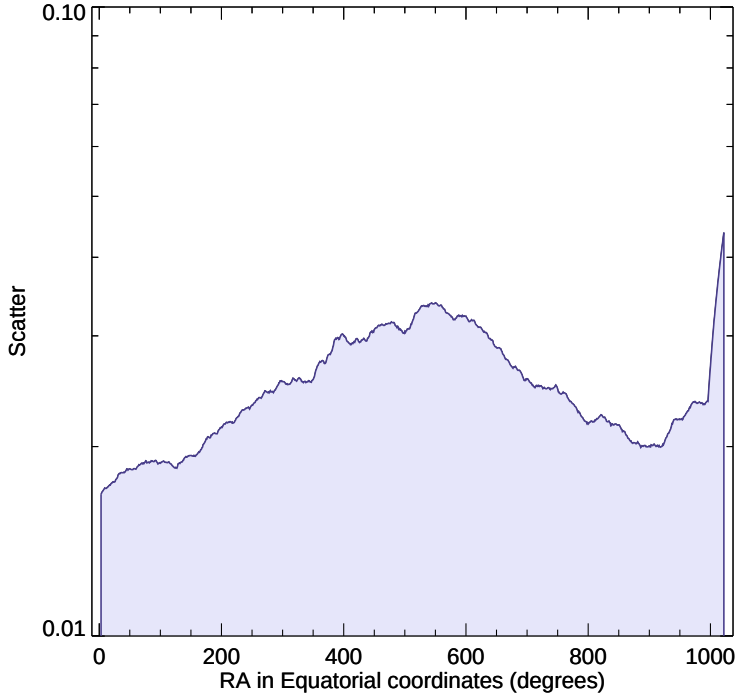

Figure 4.10: Mean scatter in the light curves with respect to the average y-pixel in which they were tracked. These results have been binned-up by 50 pixels to show the general trend across the CCD, rather than the small differences between each pixel. This plot confirms that light curves from the central and upper region of the detector have increased scatter compared to others. The former is due to solar contamination and the latter is due to vignetting and possibly degraded pixels along the bottom rows of the CCD.

y-pixel. From this, two main features are apparent. First is the increase in the noise for the observations in the centre of the detector. This is directly related to the solar contamination, described in Section 4.3.2. The second, somewhat surprising feature, is the sharp rise in the scatter of light curves in the pixels ranging from 1000 to 1024. The absence of this effect at the opposite side of the CCD suggests that this is not a simple consequence of vignetting, but rather that the upper pixels are somewhat degraded. As a result, the light curves from these regions are of significantly lower quality that the majority.

A similar method of plotting has been used in Figure 3.2, to show the relationship between the mean scatter and the RA-positions of the targets. This, when taken into account with Figure 4.11, confirms that the scatter is much greater for stars in areas of dense stellar population. As expected, the large PSF introduces a major component of noise into these light curves, due to the large size of the aperture and annulus used for making the measurements.

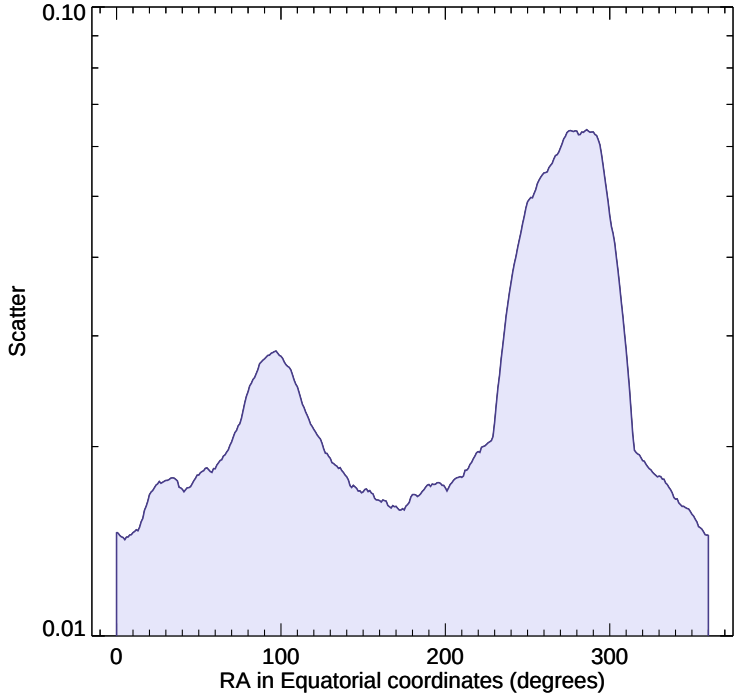

Figure 4.11: Mean scatter in the light curves with respect to their RA position in the sky. These results have been binned-up by 20 pixels to show the general trend across the sky. Taken into account with plot (a) in Figure 3.2, this confirms that the light curves of stars in dense regions are extremely susceptible to the effects of contamination in the aperture and sky-annulus.

4.6 Summary of noise characteristics in the raw light curves

Each raw light curve contains a combination of noise components, which are present on a variety of timescales and magnitudes. The dominant component will depend primarily on the stellar brightness and the nature of the star, i.e. whether it is active or quiescent. It will also depend on the target's position on the CCD and in the sky.

The impact of the noise on a light curve will ultimately determine the outcome and success of any subsequent analysis, which in this case is a search for planetary transit signatures. It is paramount to understand each factor that is contributing to the noise, so that it can be removed from the light curves without interfering with the flux from the source. It is also important to know which targets are most affected and what proportion of the total sample these constitute. This will be useful for developing automated methods of trend removal, which is the focus of the following chapter.

Chapter 5

Trend Removal Pipeline

5.1 Introduction

The previous chapter described sources of noise which are common to all types of CCD photometry, as well as those which are specific to the HI-1A light curves. One key point is that systematic, intrinsic and external components of noise are present in all photometric observations and their impact on the data will ultimately determine the success of future surveys (e.g. stellar or transit), which rely on high precision data to to produce accurate results.

5.2 Trend removing algorithms in transit surveys

Many current transit surveys have strategies to minimise and remove systematic elements of noise, prior to a search for planetary and other stellar signatures. For ground-based observations, there are a number of algorithms which are widely used to combat the common effects of atmospheric noise. Two of these are the popular Trend Filtering Algorithm (TFA) (Kovács et al., 2005) and Sysrem (Tamuz et al., 2005), which are used by the HATNet and SuperWASP projects respectively (e.g. (Kovács et al., 2010; Smith et al., 2006)). With regards to space missions, CoRoT has various teams working on different methods of noise reduction (e.g. Mazeh et al. (2009); Mislis et al. (2010); Ofir et al. (2010)), while *Kepler* has devised the Pre-search Data Conditioning pipeline (PDC) (Jenkins et al., 2010a), a fully-automated, purpose-built program which deals with the systematic effects in their light curves.

Following in the footsteps of *Kepler*, a trend removal pipeline (TRP) has been developed for the HI-1A, which is suited this instruments characteristics. Its purpose is to remove the dominating components of noise from the raw light curves, to enable the detection of real transit signals which may otherwise have gone unnoticed. By using the detrended light curves for the subsequent transit search, a successful outcome is far more likely.

An important consideration in the construction of the pipeline was finding a balance between removing components of noise and removing or modifying the genuine stellar flux. If the noise-reduction is too rigorous, this could alter the shape and depth of actual transits, which may lead to a null detection. Or instead, it could modify the shape and depth of binary eclipses, making them appear more transit-like and producing false-positives (FPs) in the transit search. To avoid these scenarios, each stage in the TRP is designed to reduce the noise but at no risk to short-duration binary and transit signals.
The performance of the pipeline will be somewhat limited by the intrinsic scatter in the light curves and therefore it is expected to be most effective for bright stars and less so for fainter targets, as discussed further in Chapter 6.

5.3 The STEREO Trend Removal Pipeline (TRP)

This is a multi-stage pipeline to reduce the various components of noise presented in Section 4.3. The thresholds reported here have been tried and tested and they provide the best results overall with regards to transit detection with BLS (Chapter 7).
The following sections describe each stage of the TRP.

5.3.1 Stage 1: Data Point Check

All light curves with fewer than 200 data points are eliminated. This removes light curves which are sparse (i.e. have less than 30 % of their data points) or which cover a total duration of less than $\sim$5.5 days. It ensures that each light curve included in the transit search has an adequate number of data points to produce reliable results with BLS.
The majority of light curves with less than 200 points will be either those with substantial telemetry drop-outs or else those of the faintest stars ($R > 10.5$), for which the tracking errors are greatest.

5.3.2 Stage 2: IQR Test

This stage is designed to remove the majority of the discontinuous light curves, such as those described in Section 4.3.1. The IQR test is a data analysis technique which measures the spread of a distribution. In this case the distribution is the observed flux and the IQR (inter-quartile range) is the difference between the 25th and 75th percentiles of the data. This is calculated by separating the data into two halves at the median and then finding the median of each half. Unlike the range, which measures the difference

between the largest and smallest value in the data, the IQR method is robust to outliers and therefore it is a reliable indicator of the spread of the flux.

A test sample consisting of randomly selected raw light curves was used to determine an appropriate IQR-threshold. As an example, the light curve in Figure 4.1 has an IQR value of 0.7 and in contrast, the light curves in Figure 4.2 both have IQR values of 0.05.

The results from the test sample indicate that a suitable cutoff value would be IQR = 0.5. This threshold is a compromise between eliminating the majority of discontinuous cases without rejecting too many large-amplitude, pulsating variables, such as Cepheids, RR Lyraes and δ-Scutis. These stars also result in high IQR values, due to their large-amplitude variations. Although they are not the focus of this research, they are objects of great interest and so it is advantageous to include them in the final sample of light curves for alternative studies.

5.3.3 Stage 3: Rejection of Outliers # 1 – Tracking accuracy

The y-pixel locations (in the frame of the CCD) are used to assess the reliability of each flux measurement, with respect to the tracking accuracy. Since the satellites are in a stable orbit their motion should not much affect the trajectory of a star on the detector as is passes through the FOV. Therefore any extreme outliers in the y-position can be attributed to inaccurate tracking, i.e. errors in the centroid function (see Section 4.3.1). Where y-pixel outliers are found, it is likely that the data point is not associated with the target star and hence it is removed from the light curve.

This test obtains the best results for light curves which are well-tracked on the majority, but have suffered occasional glitches. Two examples are given in Figures 5.1 and 5.2, where the upper panels show a portion of flux, with the corresponding y-pixel locations plotted below. In the first example there are three outliers, highlighted in green, which do not follow the general trend of the tracking. As this 8th magnitude star is fairly bright, it's low scatter means that the errors in tracking can clearly be seen as outliers in the flux. However in the second example, the outliers are not as easily distinguishable in light curve as they are in the y-pixel values. Therefore without this test, erroneous data points such as these could not be identified and so would remain in the light curves. This exemplifies the validity of this test for removing some of the systematic noise in the light curves.

The method devised to remove the erroneous points is as follows:

I If there are gaps in the data series longer than 5 hours ($\approx$ 7 points), then "bridge" points are injected

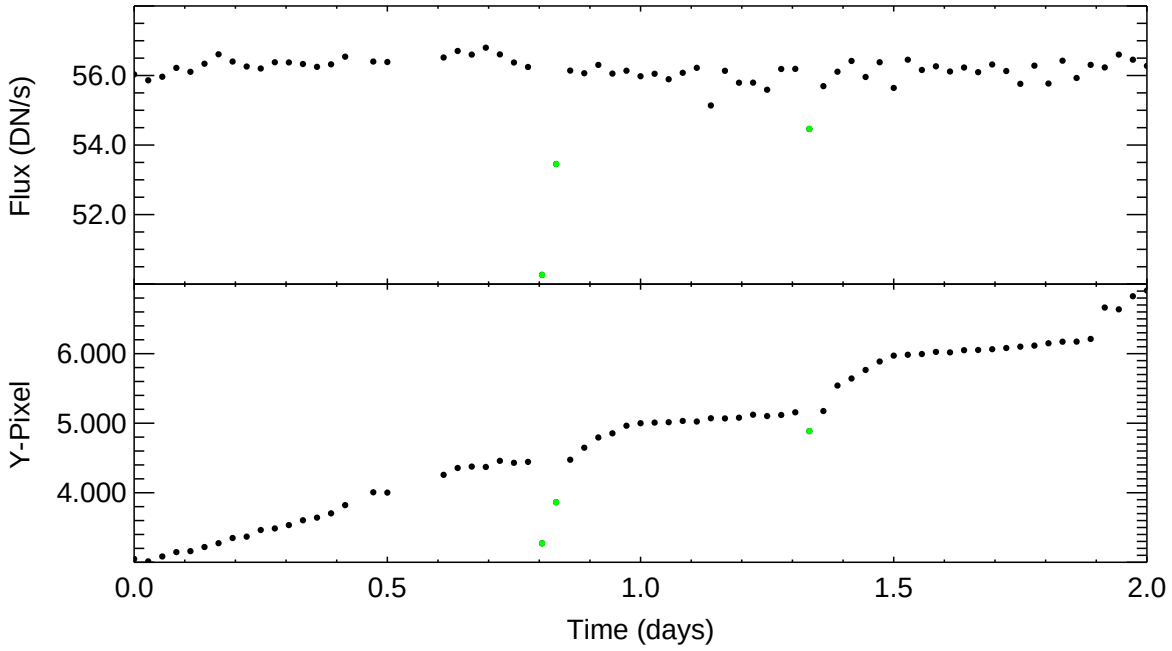

Figure 5.1: A segment of light curve is shown in the upper panel and the corresponding y-pixel values are plotted below. The green points are the outliers which are identified by Stage 3 in the TRP.

into the spaces to maintain continuity between the sections. This is necessary to avoid anomalies in the fit to the data, which arise when there are large disparities between two consecutive points. The number of bridge points used is ~ 30 % of the missing points and these are added at regular intervals to create a link between two sections of light curve which are widely separated in time. The "bridge" points are removed after the fit has been established.

II The y-pixel time-series is fitted with a box-car function with a width of 37 points (≈ 1 day). A box-car is a type of filter which smooths the data by replacing each point with the average of m adjacent measurements, where $m \equiv \mathrm{width}$. This provides a fit which represents the general, underlying trend, as a function of time. During testing, this type of filter performed better than a median filter, which replaces each point with the median of m values. The median filter more sensitive to outliers than the boxcar, meaning that when a star would drift from one y-pixel to the next (shown in Figures 5.1 and 5.2), the median would sometimes remove "good" data points as well as bad ones.

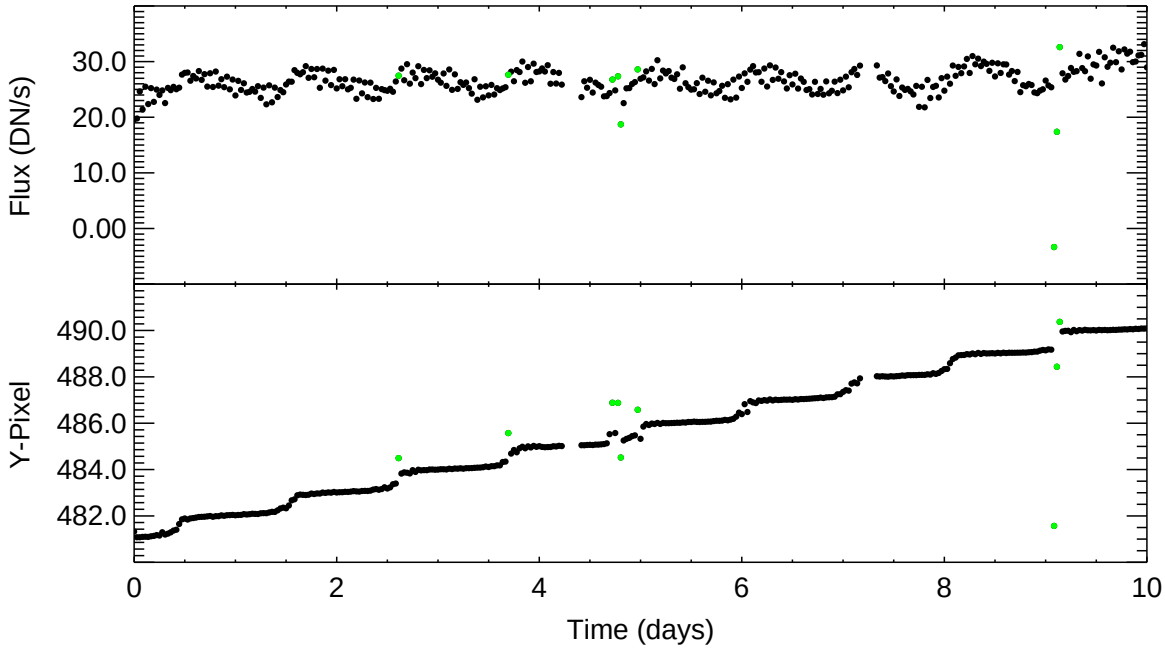

Figure 5.2: The y-pixel values plotted in the lower panel highlight the erroneous data points caused by tracking errors. Although these are not easy to identify from the light curve alone (upper panel). This example conveys the usefulness of stage 3 in the TRP for removing systematic noise.

III The residuals are obtained by removing the fit from the original data. Then their standard deviation is measured, using the IDL function *robust_sigma*.

IV The artificial points are removed and the outliers are identified from the residuals by imposing a 3-σ threshold.

V Finally the outliers are removed or, in the event that the fitting failed (e.g. Figure 5.3), the light curve is eliminated from the sample.

The last step highlights a further use for the test, in identifying composite light curves which were not removed by Stage 2 in the pipeline. In these light curves, where the tracking is evenly split between two different levels, the y-pixel data cannot be fitted by a smooth function and the method will fail. If this occurs, the light curve is removed from the sample.

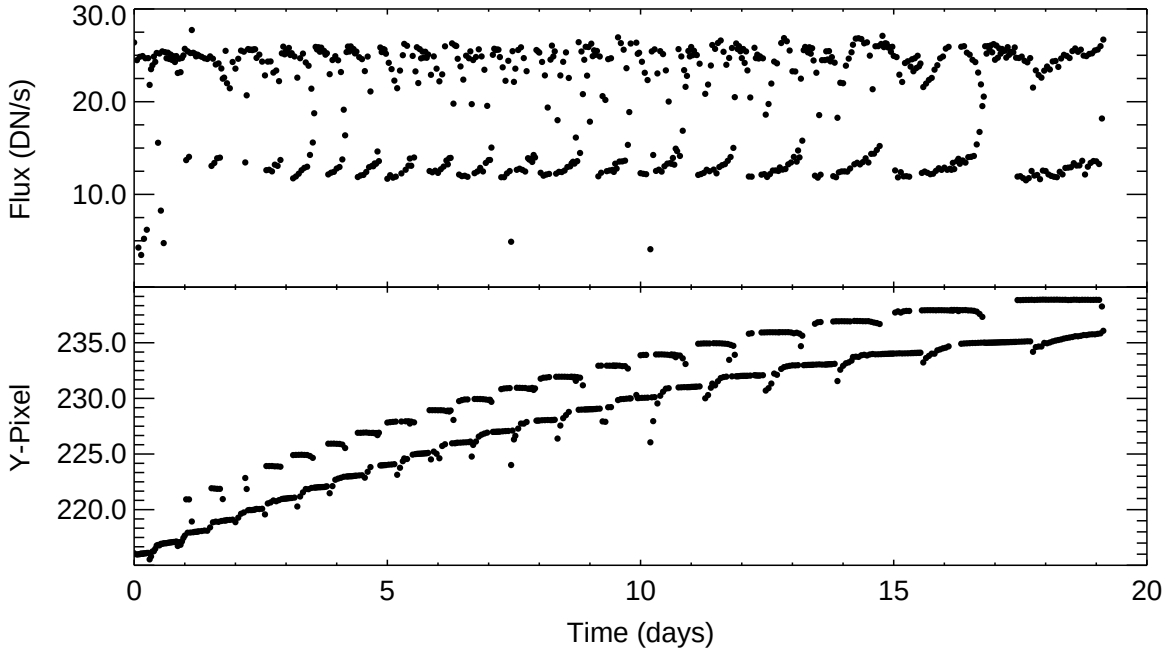

Figure 5.3: Another example of a composite light curve, where the tracking has been split between two or more stars (also see Figure 4.1). In this case, stage 3 in the TRP will eliminated the light curve from the sample.

5.3.4 Stage 4: Rejection of Outliers # 2 – Sky Error

This stage utilises the uncertainty in the background measurement to assess the reliability of the flux values.

The photometric error calculated during aperture photometry is a combination of photon noise from the source itself ($N_\star$), variance in the sky background ($\sigma^2_{\rm sky}$) and the uncertainty in the mean sky background ($\sigma^2_{\rm sky}/N_{\rm sky}$):

$$\delta F = \sqrt{N_\star + \sigma^2_{\rm sky} + \frac{\sigma^2_{\rm sky}}{N_{\rm sky}}}. \tag{5.1}$$

However, for this stage in the TRP the data count from the source, $N_\star$, is ignored, leaving only the components relating to the background measurement to serve as a test of reliability.

This test will be most applicable to light curves tracked across the centre of the FOV, towards increasing solar flux, such as that shown in Figure 5.4. In this example the upper panel shows the light curve, which has a large increase in noise towards the end. The corresponding sky-errors are plotted below, which also

show an increase in this region. The dashed line represents the 3-σ threshold. If the sky-errors exceed this line, the corresponding data points are removed from the light curve.

Removing data points should be viewed as a last resort in any noise reduction routine, it is regarded as a necessary approach at the present time. This particular stage in the TRP will be improved in future developments by modeling the solar contamination, so that it may be more effectively removed from the data, without removing the data points entirely. The consequences of this stage, in its current state, are discussed in the conclusion (Chapter 9).

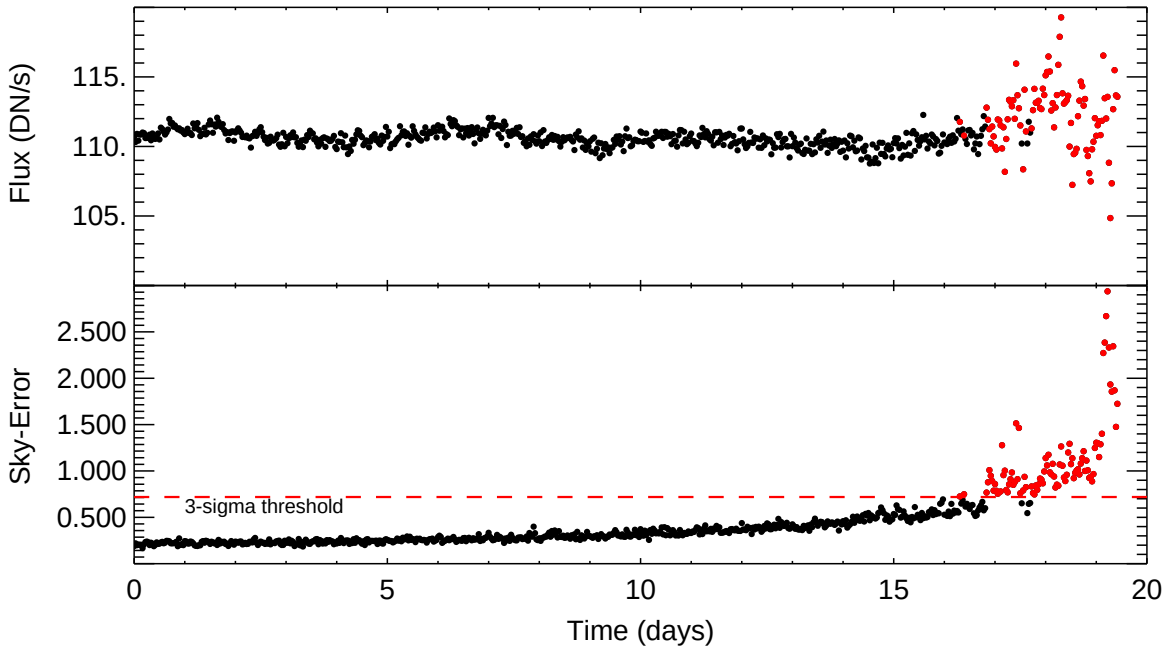

Figure 5.4: The upper panel shows the flux and below it, the estimates of the sky-error are plotted. The red points all lie above the 3-σ threshold and thus they are eliminated from the light curve. These data points were measured during a period of exceptionally high and varying background light and so they are deemed unreliable.

5.3.5 Stage 5: Iterative Non-Linear Filter (NLF)

The NLF is used to remove long-term trends in the light curves, caused by the systematics and stellar variability (where it is on similar timescales). This version is based on the type devised for CoRoT light curves (Aigrain and Irwin, 2004; Aigrain et al., 2009), but is adapted to HI-1A data, which have a longer

cadence and a greater fraction of missed data points.

The following steps constitute the NLF:

I If there are missing segments in the time-series, longer than 5 hours ($\approx$ 7 points), the light curve is split at these gaps and each segment is processed individually before being recombined at the end. Such gaps in time can affect the result of the fit.

II The edges are temporarily appended with artificial data points, as described below, so that the median function will be able to avoid outliers when determining the fit to the data.This particular approach is adopted to cope with the effects of vignetting (see Figure 4.3), where the flux can dramatically drop off at the ends of the light curves. The technique described below achieves a more accurate fit to the start and end of the light curve, even where vignetting is an issue:

i) Two arrays are defined, $\mathrm{fsub1}$ and $\mathrm{fsub2}$, which will be appended to the start and end of the section of light curve, respectively. These each have m = $\mathrm{width}/2$ points, where width is the number of points used for the median filter (see IV).

ii) Two scalar values are computed which correspond to the ranges of m data points, at the start and end of the section. This uses the averages of 3 data points at set locations, to avoid a bad estimate due to outliers. So if the data points are denoted p_i, where i = 0,...,$n-1$ (where n is the number of points in the light curve) then:

$$\mathrm{range1} = \mathrm{avg1a} - \mathrm{avg1b} = (\widehat{p_{m-3} : p_{m-1}}) - (\widehat{p_0 : p_2}) \tag{5.2}$$

$$\mathrm{range2} = \mathrm{avg2a} - \mathrm{avg2b} = (\widehat{p_{n-3} : p_{n-1}}) - (\widehat{p_{n-m-1} : p_{n-m+1}}) \tag{5.3}$$

iii) Then, for each point p_j in $\mathrm{fsub1}$ and each point p_k in $\mathrm{fsub2}$, where j,k = 0,...,$m-1$,

$$p_j = \mathrm{avg1b} - \left(j \times \frac{\mathrm{range1}}{m}\right), \quad p_k = \mathrm{avg2b} + \left(k \times \frac{\mathrm{range2}}{m}\right). \tag{5.4}$$

iv) $\mathrm{fsub1}$ is mirrored around the first data point, so that it extends beyond the start of the light curve.

v) Finally, $\mathrm{fsub1}$ and $\mathrm{fsub2}$ are appended to the start and end of the section, respectively.

An example of how edge-reflection affects the NLF is presented in Figure 5.5. This shows the light curve from the middle panel of Figure 4.3 (an example of vignetting), but for the last $\sim$ 100

points only. This can be directly compared to the case where no edge-reflection is used, in Figure 5.6. The figure captions describe the results.

III The original flux-series (appended with artificial data) is input to a median filter with a width of 5 points. This weakens the contribution from white noise and minimises any high-frequency variability on timescales of a few hours.

IV A second median filter with a width of 36 points (1 day) is applied to the output from II. This estimates the long-term trend in the light curve.

V The output from III is then smoothed using a box-car filter with a width of 3 points. This reduces the quantisation (rounding-off error) introduced by the median filter.

VI The result is then subtracted from the original data and the standard deviation of the residuals is measured using robust statistics.

VII Outliers are identified and flagged using a 3-σ threshold. The process is then repeated from step II, iterating over flagged points, until convergence (when there are no remaining outliers).

VIII The final result is removed from the original data to produce the filtered light curve, which is then normalised.

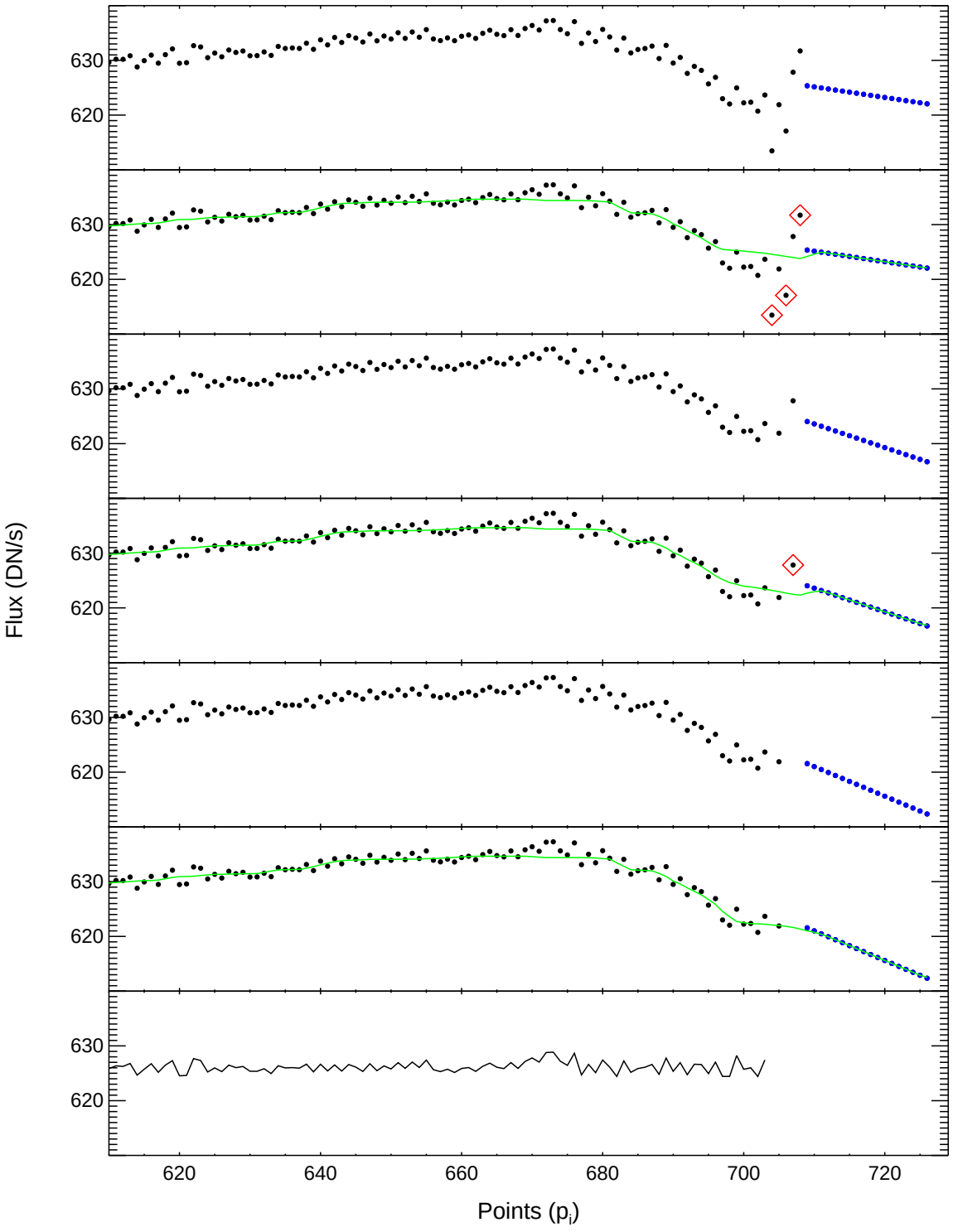

Figure 5.5: This shows multiple stages of the NLF, for a light curve with vignetting. The black dots represent the real data while the artificial points are shown in blue. The fit for each iteration is the green line and the outliers from the fit are highlighted in red triangles. Each panel shows that the method used to fit the data is robust to the outliers and the result is a good fit to the edge of the light curve. This is in comparison to Figure 5.6.

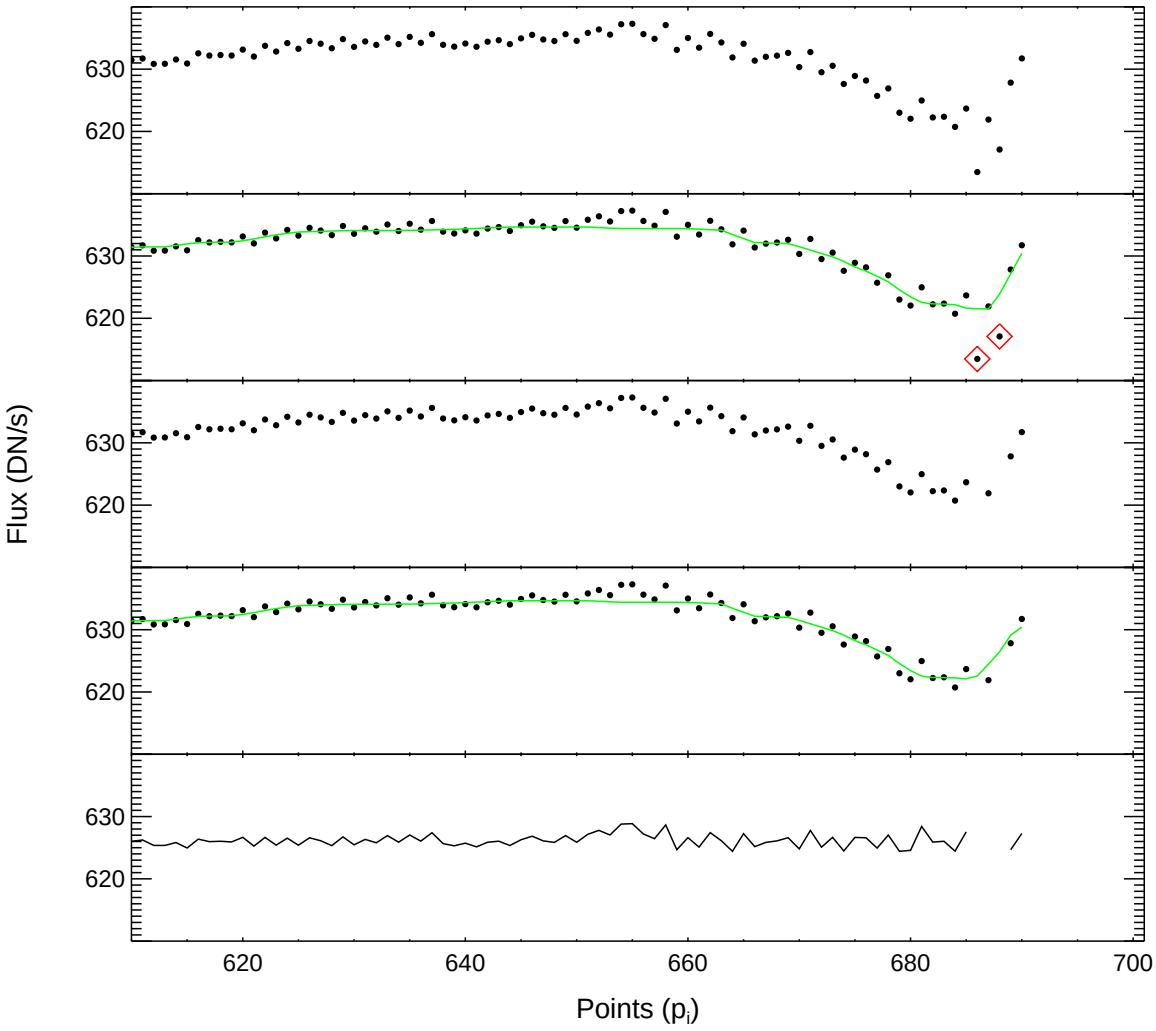

Figure 5.6: This shows the outcome of the NLF when used without padding at the edges of the data (i.e the alternative result to Figure 5.5). In this case, at each iteration, the NLF fits the spurious points at the edge of the light curve, instead of identifying them as outliers. The result is that these erroneous points remain in the filtered light curve and create a gap of nearly one day. Such data gaps can be problematic for transit searches, as they produce noise the frequency spectra used by detection algorithms. Hence padding the data is a necessary procedure.

5.3.6 Stage 6: Rejection of Outliers # 3 — Flux

The filtered, normalised light curve is sigma-clipped to remove any extreme outliers with respect to the continuum. Upward outliers are removed with a 2-σ threshold, as there is no risk to potential transit signals. However, downward outliers must be treated with caution, as any over-zealous clipping may also remove the points from transit signals or truncate those from deep eclipsing binaries.

It was found that the use of stringent thresholds in this stage could remove some of the points from deep eclipse events, resulting in the depths associated with planetary transits, i.e. ≤ 4.5 % (Brown, 2003). To avoid this effect, a relaxed threshold was imposed on downward outliers so that eclipse signals up to 9 % were maintained. However, this means that some downwards outliers remain in the detrended light curves.

5.3.7 Stage 7: Pad Gaps

Where there are significant gaps in the observations (longer than 7 hours), a small percentage of the missing data are substituted with artificial data, drawn from a Gaussian distribution. This procedure was also used on CoRoT light curves by Aigrain and Irwin (2004). The assumption made here is that the noise can be modeled from white (Gaussian) noise, with the same mean and standard deviation as the normalised light curve. For faint stars, in which the photon noise dominates, this is a good approximation. For brighter stars, while this may not be strictly true, it is adequate since only a small fraction of points are being replaced, rather than whole sections.

The aim of this stage in the TRP is not specifically to reduce the noise, but to improve the performance of transit detection, using algorithms such as BLS (Kovács et al., 2002) (see Section 7.3 for a description), as these are impeded by large data gaps. The results from an initial BLS search found a large number of FPs to be associated with light curves having significant data gaps. But by including this stage in the pipeline, this source of FPs was noticeably reduced. In addition, the signal detection efficiency (SDE), which is a measure of the significance of a signal in the presence of noise, is increased in the majority of cases where a real signal is present in a light curve with padding as opposed to no padding. The reasons for this are also explained in Section 7.3.

The histogram in Figure 5.7 shows that, for most detrended light curves, the percentage of artificial data points is < 1 %. These values were obtained by calculating, for each light curve in the sample, the number of missing data points and therefore the percentage that will be padded. By padding only a small fraction of the missing points and only in gaps longer than 7 hours, this should not interfere with the signal from a planetary transit, which, at the limit of this survey will have a duration of ≤ 7 hours (Section 1.4).

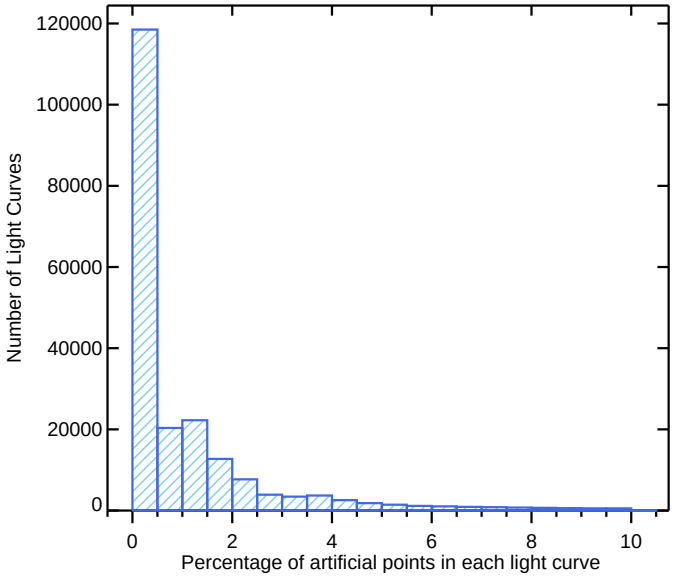

Figure 5.7: Histogram showing that the majority of light curves will contain less than 1 % of artificial data from Stage 7 in the pipeline.

5.4 TRP example results

The results of the TRP, applied to three raw light curves, are described in the following sections with the accompanying figures. In the part (a) figures, the upper panel shows the output from stages 3 and 4 (in black), plotted over the original light curve, which is shown in red. This demonstrates to use of the y-pixel locations and background uncertainties to remove unreliable flux measurements. The result of the fit (stage 5) is shown in dark blue, to demonstrate the NLF's resilience to short-duration events, such as transits. The lower panel displays the filtered, sigma-clipped and padded light curve, with any artificial data segments shown in light blue. In part (b) the light curves are phase-folded light curves, according the period found by BLS.

5.4.1 Example 1 - Solar contamination removal

The light curve in Figure 5.8 is of an A-type star with R = 8.8 and m_{HI} = 9 (HI-magnitude scale). This target was tracked across the central region of the detector and consequently its light curve shows a significant increase in noise during the last few days of the observation, due to solar contamination.

Stage 4 in the pipeline identifies the points which have significantly high uncertainties. Those found to be outside the 3-σ threshold (see Figure 5.4) are flagged and removed from the data-series. In this example it is clear that the red points do not accurately represent the stellar flux.

The NLF has reduced the low-frequency noise on timescales of 1 day, by fitting and removing the long-term systematic trend. This is evident in the detrended light curve, which shows a relatively smooth continuum, interspersed with an eclipsing binary signal. The shape of the eclipses are unaffected by the NLF and their depths are not truncated by the subsequent sigma-clip (Stage 6). Therefore this signal is still easily distinguishable from a planetary transit, which is an important result with regards to reducing the number of FPs from a transit search. Although there are fewer data points in the detrended light curve than in the original, all remaining points are genuine and reliable and the eclipse, rather than the solar flux, has become the dominant signal.

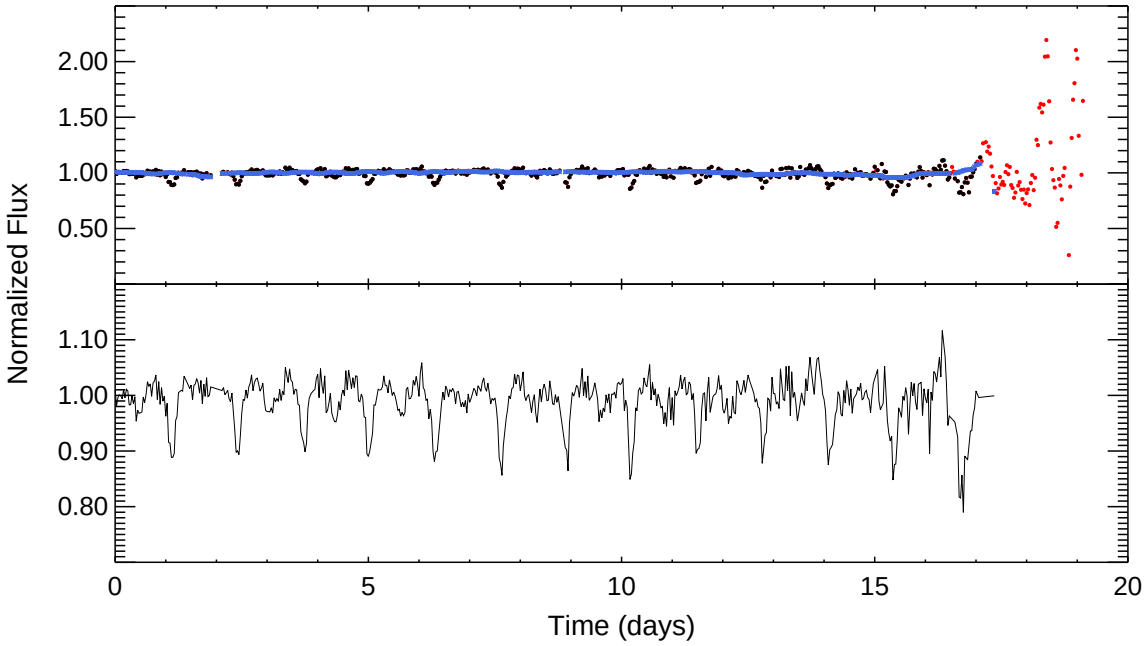

(a) The original light curve for this star, HD 50107, contains a significant contribution from the solar flux at the end of the observation. The affected data points are removed prior to performing the NLF. The filter has negligible effect on the shape of the eclipses and the sigma-clip maintains the depth which is $\sim$ 10 %. However, as can be seen in the lower panel, not all of the solar-contaminated points were removed in this instance, which appear as an unusually large "eclipse" at the end of the light curve.

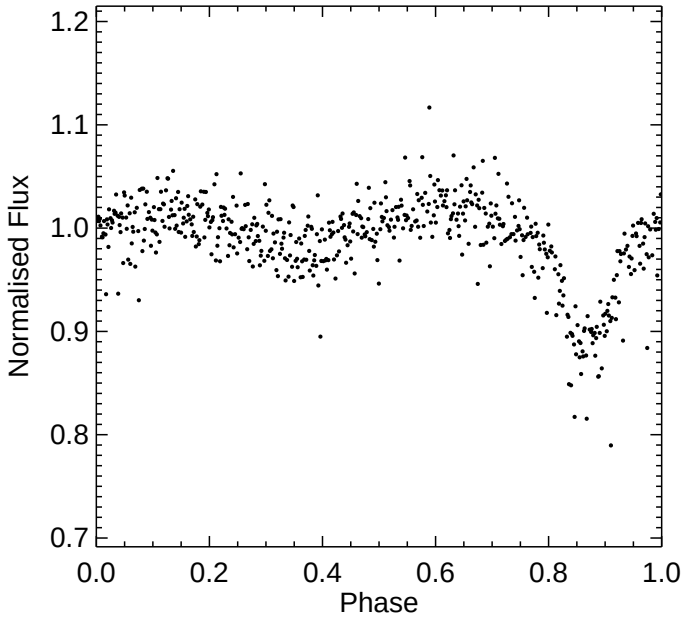

(b) The phase-folded light curve of HD 50107. The dominant signal was found with a period of 1.3 days, a duration of 3.4 hours and a depth 10 %.

5.4.2 Example 2 - Vignetting corrected

The light curve in Figure 5.9 is a bright star with R = 4.9 and m_{HI} = 5.1. While this star is not classified as a variable star, the original light curve shows small-scale variability, which is likely to be a systematic effect. Vignetting at the edges can also be seen, as this star was tracked in the lowest 100 pixels on the CCD. Consequently, due to its low position on the detector, the observations are relatively free from solar contamination.

In the upper panel it can be seen that the NLF provides a good estimate of the variations on timescales of 1 day and longer. The filter also does well to fit the points at the edges of the light curve, where the flux decreases dramatically. In the detrended light curve, a few outlier points, at the level of the eclipses remain. These could not be removed without the possibility of removing/truncating the real signal. Despite these outliers, the low-amplitude eclipses are clearly visible and the continuum has been smoothed out. A few synthetic data points have been injected into the gaps at $\sim$ 2 and just over 3 days. These points represent 3 % of the total number of data points in the final light curve. As can be seen by the phase-folded light curve, these do not interfere with the signal, which BLS detected with greater significance in the padded light curve than in the one without padding.

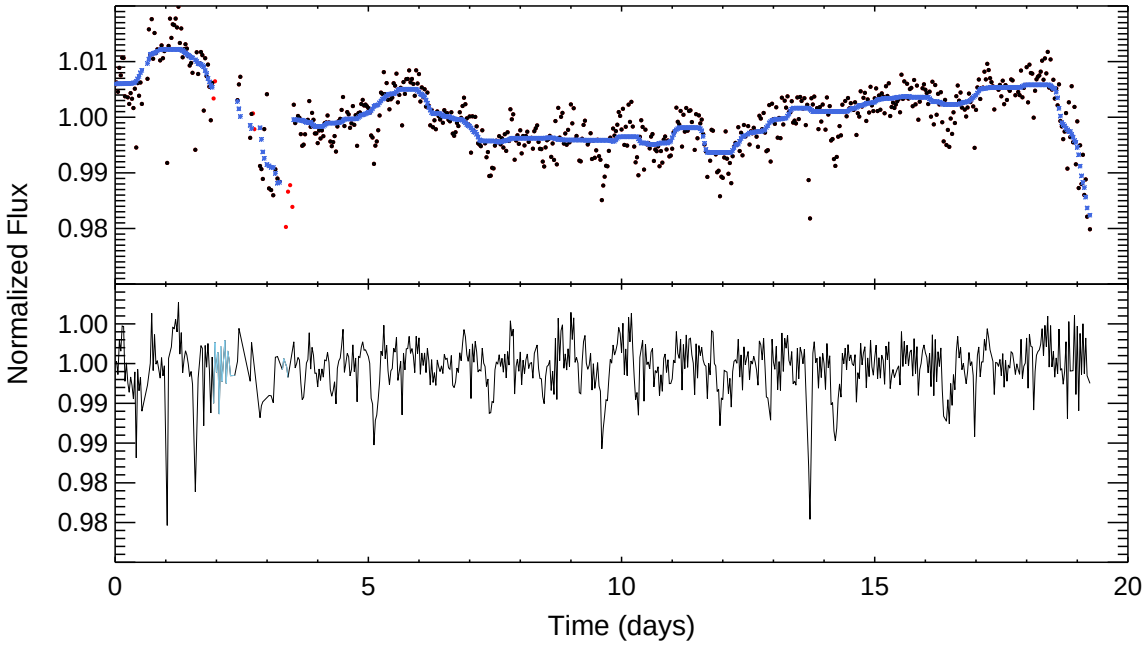

(a) The original light curve for star 18 Sgr exhibits variability from the systematics as well as vignetting at the edges. This is due to the star's relatively low position on the detector. The blue line shows that the NLF provides a good fit the long-term trend and the drop in flux at the edges, caused by vignetting. The detrended light curve has a much flatter continuum, with a few remaining outliers.

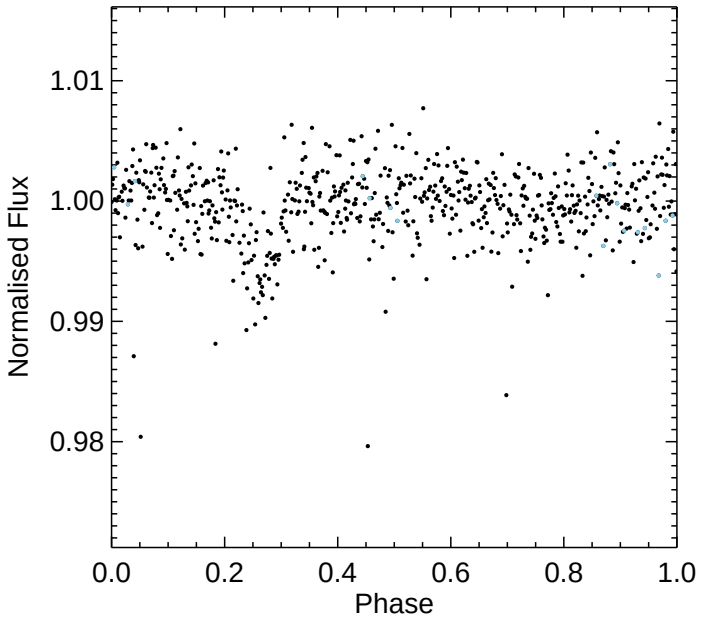

z

(b) The phase-folded light curve of 18 Sgr. The dominant signal was found to have a period of 2.3 days, a duration of 3.8 hours and a depth 0.6 %.

Figure 5.9: TRP example result 2 - Vignetting corrected.

5.4.3 Example 3 - Data gap

Figure 5.10 shows the light curve of an eclipsing binary star with R = 6.4 and $m_{\rm HI}$ = 6.6. In the original data series, the dominant features are the binary eclipses, interspersed by intrinsic stellar variability having a period of just over 1 day. There is also a substantial data gap with a duration of $\sim$ 2 days and one lasting for 8 hours, located at $\sim$ 8 and 6 days respectively.

A few data points at the end of the observation have been removed by stages 2 and 3 in the pipeline. These points come from a region which has significantly lower response, due to it's location in the corner of the CCD, meaning that any values from this region are associated with a greater uncertainty. The NLF reduces the effect of vignetting at the edges, as well as the stellar variability, which is on a similar timescale to the width of the filter. The result is a relatively flat continuum, which is more desirable for the study of transit/eclipse events. The blue line, representing the final fit to the data, shows that the binary eclipses are not affected by the filter, meaning that they are not compromised in shape or depth, with respect to the continuum. Had the sigma-clip been more stringent, these signals may have been truncated, resulting in shallower eclipses that could have been mistaken for a transit.

Both the data gaps occur where an eclipse is expected. Therefore it is inevitable that some of the of the artificial points fall inside the locations of these eclipses. This can also be seen in the phase-folded light curve. In this example, 8 % of the total number of data points are synthetic, which is an extreme case of padding. As Figure 5.7 shows, most light curves have less than 1 % of artificial data. Despite these points being injected at the locations of expected eclipses, the dominant signal is still detected by BLS with greater significance than in the alternative case (i.e. no padding).

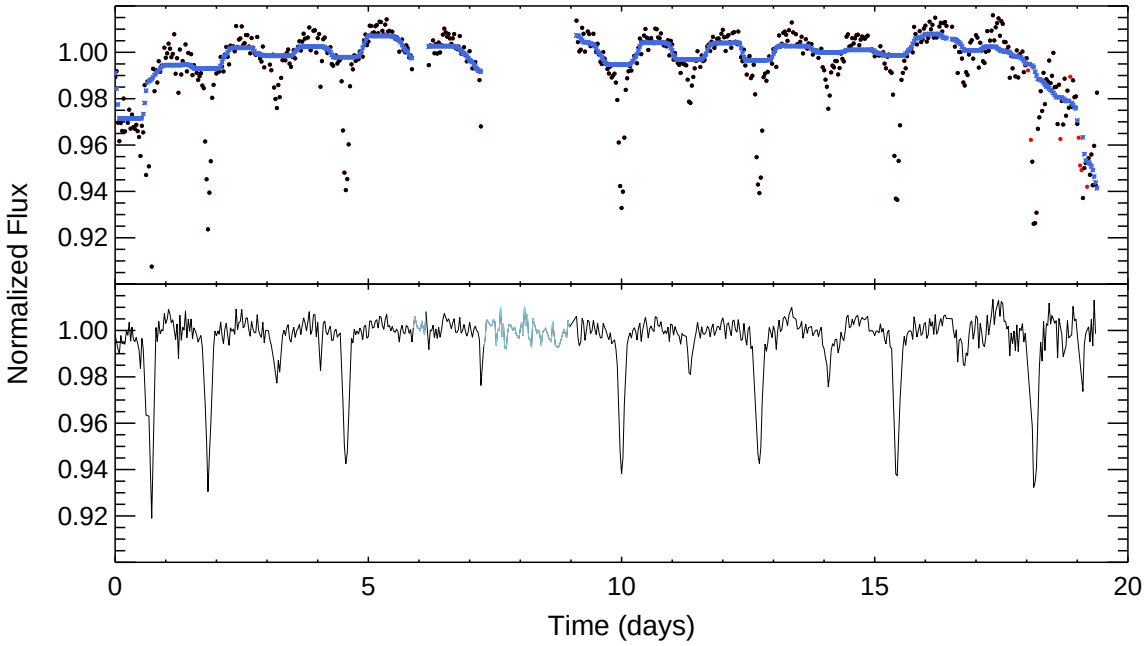

(a) The light curve for HD 100656 shows an extreme data gap lasting nearly 2 days and a smaller gap for 8 hours, located at $\sim$ 8 and 6 days respectively. Despite artificial points being injected into the detrended light curve in these gaps, the BLS algorithm still detects the dominant signal with an increased SDE, than it does in the case of no padding.

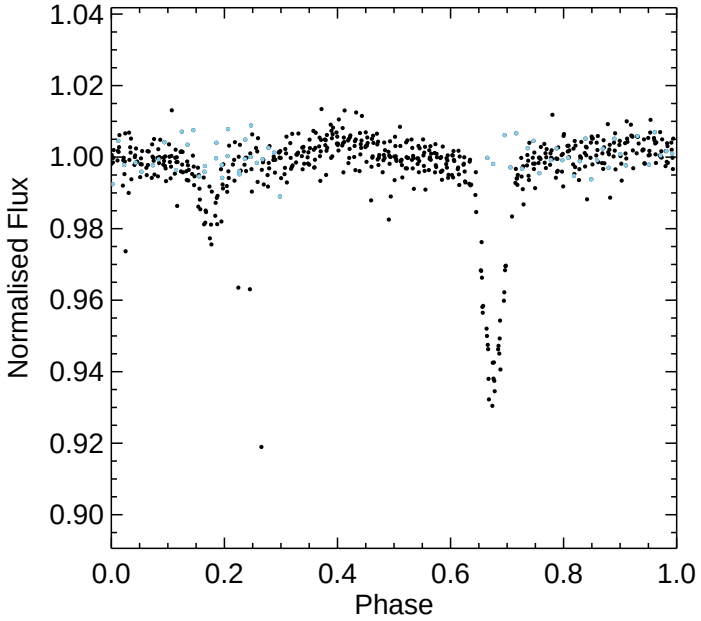

(b) The phase-folded light curve of HD 100656. The dominant signal was found to have a period of 2.7 days, a duration of 3.4 hours and a depth 0.5 %, according to BLS result.

Figure 5.10: TRP example result 2 - Treatment of data gaps.

5.5 Anomalous results from the TRP

This section illustrates a couple of scenarios which can conflict with the TRP, to produce anomalous results. These exceptional cases are problematic with regards to a transit search as they have the potential to mimic planet-like signals, which will increase the number of FPs. However, simply by being aware of these possible outcomes means that it is more likely for them to be identified and hence removed from the transit search results.

5.5.1 Scenario 1: Eclipsing binary and large-amplitude variability

The light curve in Figure 5.11 shows BD+11 1857, a currently unclassified star with $V = 9$. The original light curve in the upper panel shows deep binary eclipses and also stellar variability, with a period of ~ 7 days. In this case the NLF has modified the intrinsic nature of the light curve and has reduced alternate eclipses to a depth associated with planetary transits. This has occurred because the NLF tries to smooth out variability on timescales of 1 day, while iterating over outliers. Therefore transits and other short-duration events are essentially ignored by the filter, but longer-period signals such as these will be either partially, or wholly, filtered out.

The eclipses themselves are nearly 1 day in duration and therefore they are mostly included in the NLF, as shown by the blue line. Only the points at the extremes of the eclipses, or where there are a smaller number of points in the eclipse (where some points are missing), does the NLF iterate over these points and thus exclude them from the fit. The result is that some eclipses are maintained, whereas others are partially removed from the light curve. The smaller signals in this example appear to be much closer to the depths expected from a planetary transit.

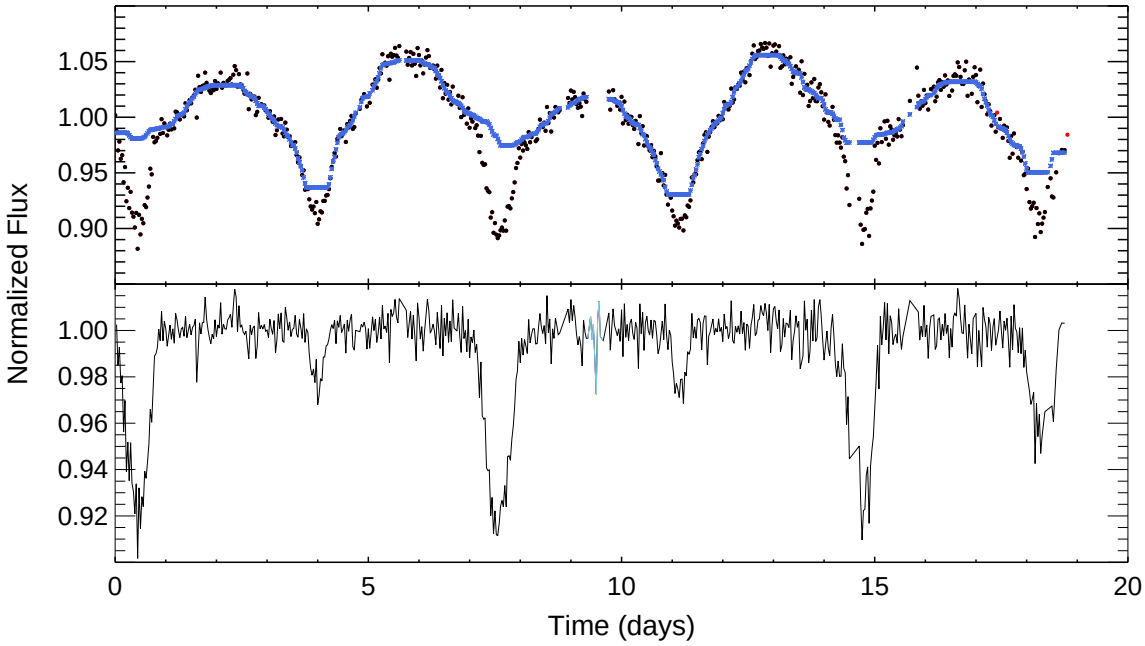

Figure 5.11: An anomalous result from the TRP due to the long-duration eclipsing binary, BD+11 1857. The upper panel shows that the one day NLF fits parts of the eclipses, so that when this component is removed, some depth remains in the detrended light curve. As the lower panel shows, this scenario is likely to be detected in a transit search, depending on the detection criteria.

5.5.2 Scenario 2: Downward outliers due to the tracking error

As explained in Section 4.3.1, some observations, particularly those with low SNRs, are prone to errors in the tracking. These occur when undersampling in the data combines with a low SNR, meaning that the source PSF cannot be well approximated by a Gaussian function and so the centroid function fails. When this happens the centroid will usually jump to the nearest point on the image that can be fitted with a Gaussian profile, which may produce a greater or lesser measurement of flux in the aperture. In the cases where the flux is less, low outliers are produced, like the ones shown in Figure 5.12. These outliers are more-or-less evenly spaced in the time-series because this is when the target is located between the centre and edge of a pixel on the CCD, which is where the flux distribution is the least Gaussian-like and where the centroid has the highest probability of failure.

As the upper panel in Figure 5.12 shows, Stage 5.3.3 in the TRP is able to accurately identify the majority of the downward outliers from their y-pixel values. However, as the bottom panel shows, some outliers

remain in the detrended light curve. This is an issue for a transit search, as these evenly-spaced points will correlated when this light curve is phase-folded on a certain trial period (see Section 7.3). Therefore, it is important for this type of FP to be considered when determining cutoff criteria for the transit search results. For example, imparting the restriction that a given transit should be longer than the width of one data point (40 minutes), may help to eliminate these scenarios from the results, without the risk of rejecting genuine transit signals (see Figure 1.3).

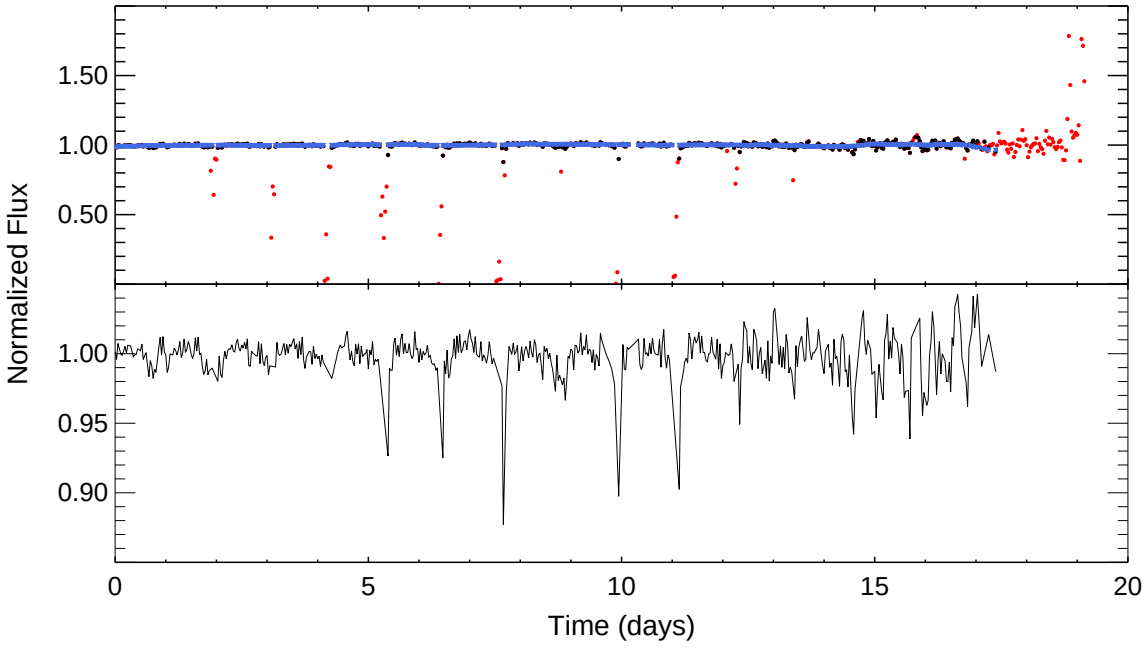

Figure 5.12: An anomalous result from the TRP due to the tracking errors which described in Section 5.5.2. This example, for HD 109376, shows a number of downward outliers in red, which result from the centroid function failing to detect the target PSF. While the TRP is able to identify and remove the majority of the downward outliers caused by the tracking error, some outliers remain, which are evenly spaced, meaning that when this light curve is phase-folded on a certain trial period, the outliers may align to produce a detectable signal.

Chapter 6

Noise Analysis

6.1 Introduction

The purpose of the noise analysis is to determine the limitations of a planet search, conducted with the detrended light curves, with respect to R-magnitude. To be able to accurately interpret the detection thresholds, the noise should be evaluated on timescales which are similar to the durations of planetary transits. As shown by Pont et al. (2006), this is a more appropriate measure for the signal-to-noise ratio (SNR) of a transit than the point-to-point scatter.

A further use for these results is to evaluate the efficiency of the trend removal pipeline (TRP), across the range of R-magnitudes, by comparing the noise in the raw and detrended light curves.

For measuring the strength of the red (correlated) noise with respect to the white (uncorrelated) noise, two methods are introduced. The first method uses the equation for the autocorrelation function, to determine the significance of trends throughout the data. The second is referred to here as the Pont method. This is based on the methods and findings presented in Pont et al. (2006), which are tested on light curves from the OGLE survey. While the autocorrelation function is general in its application, the The Pont method is specific to transit surveys, making it an appropriate method to use here. It has also been adapted by a number of notable studies in the field, e.g. Smith et al. (2006); Street et al. (2007); Miller et al. (2008); Aigrain et al. (2009), to evaluate the potential of their light curves with respect to transit detection.

With a cadence of 40 minutes for HI-1A data, it is possible that the results from both methods are not as transparent as they may be if the cadence was shorter, providing more points in a transit interval. Nevertheless the results do provide valuable insight into the nature of the correlations. Furthermore, the results from the Pont method lead to estimations of S_{r}, the detection threshold for a given orbital period and transit depth. The significance of S_{r} is discussed in Section 6.5, following the key results from the noise analyses.

6.2 Measuring correlated noise

Various sources of noise in CCD photometry were introduced in Section 4.2, such as pixel variability and intrinsic stellar variability. In this chapter, the noise is classified as either white noise (random fluctuations), or red noise (a correlation between data points). If the red noise is significant on transit timescales and is found to dominate in the data, this will have a significant impact on the detectability of a signal. Therefore, it is crucial to consider both types of noise when calculating the SNR of the data.

6.2.1 The Autocorrelation Function

The autocorrelation function, $\rho(L)$, is derived from the equation for the autocovariance function, $\gamma(L)$. This calculates the covariance of a variable x at two different times, separated by a lag L. The equation for the autocovariance function is defined below, for a discrete time-series with N data points x_i, where i=0,...,N:

$$\gamma(L) = \frac{1}{N-L} \sum_{i=0}^{N-L} (x_i - \bar{x})(x_{i+L} - \bar{x}); L = 0, 1, ..., N \tag{6.1}$$

Here L is specified by an integer number of data points, but this could equally be given as a time-difference, τ, in the case of a continuous time-series.

The autocorrelation function is obtained by normalising equation 6.1 by the variance of the sample, which is equivalent to normalising by the zeroth coefficient, i.e.:

$$\rho(L) = \frac{\gamma(L)}{\sigma^2} = \frac{\gamma(L)}{\gamma(0)}. \tag{6.2}$$

As $\rho(L)$ is normalised, it's coefficients should take a value in the range -1 $\leq \rho(L) \leq$ 1, where a result of 1 corresponds to a perfect correlation between two points. For instance, at L = 0, $\rho(0)$ = 1, since this is the autocorrelation of a data point with itself.

For a random data-series in which the data points are uncorrelated, the coefficients $\rho(L)$ will have a value of 1 at L = 0, but then fall rapidly. If the number of data points (N) is large, then the remaining coefficients should be normally distributed with a mean of zero and a scatter of $1/\sqrt{N}$. This behaviour of the autocorrelation function holds true only when there are no detectable trends in the data, i.e. white noise only. An example is shown in Figure 6.1 (a). A time-series drawn from a random distribution is shown on the left, with its autocorrelation function on the right. The coefficients are plotted against the lag, i.e. a correlogram.

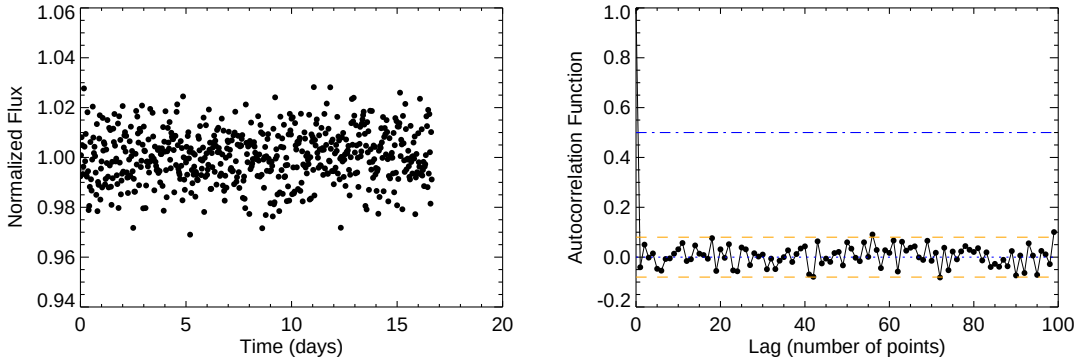

(a) The model time-series for pure white noise (with 1% scatter) is shown on the left, with it's corresponding correlogram on the right. The autocorrelation coefficients fall to nearly zero immediately and stay within the 95% confidence limits, indicating that white noise dominates here.

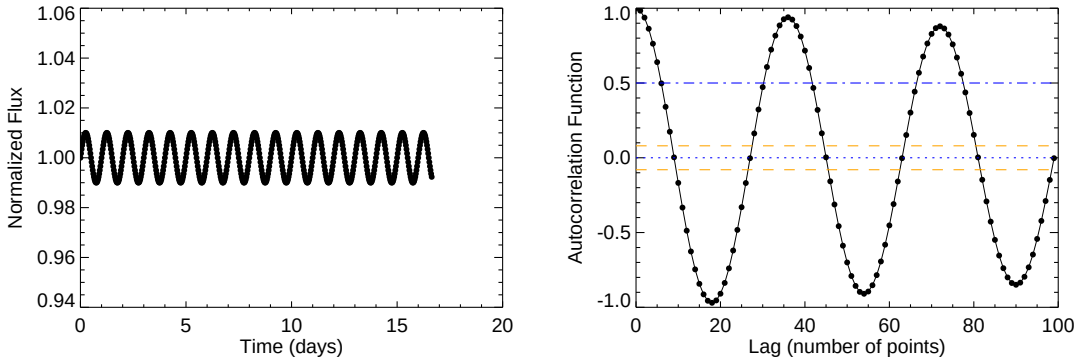

(b) The left figure shows a pure sinusoidal function having a 1-day period. This represents the extreme case of purely red noise in a light curve. The corresponding correlogram is evidence of the strong correlation between data points, especially those separated by 36 points (1-day).

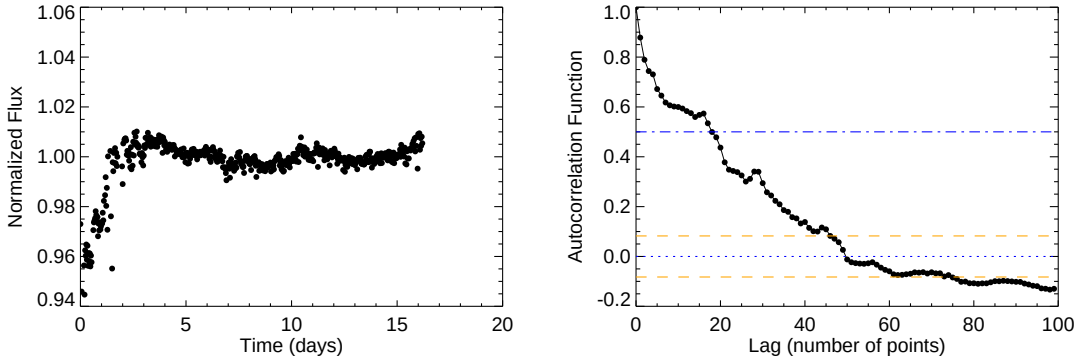

(c) The light curve of a bright, 5th magnitude star is shown on the left. This illustrates both red and white noise components in data. The adjacent correlogram indicates that the correlation between points is significant over a timescale of roughly 1.25 days (45 points). It also shows low-amplitude variations, which correspond to periodic trends on the data.

Figure 6.1: These examples show the behaviour of the autocorrelation functions for white, red and pink noise (top, middle and bottom respectively).

One key feature which is useful for determining the strength of the white noise is the half-life of the autocorrelation. This is the lag at which the function decreases to a value of 0.5 (half the maximum). If white noise dominates in the data, then the half-life should be short, e.g. 1 – 2 points. But when the correlation is strong in comparison to the white noise, then the half-life will be much longer.

If a repeatable signal(s) is present in the data, then the autocorrelation function will also oscillate at the frequency of the signal. An example illustrating this case is given in Figure 6.1 (b), which shows a model light curve with sinusoidal variability on a period of 1 day. From the point of view of planet detection surveys, a repeatable signal which is not a transit is considered as red noise. In this respect, the example shown in Figure 6.1 (b) is a case of pure red noise, for which the autocorrelation is a smoothly varying function with a period equal to 1 day. In this case the half-life is taken from the envelope of the function, which is an imaginary line that connects consecutive peaks in the correlogram. The slope of the envelope is indicative of the strength of the correlation versus the white noise. If white noise is present and dominates over the red noise, then the envelope will have a steeper gradient than if red noise dominates. In Figure 6.1 (b) the minima correspond to strong anti-correlation, where for example x_i and x_{i+L} are perfectly out-of-phase.

The final example, given in Figure 6.1 (c), shows the raw light curve of a bright STEREO target on the left. This light curve contains a combination white and red noise (from systematic trends), which gives rise to pink noise. The correlogram on the right, shows there is a strong short-scale correlation, which is significant up to ~ 45 points and in addition there is a weaker, longer-scale trend. This is indicated by increasingly negative correlations at large lags, which suggests an underlying trend on a longer timescale. A repeatable pattern with a period of 8 hours is also indicated in the correlogram, by regularly spaced peaks every 12 points, although these appear to be dampened by the white noise.

The dashed yellow lines in the correlograms mark a 95% confidence band, which is useful for interpreting the significance of the correlations with respect to white noise. The points which lie outside these lines can be associated with strong correlations, while those within the boundaries correspond to negligible correlation, at the given lag. The 95% threshold is calculated from $0 \pm 1.96/\sqrt{N}$, where 1.96 corresponds to the critical level and $1/\sqrt{N}$ is the standard deviation of the autocorrelations for a randomly distributed data-series.

6.2.2 Determining $\sigma_{\rm r}$ - The Pont method

The key points presented in Pont et al. (2006) are summarised below:

- Transit surveys often overestimate their detection yields, by ignoring the impact of correlated (red) noise on timescales of a few hours. Again, this is the duration over which planetary transits commonly occur.

- The detection threshold of a transit survey can be regarded as the minimum SNR of the data, where the signal is equal to transit depth, d and the noise, σ_d, is from the in-transit data points. However, this must take into account correlated and uncorrelated noise.

- Pont et al. (2006) propose a method to calculate $S_{\rm r}$, the significance of a detected signal. This quantity is effectively the SNR in the presence of both correlated and uncorrelated noise, which is an improvement on $S_{\rm d}$, which is the SNR in the case of purely white noise.

- They show, using candidates from the OGLE survey, that $S_{\rm r}$ provides a more robust detection threshold than $S_{\rm d}$ and allows for a greater distinction between positive and false-positive detections (demonstrated by their Figure 9). This is important because it reduces the time and resources needed to follow-up planet candidates. It also reduces the likelihood of missing true detections, by providing a more reliable cutoff that reflects the true limits of the data.

White versus red noise estimates

The classical calculation for the SNR of a detected transit is,

$$S_{\rm d} = \frac{d}{\sigma_d} = \frac{d}{\sigma_0} n^{1/2}, \tag{6.3}$$

where S_d represents the significance of a signal, with a depth d and n points in transit. The uncertainty on the depth, σ_d, is equal to the uncertainty on each measurement, σ_0, divided by $\sqrt{n}$.

The above equation is based on two assumptions: that all data points have the same uncertainty, σ_0 and that the noise is uncorrelated, i.e. purely white noise. While the first assumption may be true enough in most cases, the second is critically flawed and is the reason why so many surveys frequently over-estimate the significance of their detections.

Pont et al. (2006) suggest that the definition of σ_d should be modified to include a term for the covariance between the in-transit data points as follows:

$$\sigma_d^2 = \frac{1}{n^2}\sum_{i,j} C_{ij} = \frac{\sigma_0^2}{n} + \frac{1}{n^2}\sum_{i\neq j} C_{ij}, \tag{6.4}$$

where i and j are the indices of two in-transit measurements and C_{ij} are covariance coefficients between the ith and jth data points.

It can be seen that Equation 6.4 is equivalent to Equation 6.3 when white noise dominates, i.e. when

$$\frac{\sigma_0^2}{n} \gg \frac{1}{n^2}\sum_{i\neq j} C_{ij}. \tag{6.5}$$

In other words, if the observation is dominated by shot noise (typical for a faint star), then Equation 6.3 can be used to determine the significance of a detection. However in the majority of cases, and especially for bright stars, the covariance term should be included in the calculation of σ_d.

Pont et al. (2006) give the following formalisation to describe the covariance between two data points i and j, within a given transit:

$$\sum C_{ij} \simeq \sum_{k=1}^{N_{\rm tr}} \sum^{k{\rm th}} C_{ij}, \tag{6.6}$$

where k=1,...,$N_{\rm tr}$ and $N_{\rm tr}$ is the total number of transits. This equation is similar to the autocovariance equation, which is the unnormalised version of the autocorrelation function, given in Equation 6.2. The difference is that the calculation here is only done for the points in a given transit (k), as all other correlations are considered to be insignificant.

By using this approximation to describe only the significant correlations, the uncertainty on a transit detection in a given light curve may now be calculated from,

$$\sigma_d^2 = \frac{1}{n^2}\sum_{k=1}^{N_{\rm tr}} \mathcal{V}(n_k) n_k^2, \tag{6.7}$$

which is Equation 6 in Pont et al. (2006), where $\mathcal{V}$ is defined as,

$$\mathcal{V}(n) \equiv \frac{1}{n^2}\sum C_{ij}. \tag{6.8}$$

The consequence of having correlated noise, especially if it is the dominant component, is that σ_d does not decrease as $\sqrt{n}$, i.e. by having more in-transit points. The uncertainty will decrease much slower than this and likewise, $S_{\rm d}$ will increase much slower. This is why most transit surveys fail to correctly estimate their detection thresholds and hence why so many FPs are considered for planet candidates.

In the absence of any *a priori* knowledge (i.e. pre-signal detection) Pont et al. (2006) suggest a method for estimating the red noise on timescales of expected transits, directly from $\mathcal{V}(n)$. This method is described in the next section.

The method

To estimate the level of red noise from the systematics, it is suggested to use only those light curves which show no significant sinusoidal variability, e.g. from stellar pulsations. Therefore to identify variability in the sample, so that these light curves may be removed from the analysis, a Lomb-Scargle periodogram (Scargle, 1982; Horne and Baliunas, 1986) was used. This found significant peaks in the power spectrum for ~ 30 % of the sample. The period of the variability was either less or much greater than one day, as these signals are still present after the the one-day filter, performed by the TRP (Section 5.3.5).

The analysis was conducted on a 2-hour timescale as this is the average duration of transits having orbital periods of less than ~ 7 days (see Figure 1.6). The same analysis was also carried out for a 5-hour timescale. which is more likely to be associated with eclipsing binaries. This will serve as a useful comparison, for determining the evolution of the red noise. In the HI-1A data, timescales of 2 and 5 hours are equivalent to 3 and 7.5 points, respectively. While the former is not a significant number over which to measure the correlations, the results should still indicate the level of correlated noise, on the timescale which is most relevant to planet detection.

When the locations of the in-transit points are known, then they should be removed before calculating $\mathcal{V}(n)$, however in the absence of any *a priori* knowledge at this stage, all data points were included in the analysis.

The proposed method for estimating $\sigma_{\rm r}$ uses $\mathcal{V}(n)$ (Equation 6.8), which describes the covariance between two measurements, i and j, in a transit duration containing n points. The steps to compute $\mathcal{V}(n)$, directly from the light curve, are outlined below.

1. A time-mask is created with length equal to the corresponding timescale (2 or 5 hours). This slides over the total time-series, in intervals of 30 minutes (less than the cadence, which is 40 minutes).

2. At each interval, the mean of the flux, F_j, is calculated and the number of points within the interval, n_j, is recorded.

3. The F_j measurements are grouped according to their respective n_j and the variance of each group

is calculated. Only the results for the groups with n_j=3 and n_j=7 are used, corresponding to 2 and $\sim$ 5 hours. This value is the estimate of $\mathcal{V}(n_j)$.

Assuming the noise has both red, $\sigma_{\rm r}$ and white, $\sigma_{\rm w}$ components, these components may be extracted from $\mathcal{V}(n)$, using,

$$\mathcal{V}(n) = \frac{\sigma_{\rm w}^2}{n} + \sigma_{\rm r}^2. \tag{6.9}$$

This is Equation 9 in Pont et al. (2006), where $\sigma_{\rm w}$ is equal to the point-to-point scatter divided by $\sqrt{n}$ and n is 3 or 7.

6.3 Results of the noise analysis

6.3.1 Results from the autocorrelation method

The autocorrelation functions were calculated for the raw and detrended light curves at an integer range of lag values (L). The results which are most relevant to transit detections from the HI-1A data are the coefficients at lags between 2 and 6 points (80 mins to 4 hours), which reflect the limits of detectable transit durations in this study (see Figure 1.6 and Section 7.3). Figure 6.2 contains the correlograms for the raw and detrended data in the upper and lower panels, respectively. For interest, the same results are plotted in Figure 6.3, on a longer x-axis covering a larger range of lags. The values plotted in each figure are average results for the light curves in each magnitude bin, denoted by the key in the top right. For reference the 95% confidence lines are represented by dashed, black lines above and below the zero line. As explained in Section 6.2.1, this confidence band is useful for determining whether a correlation is significant at a given lag. Any coefficients which fall outside these lines can be taken as evidence that a correlation exists, i.e. red noise is present in the data and significant on the associated timescale.

The results in Figure 6.2 (a) show that within the timescale relevant to planetary transits, the raw light curves contain a strong to moderate component of red noise for the brightest to faintest targets, respectively. Overall at lags of 2 - 6 points, the majority of light curves contain red noise, on some scale. One thing to note however, is the difference between the autocorrelation half-lives with respect to stellar magnitude. As mentioned in Section 6.2.1, the half-life of the autocorrelations indicates the strength of the white noise, which acts to dampen the correlation between points. The results in the figure show that the light curves belonging to the fainter stars (from the 8th to 11th magnitude) exhibit similar half-lives, on a timescale of less than 40 minutes ($<$ 1 point). This suggests that although trends are present in

the data, the white noise appears to be the dominating component. In contrast, the light curves for the brightest stars (from 4th to 6th magnitude) have autocorrelation functions with longer half-lives, up to 12 hours, suggesting that in these cases the red noise dominates. This could be problematic in subsequent transit searches involving a large number of targets, since potential detections are just as likely to be from correlated noise on these timescales as they are from real transits. In essence, this figure emphasises the need for a robust and rigorous trend removal process like the TRP.

The results from the detrended data in Figure 6.2 (b) convey a far more promising outlook with regards to transit detection. The autocorrelations of these light curves suggest that the TRP is extremely effective at removing significant correlations over the range of detectable transit durations. In particular, these results show that on timescales of 2 - 4 hours, the correlation between data points is insignificant with respect to white noise. Furthermore, with the exception of the light curves from the brightest targets, the autocorrelation half-lives are now all less than 40 minutes, which confirms that the trends have been extracted effectively by the TRP. The exceptions are the light curves from the 4th-magnitude stars, which correspond to fewer than 1% of the total sample. The lower efficiency of the TRP in these cases is likely to be due to the saturation of the CCD, which occurs when the influx of photons exceeds the capacity of a pixel on the CCD (see Section 4.4). When this occurs, the photon counting becomes non-linear and so an extra element of systematic behaviour is introduced, which can not be corrected by the TRP.

Figure 6.3 shows the same results as Figure 6.2, but computed over a longer range of L, up to 1.6 days. These correlograms illustrate the evolution of the autocorrelation over a longer time. Again the results for the raw light curves are presented in the upper figure and those for the detrended data are in the lower figure. The bottom figure shows that for the 4th-magnitude stars, the autocorrelation function oscillates at various frequencies, which is evidence for repeatable trends in the data. However, as the coefficients at longer lags fall inside the 95% confidence band, the correlation on these timescales is fairly weak and for all other of the light curves, these trends are lost in the white noise.

In summary, the results found with the autocorrelation method act as a precursor to the Pont method, which can provide a more quantitative analysis regarding the white and red noise, with respect to transit detection. These results are described in the next section and are then used to evaluate the detection thresholds of a transit survey with the detrended data.

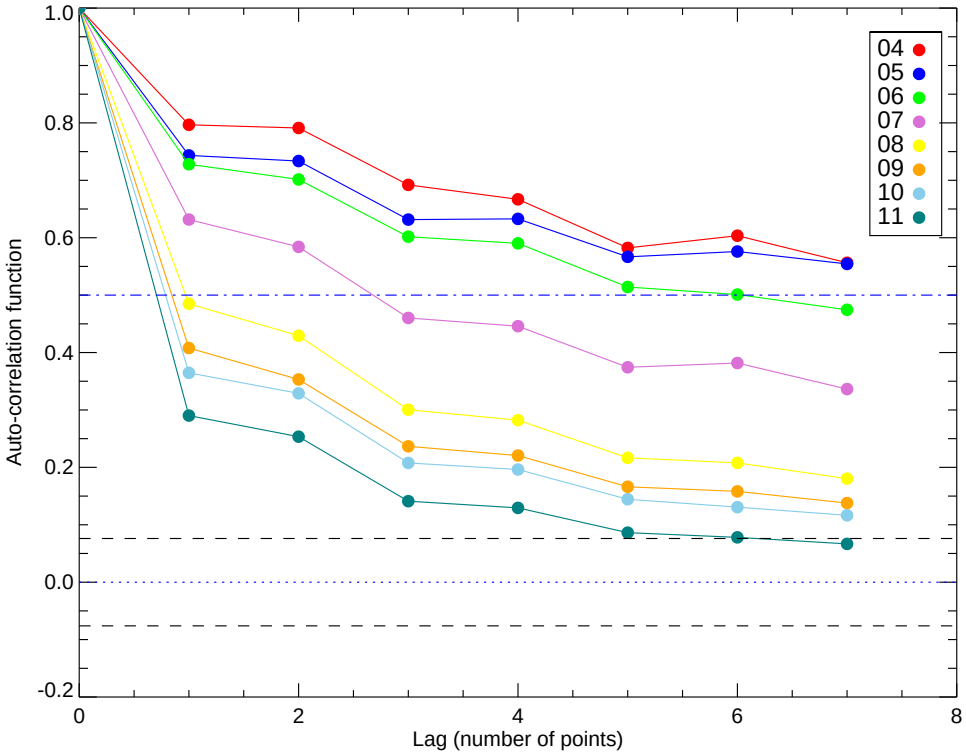

(a) The correlogram for the raw HI-1A data, for lag values in the range 0 - 7.

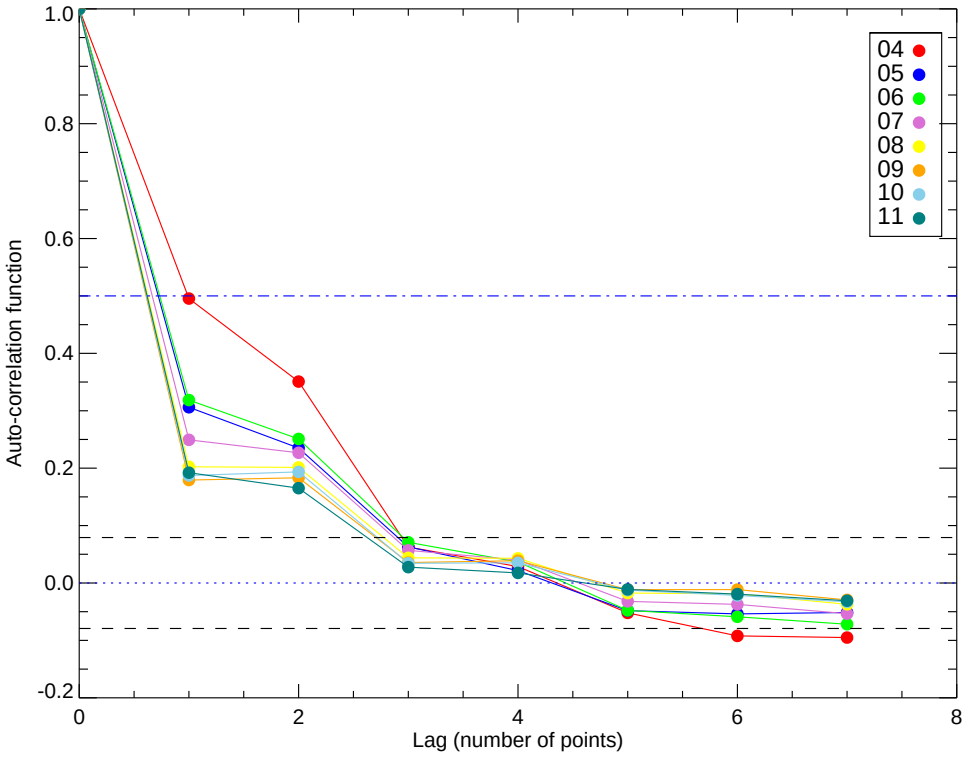

(b) The correlogram for the detrended HI-1A data, for lag values in the range 0 - 7.

Figure 6.2: Autocorrelation functions of the raw and detrended light curves, at the lag intervals most relevant to transit detection. The coefficients are averages of the light curves in each magnitude bin.

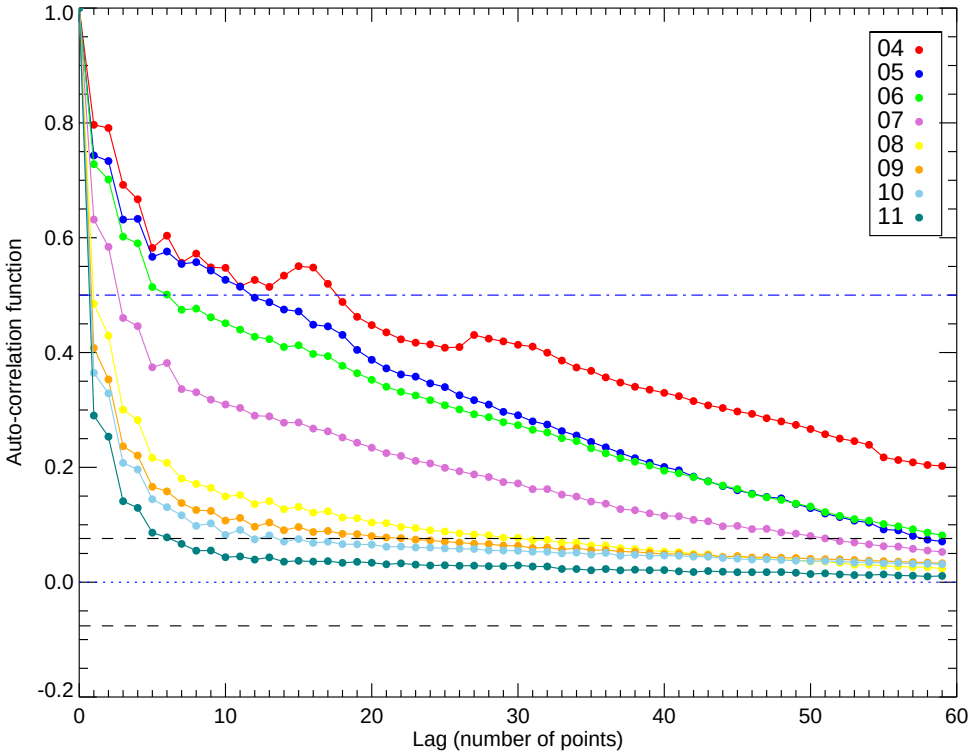

(a) The correlogram for the raw HI-1A data, for an extended range of lag values.

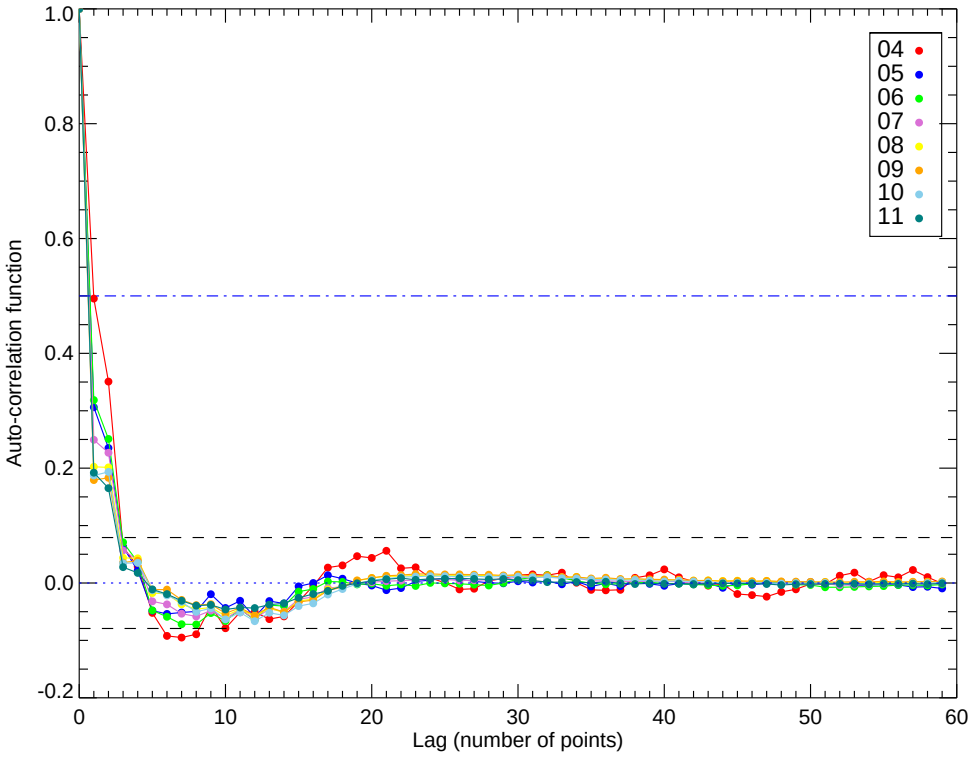

(b) The correlogram for the detrended HI-1A data, for an extended range of lag values.

Figure 6.3: Autocorrelation functions of the raw and detrended light curves, up to a lag of 60 points ($\sim$ 1.6 days). The coefficients are averages of the light curves in each magnitude bin.

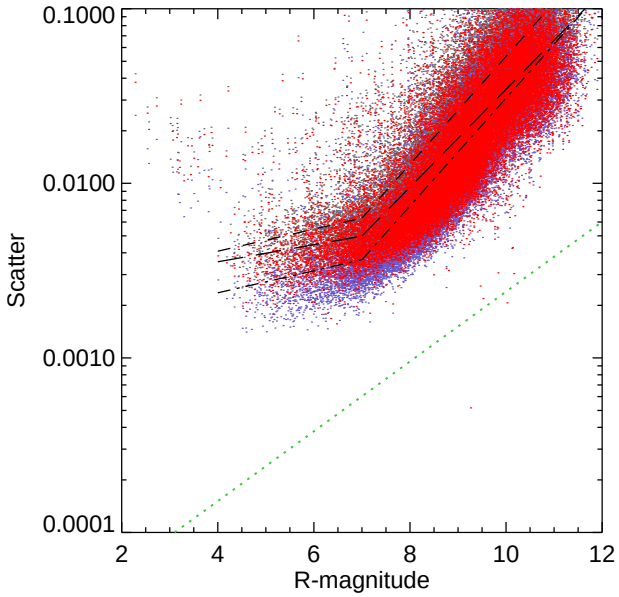

(a) pre-TRP, correlated noise on 2 hr timescale

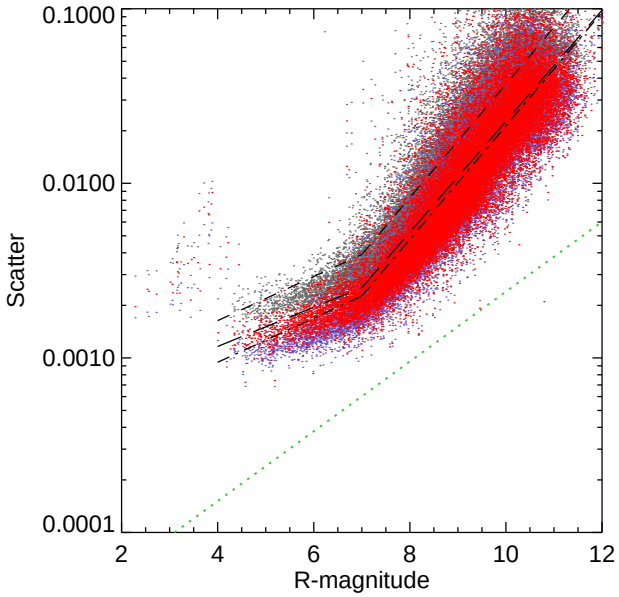

(b) post-TRP, correlated noise on 2 hr timescale

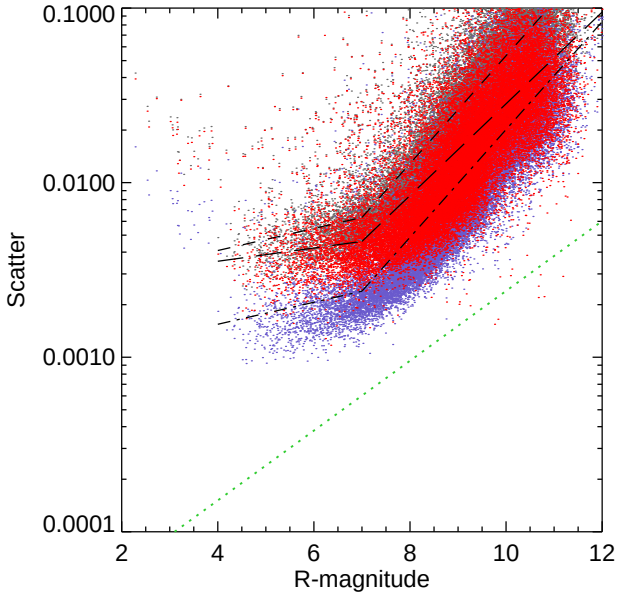

(c) pre-TRP, correlated noise on 5 hr timescale

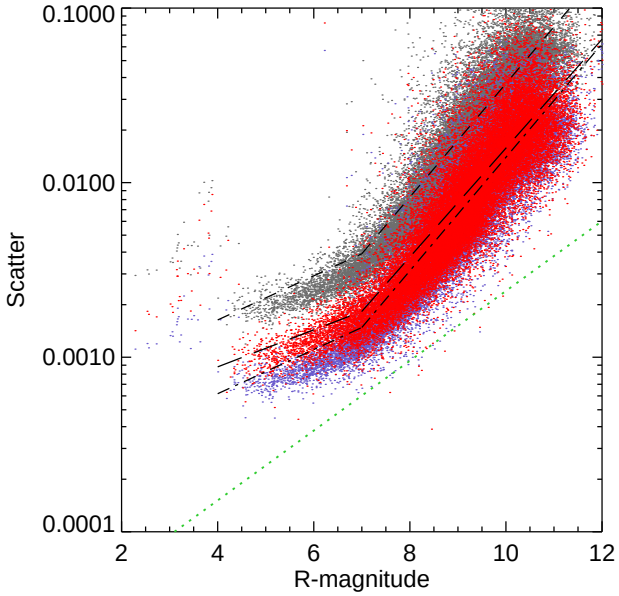

(d) post-TRP, correlated noise on 5 hr timescale

Figure 6.4: The estimated noise with respect to R-magnitude. The red noise ($\sigma_{\rm r}$) on 2 and 5 hour timescales is indicated in the upper and lower figures respectively by the red dots. The left-hand figures have the results for the original light curves, while those on the right are for the post-TRP light curves. The grey dots are the point-to-point scatter (σ_0) and the blue dots are the expected white noise ($\sigma_{\rm w}$) on the same timescales. Best-fit lines were estimated from the median of the values in each half-magnitude bin. These are overplotted as small-dashed, long-dashed and dot-dashed lines respectively, while the green dotted line shows the level of the theoretical photon noise (see Section 4.2).

Two hour timescale		Bright (at $R = 6$)	Faint (at $R = 9$)
Reduction in noise (%)	point-to-point	49	25
	σ_r	58	34
$\sigma_{\rm r}/\sigma_{\rm w}$	Pre-TRP	1.47	1.20
	Post-TRP	1.21	1.06
Gradient of $\sigma_{\rm r}$ (in $\log_{10}$)	Pre-TRP	0.05	0.28
	Post-TRP	0.11	0.32

Five hour timescale		Bright (at $R = 6$)	Faint (at $R = 9$)
Reduction in noise (%)	point-to-point	49	25
	σ_r	67	43
$\sigma_{\rm r}/\sigma_{\rm w}$	Pre-TRP	2.17	1.52
	Post-TRP	1.39	1.14
Gradient of $\sigma_{\rm r}$ (in $\log_{10}$)	Pre-TRP	0.04	0.26
	Post-TRP	0.10	0.31

Table 6.1: Statistics from the noise analysis, on timescales of 2 (above) 5 (below) hours. The values reported here are based on the results at $R = 6$ and $R = 9$, to show the comparison between bright and faint magnitudes.

6.3.2 Results from the Pont methods

The noise estimates for $\sigma_{\rm w}$ and $\sigma_{\rm r}$ are plotted in Figure 6.4, with the y-axis on a $\log_{10}$ scale. The results for the original light curves are on the left, while those for the detrended light curves are on the right. In the plots, the point-to-point (σ_0), red ($\sigma_{\rm r}$) and white ($\sigma_{\rm w}$) noise are shown as grey, red and blue points respectively and the green dotted line is the theoretical photon noise (see Section 4.4). The short-dashed, long-dashed and dot-dashed lines are the corresponding best-fit relations, estimated using the median of all measurements in each half-magnitude bin between R = 4.5 and 10.5. These were calculated in two parts, for $R \leq$7 and $R \geq$7, to accommodate the noticeable change slope at $R \sim 7$. This apparent shift in the behaviour of the noise is unexplained, but it may correspond to the magnitude at which systematic effects begin to couple with the photon noise (become multiplicative), meaning that the overall noise will increase much faster with increasing stellar magnitude.

Table 6.1 presents some key results from the noise analysis. These are the reduction in the noise made by the TRP as a percentage of the original noise level, the ratio of red to white noise and the estimated slopes of the best-fit relations, which can be compared to the theoretical photon noise with a logarithmic slope of 0.2.

6.3.3 Reduction in noise by the TRP

It is clear from the results in Table 6.1 and the plots in Figure 6.4 that the TRP significantly reduces the overall and the correlated noise in the light curves. As expected, the TRP is more effective at brighter magnitudes ($R \sim 6$), than at fainter ($R \sim 9$), where the point-to-point scatter is reduced by 49 % and 25 %, respectively. This difference for bright and faint targets is because the level of intrinsic scatter (photon noise) increases with decreasing magnitude, as indicated by the green dashed line in the plots. This means that it becomes increasingly more difficult to identify outliers in the light curves and perform the NLF, which are methods used by the TRP. In addition, there is likely to be a coupling effect, whereby some systematic effects are magnified for fainter stars. For instance, observations of fainter stars are more sensitive to contamination and are more susceptible to errors in the flat-field and background corrections. Furthermore, as discussed in Section 4.3.1, the centroid function is less accurate for fainter targets and so there may be an added component of noise due to mis-placed apertures for these targets.

With regards to the correlated noise, the statistics in Table 6.1 indicate that the TRP performs well, making reductions of 58 % and 67 % for bright stars and 34 % and 43 % for faint stars, on 2 and 5

hour timescales respectively. On a 2-hour timescale, the 34 % reduction in systematic noise is still a substantial improvement over the original light curves, while at best, a reduction of 58 % will have important consequences for transit detection (see Section 6.6).

6.3.4 Correlated versus white noise

The detrended light curves show a marked improvement in the level of correlated noise with respect to the expected white noise on the same timescales. This is illustrated by the gaps between the associated best-fit lines in the plots, which are noticeably narrower post-TRP. Also the results in Table 6.1 show that on a 2 hour timescale, the correlated noise is now comparable to the white noise at fainter magnitudes, while it remains a factor of 1.21 greater than $\sigma_{\rm w}$ at brighter magnitudes.

The larger ratio of $\sigma_{\rm r}/\sigma_{\rm w}$ for the 5-hour duration indicates that the systematic effects are more prominent on this timescale. However, this could also just be a result of having more points over which to estimate the correlations, rather than it being a true representation of the noise.

The nature of the systematic components remaining in the data is unknown at this stage, but on these timescales effects such as satellite jitter, flat-field and background errors may be the cause, in addition to short period stellar variability.

6.3.5 Noise Trends

In Figure 6.4 the green dotted line in each plot represents the relationship between photon noise and R, which has a logarithmic slope of 0.2. As discussed in Section 4.4, this line is calculated using the HI magnitude scale, but as $m_{\rm HI} \approx R$ for most cases, it serves as a suitable point of reference in the figures.

At bright magnitudes, the noise show a much flatter slope (gradient close to zero) in the pre-TRP light curves, on both timescales. A zero-gradient is associated with pure red noise, which should not increase with stellar magnitude since the systematics are related to the system and not to the source. Hence the shift in the gradient, from ≈ 0.5 for the original light curves to ≈ 0.1 for the detrended data, suggests a subtle whitening of the noise due to the TRP. The same difference in gradient is not as prominent at fainter magnitudes, for which the statistics show only a small steepening in the slope from ≈ 0.27 to ≈ 0.32, for 2 and 5 hours respectively. This is due to reasons described earlier, which are essentially that the white noise limits the effectiveness of the TRP for these light curves.

6.3.6 Total noise

The total noise as a function of R, on 2 and 5 hours, is shown in Figure 6.5. This measurement includes both red and white components and is given by,

$$\sigma_{\rm d} = \mathcal{V}^{1/2}(n) = (\frac{\sigma_{\rm w}^2}{n} + \sigma_{\rm r}^2)^{1/2}. \tag{6.10}$$

This is Equation 8 in Pont et al. (2006), which gives the uncertainty on the depth of a single transit, where n is the number of in-transit points.

Although the results in Table 6.1 show that the correlated noise is less significant on 2 hours than on 5 hours, the reverse is true of the total noise, which includes contributions from red and white components. This suggests that the dominant component is white, meaning that even on a shorter timescale, over which the correlations are small, the total noise is greater since the larger contribution from the white noise overrides this effect.

Figure 6.5 (a) also shows that while a high proportion of light curves have noise below the 1 % sigma level, those for stars with $R > 10$ are unlikely to show the signal associated with a Jupiter-Sun analog, which has a transit depth of 1 %. Whereas compared with Figure 6.5 (b), the noise will be less of a limitation to the detection of binaries, which have equivalent depths but longer durations. For this reason, the detection criteria for the transit search must be considered carefully, so that the results are not overwhelmed by binaries. These criteria are discussed in the next chapter, in relation to the transit search.

With regards to actual detections, the period, transit duration, depth and magnitude are all factors which will determine the detectability of a transit signal, since they will all affect the total SNR. This dependence of the SNR on the transit parameters is discussed in the following section.

6.4 Estimated detection thresholds

The equation for estimating the uncertainty on a transit depth, $\sigma_{\rm d}$, when there are $N_{\rm tr}$ transits observed, was given be Equation 6.10, but is repeated below for ease of reference:

$$\sigma_d^2 = \frac{1}{n^2} \sum_{k=1}^{N_{\rm tr}} \mathcal{V}(n_k) n_k^2.$$

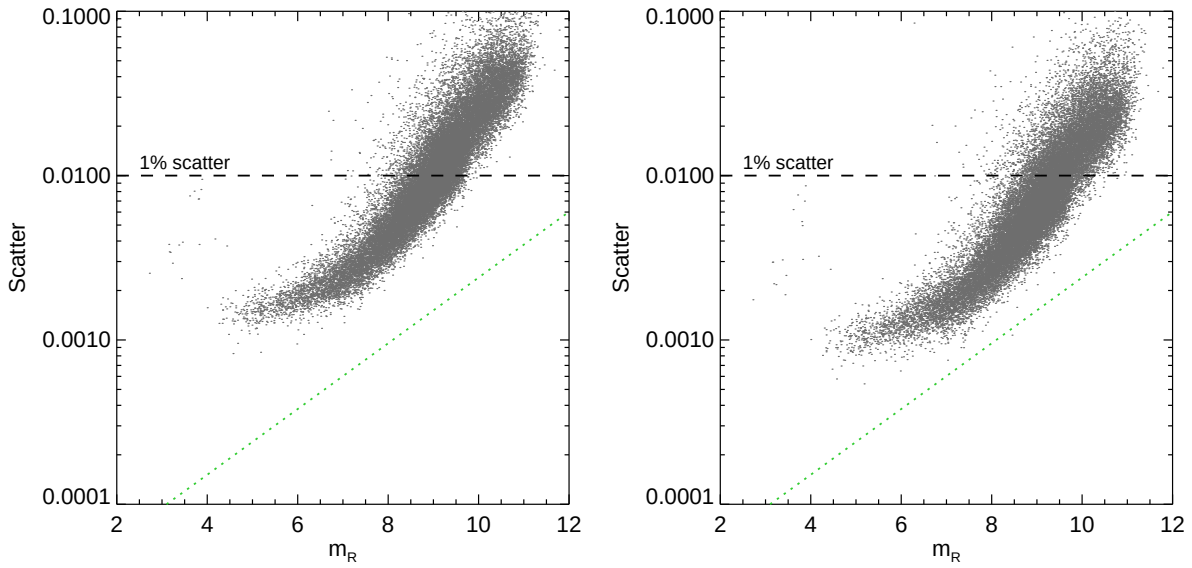

(a) Total noise on 2 hours.

(b) Total noise on 5 hours.

Figure 6.5: The total noise plotted against R, on 2 (left) and 5 (right) hours. This is equivalent to the uncertainty on a single transit and is estimated from the $\mathcal{V}(n)$ function, using Equation 6.10.

In this equation n_k is the number of data points in each transit k. Using this formula, the SNR for a given detection can be expressed as,

$$S_r^2 = d^2 \frac{n^2}{\sum_{k=1}^{N_{tr}} n_k^2 \mathcal{V}(n_k)}, \tag{6.11}$$

where $S_{\rm r}$ is the significance of a transit, with depth d. This is Equation 7 in Pont et al. (2006).

When n_k and $N_{\rm tr}$ are established from the parameters of a detected transit, then $\mathcal{V}(n)$ can be accurately measured from the light curve. However, prior to the transit search, $S_{\rm r}$ can instead be used as a guide to the detection limits, for a given range of transit depths and orbital periods. To use it this way requires the basic assumption that all transits have an equal number of data points, i.e. $n_k \approx n/N_{\rm tr}$. Then $S_{\rm r}$ can be predicted from the following modified version of Equation 6.11, where $\sigma_{\rm r}$ and $\sigma_{\rm w}$ are taken from the noise estimates, with n_k = 3 (for a 2-hour duration):

$$S_{\rm r}^2 = \frac{d^2}{(\sigma_{\rm w}^2/n) + (\sigma_{\rm r}^2/N_{\rm tr})}. \tag{6.12}$$

Hence this equation has been used to calculate $S_{\rm r}$ for a range of periods and depths which are expected to be detectable in the HI-1A light curves, of which the findings are presented in Figure 6.6.

6.5 Using $S_{\rm r}$ as a guide to transit-detection limits

Figures 6.6 (a) and (b) show $S_{\rm r}$ as a function of R, for a range of orbital periods and transit depths. Part (a) shows the full range of $S_{\rm r}$ values, whereas part (b) focuses around a critical region, where the detection threshold is expected to lie. Pont et al. (2006) demonstrate that, while the threshold depends on a number of parameters, including the choice of transit detection algorithm (see Chapter 7), it will typically lie between $S_{\rm r}$ = 7 and 9.

The results for transit depths of 0.5, 1, 2 and 3 %, are plotted (see the key in the top right corner). At each depth, $S_{\rm r}$ has been calculated for seven orbital periods, ranging from 1 to 7 days (in integer steps). The points connected by the solid lines have the same period and the direction of increasing period is indicated. For each depth (colour coded), the upper-most line corresponds to a 1-day period and each subsequent line shows the results for a period 1 day longer than the line above it.

6.5.1 $S_{\rm r}$ dependence the transit depth and period

The results in Figure 6.6 show that for a constant orbital period, the dependence of $S_{\rm r}$ on magnitude grows with increasing transit depth, as implied by the increase in gradient between $R \sim 5$ and $R \sim 10.5$. For stars fainter than $R \sim 10.5$, the depth appears to have a minimal effect on $S_{\rm r}$, which remains below a value of four. This suggests that the noise will dominate any transit-like signals from stars with $R \geq 10.5$. The flat slope at the bright end ($R < 5$) is a consequence of total noise limit (illustrated in Figure 6.5). This means that the SNR can not improve for these stars, as the noise in their light curves is subject to a lower limit which is non-zero.

Figure 6.6 also shows that as the depth increases, there is a greater overlap between $S_{\rm r}$ values for different periods. For example, a 2 % depth with a 1-day orbit would be easier to detect than a 3 % depth in a 3-day orbit. This means that deep (> 2 %), short-period signals will be the easiest to detect. However, for shallow depths ($0.5 - 1$ %), there is much less dependence on the period, meaning that having more observations will only increase the detection statistic by a marginal amount.

Based on a detection threshold at $S_{\rm r}$ = 8, these results show that in the HI-1A transit survey only those stars with $R < 9.5$ will present any kind of detectable signal. However, a threshold of 8 is not definitive (depends on the transit detection algorithm) and in fact signals are likely to be detectable down to $S_{\rm r}$ = 4, so it is possible that a few transits may be detectable at magnitudes fainter 9.5.

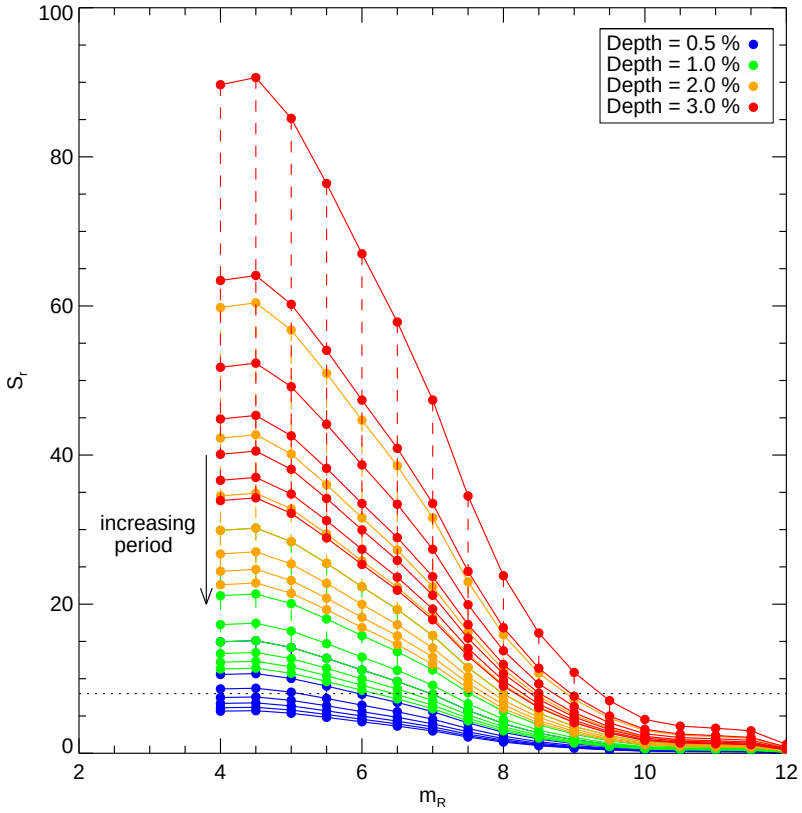

(a) S_r versus R, on 2 hours, for different transit depths and orbital periods.

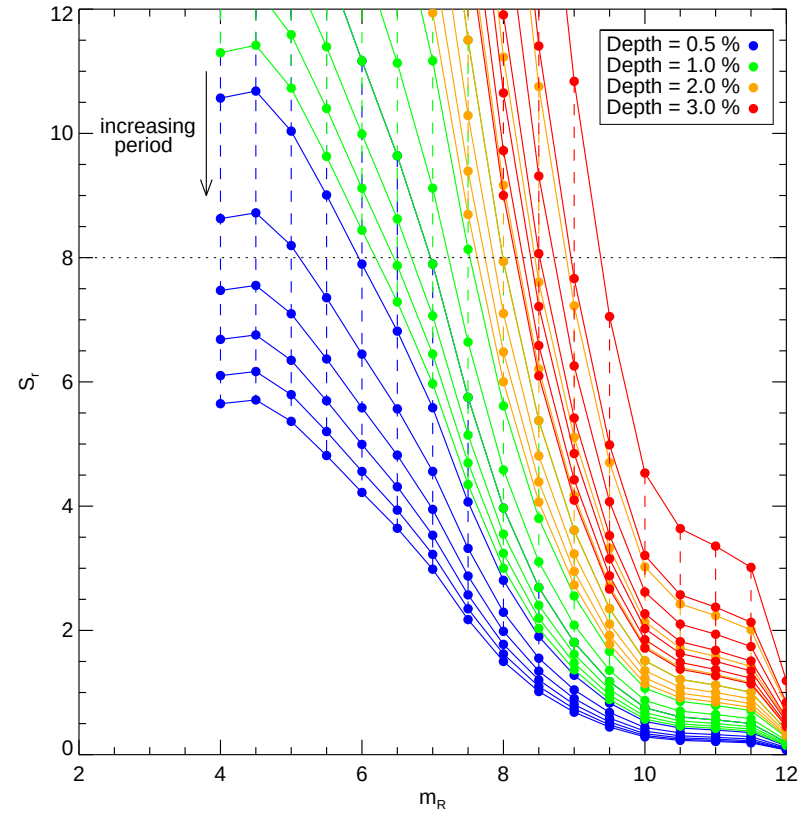

(b) Same part (a), but focussed on $S_r = 8$, the expected detection threshold.

Figure 6.6: S_r versus R, for different transit depths and orbital periods. Based on total noise on a 2

6.5.2 $S_{\rm r}$ dependence the transit duration

According to Figure 1.6, short-period planets ($\leq$ 7 days) are associated transit durations of 3 hours, as well as 2 hours. Therefore the $S_{\rm r}$ values were calculated for a 3-hour duration, to determine the effect of having an extra point in each transit. In these calculations the noise values for the 2-hour transit duration were adopted, as these are more representative of the noise than the values for the 5-hour duration.
Figure 6.7 shows the results. By comparing this with the 2-hour results in Figure 6.6, it is seen that a having a slightly longer transit duration will have negligible impact on the transit search results. This also makes no difference to the detection threshold in terms of magnitude. On the other hand, eclipsing binaries will have much stronger detection statistics, for equivalent depths and periods, since on timescales of at least 5 hours the total noise is lower (Figure 6.5) and hence the values of $S_{\rm r}$ will be greater.

6.5.3 Impact of the TRP on detection possibilities

Figure 6.8 shows the behaviour of $S_{\rm r}$ with magnitude, for a 2-hour transit in the original light curves. This suggests that without the TRP, no transit signals with depths smaller than 2 % would have been detectable in the transit search. Furthermore, only those targets with $R < 8$ would have been regarded as good planetary candidates, which corresponds to just 15 % of the total sample of $\sim$ 57,000 targets.
This comparison highlights that the trend reduction process is crucial to the success of the transit survey.

6.6 Chapter summary

Using the methods and assumptions outlined in Pont et al. (2006), the noise in the raw and detrended light curves was measured on 2 and 5-hour timescales. A 2-hour timescale corresponds to the typical transit duration expected from planets in orbits shorter than 7 days, while a 5-hour duration is more appropriate for eclipsing binaries with similar orbital periods. As discussed in Pont et al. (2006), it is the correlated noise from the systematics, on timescales of a few hours, that has the biggest impact on transit detection. The limits of the HI-1A transit survey, with respect to a range of orbital periods and transit depths was predicted from the red and white noise a 2-hour timescale, using Equation 6.12. This equation gives the SNR for a detected signal, on timescales equal to the duration of the signal.

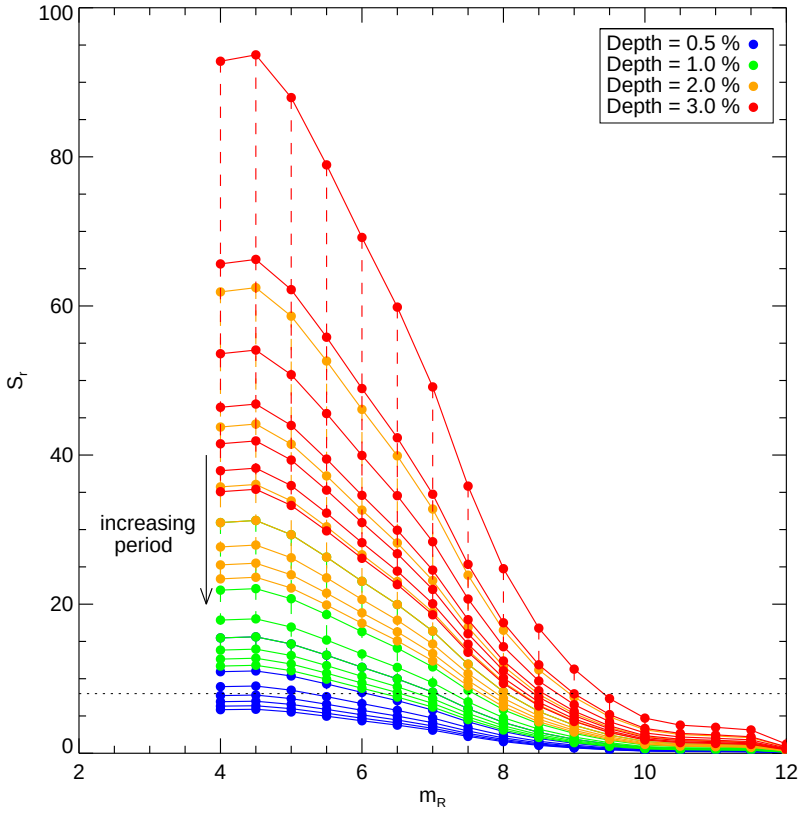

(a) S_r versus R, on 3 hours, for different transit depths and orbital periods.

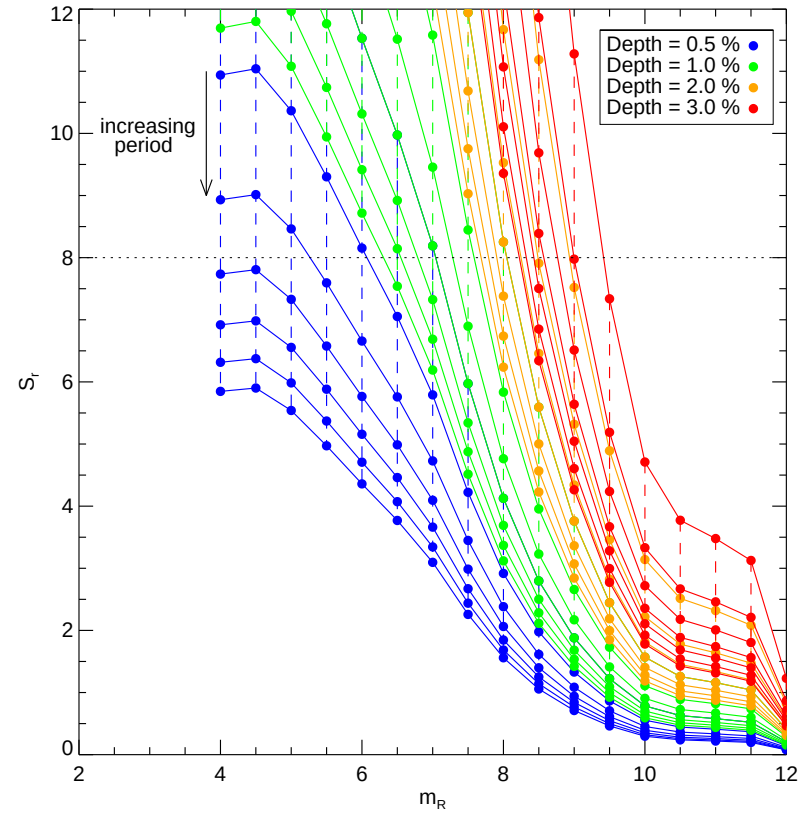

(b) Same part (a), but focussed on $S_r = 8$, the expected detection threshold.

Figure 6.7: S_r versus R, for different transit depths and orbital periods. Based on a 3 hour timescale.

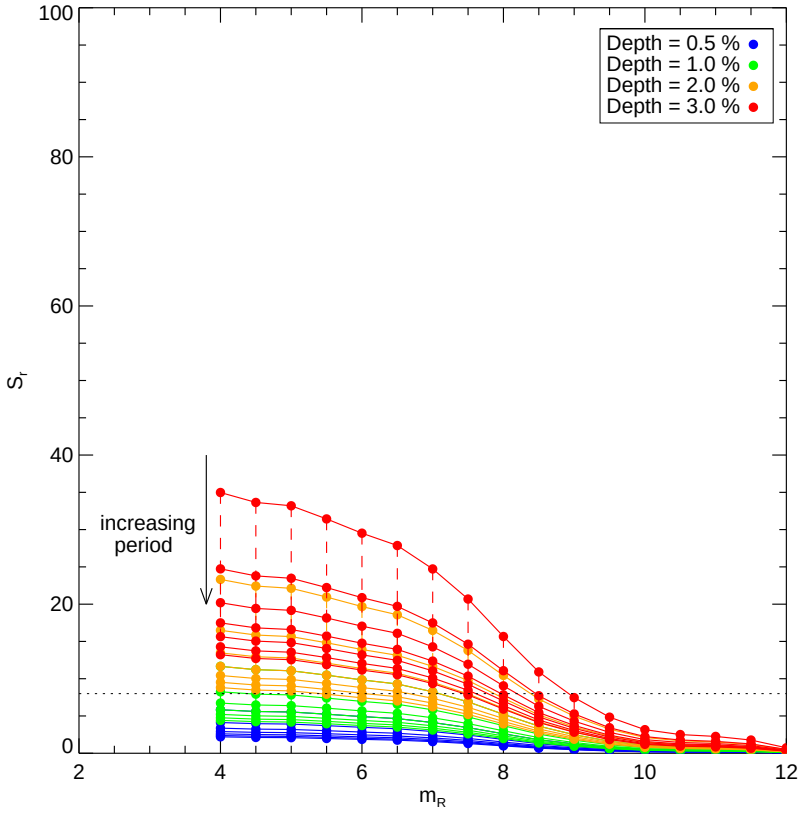

(a) S_r versus R, on 2 hours, for different transit depths and orbital periods.

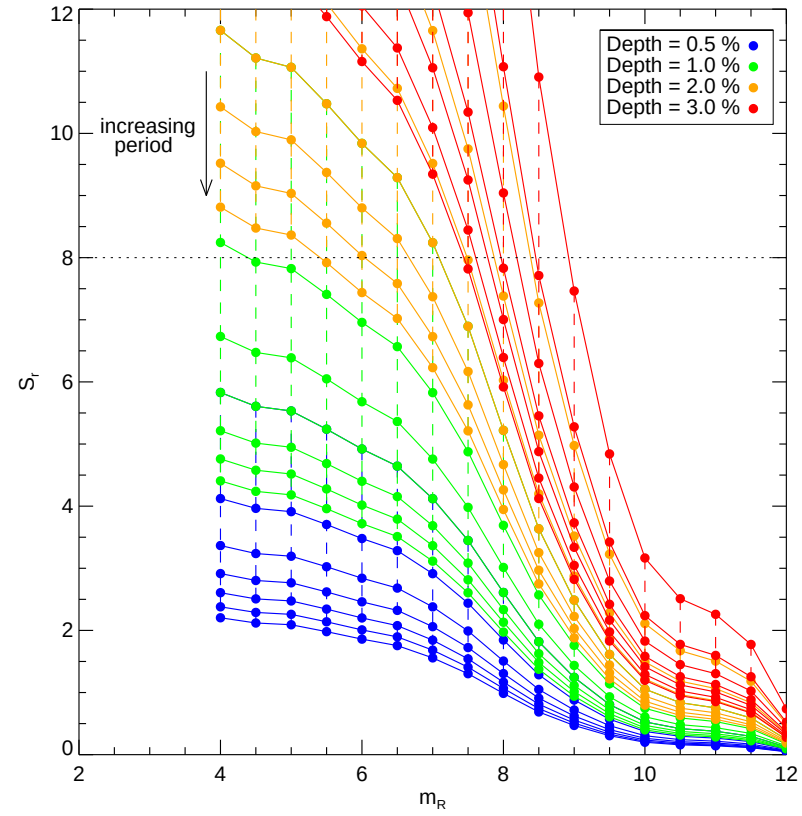

(b) Same part (a), but focussed on $S_r = 8$, the expected detection threshold.

Figure 6.8: S_r versus R, for the original light curves, for different transit depths and orbital periods.

6.6.1 Noise summary

The key results from the noise analysis may be summarised as follows:

- The TRP is found to reduce the overall noise in the light curves (point-to-point) by 49 % and 25 %, at bright (R = 6) and faint (R = 9) magnitudes respectively.
- On a 2-hour timescale, the TRP is found to reduce the correlated noise in the light curves by 58 % and 34 %, at bright and faint magnitudes respectively.
- The difference between the improvements for bright and faint magnitudes, is because the TRP is limited by photon noise, which increases with decreasing magnitude. As the systematics are easier to identify in the light curves of brighter stars, the TRP is more effective at these magnitudes.
- The increase in the gradient of the noise at R = 7 may be explained by a coupling effect between the systematics and white noise, as explained in Section 6.3. For fainter stars systematic effects such as vignetting and undersampled PSFs may cause a multiplicative effect in the overall noise, hence the increased slope.
- The level of red noise in the post-TRP light curves, on a 2-hour timescale, is found to be 20 % and 5 %, for bright and faint magnitudes respectively, indicating that the dominant component of noise in the light curves is white.

With regards to the last point, this is especially relevant for the transit search performed subsequently, as the method used for detection, the BLS algorithm (Kovács et al., 2002), assumes white noise. If the noise were dominated by systematics, e.g. if the raw light curves were used, there would be a much greater higher proportion of false-positive results as a consequence. Instead, with the improved data, the number of FPs should be kept to a minimum, allowing for a more efficient post-analysis and hence a more reliable list of candidates to follow-up.
The BLS algorithm and it's implementation are described in Chapter 7, followed by the results from the transit search.

6.6.2 Outcome for planet detection

The behavior of S_{r} with respect to magnitude is shown in Figure 6.6. This is for the range of transit periods and depths which are expected to be detectable in the HI-1A data. These results suggest the

following implications for planet detection:

- For a threshold of $S_{\rm r}$ = 8, the limiting magnitude for a transit survey is $R \sim 9.5$. Although as suggested in Section 6.5.1, it is likely that signals with $S_{\rm r} \geq 4$ may be detectable, hence the limiting magnitude is probably closer to R = 10.5. Therefore the transit search should involve approximately 46,000 individual targets.

- For $S_{\rm r} \geq 8$, transit depths of 1 % and 0.5 % are detectable around stars with $R \leq 7.5$ and $R \leq 6$, respectively. This would mean that only $\sim$ 5400 and $\sim$ 1000 targets might display such signals. But if it is the case that positive detections can be made with $S_{\rm r} \geq 4$, then the number of targets will increase to $\sim$ 14000 and $\sim$ 5400 respectively, making the prospect of finding a Hot-Jupiter far more likely.

- Having a slightly longer transit duration of $\sim$ 3 hours, which would add at least one extra data point per transit, does not significantly increase the likelihood of detection. However, having a shorter period, increasing the number of transits ($N_{\rm tr}$, has a much greater effect on the $S_{\rm r}$ values, especially for deeper signals. For shallower transits, i.e. $\leq$ 1 %, the period will have a much smaller effect on the detection capability.

- Considering these results, it is possible to predict that the outcome of the BLS transit search (presented in the next chapter) will have a high proportion of detections from deeper transits, in short-period orbits ($\leq$ 4 days). However, it is entirely possible to detect signals with depths as shallow as 0.5 % around the brightest stars, if they exist.

Chapter 7

Searching for transits

7.1 Introduction

The focus of the work presented so far has been on understanding the impact on the HI-1A light curves from various systematic and external influences. Many of these influences were introduced in Chapter 4, with examples to illustrate their effect on the raw data. The TRP, which removes the most problematic trends from the data, was described in Chapter 5 and examples were given of its impact on three typical light curves (shown in Figures 5.8, 5.9 and 5.10). Considered with the results from the noise analysis in Chapter 6, these examples are reason to regard the TRP as an effective mechanism for reducing the systematic noise in the data, whilst having negligible impact on real transit-like signals.

This chapter introduces the search for transit signals in the detrended, HI-1A light curves. The search was conducted using the original box least-squares (BLS) algorithm of Kovács et al. (2002), one of many transit detection algorithms (TDAs), which are used to find planetary signatures in photometric data.

The next section gives a brief discussion of a few alternative detection methods used by other transit surveys and reasons why BLS was chosen for the HI-1A survey. This is followed by a description of the BLS method (Section 7.3) and then details of its implementation (Section 7.4). In section 7.5 the method for establishing a suitable detection threshold for the BLS test statistic is set out. This involved creating a set of noise-only models, based on the characteristics of the HI-1A data, then determining the proportion of BLS detections that may be due to noise in the data (FPs). The last section has the results from BLS, filtered by a set of selection criteria. These results set the scene for Chapter 8, which gives a more detailed discussion of false-positives (FPs) and introduces simple tests to distinguish these from genuine transit detections.

7.2 Methods of Transit Detection

As explained in Section 1.2, most transit surveys are wide-field to enable them to observe enough stars for a transit to be observed, due to geometric alignment probabilities. However, as most observations are also degraded by noise and data gaps, the detection algorithms can often fail to detect transit signals, meaning that the minimum number of targets needs to be of the order of 10^4 to give a positive outcome from a transit search.

Being able to search large numbers of light curves in a fast automated manner is one motivation for the development of detection algorithms. Another is their superior ability to identify transits in light curves, where the noise would otherwise mask the presence of a signal. But overall, they provide objective detection criteria for identifying planetary candidates within a vast sample of observations.

Most TDAs are formulated around specific characteristics of transits, namely a repeatable signal, a non-sinusoidal box-shape (see Section 1.2.1) and having a long orbital period with respect to the transit duration ($P >> T_{\rm dur}$). These general rules are used to construct models of the expected signal, with a range of parameters such as the orbital period, duration and phase. These are called free parameters, meaning that they are varied over many iterations of the model to find the best fit for a particular set. The fit is usually evaluated by a test statistic that conveys the detection of a signal when it exceeds some threshold value. Therefore this statistic can be a reliable indicator that the detection is due to a genuine signal (as opposed to noise), so long as an appropriate threshold can been established. This will depend on the specifics of the survey and the search parameters.

The formulation of a test statistic is different, depending on the underlying principles of the method. For example, the matched-filter method, which has undergone many adaptations (Kay, 1998; Jenkins, 2002; Jenkins et al., 2010a), is applied in the time domain, by convolving the light curve with a set of models, computed for different transit parameters. The best fit model will produce the largest test statistic, T, where

$$T = \sum_{i=1}^{N} \frac{F_i M_i}{\sigma_i^2}. \tag{7.1}$$

In the above equation, which is equivalent to Equation 1 in Tingley (2003a), F_i are the flux of the data points, where i=1,...,N, M_i is the model and σ_i are the uncertainties on each measurement, which are assumed to be drawn from a Gaussian distribution (white noise). The matched-filter is the method of choice for the *Kepler* survey (Jenkins et al., 2010b) and follows a sophisticated "pre-whitening" process to remove systematic trends from the data prior to the transit search.

In the handful of studies which have compared the performance of TDAs (Tingley, 2003a,b; Moutou et al., 2005; Enoch et al., 2012), the matched-filter and BLS (and their variations) have been found to excel over other methods such as Bayesian (Defaÿ et al., 2001), cross-correlation (Udalski et al., 2002a) and analysis of variance (AoV) (Schwarzenberg-Czerny and Beaulieu, 2006) methods. While each comparison study differs in their methodologies, the consensus is that algorithms based on the simple properties of the transit are more efficient detection tools than more sophisticated TDAs such as the Bayesian method, which is based on Bayes' Theorem (Bayes, 1764). This later approach relies heavily on prior information (the "*prior*"), which includes details of the noise and assumptions based on the results from statistical studies (e.g. Santos et al. (2001); Johnson et al. (2010)), which assess the probability of detection for different orbital parameters and stellar types. One advantage of the Bayesian method is that the test statistic evolves as new information is incorporated into it, for example, by providing the time dependence of the correlations in the noise. In this respect, the Bayesian approach is superior over simpler methods, which have no external input in their test statistics. However, errors in the assumptions may cause this method to fail in circumstances where the *prior* conflicts with the observation. Therefore, the Bayesian approach is regarded as being better suited to the characterisation, rather than the detection of transit signals, when the available information can improve the accuracy of the detection statistic and not hinder it.

While the comparison studies show that the matched-filter detector and BLS outperform other methods (with regards to signal detection), the choice of TDA should always be suited to the requirements and sensitivities of each survey. Below is a list of reasons why BLS is suited to the HI-1A survey:

1. BLS is proven to be highly efficient at detecting short-period transits in the presence of high noise (Enoch et al., 2012). Since over half of the targets in the HI-1A sample are faint ($R > 9$) and all light curves are dominated by white noise, this attribute is well suited to the HI-1A survey, which is most sensitive to periods ≤ 7 days.

2. The total processing time is minimised by ignoring subtle effects such as ingress, egress and limb-darkening (Section 1.2). This will have little consequence for the HI-1A survey since, for a $2 - 3$ hour transit duration, the relatively short time spent in ingress and egress will not be measurable, due to the 40-minute cadence of the observations.

3. BLS is easy to implement and adapt to the requirements of the survey (see Section 7.4).

4. BLS has provided positive planet detections in nearly all of the major surveys, including CoRoT (Carpano et al., 2009), SuperWASP (Hebb et al., 2009) and OGLE (Udalski et al., 2002b). This demonstrates that it is effective and also adaptable to a variety of light curves and observational constraints.

Ideally, given ample time and resources, the search would be conducted with more than one TDA as, in the comparison studies, no method outperformed the others for all types of transit signal.
In one comparison between BLS and AoV, on real WASP data (Enoch et al., 2012), it was found that while BLS made the most detections overall, the AoV was able to identify transit signals which were missed by BLS and vice versa. In this study, BLS proved its superior detection capability in the presence of white noise, but showed its weakness in the presence of red noise, i.e. for brighter targets. Since more than 97 % of the HI-1A targets are fainter than R = 6 and these have negligible red noise (see Section 6.3), the weakness of BLS to red noise should be of little consequence to the HI-1A survey.

7.3 BLS

The BLS algorithm (Kovács et al., 2002) searches for the box-shaped signal associated with a transit, by performing direct least-squares fits of step-functions to the phase-folded light curve. A summary of the algorithm and its use, as described in Kovács et al. (2002), is set out below,

1. Limits are assigned to the search parameters, which are chosen to suit the sensitivity of the survey. These limits will affect the value of the test statistic for a given detection, the consequences of which are discussed in the next section. The search parameters for BLS are as follows:

   - the range of test periods, P_0.
   - the range of fractional transit lengths, q.
   - the number of bins, nb, for binning the phase-folded light curve. This is an option included in the algorithm to reduce the computing time (see below).
   - the number of independent frequencies, nf, or periods, np.

2. Each data point, f_i, in a light curve with i=1,...,N observations, is assigned a weight defined by, $w_i = \sigma_i^{-2} [\sum_{j=1}^{N} \sigma_j^{-2}]^{-1}$, where σ_i are the uncertainties on the data points (and the noise is assumed to be Gaussian distributed).

3. For each P_0 in the range of search periods, the light curve is phase-folded. The corresponding phase of a point at time t_i, is:

$$p_{t_i} = \frac{t_i \; mod \; P_0}{P_0}. \tag{7.2}$$

The data points in the phase-folded light curve are now denoted by $\tilde{f}_i$ and their weights by $\tilde{w}_i$.

4. The phase-folded light curve is partitioned into nb bins and the points in each bin are averaged. The value of nb should be sufficiently large to ensure there are an adequate number of data points in each bin. This prevents random outliers from affecting the result by creating a spurious signal (see Section 7.4).

5. A step function with two discrete levels, L and H, is fitted to the phase-folded, binned light curve, where L and H represent the in and out of transit levels respectively. These are adjusted for different values of q (fractional transit duration) to find the best-fit for each P_0.

The best-fit value is calculated by the method of least-squares fits, which computes the sum of the absolute deviations of the residuals from the fit. This value and the relative amplitude of the signal constitute the test statistic, given as:

$$SR = \left\{ \frac{(\sum_{i=i_1}^{i_2} \tilde{w}_i \tilde{f}_i)^2}{\sum_{i=i_1}^{i_2} \tilde{w}_i [1 - \sum_{i=i_1}^{i_2} \tilde{w}_i]} \right\}^{\frac{1}{2}}, \tag{7.3}$$

where i_1 and i_2 are the indices of the first and last points in L. This is also referred to as the signal residue (SR) and corresponds to the power at each P_0 in the BLS periodogram (see Figure 7.1).

6. The maximum signal residue, $\mathrm{SR_{max}}$, over all trials of P_0 (i.e. the highest peak in the periodogram) is used to calculate the signal detection efficiency (SDE):

$$\mathrm{SDE} = \frac{\mathrm{SR_{max}} - \langle \mathrm{SR} \rangle}{\sigma(\mathrm{SR})}, \tag{7.4}$$

which is the significance of the detected signal, where $\langle \mathrm{SR} \rangle$ and $\sigma(\mathrm{SR})$ are the average and standard deviation of the frequency spectrum.

The SDE indicates the quality of the fit and therefore given an appropriate threshold it may be used as a tool for distinguishing between detections of genuine signals and FPs. The threshold will depend on the noise characteristics of the data, the number of FPs which are reasonable in the results and also

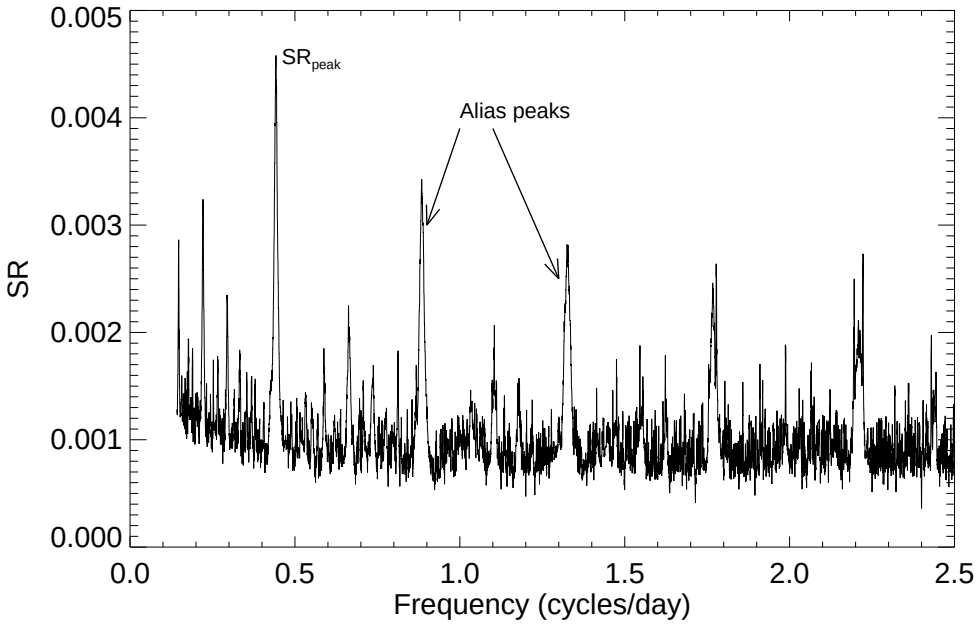

Figure 7.1: An example of the BLS power spectrum, for a light curve with a signal on a period of 2.26 days, corresponding to a frequency of 0.44 cycles/day. As the search is carried out in phase-space, there is residual power at multiples of the true frequency, i.e. aliasing.

on the choice of the search parameters (see Section 7.4), hence its value should be determined for each combination of these factors (see Section 7.5).

7.4 Implementation

As BLS performs the fitting in phase-space, the power spectrum is computed in the frequency domain. This maintains a constant phase shift between consecutive test periods (Burke et al., 2006), but it also means that the detection is sensitive to data gaps as these produce spurious signals (noise), due to a uneven distribution of points in the bins. Also aliasing, which is residual power at multiples of the true period may reduce the detectability of a signal (See Figure 7.1). A further consequence of searching frequency space is that, for a given range of P_0 and value of np, there will be higher period resolution for short-period (high-frequency) signals than for longer-period (low-frequency) signals. This means that the error in the period of a detected transit will increase with increasing period and is why BLS is better suited to detecting short-period signals.

Due to the significant time gap of $\sim$ 1 year between each observation of a target, linking the separate data sets and searching for periods longer than 7 days is unlikely to result in more detections due to the

increase in noise from the gaps and the decrease in efficiency of BLS at longer periods. Instead, the results from performing BLS on both the single and combined data sets, using the same parameters, can be used to determine the impact on the detection efficiency from extensive data gaps in the time series. The parameters for the transit search are as follows:

- $P_0 = 0.9 - 7$ days.

  - The lower limit comes from requiring at least 2 points in a transit, which amounts to a duration of 80 minutes. For this transit duration the orbital period is not expected to exceed 1 day (see Figure 1.6). The corresponding maximum frequency is still well below the Nyquist frequency (maximum detectable frequency), which equates to a period of 0.05 days.

  - The upper limit, although stringent, will ensure at least 3 full transits are present in a full, 20-day observation.

- $q = 0.01 - 0.06$.

  - The range of fractional lengths, q, will affect the speed of BLS, as this is a free parameter in the computation of the power spectrum. The total running time can be reduced by restricting this parameter to a realistic range for transits. The minimum and maximum values chosen here correspond to the fractional transit durations of currently detected transiting planets (see Figure 7.2).

- $nb = 300$.

  - Having a large number of bins, nb, will also reduce the processing time. However, to avoid a loss of resolution and detection efficiency, the number of bins should be chosen so that the shortest fractional transit duration is not lost within a single bin. Having 300 bins ensures that a 2 % fractional transit duration will be spread across 3 bins, as is suggested by Kovács et al. (2002).

- $nf = 3000$.

  - The number of independent frequencies, nf, dictates the resolution of the detected period. As mentioned previously, the resolution will be higher for short periods and decrease with increasing period. With $nf = 3000$, even at the maximum period of 7 days, the resolution is still $\sim$ half the image cadence at 23 minutes.

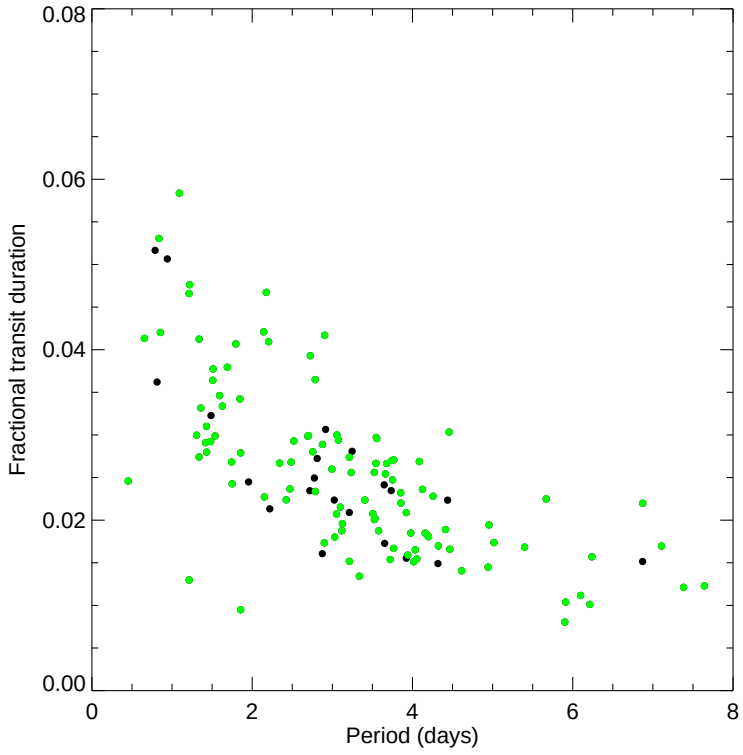

Figure 7.2: Fractional transit duration (q) versus period for transiting planets detected to date, where the period is the measured orbital period and the q is estimated from Equation 1.3, for circular orbits, with i = 90 °. The black points have measured eccentricities close to zero, while for the green points this quantity is unknown. Data accurate as of 1st April 2012, from the Extrasolar Planet Database (http://exoplanet.eu, Schneider, 1995).

7.5 Establishing the SDE threshold

As described previously, the SDE, which is calculated with Equation 7.4, indicates the quality of the BLS fit to the detected signal. This means that it can be used to distinguish between signals of genuine astrophysical origin and those which are due to noise artifacts in the data.

The precise value of the SDE for a given detection will depend the parameters of the search (described in Section 7.4) and the length of each data series. For instance, Kovács et al. (2002) explain that, when all other parameters are kept constant, increasing the number of frequencies nf, or the range of trial periods P_0, will result in a greater SDE for a given detection. This is because the average and standard deviation of the signal residue ($\langle \mathrm{SR} \rangle$) and $\sigma(\mathrm{SR})$ in Equation 7.4), will decrease for larger nf and a wider search space. Increasing the duration of the observation will also increase the value of the SDE, as this will provide more points in each bin, which will result in lower noise. However, this will only be the case if the time-series is continuous, i.e. if there are no significant data gaps. This is because data gaps result in an uneven distribution of points in the bins, which increases the scatter in the binned, phase-folded light curve and results in a lower SR_{peak}, hence SDE will instead be reduced.

As the SDE depends on the search parameters and on the nature of the observations, it was necessary to establish an appropriate threshold that is specific to the HI-1A light curves and for each realisation of nf, nb and range of P_0. Although there will not be an exact cutoff to separate genuine and false detections, the threshold should provide the best possible compromise between detecting genuine signals, while avoiding the majority of FPs due to noise, so that they do not overwhelm the results.

One way to establish a threshold is to perform BLS on a set of noise-only model light curves which represent the HI-1A time-series and have the appropriate levels of noise. Then by considering the range of SDE values from the noise-only models, an appropriate detection threshold can be determined for the transit search using the real data.

7.5.1 Model light curves

A set of 1000 model light curves were constructed using the time series and noise characteristics of the HI-1A light curves. These were based on the proportions of stars in each magnitude range, to ensure that the models contain an accurate distribution of noise values. Table 7.1 shows these proportions, with respect to the total sample of $\sim$ 46,000 targets with $R \leq 10.5$. As shown in Section 6.5, only the targets brighter than this magnitude are considered to have the potential to present a detectable transit signal.

For each time-series an array of flux values were drawn from a Gaussian distribution and scaled to the magnitude of the scatter in the corresponding HI-1A light curve. Correlated noise was not included as this is regarded as negligible for the majority of stars and only ~ 20 % for the brightest ($R \leq 6$), which constitute < 3 % of the whole sample.

As was mentioned in Section 6.2.2, approximately 30 % of the detrended light curves have significant periodic variability following the TRP. The non-linear filter (NLF, Section 5.3) fits and removes a one-day component from the light curves, meaning that the majority of this remaining variability is on timescales much shorter than one day. To account for the consequences of this in the transit search, small-amplitude sinusoidal signals, with periods ranging from 0.1 to 0.5 days, were superimposed onto the noise in 30 % of the models.

From the noise-only models, a duplicate set were constructed and injected with simulated transits. The transits had periods ranging from 1 to 7 days, with transit durations of 2 hours for an orbital period of ≤ 4 days or 3 hours for and orbital period of > 4 days (see Figure 1.6) and transit depths from 0.5 % $-$ 2 %. An example of a noise-plus-transit model is shown in Figure 7.3. Whereas the noise-only models can be used set the SDE threshold in the real transit search, the noise-plus-transit models could be used to anticipate the performance of BLS, with regards to detecting genuine transit-like signals in the HI-1A light curves.

Two additional sets of light curves were constructed, by linking the original noise-only and noise-plus-transit models, to simulate combining the individual data-sets for each target. These linked models were created from $2 - 5$ single models, with a gap of 345 days between the end of one data-set and the beginning of another. Performing the BLS analysis on the linked models may determine the outcome of a transit search using the linked light curves for each target, e.g. whether this increases the detectability of a signal or not.

The BLS results from the single and linked model light curves are presented in the following section.

7.5.2 BLS results from the model light curves

The resultant SDEs from a BLS search using the single models with noise-only (a) and noise-plus-transits (b) are shown in Figure 7.4. The vertical dashed-line in histogram (a), at SDE = 7.4, is the threshold below which 95 % of the noise-only detections lie. Setting the cutoff at this value means that the results from the transit survey should only include about 5 % of possible FPs due to noise.

R-magnitude bin	Percentage of total sample (%)
$4-5$	0.5
$5-6$	1.5
$6-7$	4.5
$7-8$	12
$8-9$	29
$9-10$	37.5
$10-10.5$	15

Table 7.1: The percentages of HI-1A targets in each R-magnitude bin, out of $\sim$ 46,000 targets. These proportions were used to construct a sample of 1000 model light curves, to determine an appropriate SDE threshold for the transit search using the real data.

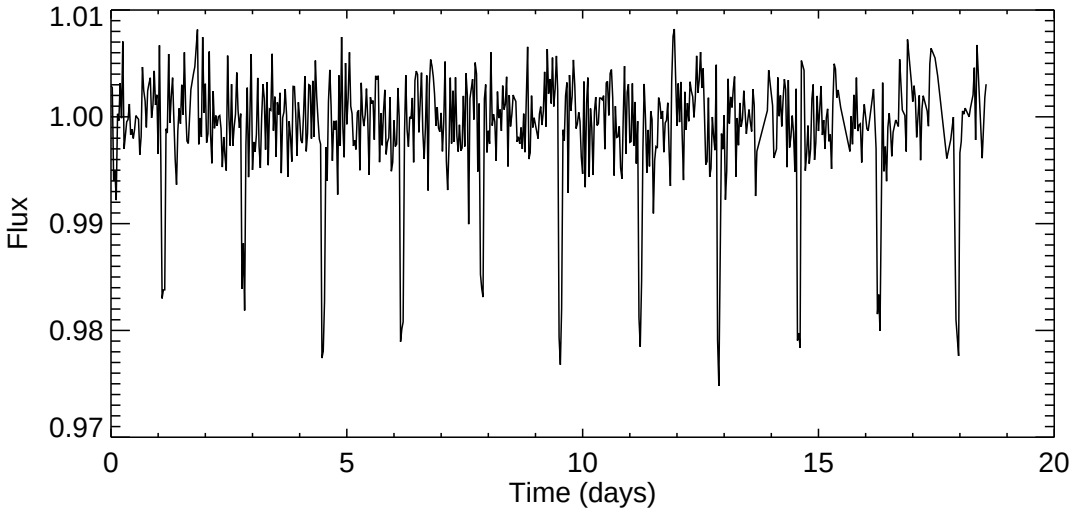

Figure 7.3: An example of a noise-plus-transit model light curve, with Gaussian-only noise. These transits have a period of 1.7 days, a duration of 2 hours and a depth of 1.9 %. The scatter represents a $7-8$th magnitude star and is $\sim$ 0.003, resulting in a SNR of $\sim$ 6.

The results for the single and linked models are given in Table 7.2. With regards to the single models, the outcome from the BLS search is that detectable signals are found in $\sim$ 20 % of the noise-only light curves. This means that in a transit search with $\sim$ 46,000 targets, of which only a tiny fraction will harbor transiting planets, BLS could produce $\sim$ 9000 FPs due to noise and variability alone. These results do not take into account for eclipsing binaries, which are also expected in the results.

A detection threshold at SDE = 7.4 could effectively eliminate 95 % of the noise-FPs, reducing their numbers to $\sim$ 450. However, this will be at the risk of rejecting genuine planet candidates, as the results also show that the simulated transits were detected down to SDE = 3.5. This means that there is no clear cutoff that will ensure that all authentic detections are included in the results, while at the same time rejecting the majority of FPs. Instead the threshold must be based on the number of FPs, due to noise, that are manageable in this transit survey. As the number of potential FPs far outweighs the number of potential planets, setting the threshold at 7.4 is regarded as the most appropriate choice.

7.5.3 Individual versus linked light curves

The results in Table 7.2 indicate that a BLS search using the linked light curves will result in more FPs than from the single light curves and detect only 14 % of genuine signals, in comparison with the 23 % that were found from just one observation. It is also shown that BLS is less sensitive to shorter orbital period in the linked light curves.

With regards to the FP detections, it could be that having more data points in the linked data can lead to more possibilities of noise coinciding to produce spurious, significant signals. Conversely, the lower rate of positive detections is suggestive that the gaps between observations do create more noise in the power spectra. This would explain why longer period transits are less significant, as these provide fewer in-transit data points, which would result in a lower SDE value.

7.6 Detection criteria and results

In addition to imposing a detection threshold of SDE $\geq$ 7.4, other criteria can also be applied to the BLS results to avoid an overwhelming number of FPs from eclipsing binaries, long-period variability and correlated the noise. Imposing these extra restrictions on the detections will ensure that the results represent the most likely planetary candidates. However, further analysis will be necessary to determine the true nature of the detected signals, as discussed in Chapter 8.

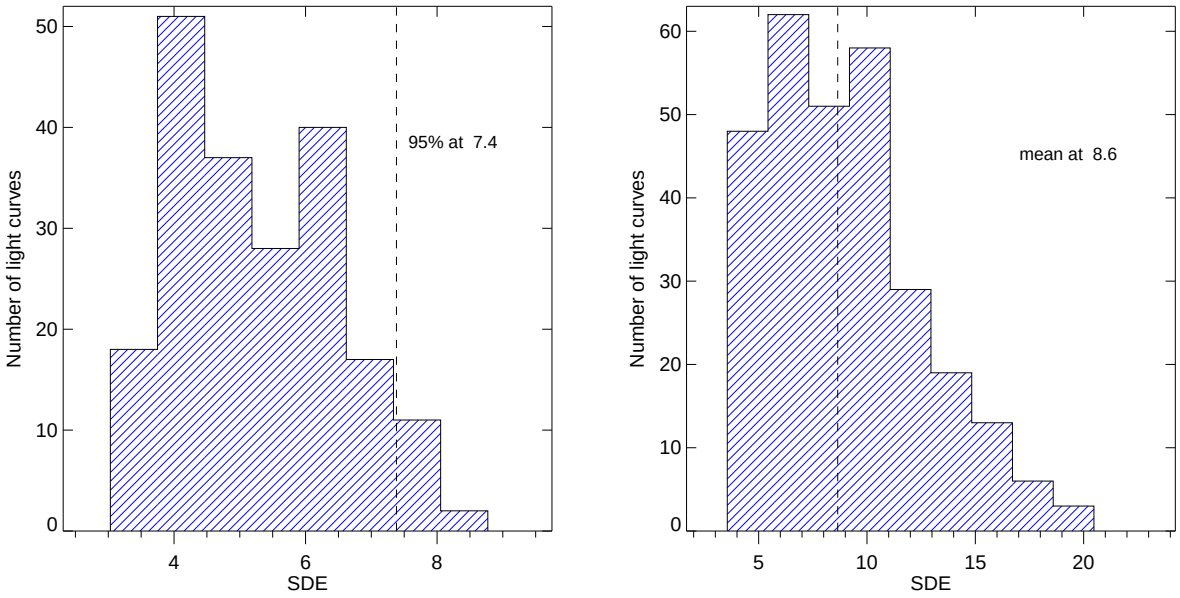

(a) The SDE distribution of the BLS results for the noise-only models.

(b) The SDE distribution of BLS results for the transit-injected models.

Figure 7.4: The BLS results for the noise-only and transit-injected models. 1000 model light curves were created, based on the time-series of the HI-1A light curves with noise drawn from a Gaussian distribution and scaled to the point-to-point scatter in the real light curves. A second set of transit-injected models were constructed, for a range of periods, depths and transit durations. The BLS results for the noise-only and transit-injected models are shown in (a) and (b), respectively.

Statistic	Single		Linked	
	noise only	noise+transit	noise only	noise+transit
Number of detections (out of 1000)	204	289	234	141
Mean SDE	5.2	8.6	10.2	12
Min SDE	3	3.5	4	4.5
Max SDE	8.3	20.5	19.2	53
Mean period (days)	1.3	3.8	1.4	2.7
Mean depth (%)	0.019	0.015	0.012	0.009
Mean sigma	0.018	0.006	0.016	0.008
Number of variables (out of 300)	122	69	129	21

Table 7.2: SDE statistics from the BLS results for the model light curves.

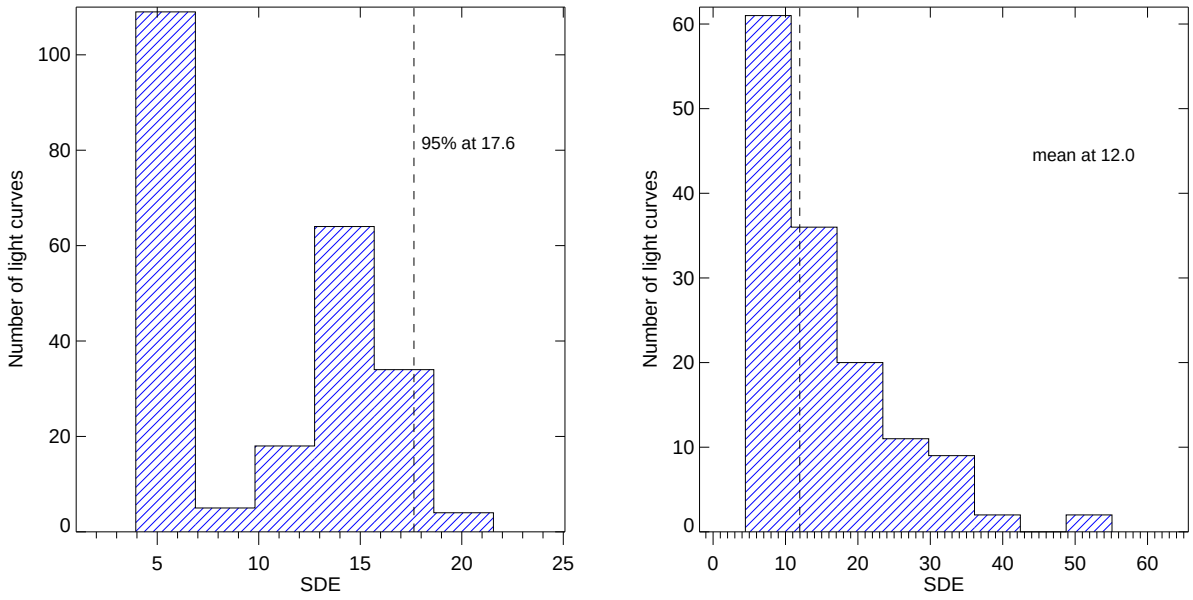

(a) The SDE distribution of the BLS results the combined models.

(b) The SDE distribution of BLS results for the combined models with transits injected.

Figure 7.5: These plots show the outcome of BLS on the linked model light curves, which were constructed by linking together the single models. These results serve as a comparison of the BLS performance for long-duration observations with substantial data gaps, as opposed to short-duration observations, but without large gaps between data points.

All the detection criteria used for this transit search were:

1. **Number of in-transit data points (n)**: The detected signal should have $2 \leq n \leq 8$.

   - The upper limit is chosen with respect to Figure 1.6, which indicates that the maximum transit duration for orbital periods of ≤ 7 days is not expected to exceed ~ 4 hours. This duration corresponds to 6 data points, but the upper limit was raised to 8, to account for possible "smearing" of the transit shape, due to the substantial cadence of the observations. As Kipping (2010) shows, having a long integration time can broaden the apparent transit duration by as long as the length of the image cadence, which for HI-1A is 40 minutes.

2. **Depth (δ)**: $0 < \delta \leq 4$ %.

   - The lower limit is necessary because BLS also detects negative depths (i.e. upward signals) in light curves. This anomalous effect can be explained by Equation 7.3, which shows that the determination of the maximum peak in the power spectrum contains a squared summation over the in-transit flux measurements. As a consequence, the sign on the depth, meaning that negative depths can also be detected. The upper limit comes from the maximum depth expected from planetary transits. Setting a cutoff for the depth reduces the number of FPs which are almost certain to be eclipsing binaries, as opposed to planets. Figure 7.6 shows that the transit depths of detected planets have, to this date, not exceeded 3 %. Therefore, allowing a cutoff at 4 % does not risk rejecting genuine candidates.

3. **BLS test statistic (**SDE): SDE $\geq$7.4, as discussed in Section 7.5.2.

7.6.1 The BLS results for the HI-1A transit search

The results from the BLS transit search for the real HI-1A light curves are presented in Table 7.3. This shows the filtered results, in accordance with the selection criteria described previously.

The average SDE and orbital period detected are both similar to the results for the model transit light curves, although the maximum value for the SDE is slightly lower than the corresponding value from the models.

These results include more than 100 targets for which the detection applies to only one light curve, when there were > 2 individual light curves. This means that the signal detection in the other light curves

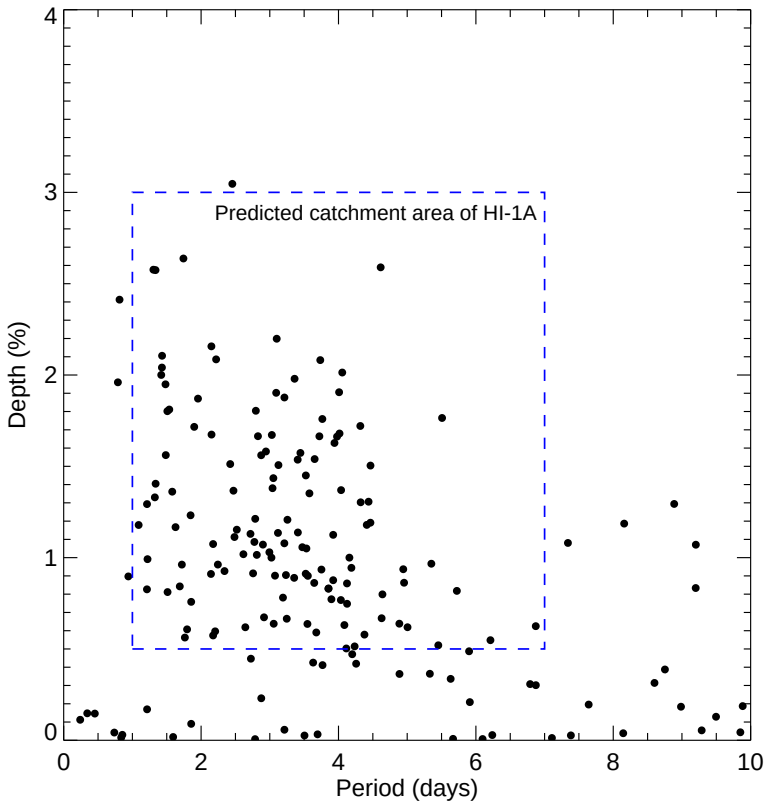

Figure 7.6: The transit depth versus orbital period for all transiting planets detected to date. The area outlined by the blue dashed lines highlights the range of orbital periods and transit depths which the HI-1A survey is most sensitive to and which correspond to the majority of transit detections made to date. The information is accurate as of 1st April 2012, from the Extrasolar Planet Database (Schneider, 1995).

	BLS results
Total number of light curves	235
Number of unique targets	174
Mean SDE	8.3
Min SDE	7.4
Mean SDE	17.5
Mean period (days)	3.9
Mean depth (%)	2.2

Table 7.3: Statistics of the BLS results from the transit search with the HI-1A light curves.

did not meet the selection criteria. The reasons for this may be due to additional noise in other observations, shorter observation lengths or a greater proportion of missed points. The analysis of candidates is presented in the next chapter.

Chapter 8

Candidate Classification

8.1 Introduction

This chapter describes the process of filtering the results from the BLS transit search (Chapter 7), to identify the most likely planetary candidates for ground-based follow-up observations. Even with the reduction of systematic trends and the use of strict detection criteria, the majority of the results are still expected to be due to FPs, since the number of transit-mimicking scenarios far outweighs the number of detectable transiting planets. For example, a common FP source is blended light curves which contain a diluted signal from a stellar binary eclipse (see Section 8.2.3).

False-positives are an issue for all transit surveys, including CoRoT and *Kepler*, despite their superior photometric precision. An early study into the initial rate of FPs for CoRoT, found $\sim$ 98 % of all detections to be non-planetary, which were mostly due to blends (Almenara et al., 2009). While recent studies for *Kepler* find rates of $30 - 35$ % for Hot-Jupiter detections and $\sim$12 % for Earth-sized planets (Santerne et al., 2012; Fressin et al., 2013). With regards to HI-1A, the rate of FPs may be comparable CoRoT's initial rate, as both these surveys have substantial PSFs, enabling a higher rate of contamination in the light curves.

The precise rate of FPs in any given survey depends on a number of factors, including the size of the PSF, the level of noise in the data, the choice of TDA (Section 7.2) and the detection criteria. Whereas detector characteristics like the PSF cannot be changed, modifications can be made to the noise reduction methods and the parameters of the search, to reduce the proportion of FPs in the results. Therefore, the outcome from the analysis of the BLS results may be useful for implementing improvements to the TRP and making adjustments to the search parameters, which would improve the outcome of future transit searches.

Often the most reliable approach for identifing FPs, is a visual inspection of the candidate light curves, as it uses key physical traits to disregard non-transit signals (see Section 8.3.5). However, when the yield

of the detections is large, or when a suspected signal is ambiguous, then other methods (FP tests) may be used to distinguish between likely and unlikely planetary candidates. If they are reliable and may be automated, these tests will offer an effective method for removing the most likely FPs from a large number of detections.

This chapter introduces a selection of FP-tests, which were applied to BLS detections from the transit search. These tests are described in Section 8.3, following a discussion of the main sources of FPs, in Section 8.2. The outcomes of the tests for the whole sample of candidates are presented in Section 8.4, followed by descriptions for some individual detections. These results are used to gauge the reliability of the FP tests. The final section in this chapter summarises the findings of the BLS transit search and discusses a number of potential changes that might improve the outcome of subsequent transit searches with the HI-1A light curves.

8.2 Sources of FPs

8.2.1 Correlated noise from the systematics

Systematic noise which is correlated on the timescales of transits are a source FPs. This is why an effective trend removal process should be applied to the data before a transit search. For example, as explained in Section 4.3.3, if vignetting is prominent, then a phase-folded light curve can produce a detectable transit-like dip. This specific scenario was found to be a main contributor to FPs prior to the inclusion of the non-linear filter in the TRP (Section 5.3.5). This obtains an accurate fit to the edges of light curves with vignetting and so helps to remove this effect. Another source of systematic noise that can produce a FPs was presented in Section 5.5.2. This showed roughly periodic downward outliers due to tracking errors, which are not fully removed by the TRP due to the conservative sigma-clip of 9-σ, which would leave outliers of up to 9 % remaining in the data.

8.2.2 Stellar variability

Despite the fact that most TDAs, including BLS, search for box-shaped signals from transits, some types of stellar variability will also produce signals in the phase-folded light curves, which may constitute a detection. Non-sinusoidal variability from pulsations, spots or granulations, can all produce signals within the detection criteria if they are low amplitude and occur on timescales of a few hours.

With regards to the HI-1A data, the 1-day trend removed by the TRP will have little effect on the short-scale variability, i.e. $P << 1$ day. Therefore any small-amplitude, short-period variability of this nature is considered to be a potential source of FPs.

For *Kepler*, which has the precision to detect Earth-sized planets (depths ~ 0.01 %), stellar spots and surface granulations are of even greater importance, as they can mask the transit signal from such planets. However, HI-1A is not sensitive to such small transit depths, therefore they are not a concern in this survey.

8.2.3 Eclipsing Binaries

Eclipsing binaries (EBs) are a primary cause of FPs for all transit surveys, due to the abundance of EB systems and the different configurations which can mimic a transit-like signal. These types of FP increase with the size of the PSF and aperture, as this increases the likelihood of contamination, especially in crowded-fields.

The most common EB configurations which can mimic transits are:

1. A stellar binary blended with the light from a third star, which may or may not be physically related to the binary system. The blending dilutes the depth of the binary eclipse to a level comparable with transits, making the signal similar to one expected from a planet. Furthermore, if the two components of the binary are similar in size, then the eclipses will be of equal depth, hence this type of signal is indistinguishable from transits.

2. A binary that is inclined to the line-of-sight and producing a grazing eclipse. Such signals are also associated with smaller depths and shorter durations than typical EBs and therefore these FPs can also be difficult to identify (see Section 8.3.5).

3. An EB, where the primary component is giant star and the secondary is a dwarf star or a brown dwarf. These configurations can produce signal depths with are similar to that from a giant planet around a dwarf star. This situation usually requires spectroscopic follow-up to determine the masses of the two components, so that the nature of the signal can be verified.

8.3 Tests for FPs

8.3.1 Multiple detections

This test is specific to the HI-1A transit search. It takes advantage of the nature of the observations, in that most targets have ≥ 3 individual light curves within the full scope of the data (2007 to 2011). This means that if there is a genuine signal to be detected, it should be found in each individual light curve for that that target. Conversely, if a detection is found in only one light curve when the target has been observed multiple times, then the signal is more likely to be an artifact of noise, as opposed to a genuine signal. However, if a target has ≤ 2 individual light curves, then it should still be considered as a possible candidate, until it can be verified by other FP tests.

8.3.2 Planet likelihood – $\eta_\star$

For each signal detected, the orbital parameters can be used to establish its planet likelihood, from the ratio of the observed to expected transit duration, given the period and depth of the signal.

This concept was explored by Tingley and Sackett (2005), who have developed a statistical tool called the Exoplanet Diagnostic ($\eta_\star$), which has aided the verification of planet candidates in surveys such as SuperWASP (Lister et al., 2007; Wilson, 2007) and CoRoT (Almenara et al., 2007). In Tingley and Sackett (2005) it is shown that a planet in a circular orbit, with zero eccentricity, will have a transit duration given by the equation below,

$$D = 2Z(R_{\rm p} + R_\star)\left(\frac{P}{2\pi G M_\star}\right)^{1/3}. \tag{8.1}$$

This takes into account the orbital period (P), the radii of the two components, $R_{\rm p}$ and $R_\star$ and the mass of the host star, $M_\star$. The parameter labeled Z is a function of the projected inclination of the transit and essentially "absorbs" the geometric properties of the transit (Tingley and Sackett, 2005). This factor takes a value of 1 one for an exact edge-on alignment (i = 90 °) and decreases to zero as i increases. The assumptions of a circular, non-eccentric orbit are reasonable for close-in (short-period) systems, which are the focus of this survey.

Equation 8.1 shows that the expected transit duration is directly proportional to the sum of the radii of both components of the system. As such, the duration for a transit should be much shorter than that for a binary eclipse, since a planet-star system will have a smaller combined radii than a star-star system. Using this key feature, the planet likelihood of a detected signal can be determined from the ratio of the

measured transit duration, $D_{\rm obs}$, to D, the expected duration for the given period and depth of the signal. This ratio is the basis for the Exoplanet Diagnostic, which takes the following form:

$$\eta_\star = \frac{D_{\rm obs}}{2Z(1+\sqrt{(}\delta/1.3)} \left(\frac{2\pi G M_\odot}{P}\right)^{1/3} R_\star^{7/12} R_\odot^{5/12}, \tag{8.2}$$

where δ is the depth of the transit. This is Equation 12 in Tingley and Sackett (2005), which is the suggested formula when the size of the planet is unknown, but the size of the host star ($R_\star$) can be estimated, or set to a constant value. If $R_\star$ is known precisely, from spectroscopic or asteroseismic observations, then the Exoplanet Diagnostic should prove to be a reliable test for FPs. The consequences of estimating $R_\star$ are discussed below.

In the implementation of this test on the HI-1A candidates, for which information of the stellar radii are lacking, $R_\star$ is set to equal one solar radius (1 $R_\odot$) and Z = 1 (i.e. edge-on alignment). Then, $\eta_\star$ is calculated for each detection, by inputting the BLS results for P, δ and $D_{\rm obs}$, into Equation 8.2. A value of $\eta_\star > 1$ is suggestive of an EB rather than a planet, as this reflects a longer than expected transit duration given the period and depth of the detected signal. Whereas $\eta_\star << 1$ is much more likely to be associated with a planet transiting the host, than another star.

In the absence of information regarding the host star and the system alignment, setting a constant solar radius for $R_\star$ and Z = 1 maintains the validity of this test, so long as the following consequences are considered.

- If $R_\star$ is overestimated then $\eta_\star$ will be also be overestimated. For example if the stellar radius is actually equal to 0.5 $R_\odot$, then $\eta_\star$ will be increased by a factor of $\sim$ 1.5. However, if the detection is of a genuine planetary signal (which typically gives $\eta_\star << 1$), then the risk of rejecting the candidate is low, as an increase of 1.5 will not push a low statistic ($\eta_\star \leq 0.5$) over the limit. This means that situations where one star is a brown dwarf for example, may be indistinguishable from genuine detections of planets.

- If $R_\star$ is underestimated then $\eta_\star$ will also be underestimated, which may lead to a FP being wrongly included as a planet candidate. For example, $\eta_\star$ will be smaller by a factor of 2/3 for a star with an actual radius of 2 $R_\odot$. However, for giant stars ($R_\star \gg R_\odot$), which are less likely to be hosting a planet, $D_{\rm obs}$ will be much longer, so the effect of underestimating $R_\star$ will be counteracted (see Equation 8.2).

- For grazing eclipses, where $Z < 1$ and $D_{\rm obs}$ is short, $\eta_\star$ will again be underestimated. The test may not be useful for removing this type of FP.

The most useful application of this test will be in identifying blended stellar binaries, in which the components are similar in size and produce similar signal depths in the light curve. These scenarios are difficult to identify visually because BLS will usually measure half the true period so that the phase-folded light curve will only show one signal. However, inputting this value for the period in Equation 8.2 will increase $\eta_\star$ by a factor of ~ 1.6, hence some of these FPs may be identifiable from their high Exoplanet Diagnostics.

8.3.3 $S_{\rm r}$ versus $S_{\rm d}$

As described in Section 6.4, the significance of a detection, $S_{\rm r}$, can be calculated explicitly for a detected signal, using the locations of the in-transit data points and the transit parameters. With this information $S_{\rm r}$ and its white noise equivalent $S_{\rm d}$, can be calculated using Equations 6.3 and 6.12, respectively. These results may then be used to evaluate the level of correlated noise in a given light curve (i.e. $S_{\rm r}/S_{\rm d}$), which could be an indicator of FPs from systematic noise or stellar variability.

8.3.4 Contamination test

As explained in Section 3.5, each flux measurement is obtained by summing the data counts within a circular aperture of radius 2.5 pixels, centred on the target. If the centre of the targets' PSF has been accurately located (using the centroid function), then the aperture will contain all the light from the target. However, in crowded fields, where the density of stars is high, any neighbouring stars within a certain distance to the target, may also contribute light to the aperture, thereby contaminating the flux measurement.

The distance from a target at which a neighbour might contaminate the aperture is dependent on the size and shape of the PSF. However, the precise level of contamination in a light curve will also depend on relative magnitudes of the target and neighbour.

For surveys such as *Kepler* and CoRoT, which benefit from extensive ground-based observations of their target fields, the level of contamination in any given light curve may be evaluated accurately using the available information. However, for HI-1A, which monitors $\sim 20\ ^\circ$ of the whole sky (≈ 250 times CoRoTs FOV), such a census of its FOV does not yet exist. This means that determining the level of

contamination for an HI-1A candidate will be subject to the available catalogue information (i.e. the locations and magnitudes) regarding all stars in the vicinity of the target.

When the required information is available, then the method outlined below will be a useful test for filtering FPs, which are expected to be plentiful, considering the substantial PSF of the HI-1A detector.

The Method:

In their determination of the large-scale flat-field correction, Bewsher et al. (2010) found the HI-1A PSF to be well-approximated by a Gaussian function. In other words, the equation for the Gaussian distribution, given below, can be used to determine the distribution of flux from a source on the CCD:

$$f(x) = \frac{1}{\sigma\sqrt{2\pi}} \exp\left[-\frac{(x-x_0)^2}{2\sigma^2}\right]. \tag{8.3}$$

Here x_0 is the centre of the PSF, x is an arbitrary point on the detector and σ is the standard deviation, which is given by,

$$\sigma = \frac{\mathrm{FWHM}}{2\sqrt{2\ln 2}}. \tag{8.4}$$

As stated in Section 2.2, the FWHM of HI-1A is $\sim$ 1.5 image pixels. This equates to 1.75 arcmin, which gives σ = 0.74 arcmin, for all point sources regardless of magnitude.

It is possible that, as a consequence of undersampling (Section 4.3.1) combined with low SNRs, the PSFs of fainter stars may not necessarily be well-described by a Gaussian function. But for the purpose of this test, which is simply to obtain an estimate for the amount of contamination in an aperture, a Gaussian profile will provide a good enough approximation.

Equation 8.3 can then be used to establish the fraction of flux, F_{n}, which enters the aperture from a neighbouring star. The level of contamination, $\mathcal{C}$, will be estimated from:

$$\mathcal{C} = \frac{F_{\mathrm{n}}}{(F_{\mathrm{t}} + F_{\mathrm{n}})}, \tag{8.5}$$

where F_{t} is the fraction of flux from the target (i.e. 1).

This method requires that the magnitudes of both target and neighbour be known, so that the relative contributions of flux to the aperture can be measured. For example, if 50 % of a neighbour's flux falls within the aperture, but this star is only one tenth as bright as the target, then overall it will contribute less than 5 % to the final flux measurement. However, if the magnitudes are not available, then $\mathcal{C}$ can only provide an upper limit, i.e. "high-risk" candidates, based on the proportions of flux entering the aperture. It is an upper limit because the selection criteria (Section 3.4) ensures that each target is the brightest star within a 6 pixel radius.

The SIMBAD online database[1] was utilized to find all neighbouring stars to each candidate, where a neighbour is defined being within 2.4 arcmin of the target. This this distance is equal to the sum of the aperture radius and the distance at which the flux drops off to 10 % of its maximum amplitude.
With the locations and magnitudes (where they were available), the level of contamination in a light curve was estimated as follows:

1. Two sets of 2-D grids, $\mathrm{array1}$ and $\mathrm{array2}$ are generated. These will contain the distribution of flux in the x and y directions on the CCD and within the aperture, respectively. The grids are centred on coordinates of the target and extend over 20 $\times$ 20 arcmin, in sub-squares of 0.1 $\times$ 0.1 arcmin.

2. Using the information from SIMBAD, the distance, dist, between the target and neighbour is calculated in arcmin. This will serve as x_0 in Equation 8.3.

3. If a neighbour's magnitude is available then the ratio of fluxes between the target and neighbour is estimated. Otherwise this step is missed.
   The ratio of fluxes from the target (f_t) and neighbour (f_n) are calculated from,
   $$f_n/f_t = 10^{\frac{m_n - m_t}{-2.5}}, \tag{8.6}$$
   where m_0 and m_n are the V-magnitudes of the target and neighbour, respectively.

4. The distribution of flux from the neighbour over the grid, $\mathrm{array1}$, was calculated using Equation 8.3, where each x is a sub-square on the grid and x_0 = dist.

5. Step 4 is repeated for $\mathrm{array2}$, which will have the amount of flux from the neighbour within the aperture.

6. The fraction of flux from the neighbour, falling into the aperture is found from,
   $$\mathrm{frac\_flux} = \frac{\mathrm{array2}}{\mathrm{array1}}, \tag{8.7}$$
   and then the final value for the contamination from the neighbour is given by:
   $$\mathcal{C} = \frac{f_\mathrm{n}/f_t \times \mathrm{frac\_flux}}{1 + (f_n/f_t \times \mathrm{frac\_flux})}. \tag{8.8}$$

[1] http://simbad.u-strasbg.fr/simbad/, Wenger et al. (2000).

This process is repeated for all neighbouring stars belonging to the target, but each value of $\mathcal{C}$ is recorded individually, rather than being combined. If any single value of $\mathcal{C}$ exceeds 50 % then the aperture is considered as highly contaminated and that target is flagged as a potential FP. Although, it may be that values of $\mathcal{C}$ which are less than 50 % also constitute contamination and therefore this should be investigated.

As noted above, this test is limited by the availability of catalogue magnitudes for the neighbouring stars and therefore it may not be suitable for all candidates. In these cases, candidate verification must rely on the other tests.

8.3.5 Visual inspection

This is usually carried out to verify the remaining candidates, after the statistical tests have been used to remove the most likely FPs. However, since the initial number of candidates from this transit search is small, the visual inspection is instead used in unison with the other FP tests, to gain a better understanding of their reliability and hence to establish a more robust vetting process for future use.

Visual inspection is used to find the most transit-like signals based on the following key features in the light curves:

1. The signal should present a relatively flat bottom, as illustrated in Figure 1.5. But as mentioned in Section 1.2.1, due to the long cadence of the HI-1A data, a 2 hour transit will only contain ~ 3 data points, meaning that a strict U-shaped signal is not required to indicate a planetary transit. However, a strict V-shaped signal is still more likely to be associated with an eclisping binary than a planet.

2. The light curve should be relatively free from low outliers, which can align in the phase-folded light curve to produce a detectable signal (see Figure 5.5.2).

3. The light curve should be free from vignetting and other systematic trends which can also align in the phase-folded light curve and mimic a transit signal (see Figure 5.4.2).

4. The transit should not appear overly wide, which is suggestive of a deep binary eclipse that has been truncated by the TRP. This scenario was found to be a significant source of FPs in previous transit searches, prior to an adequate TRP. However the current version is designed to maintain deep eclipse signals down to ~ 10 %, which should produce far fewer FPs as a result.

5. The depth of the signal must be consistent from transit to transit. Signals with alternating depths are an obvious sign of a binary system having two stars with different sizes. Although in the case of alternating depths, BLS will usually detect the true period for the system and hence both signals will be present in the phase folded light curve.

8.3.6 Results from stellar studies

As mentioned previously, HI-1A monitors ~ 20 % of the whole sky, meaning that a large proportion of the stars in its FOV are still relatively under-observed and information regarding their nature is scarce. However some targets (especially brighter ones) have been extensively studied by other surveys, providing useful information which can give clues to a candidate's authenticity. In particular, knowledge of a candidate's spectral type, variability and stage of evolution are all useful indictors for planet likelihood. For example, a 1 % signal depth from a giant star ($R_\star >> R_\odot$), is far more likely to be due to another star than a planet, hence this signal would be flagged as a potential FP.

8.4 Outcomes of the FP test results

The FP test results are discussed here in advance of the visual inspection, to evaluate the potential of the tests described previously, as reliable indicators of a candidates authenticity.

The initial yield of detections was filtered from 174 to 33 unique candidates, based on the premise of the first FP test (Section 8.3.1), which ensures that each detected signal is present in more than one light curve of a candidate. Therefore each of these remaining candidates have detectable signals in two or more light curves, with the exception of two candidates for which only one light curve was produced.

8.4.1 $S_{\rm r}$ versus R-magnitude

Figure 8.1 shows $S_{\rm r}$ versus R for the 33 remaining candidates. These results are plotted over the tracks produced by the model simulations (Figure 6.6, Section 6.5), except that in this figure only the 3-day track is shown. This was to avoid over-complicating the figure and also because 3 days is the average duration for the majority of the detections and therefore is the most relevant. As in Figure 6.6, each track adheres to the key and the candidates are plotted in the corresponding colours, after being rounded to the nearest depth. Those which were found to be contaminated by ≥ 50 % by a neighbour are plotted with star symbols. However, this this does not include the "high-risk" candidates, which potentially

have > 50 % contamination, but in the absence of a magnitude for the neighbour, $\mathcal{C}$ can not be fully determined (Section 8.3.4).

The figure shows that the candidate presenting the lowest depth (blue dots), at ~ 0.5 %, has $S_{\rm r}$ values which are greater than expected from the models, which are indicated by the solid lines. The two different values of $S_{\rm r}$ in this case indicate that one of the light curves has a greater level of noise than the other. The figure also shows that signals up to 1 % are detectable at $R > 7.5$, which was the threshold proposed by the models.

Not considering the contaminated results, the detections with 2 and 3 % depths appear to fall into two groups. One is in accordance with the models, while the other has considerably lower than expected $S_{\rm r}$ values for the depth of the signal. The latter group is therefore considered with caution, since low $S_{\rm r}$ values are attributed with stellar variability and correlated noise. Similarly, the two candidates with the deepest detected signals (4 %) should also be treated with care, as again their $S_{\rm r}$ values are low with respect to the majority of the detections, despite their large depths.

Another observation from the figure is that the contaminated light curves all belong to fainter targets. This is expected to be the case as their lower contribution of flux to the aperture is more likely to be overpowered by that of neighbouring stars, whereas bright targets are less sensitive to additional light entering the aperture. But perhaps unexpectedly is the fact that most of these detections have fairly large $S_{\rm r}$ values, which may be cause for concern for the other candidates which have large $S_{\rm r}$ values with respect to the models. It may be the case that $S_{\rm r}$ values exceeding a certain threshold could be another indicator of contamination, that could be used when it is not possible to determine $\mathcal{C}$.

Lastly, having exceptionally low $S_{\rm r}$ values with respect to the signal depth could be another indicator of EBs, blended or otherwise, but prior to the visual analysis. This is because if BLS is able to correctly measure the orbital period for an EB with two different depths, then the locations of the "in-transit" points will only account for one of the eclipses in the phase-folded light curve and not the other. In this case, $S_{\rm r}$ should be low, as the points remaining from the second eclipse will add a component of correlated noise in the data.

8.4.2 $S_{\rm r}$ versus $S_{\rm d}$

Figure 8.2 is a plot of $S_{\rm r}$ versus $S_{\rm d}$. The dashed line represents a 1:1 relation, while the dotted line corresponds to a 2:1 relation, which indicates a lower signal significance as a result of correlated noise,

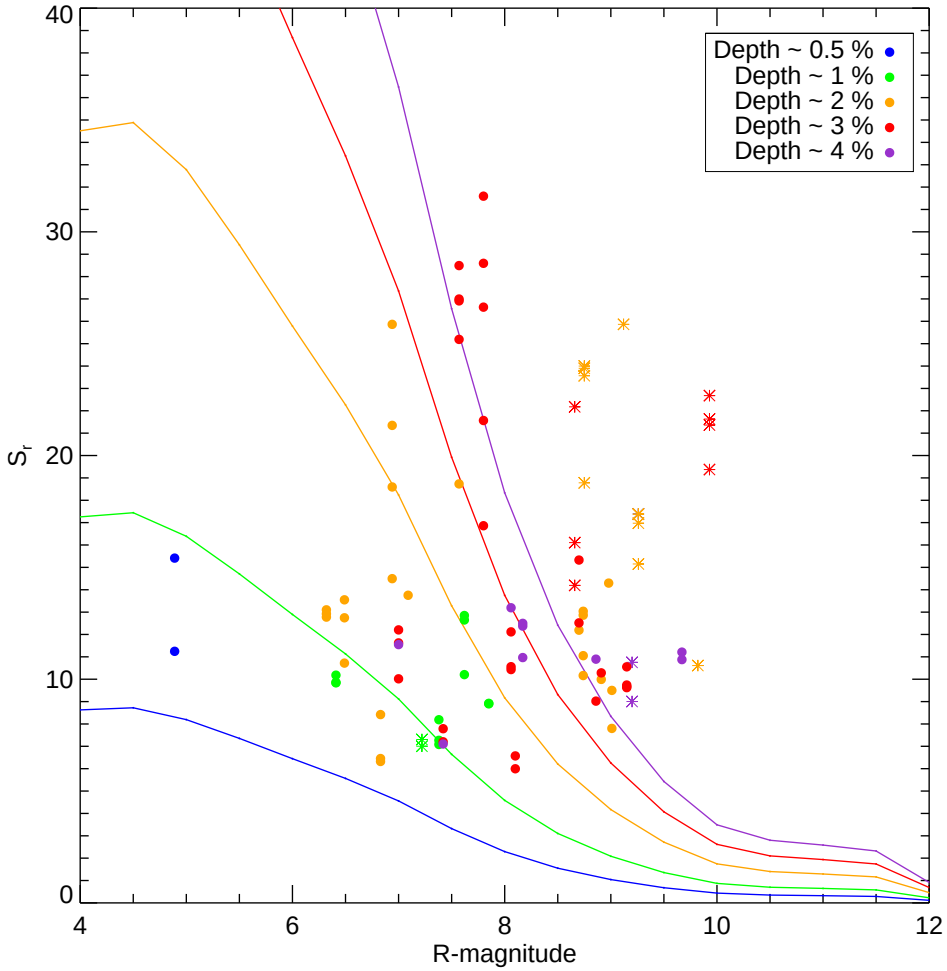

Figure 8.1: $S_{\rm r}$ versus R for the detected signals, plotted against the model results from Section 6.5. For each detected signal the depth has been rounded to the nearest value given in the key. The star symbols represent the contaminated light curves.

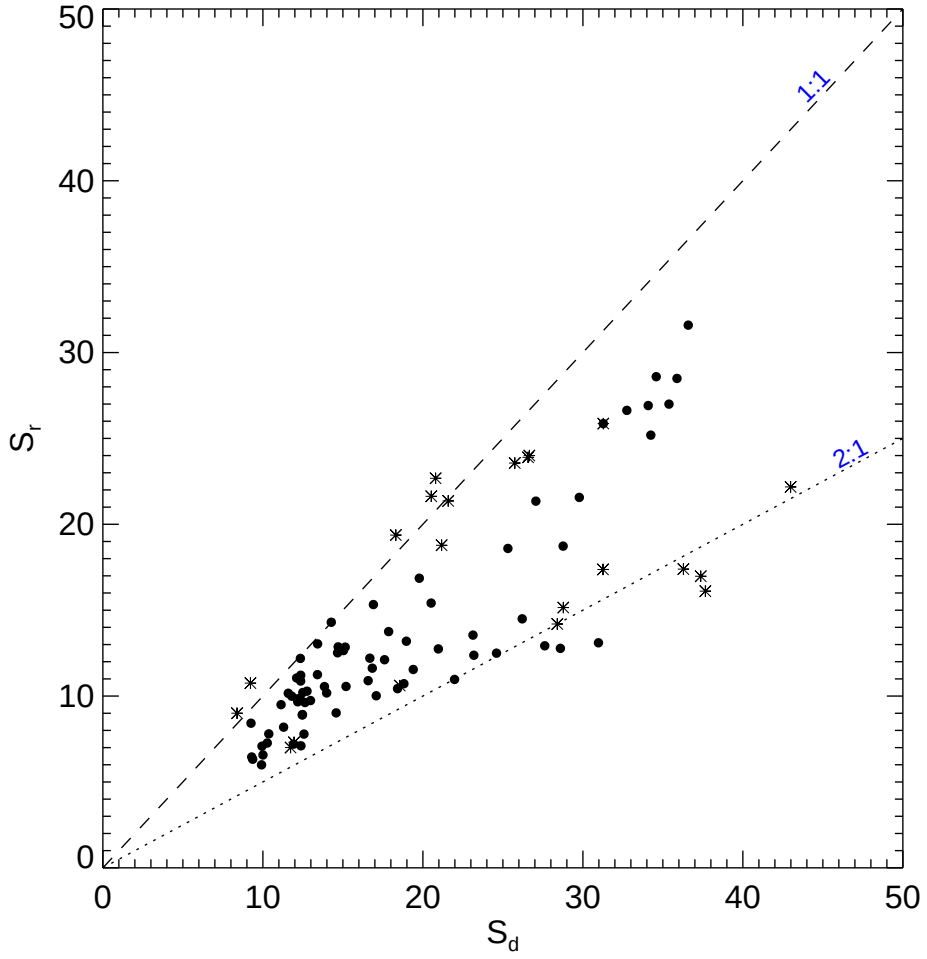

Figure 8.2: S_r versus S_d for the detected signals. The dashed line is the 1:1 relationship, while the dotted line corresponds to the 2:1 relationship between these statistics.

as the calculation of S_d (Equation 6.3) does not account for this. It follows that any detections with points on the 1:1 line should be more reliable on those along the 2:1 line. All points in between these two lines are therefore less trustworthy the further they are from the 1:1 relation. If this test were to be used to identify FPs, then all candidates with points on, or below, the dotted line would be flagged.

8.4.3 Planet likelihood – $\eta_\star$

Figure 8.3 shows the transit duration versus period for the detections, alongside those for the planets which have already been detected with the transit method[2]. The HI-1A candidates are plotted in yellow, with the planets confirmed by other surveys in black. The light curves found to be contaminated are

[2]Information accurate as of 1st April 2013, www.exoplanet.eu (Schneider, 1995).

again represented by stars and plotted in red for a greater distinction, while the blue diamonds highlight the detections which have $\eta_\star > 1$ (calculated from Equation 8.2). These detections are more likely to be from binaries than planets, as their signal durations are significantly longer than expected, given the period and depth from the observations. One apparent result from the figure is that the Exoplanet Diagnostic, $\eta_\star$, is unable to accurately identify EBs in the contaminated light curves, as none of these have $\eta_\star > 1$. This could be due to many reasons, but the most likely is that their $R_\star$ (in Equation 8.2) are underestimated and so $\eta_\star$ is also underestimated. However, as the figure also shows, the detections which have been highlighted by blue diamonds, all lie on the border or outside the space occupied by the confirmed planets. Therefore it is certain that this test will still be a useful for identifying EBs, when the light curves are not contaminated.

The full range of $\eta_\star$ values are plotted in Figure 8.4, with the fractional transit duration, q, plotted on the y-axis. The contaminated light curves are again represented by star symbols for distinction. This and Figure 8.3 show that the Exoplanet Diagnostic and the contamination test may be complementary to each other, as they are based on different characteristics of EB signals and hence together they will identify a much wider range of FPs.

As in the determination of $\mathcal{C}$ (Section 8.3.4), $\eta_\star$ is also limited by the available catalogue information and it is somewhat less reliable in the absence of this. In particular, if $R_\star$ is known, then $\eta_\star$ can be more accurately estimated and this would avoid underestimations for targets with $R_\star > R_\odot$.

When $\eta_\star$ can be more accurately determined, by substituting the correct value for $R_\star$ in the equation, then it is likely that many of the candidates with $0.5 \leq \eta_\star \leq 1$. Then more FPs could be correctly identified and removed from the follow-up studies.

8.5 Candidate classification from visual inspection

This section presents the combined results of the FP tests and those of the visual inspections, from which the candidates were classified into one of the following categories:

- Variables
- Eclipsing binaries
- Planet-like
- Noise

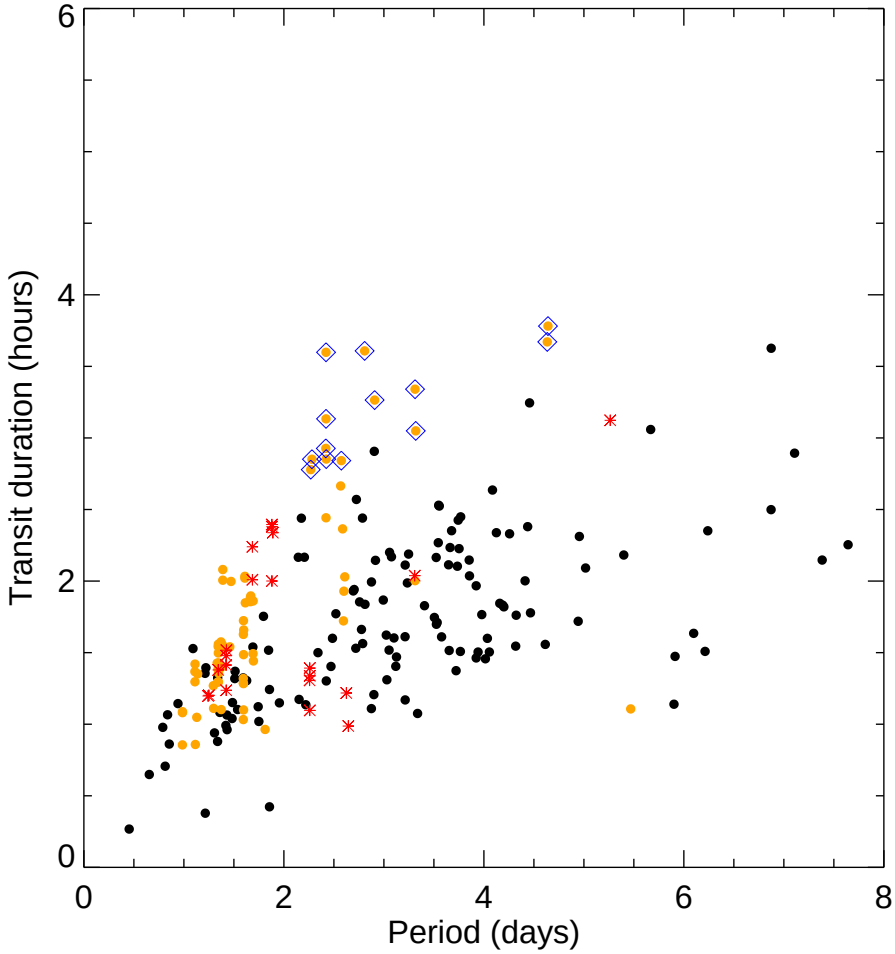

Figure 8.3: Transit duration versus period for the detected signals (plotted in yellow), along with those for planets from the Exoplanet Database, which are plotted in black. The red stars are the contaminated light curves and the blue diamonds highlight the detections with $\eta_\star > 1$, which are more likely to be due to EBs than planets.

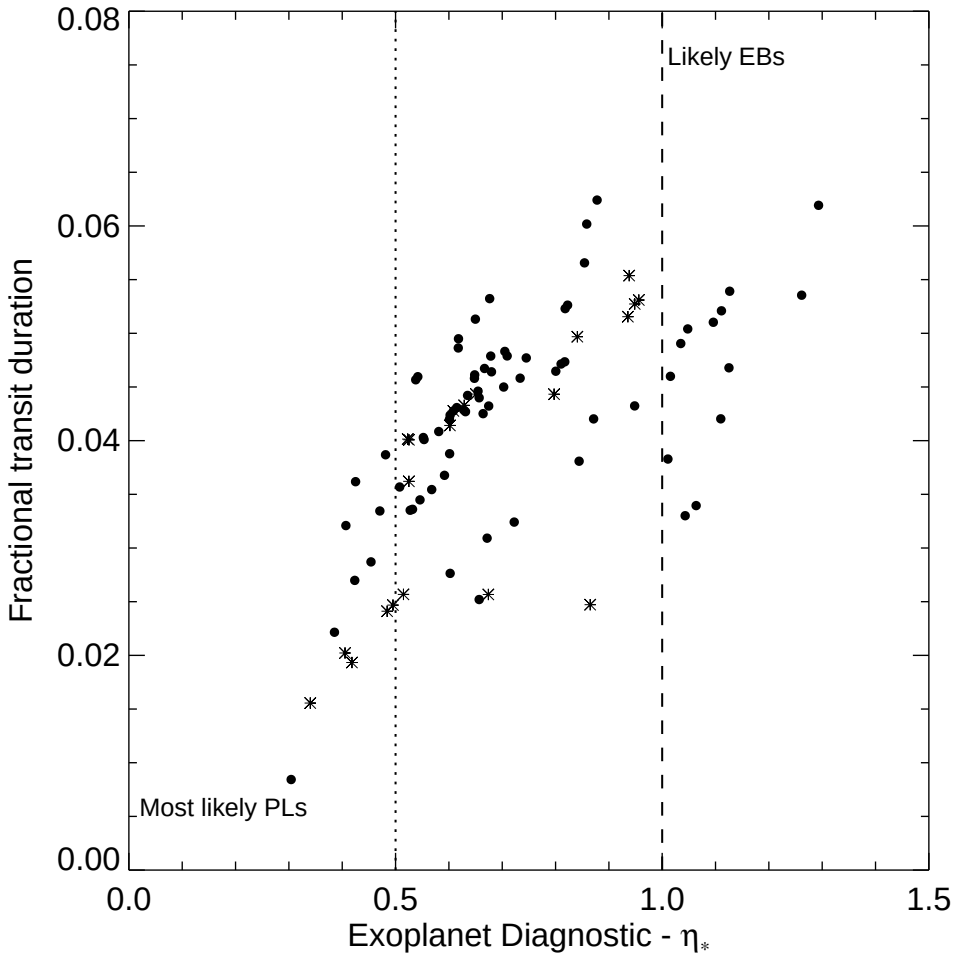

Figure 8.4: Fractional transit duration versus $\eta_\star$ for the detected signals. The Exoplanet Diagnostic is designed to separate the most from the least likely planetary candidates, based on the ratio of their observed and expected transit durations. A typical binary eclipse will have a longer fractional duration than a planetary transit due to the larger sizes of the components of a binary system, compared to a planet-star system.

The classifications listed above are based solely on the visual interpretations of the signals in both the time-series and phase-folded light curves, adhering to the guidelines set out in Section 8.3.5. According to these criteria, the BLS results contain 8 variable stars, 21 eclipsing binaries, 3 planetary candidates and 1 due to noise.

The candidates which display the most transit-like signals have been categorised as "Planet-like". However, after taking into account the FP test results and the catalogue information from previous stellar studies, it was found that these candidates are more likely to be eclipsing binaries, rather than genuine planetary systems. This is discussed further in Section 8.7.3.

Table 8.1 gives the average values from the FP tests and the BLS parameters, in relation to each candidate's category, based on the visual inspections. These results show that, on average, the binaries have the highest SDE and $S_{\rm r}$ values, which will be due to their relatively longer durations and greater depths. The lowest $S_{\rm r}$ values are associated with the variables and therefore this conveys the higher level of correlations in these light curves. The high $S_{\rm r}$ value associated with the noise detection means that this test is not useful for identifying this FPs which are due to tracking errors.

Parameter	Variable	Binary	Planetary	Noise
Total number	8	21	3	1
R-mag	7.3	8.5	6.5	7
Average SDE	9.1	11	8.4	8
Average $S_{\rm r}$	8.3	13.7	11	13.7
Average $\eta_\star$	0.6	0.6	0.8	0.3
Average Period (days)	1.3	1.6	1.7	5.5
Average Depth (%)	1.6	2.7	0.8	2.5

Table 8.1: The FP test results and BLS parameters, according to the visual classifications.

8.5.1 FP-results in perspective

Figures 8.5 to 8.8 correspond to the same relations presented in Section 8.4, but these are colour-coded by the visual classifications. This helps to place the FP test results into focus, with regards to their ability to accurately identify the least likely planetary candidates.

The figures in this section are summarised as follows:

- $S_{\rm r}$ vs R

  Figure 8.5 shows that the detections with the highest $S_{\rm r}$ values are all due to EBs (yellow points) and those with the lowest values correspond to variables (blue points) and also EBs. The first group of EBs, with the high $S_{\rm r}$ values, all have eclipse signals of roughly equal depths in their light curves and as such, BLS has only detected half the true period of the system. This means that when the light curve of phase-folded on the BLS period, only one eclipse can be seen. So when the "in-transit" data points are removed, prior to the calculation of $S_{\rm r}$ (Section 6.4), the points from both eclipse signals are removed. This results in a low noise estimate for a significant signal ($2 - 3$ %), which is reflected by high $S_{\rm r}$ values.

  In contrast, the group of EBs with low $S_{\rm r}$ values all have two visibly different eclipses in their light curves. In these cases, BLS has detected the true period of the system, meaning that when the light curve is phase-folded on this period, two distinct eclipses can be seen. An example of this is shown in Figure 8.11. In this case, only the "in-transit" data points for the larger eclipse are removed prior to the calculation of $S_{\rm r}$. This is because BLS only reports the results based on the dominant signal. Due to the remaining eclipse, the correlated noise in the light curve is greater and the result is a lower $S_{\rm r}$ value. A similar effect occurs for the variable stars, as conveyed by Figure 8.10. In this case, the detected period is an alias of the true period, meaning that the phase-folded light curve displays multiples of the signal. In the same way as for the EBs, the correlated noise which was estimated for these light curves is high, hence the $S_{\rm r}$ values are low.

  The detection due to noise (red point on the figure) has a relatively high $S_{\rm r}$ value, which confirms that this type of FP (shown in Figure 5.5.2) is difficult to distinguish by the $S_{\rm r}$ values alone.

  All the planet-like signals (green points), which have depths ranging from 0.7 % to 1 %, have high $S_{\rm r}$ values for their magnitudes and much higher than the proposed threshold of $S_{\rm r}$ = 8. As there are no reliable planet candidates, it is difficult to determine whether these would also reside above the proposed $S_{\rm r}$ threshold of 8.

- $S_{\rm r}$ vs $S_{\rm d}$

  Figure 8.6 confirms that $S_{\rm r}/S_{\rm d}$ (the ratio of red to white noise) is not a particularly useful test for identifying the EBs that display similar signal depths (discussed for the previous figure). As can be seen, most of these are in accordance with the 1:1 relation. However, the figure also shows that all points along and below the 2:1 line (high red noise) all belong to the second group of EBs, those

with two distinct depths (also discussed for the previous figure). Therefore, the 2:1 line may be a useful cutoff for eliminating this specific type of FP.

- Transit duration vs period

  Figure 8.7 shows the planets with confirmed detections[3] as black points, with the HI-1A candidates overlaid, in their respective colours. This shows that the vast majority of FP detections are indistinguishable from real planets, with respect to their periods and durations. However this will be the result of the detection criteria (Section 7.6), which purposely restrict the results to a specific range of signal parameters.

  The Exoplanet Diagnostic is shown to highlight a few EBs and variables as well as one of the planet-like candidates, which is discussed further in Section 8.7.3. It follows again from the selection criteria that this FP test is limited for the current sample of results, but that it will undoubtedly be more useful for a wider range of candidates, which would follow from a search that allowed for a wider range of results.

- Fractional transit duration vs $\eta_\star$

  Figure 8.8 shows that a few detections due to noise, variability and EBs lie on the left of the dotted line, indicating that they are desirable planet candidates, according their $\eta_\star$ values. This result confirms that the Exoplanet Diagnostic test fails to eliminate certain types of FP, especially grazing EBs and spurious noise, which both produce short-duration signals with respect to their period.

  The majority of the detections lie between the dashed and dotted lines and therefore are neither likely nor unlikely planet candidates. However, it is probable that if the stellar radii of the these stars is known and can be substituted into the equation for $\eta_\star$ (Equation 8.2), that many of these points would be pushed over the dashed line at $\eta_\star$ = 1. This is because a number of the candidates are likely to be giant stars, which have $R_\star >> R_\odot$ and therefore their $\eta_\star$ values will be significantly underestimated. Therefore having additional information for these targets, which may indicate their size will improve the performance of the Exoplanet Diagnostic as an indicator of FPs.

[3] from the Extrasolar planet database (Schneider, 1995). Information accurate as of 1st April 2013

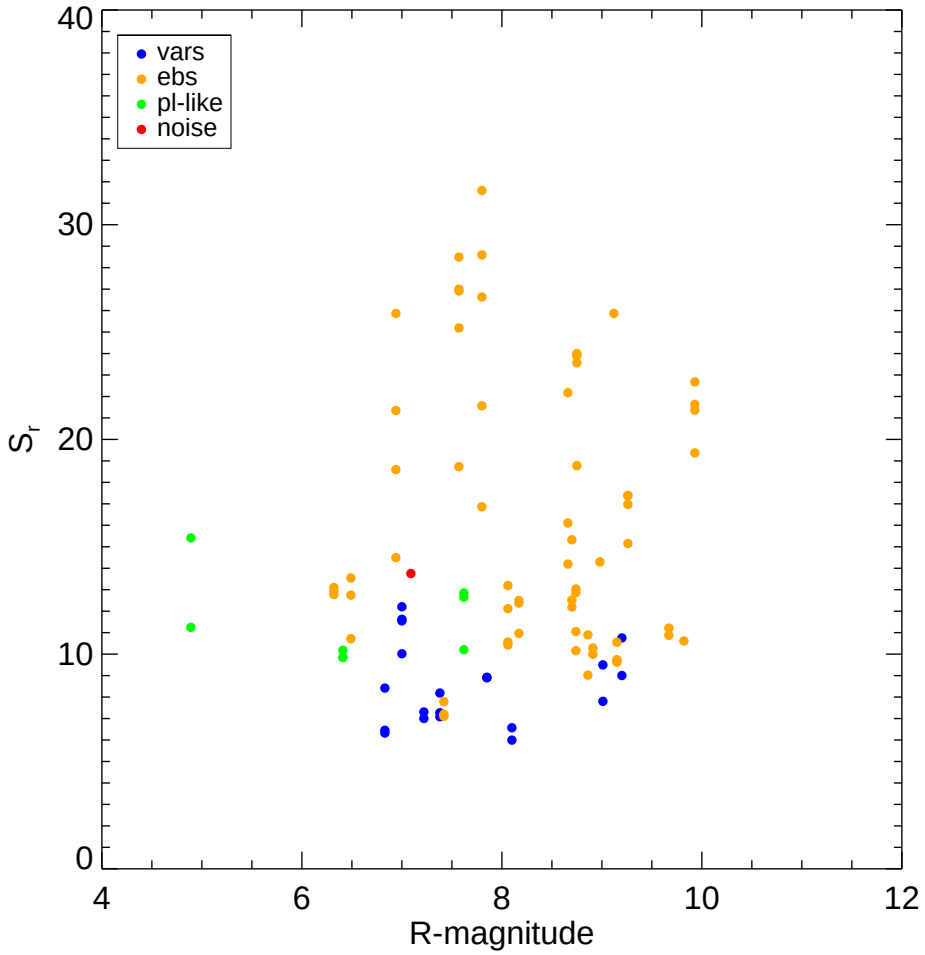

Figure 8.5: $S_{\rm r}$ versus R, with the candidate classifications.

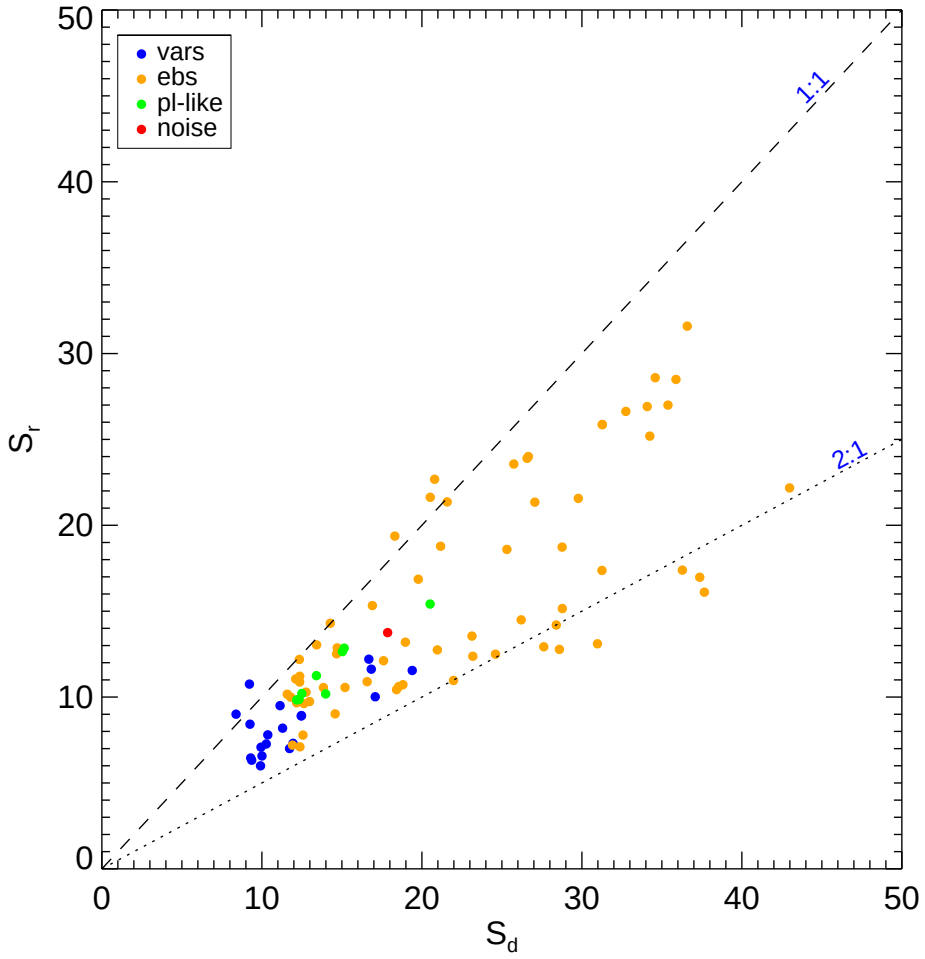

Figure 8.6: $S_{\rm r}$ versus $S_{\rm d}$, with the candidate classifications.

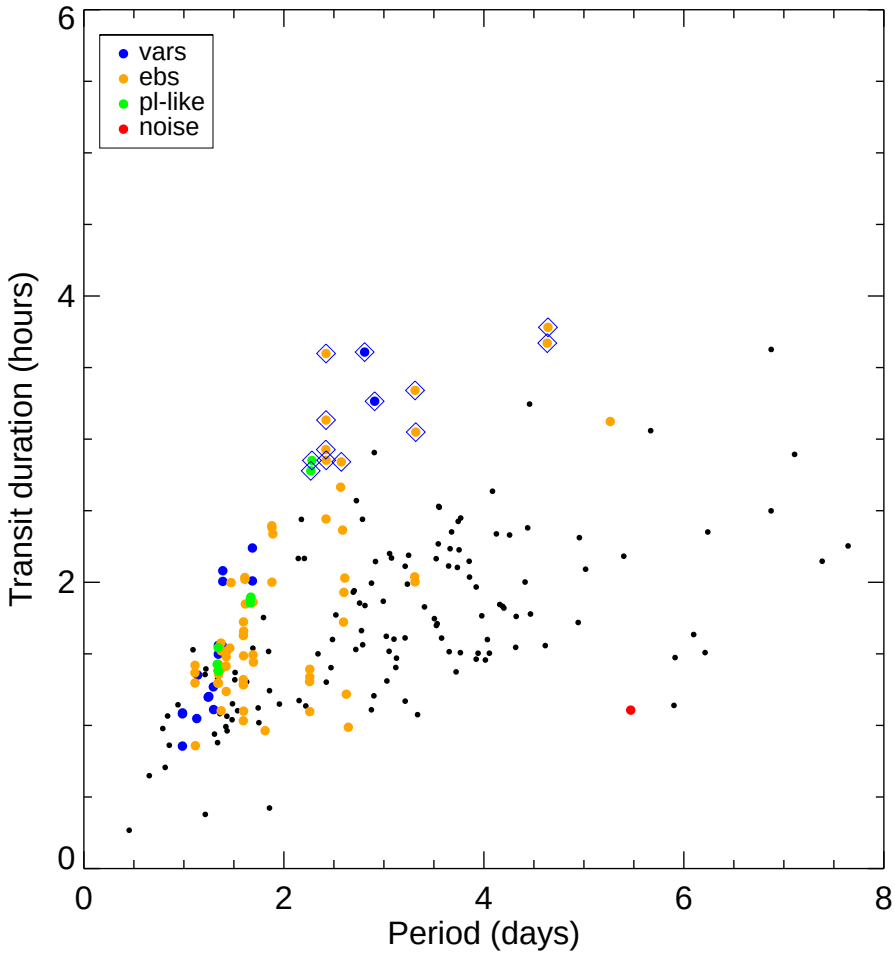

Figure 8.7: Transit duration versus orbital period, with the candidate classifications plotted over existing confirmed planet hosts, according to the Extrasolar planet database (Schneider, 1995).

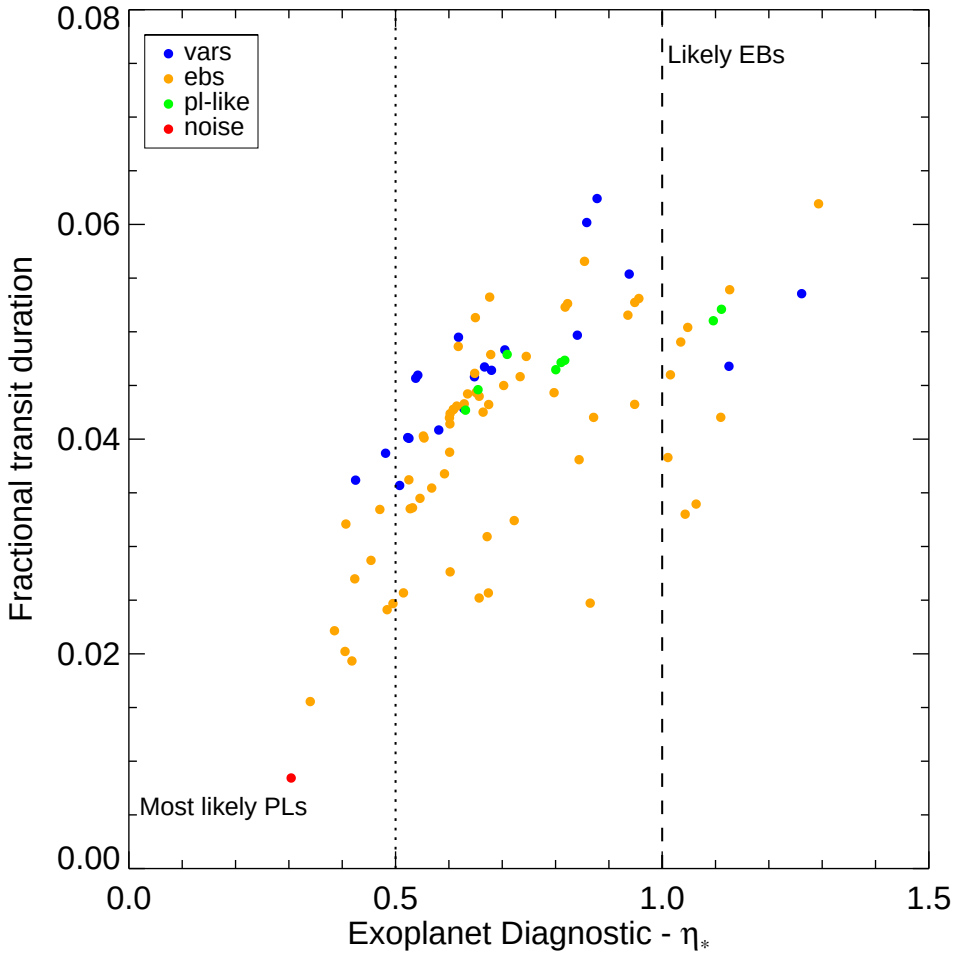

Figure 8.8: Fractional transit duration versus the Exoplanet Diagnostic, with the candidate classifications.

8.6 Distribution of detections on the CCD

One of the most important results from the transit search is conveyed by Figure 8.9. This shows a histogram of the number of detections with respect to their average y-pixel on the CCD, i.e. the distribution of candidates in the FOV. As the figure shows, there is a distinct lack of detections from the central pixels, while the majority have been made from targets in the upper and lower pixels.

It is certain that this outcome is caused by the presence of solar flux and CMEs, in and around the centre of the FOV. Therefore the treatment of these sources of noise by the TRP must be reconsidered, to improve the chance of detection in future searches.

In the current version of the TRP, data points are removed if they are found to be highly contaminated by solar flux. While this results in a lower scatter for the detrended light curve, it can sometimes remove a considerable fraction of data points from the original time series (see Figure 5.4). Not surprisingly, this has important consequences for BLS, which requires a certain amount of data points in order to detect a signal. Also as discussed in Section 7.3, the value of the SDE for any given signal is related to the total length of the observation (i.e. number of data points). Therefore, for the targets in the centre of the FOV, removing the contaminated data points does not improve the outcome of signal detection, so other methods for reducing the noise should be investigated.

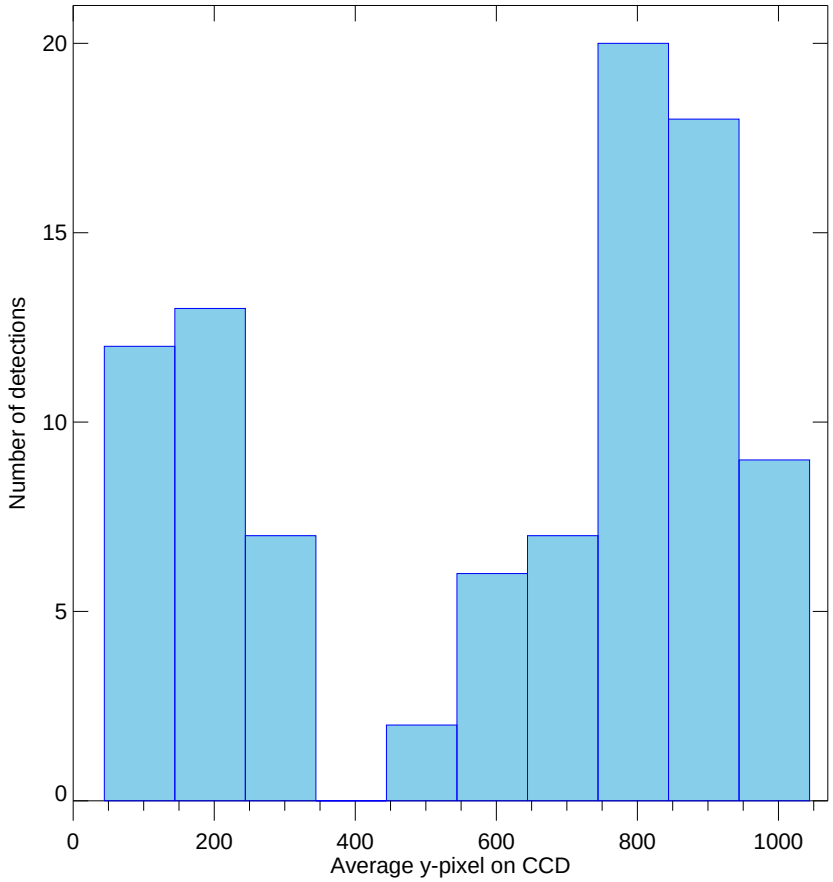

Figure 8.9: A histogram showing the distribution of detections, with respect to their average y-pixel on the CCD. This shows far fewer detections were made in the central region on the CCD, with the vast majority being from the outer pixels. This is almost certainly a result of solar contamination, in the form of direct solar flux and CMEs, which contaminate the central pixels more the upper and lower pixels.

8.7 Examples of individual detections

8.7.1 MW Vir

Figure 8.10 (a) shows the original and detrended light curves, in the upper and lower panels respectively, for the 2008 observation of MW Vir. This is one of 8 FPs in the final sample which are due to stellar variability. As seen in the figure, the variability in this light curve occurs on a period of 0.264 days (Pribulla et al., 2009), rather than 0.98 days, as reported by BLS. This has been caused by restricting the BLS search period to 0.9 days (Section 7.4), which has resulted in a multiple of the true period being detected, due to aliasing.

A comparison of the original and detrended light curves, show that the 1-day NLF, effected by the TRP, has negligible impact on the stellar variability. The data gap, which is present at $\sim$ 13 days, has been partially padded with artificial points, as described in Section 5.3.7.

Figure 8.10 (b) shows the light curve folded on the BLS-period, which confirms that the signal detected is an alias and that the true period is 1/4 of that found by BLS. This also conveys why the $S_{\rm r}$ statistic for this detection is lower than expected (see Figure 8.1), i.e. there is a definite correlation in the data points. It follows from Figure 8.5, that in fact all variables have low $S_{\rm r}$ values, for the same reason.

A low $S_{\rm r}$ value is, in this case, the only indicator against this being a genuine detection. As seen by the values in Table 8.2, this would pass all other FP-tests, since it is not contaminated, has a low $\eta_\star$-value and the ratio $S_{\rm r}/S_{\rm d}$ is far from a 2:1 relation. Therefore it is seen that short-period variables are difficult to identify as FPs, in the absence of the $S_{\rm r}$ statistic.

Possibly, the best way of reducing this type of FP is to lower the minimum search period applied to BLS. This would ensure that the correct period is detected for these targets, which could then be eliminated by imposing a minimum period of ≥ 0.9 days to the initial results.

SDE	8.81
$S_{\rm r}$	8.42
$S_{\rm d}$	9.25
$\eta_\star$	0.42
Contaminated ?	No

Table 8.2: FP test results for MW Vir.

Orbital period (days)	0.98 ± 0.01
Transit duration (hours)	0.85
Transit depth (%)	1.7

Table 8.3: BLS detection results for MW Vir.

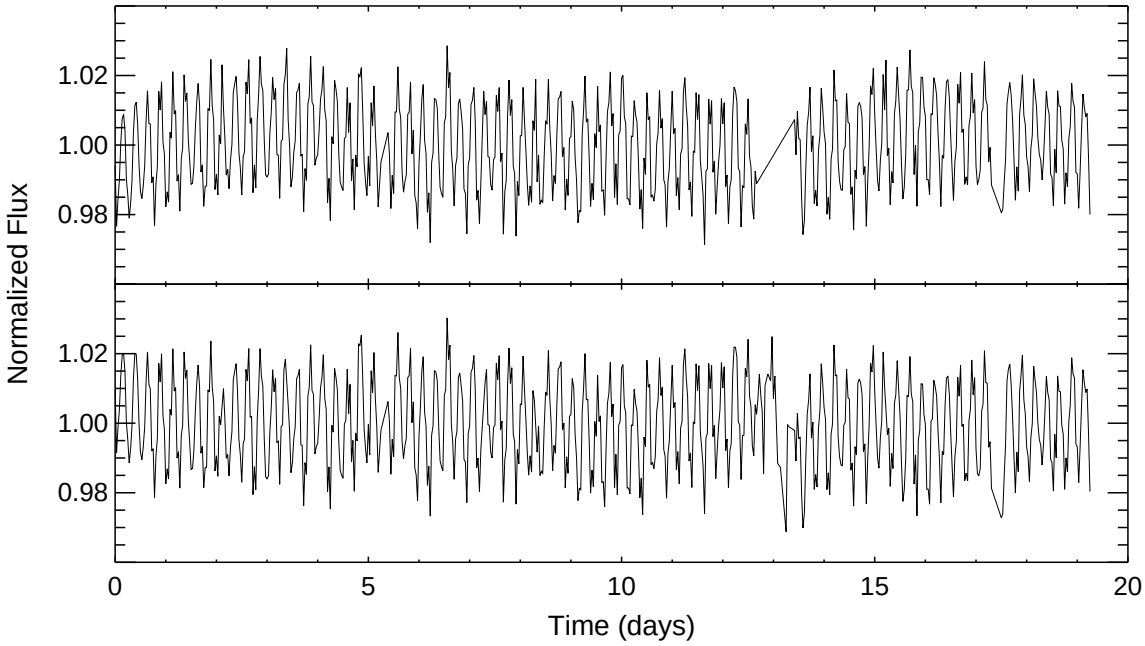

(a) The 2008 observation of V*MWVir, with R = 6.8. This variable star has a period of 0.246 days, as measured by Hipparcos (Pribulla et al., 2009), therefore the 1-day NLF has negligible effect on the variations. The data gap in the original light curve, at $\sim$ 13 days, was lightly padded by the TRP, to avoid spurious signals in the frequency spectrum.

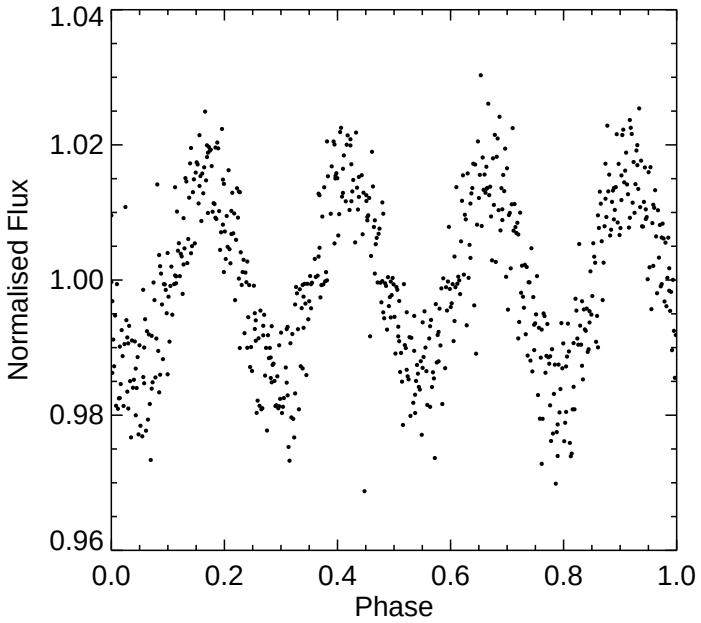

(b) The phase-folded light curve shows that an alias period was detected by BLS, four times greater than the true period of the signal. This is due to aliasing, caused by imposing a minimum search period of 0.9 days.

8.7.2 HD13018

Figure 8.11 (a) shows the original and detrended light curves for HD13018, an A-type star with $R = 6.5$. This observation is one of the few which are wholly uninterrupted and lasting ~ 20 days, whereas most others are affected by data gaps or are considerably shorter in duration. At this time HD13018 is not yet classified as an EB and has no neighbours listed in the catalogues within 4 arcmin.

The light curve displays two distinct eclipse-like signals with different depths, which are unaltered by the TRP. As such BLS detects the correct period of the system, which is found to be ~ 2.6 days. This is also shown in the phase-folded light curve in Figure 8.11 (b), although an alias period is detected in the combined and phase-folded light curve, presented adjacent.

This type of EB, although easy to identify visually, is also flagged as a potential FP in two of the tests. First, the $S_{\rm r}/S_{\rm d}$ ratio is closer to the 2:1 than to the 1:1 relation, indicating a high level of correlated noise. Second, its $\eta_\star$ value is close to one, which suggests that this candidate may be a binary rather than planetary candidate. Therefore without inspecting the light curve, this candidate could be eliminated from these simple statistical tests.

Other types of binary, with visually identical eclipses, are far more difficult to distinguish since BLS will detect half of the true period in this case, meaning that the phase-folded light curve will only show one signal. This was discussed in Section 8.5.1.

SDE	13.46
$S_{\rm r}$	13.55
$S_{\rm d}$	23.13
$\eta_\star$	0.95
Contaminated ?	No

Table 8.4: FP test results for HD 13018.

Orbital period (days)	2.57 ± 0.06
Transit duration (hours)	2.7
Transit depth (%)	2.2

Table 8.5: BLS results for HD 13018.

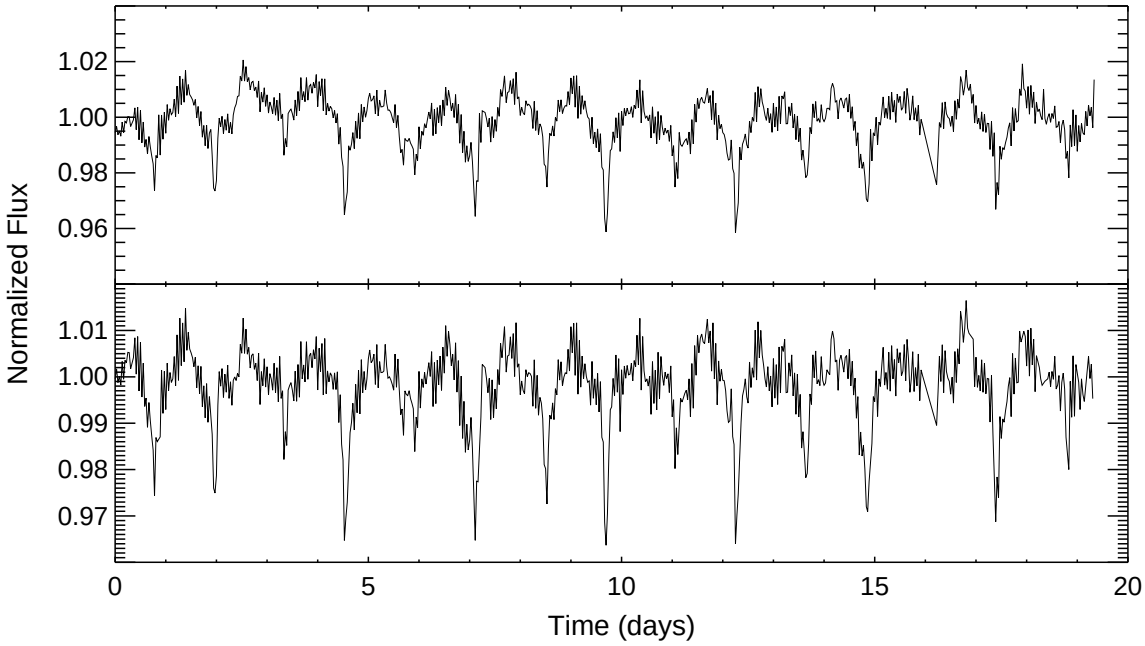

(a) The shows the 2008 observation of HD13018, an A-type star with R = 6.5 The TRP has negligible effect on the signals from both components.

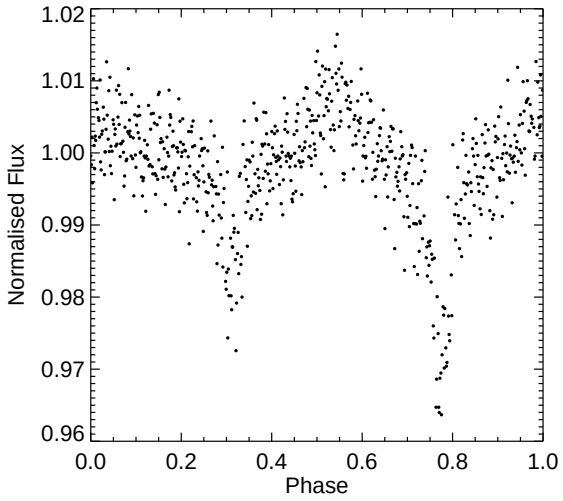

(b) The phase-folded light curve shows two distinct binary signals, with the same period, but different depths.

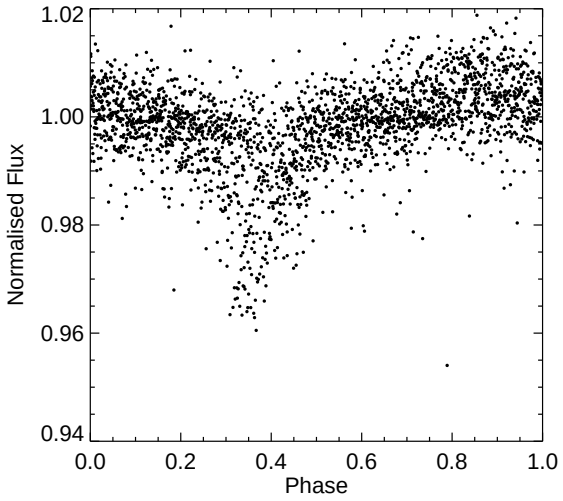

(c) Half the true period is found by BLS in the the linked light curve, which combines four separate observations.

Figure 8.11: HD 13018. A binary star, detected by BLS with SDE = 13.5 and $S_{\rm r}$ = 13.6.

8.7.3 Planet-like results

18 Sgr

Figure 8.12 (a) shows the 2007 observation of the bright star 18 Sgr, with R = 4.89. This target was tracked throughout the lowest 100 pixels on the detector, resulting in vignetting at the edges of the light curve. However, its position on the CCD also means that the data have relatively low solar contamination and hence low scatter, which a crucial factor in the detection of this signal. In the detrended light curve the vignetting is effectively removed, leaving a flat continuum, but with a few remaining outliers at the edges.

The detected signal is measured with a depth of 0.7 %, an orbital period of 2.38 days and a transit duration of 2.85 hours. This gives a fractional transit duration of ~ 0.05, which is relatively high compared to the values for currently detected planets, as shown in Figure 7.2.

Based on a visual inspection of the phase-folded light curve in Figure 8.12 (b), the signal was classified as transit-like due to its flat bottom and shallow depth. A shallow, possible secondary eclipse, with a depth of ~ 0.4 % is also conveyed in this figure and is accentuated in the adjacent plot of the combined dataset.

Both the contamination and $S_{\rm r}$ tests give results which enhance the plausibility of this being a planetary candidate. It has no listed neighbours in the SIMBAD database and its $S_{\rm r}$ value is ~ 1.5 times greater than expected for the depth and period (c.f. model results). However, since $\eta_\star > 1$, the detection would be flagged as a potential FP, which is more likely to be from an eclipsing binary, based on its duration.

This result is therefore a good example of the usefulness of the Exoplanet Diagnostic in identifying unlikely planetary candidates, since this star is in fact believed to be a cool, late-type giant, which is less likely to present a detectable planetary transit.

SDE	8.12
$S_{\rm r}$	15.41
$S_{\rm d}$	20.51
$\eta_\star$	1.11
Contaminated ?	No

Table 8.6: FP test results for 18 Sgr. If this star is a giant, then its $\eta_\star$ value is underestimated, since $R_\star \gg 1\ R_\odot$.

Orbital period (days)	2.28 ± 0.06
Transit duration (hours)	2.85
Transit depth (%)	0.7

Table 8.7: BLS results for 18 Sgr.

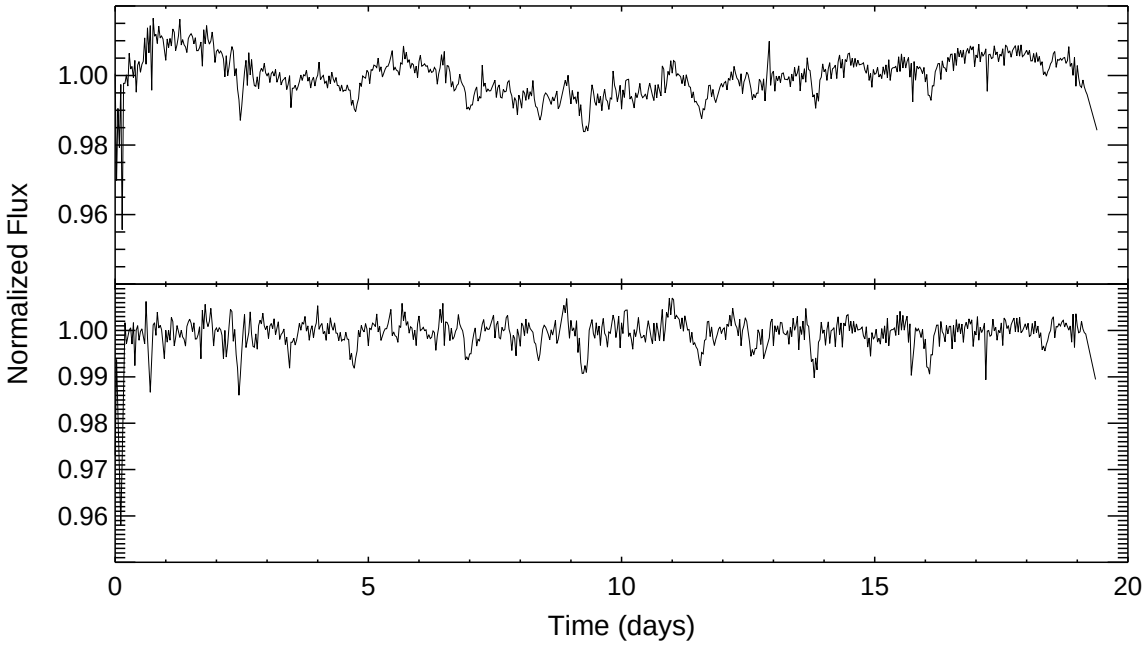

(a) The TRP removes the long-term systematic variability in the original light curve and corrects for the majority of vignetting at the edges. A few outliers are also removed, although some remain at the start of the light curve.

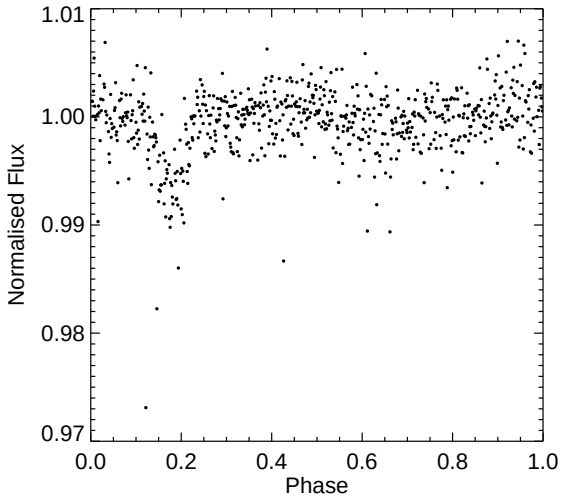

(b) The phase-folded light curve shows a definite signal of < 1 %, despite a few outliers from the start of the observation.

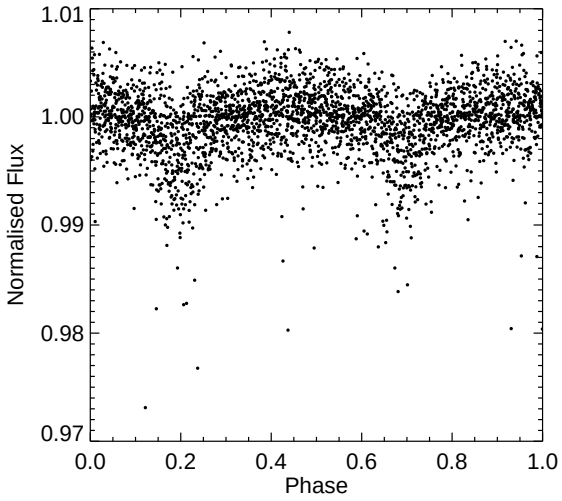

(c) The signal is less noticeable in the phase-folded, linked light curve, which contains five (three partial) observations.

Figure 8.12: *18 Sgr. A possible late-type giant star with no listed companions, detected by BLS with SDE = 8.1 and $S_{\rm r}$ = 15.4.

HD189365

The light curve shown in Figure 8.13 (a) is of HD189365, the second brightest candidate, with R = 6.41. As in the previous example, this target was also tracked in the lowest 100 pixels on the detector and as a result its original light curve displays similar vignetting, which is reduced by the TRP.

Both phase-folded plots in Figures 8.13 (b) and (c) show the detected signal and a secondary dip, which is more evident in the latter plot of the combined dataset. The primary signal was found to have a depth of 0.78 %, a period of 1.67 days and a transit duration of 1.9 hours, giving a fractional duration of ~ 0.05. This is similar to the previous example, which was the first factor to undermine the planet-likeliness of the detected signal. Likewise, this candidate has a value for $\eta_\star$ which is closer to unity than zero and therefore indicative of it being an eclipsing binary, rather than a planetary system.

In support of the status of this candidate are the $S_{\rm r}$ and contamination tests. The value for signal significance is in accordance with the model results and the contamination risk was found to be negligible, with the closest neighbours at a distance of 3 arcmin and with a fraction of the flux equal to 1/25. Therefore it is once again that the Exoplanet Diagnostic that is the most indicative of this candidates false-likelihood. By using the parallax and B,V-magnitudes from the Hipparcos observations (van Leeuwen, 2007), an absolute magnitude of M_V = 1.27 was calculated from the standard equation for the distance modulus. This result and a corresponding $B - V$ = 0.9, indicate that, like *18Sgr, this candidate is also a giant and therefore this detection is less likely to be due to a planetary candidate. This is despite there being no listed binary companion at the current time. If this is indeed a giant, then a more accurate determination of $\eta_\star$, using a larger $R_\star$, would increase its value, making the detection even more questionable.

SDE	9.34
$S_{\rm r}$	10.18
$S_{\rm d}$	13.98
$\eta_\star$	0.82
Contaminated ?	No

Table 8.8: FP test results for HD 189365.

Orbital period (days)	1.67 $\pm$ 0.04
Transit duration (hours)	1.9
Transit depth (%)	0.78

Table 8.9: BLS results for HD 189365.

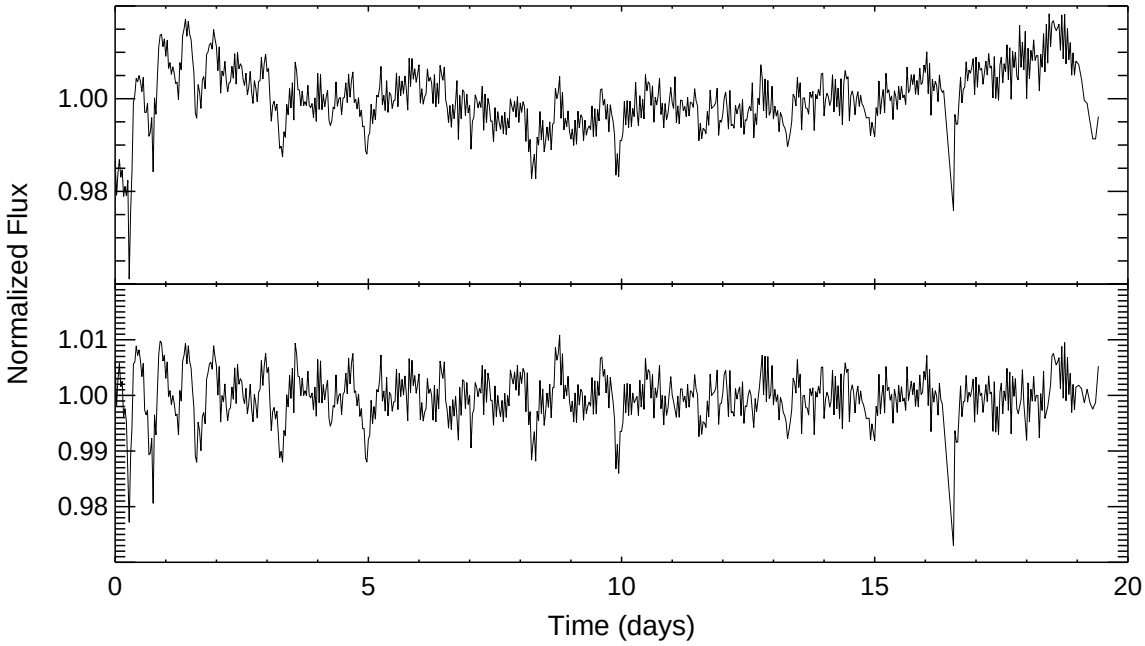

(a) The TRP reduces the effects of vignetting at the start and end of the original light curve. A few outlier points remain in the detrended light curve, but a signal is clearly visible.

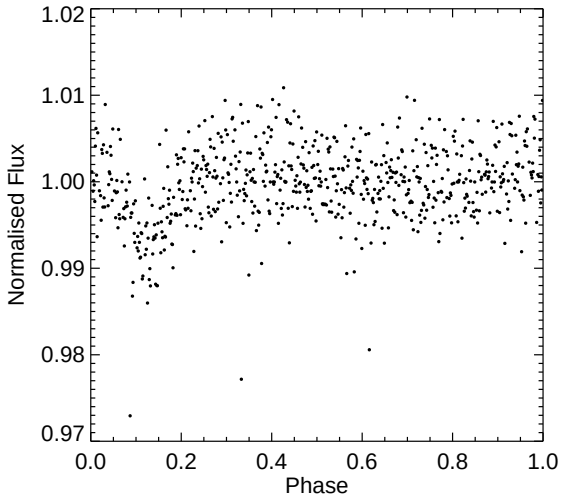

(b) The phase-folded light curve shows the signal, which has a depth of ~ 0.8 %.

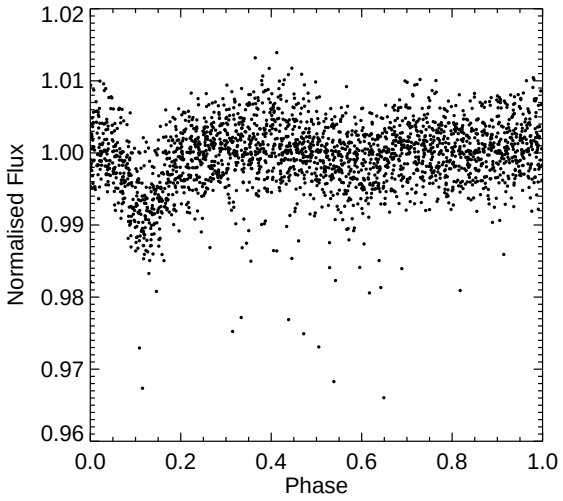

(c) BLS finds the same signal in the linked light curve, which contains four observations.

Figure 8.13: HD 189365, a possible giant, detected by BLS with SDE = 9.3 and $S_{\rm r}$ = 10.1.

HD196816

The third planet-like candidate, HD196816, is presented in Figure 8.14. With R-mag = 7.78, this candidate is fainter and hence produces more noise that the previous two examples. The original light curve shows vignetting for the third time in these examples, which is therefore a common theme.

While BLS reports the depth of the signal as 1.1 %, the phase-folded light curves in Figures 8.14 (b) and (c) indicate that this measurement may be a slight underestimate, due to the greater scatter in the light curve. The period and depth of the signal are 1.35 days and 1.38 hours, giving a fractional transit duration of ~ 0.04, which is considered relatively high for this period, in comparison to the confirmed detections (Figure 7.2). Despite this, out of all of these examples, $\eta_\star$ has the lowest value for this candidate at 0.63, which therefore does not immediately suggest that this is a potential FP.

This star has two neighbours at distances of 1.5 and 2.4 arcmin, however, both these stars are approximately 20 times fainter than the target and were found to contribute only 4 and 2 % of their flux to the aperture, respectively. Therefore, this candidate is not considered to be contaminated. In addition, the $S_{\rm r}$ value of ~ 13 is almost twice as high as the value measured from the models for this scenario, indicating a strong signal.

The only factor against the likeliness of this detection being a genuine planetary transit is its classification in the 1982 Michigan Catalogue of Two-dimensional Spectral Types for the HD stars (Houk, 1982), in which it is listed as an A-type giant (Houk, 1982). This being the case, the Exoplanet Diagnostic is underestimated, as for the previous examples and it is probable that is should be much greater than 1 for this detection.

SDE	7.78
$S_{\rm r}$	12.85
$S_{\rm d}$	15.14
$\eta_\star$	0.63
Contaminated ?	No

Table 8.10: FP test results for HD 196816.

Orbital period (days)	1.35 ± 0.03
Transit duration (days)	1.38
Transit depth (%)	1.1

Table 8.11: BLS results for HD 196816.

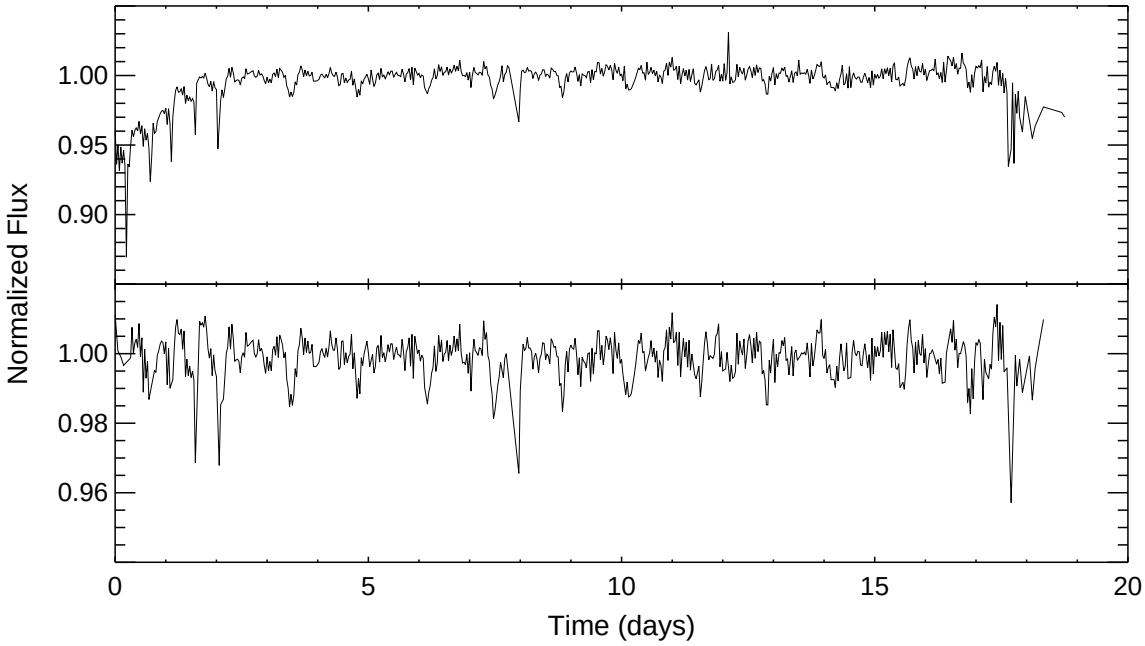

(a) The TRP reduces the vignetting and removes some spurious data points.

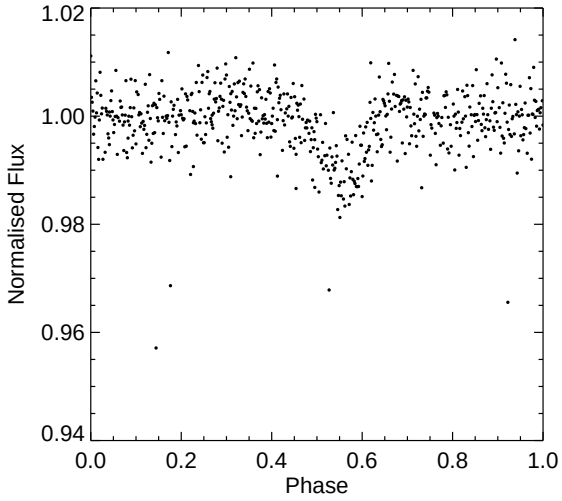

(b) The phase-folded light curve shows a 1 % signal in the light curve.

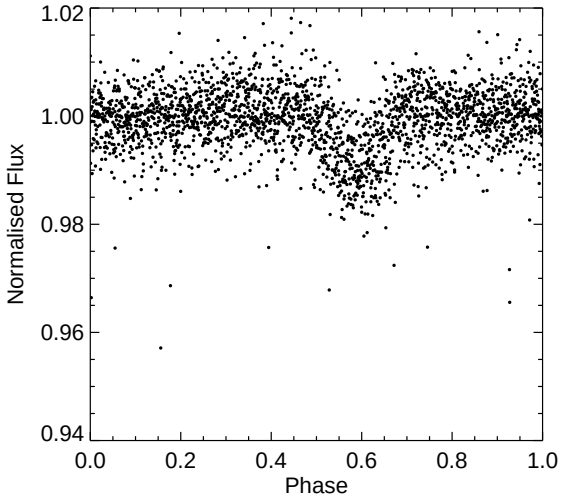

(c) The linked light curve confirms the signal with the same period.

Figure 8.14: HD 196816, a possible giant, detected by BLS with SDE = 7.8 and $S_{\rm r}$ = 12.8.

8.8 Chapter summary and conclusions

The key results from the HI-1A transit search are summarised in this section, followed by a few concluding remarks.

This chapter begins with a discussion of the main types of FP expected in transit surveys. With regards to the HI-1A survey, blended EBs are expected to be prominent, owing to the large PSF of a source on the detector. In addition, many unblended EBs are expected since eclipsing binaries are easier to detect than planets. Stellar variability is also anticipated, however the effects of aliasing, which are discussed in Section 8.7.1, were not considered prior to these results.

Section 8.3 describes a series of tests, that may be aid in the identification of FPs in a large number of possible candidates. These tests include the Exoplanet Diagnostic, $S_{\rm r}/S_{\rm d}$, (i.e. red to white noise ratio), a test for contamination (using available catalogue information) and $S_{\rm r}$ versus R (compared to the expected values from the models). The most resilient test is based on a visual inspection of the individual light curves, from which stellar variability, noise and most types of EBs can be easily identified. However, the only test which was carried out on the initial yield of detections, was based on the premise that each detected signal, if it is genuine, should be detectable in at least two or more individual light curves belonging to that target. This single stage of eliminations reduced the sample of candidates from 174 to 33, and the number of individual light curves from 235 to 94.

The results of the FP tests for the 33 remaining candidates are presented in a series of plots (Figures 8.1 to 8.4) and discussed in Section 8.4. This is followed by the outcome of the visual inspection of each light curve, which results in each candidate being classified as either a variable, EB, noise or planet-like candidate. Figures 8.5 to 8.8 again show the FP-results, but in light of the candidate classifications. This highlights the reliability of the tests in determining the planet likelihood of a detection.

It is difficult to fully interpret the results of the candidate analysis, as no candidate passed every test. The three candidates considered as the most planet-like from the visual analysis were invalidated as potentials when it was discovered that they were more likely to be giants than main-sequence stars. If this is the case, then it is likely that the $\eta_\star$ values (from the Exoplanet Diagnostic) which belong to these candidates would be much greater, when calculated with the correct stellar radius, which would further undermine their planetary nature.

Given below are the conclusions of the transit search based in the results from this and previous sections:

- The smallest depths detected by BLS were for the brightest targets with $R \leq$7.5, as expected from

the model results. This suggests that shallow signals, ≤ 1 %, are not detectable around fainter stars, meaning this transit survey is limited by the number of bright targets which can be monitored by HI-1A.

- The three smallest signals were all detected in light curves which were tracked throughout the lowest 100 pixels on the detector. The reason for this is not well understood, however it is believed to be because observations taken low down or high up on the detector have much less solar contamination. Since solar flux increases the noise and also the background radiation, this may be another limiting factor in the detection of this type of signal.

- It was found for some candidates that only 2/3, 2/4 or 3/4 light curves presented a detectable signal, despite each being subject to the same TRP and search parameters. This is believed to be related to the number of points and length of observation, since, in the case of a null detection, often the corresponding light curve had a much lower fraction of data points. This relates to the previous point, as light curves which have been tracked across the centre of the detector all have much higher scatter towards the end of their observation, which is usually removed by the TRP, thus reducing the number of data points in the light curve.

- All signals detected with depths ≥ 2 % belong to eclipsing binaries, both blended and unblended.

- With the exception of the noise detection, there is a bias towards shorter periods, < 2 days, which is expected since BLS is proven to be more efficient in detecting short-period signals.

- There is no single FP-test which is able to accurately identify all FPs. Instead, it is found that they complement each other, by finding different types of false signal. As such, implementing them in a sequence with the appropriate thresholds, will result in a more effective candidate pipeline.

- Both the Exoplanet Diagnostic and the contamination test are limited by the the available catalogue information. The former would benefit from an accurate determination of the stellar radius, so as not to underestimate this value for giant-type stars, while the latter was lacking from magnitude values of neighbours, meaning that the full extent of the contamination could not be determined.

- These results are not believed to reflect the full use of the FP tests, given the restrictions on the detection criteria (Section 7.6), which were imposed to control the output of results. In doing to this may have biased the results and eliminated possible planetary detections. It is concluded that

repeating the transit search and relaxing the detection criteria, perhaps by lowering the $S_{\rm r}$ threshold, might provide more planet-like candidates. Although this would also increase the number of FPs and hence an automated candidate-pipeline, using the FP-tests and appropriate thresholds, would be required.

- In addition to the previous remark, extending the minimum period of the subsequent transit search would help to avoid short-period variables in the results, which are due to aliasing (see Section 8.7.1).

Chapter 9

Conclusions

The trend removal pipeline (TRP) presented in this thesis is the latest and most effective version of an algorithm for removing systematic trends in the data from STEREO's HI-1A instrument. This version is shown to significantly reduce the noise in the light curves, with negligible impact on transit-like signals (see Figure 5.9). According to the results from the noise analysis (Chapter 6), the TRP makes a transit survey for planets a realistic feat, which would not have been possible with the original light curves (see Figure 6.8). Using the detrended data, the search was opened up to all stars in the HI-1A FOV with $R \leq 10.5$, which amounts to $\sim$ 46,000 targets.

The transit search was conducted using the BLS transit detection algorithm. This produced a modest number of detections, subject to strict detection criteria (see Section 7.6). Included in the results were the signals from stars with $R \leq 8$, with depths of ≤ 1 % and high $S_{\rm r}$ values, ranging from 7 to 15. Although few, this confirms that planetary signatures should be easily detectable in the HI-1A data. However, according to the FP test results, none of these detections provided a veritable planet candidate, meaning that more work is required.

The results of the work presented in this thesis has inevitably lead to a better understanding of the light curve characteristics, the sources of noise, the outcomes of the TRP and the limits of the BLS algorithm. In light of this, the factors which are now believed to be the most detrimental to the success of the transit search can be confidently addressed. These factors are discussed below, along with suggestions to rectify each of them. This will essentially constitute the future work to be undertaken, with the goal of increasing the number of authentic planet candidates from the transit survey.

The factors hindering the transit search and ways to eliminate them:

1. The SDE threshold is too high - lowering the cutoff could improve outcome of the search.

   - A threshold of SDE = 7.4 is expected to eliminate $\sim$ 95 % of FPs due to noise and stellar variability. However, as shown (Section 7.5.2), this cutoff also risks rejecting genuine signal

detections. While lowering the SDE threshold will significantly increase the number of FPs in the results, now that methods to identify them are better understood, they can be more effectively managed in future searches.

- Lowering the SDE will also allow the detection of signals in shorter-duration light curves. These are mostly associated with targets in the centre of the FOV, which were truncated by the TRP, to remove the effects of solar contamination. As discussed in Section 7.4, the SDE values for signals in these light curves will be lower than expected. This also explains why there were signals detected in some, but not all, the light curves belonging to a candidate, as it was found that the null detections were associated with a lower number of data points.

2. There are not enough "good" light curves, particularly for bright stars ($R \leq 8$).

A "good" light curve is defined as having a minimum SNR and maximum number of data points. Both these factors would be improved with the following modifications, which apply to the production of light curves (Chapter 3) and the TRP (Chapter 5):

- Improvements to the centroid function: Due to tracking errors causing composite light curves (Figure 4.1), almost 2500 of the initial yield of targets with $R \leq 10.5$ were rejected. The tracking errors are a result of a failure in the centroid function, which in turn are caused by undersampled PSFs and low SNRs. This means that the 2-D Gaussian profile, used by the centroid, is unlikely to be the optimum fit for fainter targets and those is areas of high background contamination. Instead, this could be replaced with a variable-width non-Gaussian profile, e.g. with a rectangular shape. This should result in a more optimal SNR for fainter targets, by more accurately determining the centre of the source PSF and thereby reducing the amount of background flux entering the aperture. Furthermore this method will reduce the risk of centroid failure, meaning that less targets will be rejected at stages 2 and 3 in the TRP (Sections 5.3.2 and 5.3.3 respectively).

- Improvements to the TRP: The targets tracked in the centre of the FOV have the greatest amount of solar contamination. In the current version of the TRP, this component of noise is removed from the data by eliminating the data points with the greatest amount of uncertainty. However, this truncates the time-series in the affected light curves, which now appears to be extremely detrimental to the detection of signals from these targets (see Figure 8.9). This outcome would almost certainly be improved with an alternative method to remove this type of noise, without

removing the actual data points themselves. For example, if the light from solar flux and CMEs can be estimated, then their components could be disentangled from the source the flux.

3. Limitations of the BLS algorithm - conduct the search with a different TDA.

   - As explained in Section 7.2, there are many different approaches to transit detection and each one has their own strengths and limitations. It has been shown that BLS is a highly effective algorithm for detecting short-period transit-like signals, however it is possible that one of the other methods, e.g. the matched-filter, or the analysis of variance, could provide additional candidates, which were not detected by BLS.

4. The detection criteria are overly-strict (Section 7.4).

   - The detection criteria were chosen to limit the number of FPs due to EBs and other astrophysical sources. However, as shown by the results, having an overly-strict period range does not avoid FPs due to short-period variables, as an alias of the true signal is detected instead (see Section 8.7.1). A more effective method would therefore be to extend the lower limit on the search-period, to ~ 0.1 days. This would lead to the detection of the true period for these targets, which could then be eliminated by imposing the criteria of Period ≥ 0.9 days to the results.

Aside from the primary goal of this work, to detect transits, it should be noted that the current detrended light curves are of excellent quality for alternative studies. The advantage of having observations of each target, taken over multiple years, means that the data is also very well suited to long-term studies of stellar variability, especially for Be stars and δ Scutis. Given the time, this is another possible route for the future work to take.

The present version of the TRP and the results of the noise analysis (Chapters 5 and 6) have recently been published (Whittaker et al., 2013). These results illustrate the issues affecting the HI-1A data, but also the improvements which can be made to increase the successes of stellar studies using the data. The methods and techniques implemented in the TRP are extremely adaptable and applicable to similar situations, which rely on the data from an instrument build for alternative purposes. As such it is hoped that this may benefit the wider community, in the same way that my work has benefited from others.

References

S. Aigrain and M. Irwin. Practical planet prospecting. *MNRAS*, 350:331–345, May 2004.

S. Aigrain, F. Pont, F. Fressin, A. Alapini, R. Alonso, M. Auvergne, M. Barbieri, P. Barge, et al. Noise properties of the CoRoT data. A planet-finding perspective. *A&A*, 506:425–429, October 2009.

J. M. Almenara, H. J. Deeg, C. Régulo, and R. Alonso. Comparison of False Alarm Rejection Methods used in CoRoT Blind Test 2. In C. Afonso, D. Weldrake, and T. Henning, editors, *Transiting Extrapolar Planets Workshop*, volume 366 of *Astronomical Society of the Pacific Conference Series*, page 183, July 2007.

J. M. Almenara, H. J. Deeg, S. Aigrain, R. Alonso, M. Auvergne, A. Baglin, M. Barbieri, P. Barge, et al. Rate and nature of false positives in the CoRoT exoplanet search. *A&A*, 506:337–341, October 2009.

G. Á. Bakos, J. D. Hartman, G. Torres, B. Béky, D. W. Latham, L. A. Buchhave, Z. Csubry, G. Kovács, et al. HAT-P-34b-HAT-P-37b: Four Transiting Planets More Massive than Jupiter Orbiting Moderately Bright Stars. *AJ*, 144:19, July 2012.

T. Bayes. An Essay Toward Solving a Problem in the Doctrine of Chances. *Philosophical Transactions of the Royal Society of London*, 53:370–418, 1764.

D. Bewsher, D. S. Brown, C. J. Eyles, B. J. Kellett, G. J. White, and B. Swinyard. Determination of the Photometric Calibration and Large-Scale Flatfield of the STEREO Heliospheric Imagers: I. HI-1. *Solar Phys.*, 264:433–460, July 2010.

D. S. Brown, D. Bewsher, and C. J. Eyles. Calibrating the Pointing and Optical Parameters of the STEREO Heliospheric Imagers. *Solar Phys.*, 254:185–225, January 2009.

T. M. Brown. Expected Detection and False Alarm Rates for Transiting Jovian Planets. *ApJL*, 593: L125–L128, August 2003.

C. J. Burke, B. S. Gaudi, D. L. DePoy, and R. W. Pogge. Survey for Transiting Extrasolar Planets in Stellar Systems. III. A Limit on the Fraction of Stars with Planets in the Open Cluster NGC 1245. *AJ*, 132:210–230, July 2006.

S. Carpano, J. Cabrera, R. Alonso, P. Barge, S. Aigrain, J.-M. Almenara, P. Bordé, F. Bouchy, et al. Planetary transit candidates in Corot-IRa01 field. *A&A*, 506:491–500, October 2009.

C. Defaÿ, M. Deleuil, and P. Barge. A Bayesian method for the detection of planetary transits. *A&A*, 365:330–340, January 2001.

L. R. Doyle, J. A. Carter, D. C. Fabrycky, R. W. Slawson, S. B. Howell, J. N. Winn, J. A. Orosz, A. Prˇsa, et al. Kepler-16: A Transiting Circumbinary Planet. *Science*, 333:1602–, September 2011.

R. Drummond, B. Vandenbussche, C. Aerts, F. De Oliveira Fialho, and M. Auvergne. Jitter Correction Algorithms for the COROT Satellite Mission. *PASP*, 118:874–884, June 2006.

B. Enoch, C. A. Haswell, A. J. Norton, A. Collier-Cameron, R. G. West, A. M. S. Smith, and N. R. Parley. Transit algorithm performance using real WASP data. *A&A*, 548:A48, December 2012. doi: 10.1051/0004-6361/201219771.

C. J. Eyles, R. A. Harrison, C. J. Davis, N. R. Waltham, B. M. Shaughnessy, H. C. A. Mapson-Menard, D. Bewsher, S. R. Crothers, J. A. Davies, et al. The Heliospheric Imagers Onboard the STEREO Mission. *Solar Phys.*, 254:387–445, February 2009.

J. Fang and J.-L. Margot. Architecture of Planetary Systems Based on Kepler Data: Number of Planets and Coplanarity. *ApJ*, 761:92, December 2012.

D. A. Fischer and G. W. Marcy. Multiplicity among M dwarfs. *ApJ*, 396:178–194, September 1992. doi: 10.1086/171708.

S. L. Freeland and B. N. Handy. Data Analysis with the SolarSoft System. *Solar Phys* , 182:497–500, October 1998.

F. Fressin, G. Torres, D. Charbonneau, S. T. Bryson, J. Christiansen, C. D. Dressing, J. M. Jenkins, L. M. Walkowicz, et al. The False Positive Rate of Kepler and the Occurrence of Planets. *ApJ*, 766:81, April 2013.

B. S. Gaudi, D. P. Bennett, A. Udalski, A. Gould, G. W. Christie, D. Maoz, S. Dong, J. McCormick, et al. Discovery of a Jupiter/Saturn Analog with Gravitational Microlensing. *Science*, 319:927–, 2008.

R. L. Gilliland, G. W. Marcy, J. F. Rowe, L. Rogers, G. Torres, F. Fressin, E. D. Lopez, L. A. Buchhave, et al. Kepler-68: Three Planets, One with a Density between that of Earth and Ice Giants. *ApJ*, 766: 40, March 2013.

P. Goldreich and W. R. Ward. The Formation of Planetesimals. *ApJ*, 183:1051–1062, August 1973. doi: 10.1086/152291.

C. Han, A. Udalski, J.-Y. Choi, J. C. Yee, A. Gould, G. Christie, T.-G. Tan, M. K. Szymański, et al. The Second Multiple-planet System Discovered by Microlensing: OGLE-2012-BLG-0026Lb, c—A Pair of Jovian Planets beyond the Snow Line. *ApJL*, 762:L28, January 2013.

L. Hebb, A. Collier-Cameron, B. Loeillet, D. Pollacco, G. Hébrard, R. A. Street, F. Bouchy, H. C. Stempels, et al. WASP-12b: The Hottest Transiting Extrasolar Planet Yet Discovered. *ApJ*, 693: 1920–1928, March 2009.

M. J. Holman, D. C. Fabrycky, D. Ragozzine, E. B. Ford, J. H. Steffen, W. F. Welsh, J. J. Lissauer, D. W. Latham, et al. Kepler-9: A System of Multiple Planets Transiting a Sun-Like Star, Confirmed by Timing Variations. *Science*, 330:51–, October 2010.

J. H. Horne and S. L. Baliunas. A prescription for period analysis of unevenly sampled time series. *ApJ*, 302:757–763, March 1986.

N. Houk. *Michigan Catalogue of Two-dimensional Spectral Types for the HD stars. Volume_3. Declinations -40_fnof0 to -26_fnof0.* Department of Astronomy, University of Michigan, 1982.

S. B. Howell, B. Koehn, E. Bowell, and M. Hoffman. Detection and Measurement of Poorly Sampled Point Sources Imaged With 2-D Array. *AJ*, 112:1302, September 1996.

J. M. Jenkins. The Impact of Solar-like Variability on the Detectability of Transiting Terrestrial Planets. *ApJ*, 575:493–505, August 2002.

J. M. Jenkins, D. A. Caldwell, H. Chandrasekaran, J. D. Twicken, S. T. Bryson, E. V. Quintana, B. D. Clarke, J. Li, et al. Overview of the Kepler Science Processing Pipeline. *ApJL*, 713:L87–L91, April 2010a.

J. M. Jenkins, H. Chandrasekaran, S. D. McCauliff, D. A. Caldwell, P. Tenenbaum, J. Li, T. C. Klaus, M. T. Cote, and C. Middour. Transiting planet search in the Kepler pipeline. In *Society of Photo-Optical Instrumentation Engineers (SPIE) Conference Series*, volume 7740 of *Society of Photo-Optical Instrumentation Engineers (SPIE) Conference Series*, July 2010b.

J. A. Johnson, K. M. Aller, A. W. Howard, and J. R. Crepp. Giant Planet Occurrence in the Stellar Mass-Metallicity Plane. *PASP*, 122:905–915, August 2010.

P. Kalas, J. R. Graham, and M. Clampin. A planetary system as the origin of structure in Fomalhaut's dust belt. *Nature*, 435:1067–1070, June 2005. doi: 10.1038/nature03601.

S. R. Kane, W. I. Clarkson, R. G. West, D. M. Wilson, D. J. Christian, A. Collier Cameron, B. Enoch, T. A. Lister, et al. SuperWASP-N extrasolar planet candidates from fields 06h - RA - 16h. *MNRAS*, 384:1097–1108, March 2008. doi: 10.1111/j.1365-2966.2007.12722.x.

Steven M. Kay. *Fundamentals of Statistical Signal Processing, Volume II:Detection Theory*. Prentice Hall, 1998.

D. M. Kipping. Binning is sinning: morphological light-curve distortions due to finite integration time. *MNRAS*, 408:1758–1769, November 2010.

G. Kovács, S. Zucker, and T. Mazeh. A box-fitting algorithm in the search for periodic transits. *A&A*, 391:369–377, August 2002.

G. Kovács, G. Bakos, and R. W. Noyes. A trend filtering algorithm for wide-field variability surveys. *MNRAS*, 356:557–567, January 2005.

G. Kovács, G. Á. Bakos, J. D. Hartman, G. Torres, R. W. Noyes, D. W. Latham, A. W. Howard, D. A. Fischer, et al. HAT-P-15b: A 10.9 Day Extrasolar Planet Transiting a Solar-type Star. *ApJ*, 724: 866–877, December 2010.

T. A. Lister, R. G. West, D. M. Wilson, A. Collier Cameron, W. I. Clarkson, R. A. Street, B. Enoch, N. R. Parley, et al. SuperWASP-North extrasolar planet candidates: candidates from fields 17h<RA<18h. *MNRAS*, 379:647–662, August 2007.

G. Lo Curto, M. Mayor, W. Benz, F. Bouchy, G. Hébrard, C. Lovis, C. Moutou, D. Naef, et al. The HARPS search for southern extra-solar planets . XXXII. New multi-planet systems in the HARPS

volume limited sample: a super-Earth and a Neptune in the habitable zone. *A&A*, 551:A59, March 2013a.

G. Lo Curto, M. Mayor, W. Benz, F. Bouchy, G. Hébrard, C. Lovis, C. Moutou, D. Naef, et al. The HARPS search for southern extra-solar planets . XXXII. New multi-planet systems in the HARPS volume limited sample: a super-Earth and a Neptune in the habitable zone. *A&A*, 551:A59, March 2013b.

C. Marois, B. Macintosh, T. Barman, B. Zuckerman, I. Song, J. Patience, D. Lafrenière, and R. Doyon. Direct Imaging of Multiple Planets Orbiting the Star HR 8799. *Science*, 322:1348–, November 2008.

M. Mayor and D. Queloz. A Jupiter-mass companion to a solar-type star. *Nature*, 378:355–359, November 1995. doi: 10.1038/378355a0.

M. Mayor, M. Marmier, C. Lovis, S. Udry, D. Ségransan, F. Pepe, W. Benz, J. . Bertaux, et al. The HARPS search for southern extra-solar planets XXXIV. Occurrence, mass distribution and orbital properties of super-Earths and Neptune-mass planets. *ArXiv e-prints*, September 2011.

T. Mazeh, P. Guterman, S. Aigrain, S. Zucker, N. Grinberg, A. Alapini, R. Alonso, M. Auvergne, et al. Removing systematics from the CoRoT light curves. I. Magnitude-dependent zero point. *A&A*, 506: 431–434, October 2009.

A. A. Miller, J. Irwin, S. Aigrain, S. Hodgkin, and L. Hebb. The Monitor project: the search for transits in the open cluster NGC 2362. *MNRAS*, 387:349–363, June 2008. doi: 10.1111/j.1365-2966.2008.13236.x.

D. Mislis, J. H. M. M. Schmitt, L. Carone, E. W. Guenther, and M. Pätzold. An algorithm for correcting CoRoT raw light curves. *A&A*, 522:A86, November 2010.

C. Moutou, F. Pont, P. Barge, S. Aigrain, M. Auvergne, D. Blouin, R. Cautain, A. R. Erikson, et al. Comparative blind test of five planetary transit detection algorithms on realistic synthetic light curves. *A&A*, 437:355–368, July 2005.

D. Nesvorný, D. M. Kipping, L. A. Buchhave, G. Á. Bakos, J. Hartman, and A. R. Schmitt. The Detection and Characterization of a Nontransiting Planet by Transit Timing Variations. *Science*, 336:1133–, June 2012.

A. Ofir, R. Alonso, A. S. Bonomo, L. Carone, S. Carpano, B. Samuel, J. Weingrill, S. Aigrain, M. Auvergne, A. Baglin, et al. The SARS algorithm: detrending CoRoT light curves with Sysrem using simultaneous external parameters. *MNRAS*, 404:L99–L103, May 2010.

J. A. Orosz, W. F. Welsh, J. A. Carter, D. C. Fabrycky, W. D. Cochran, M. Endl, E. B. Ford, N. Haghighipour, P. J. MacQueen, et al. Kepler-47: A Transiting Circumbinary Multiplanet System. *Science*, 337:1511–, September 2012. doi: 10.1126/science.1228380.

A. J. Pickles. A Stellar Spectral Flux Library: 1150 - 25000 A (Pickles 1998). *VizieR Online Data Catalog*, 611:863, September 1998.

F. Pont, S. Zucker, and D. Queloz. The effect of red noise on planetary transit detection. *MNRAS*, 373: 231–242, November 2006.

T. Pribulla, S. M. Rucinski, H. DeBond, A. De Ridder, T. Karmo, J. R. Thomson, B. Croll, W. Ogłoza, B. Pilecki, and M. Siwak. Radial Velocity Studies of Close Binary Stars. XIV. *AJ*, 137:3646–3654, March 2009.

D. Queloz, D. Anderson, A. Collier Cameron, M. Gillon, L. Hebb, C. Hellier, P. Maxted, F. Pepe, et al. WASP-8b: a retrograde transiting planet in a multiple system. *A&A*, 517:L1, July 2010.

D. Raghavan, H. A. McAlister, T. J. Henry, D. W. Latham, G. W. Marcy, B. D. Mason, D. R. Gies, R. J. White, and T. A. ten Brummelaar. A Survey of Stellar Families: Multiplicity of Solar-type Stars. *ApJS*, 190:1–42, September 2010. doi: 10.1088/0067-0049/190/1/1.

A. Santerne, R. F. Díaz, C. Moutou, F. Bouchy, G. Hébrard, J.-M. Almenara, A. S. Bonomo, M. Deleuil, et al. SOPHIE velocimetry of Kepler transit candidates. VII. A false-positive rate of 35% for Kepler close-in giant candidates. *A&A*, 545:A76, September 2012.

N. C. Santos, G. Israelian, and M. Mayor. The metal-rich nature of stars with planets. *A&A*, 373: 1019–1031, July 2001.

J. D. Scargle. Studies in astronomical time series analysis. II - Statistical aspects of spectral analysis of unevenly spaced data. *ApJ*, 263:835–853, December 1982.

A. Schwarzenberg-Czerny and J.-P. Beaulieu. Efficient analysis in planet transit surveys. *MNRAS*, 365: 165–170, January 2006.

A. M. S. Smith, A. Collier Cameron, D. J. Christian, W. I. Clarkson, B. Enoch, A. Evans, C. A. Haswell, C. Hellier, et al. The impact of correlated noise on SuperWASP detection rates for transiting extrasolar planets. *MNRAS*, 373:1151–1158, December 2006.

D. G. Socker, R. A. Howard, C. M. Korendyke, G. M. Simnett, and D. F. Webb. NASA Solar Terrestrial Relations Observatory (STEREO) mission heliospheric imager. In S. Fineschi, C. M. Korendyke, O. H. Siegmund, and B. E. Woodgate, editors, *Society of Photo-Optical Instrumentation Engineers (SPIE) Conference Series*, volume 4139 of *Society of Photo-Optical Instrumentation Engineers (SPIE) Conference Series*, pages 284–293, December 2000.

R. A. Street, D. J. Christian, W. I. Clarkson, A. Collier Cameron, B. Enoch, S. R. Kane, T. A. Lister, R. G. West, D. M. Wilson, et al. Superwasp-n extrasolar planet candidates between 18 ¡ ra ¡ 21 h. *Monthly Notices of the Royal Astronomical Society*, 379(2):816–832, 2007. doi: 10.1111/j.1365-2966.2007.11987.x.

M. C. Stumpe, J. C. Smith, J. E. Van Cleve, J. D. Twicken, T. S. Barclay, M. N. Fanelli, F. R. Girouard, J. M. Jenkins, et al. Kepler Presearch Data Conditioning I - Architecture and Algorithms for Error Correction in Kepler Light Curves. *PASP*, 124:985–999, September 2012.

T. Sumi, D. P. Bennett, I. A. Bond, A. Udalski, V. Batista, M. Dominik, P. Fouqué, D. Kubas, A. Gould, et al. A Cold Neptune-Mass Planet OGLE-2007-BLG-368Lb: Cold Neptunes Are Common. *ApJ*, 710:1641–1653, February 2010.

O. Tamuz, T. Mazeh, and S. Zucker. Correcting systematic effects in a large set of photometric light curves. *MNRAS*, 356:1466–1470, February 2005.

B. Tingley. A rigorous comparison of different planet detection algorithms. *A&A*, 403:329–337, May 2003a.

B. Tingley. Improvements to existing transit detection algorithms and their comparison. *A&A*, 408: L5–L7, September 2003b.

B. Tingley and P. D. Sackett. A Photometric Diagnostic to Aid in the Identification of Transiting Extrasolar Planets. *ApJ*, 627:1011–1018, July 2005.

G. Torres, F. Fressin, N. M. Batalha, W. J. Borucki, T. M. Brown, S. T. Bryson, L. A. Buchhave, D. Charbonneau, et al. Modeling Kepler Transit Light Curves as False Positives: Rejection of Blend Scenarios for Kepler-9, and Validation of Kepler-9 d, A Super-earth-size Planet in a Multiple System. *ApJ*, 727: 24, January 2011.

A. H. M. J. Triaud, D. R. Anderson, A. Collier Cameron, A. P. Doyle, A. Fumel, M. Gillon, C. Hellier, E. Jehin, et al. WASP-80b: a gas giant transiting a cool dwarf. *A&A*, 551:A80, March 2013.

A. Udalski, B. Paczynski, K. Zebrun, M. Szymanski, M. Kubiak, I. Soszynski, O. Szewczyk, L. Wyrzykowski, et al. The Optical Gravitational Lensing Experiment. Search for Planetary and Low-Luminosity Object Transits in the Galactic Disk. Results of 2001 Campaign. *AcA*, 52:1–37, March 2002a.

A. Udalski, K. Zebrun, M. Szymanski, M. Kubiak, I. Soszynski, O. Szewczyk, L. Wyrzykowski, and G. Pietrzynski. The Optical Gravitational Lensing Experiment. Search for Planetary and Low- Luminosity Object Transits in the Galactic Disk. Results of 2001 Campaign – Supplement. *AcA*, 52: 115–128, June 2002b.

F. van Leeuwen. Validation of the new Hipparcos reduction. *A&A*, 474:653–664, November 2007.

M. Wenger, F. Ochsenbein, D. Egret, P. Dubois, F. Bonnarel, S. Borde, F. Genova, G. Jasniewicz, et al. The SIMBAD astronomical database. The CDS reference database for astronomical objects. *A&AS*, 143:9–22, April 2000.

G. N. Whittaker, I. R. Stevens, and V. Sangaralingam. STEREO trend removal pipeline and planet detection possibilities. *MNRAS*, April 2013.

D. M. Wilson. SuperWASP - Transiting Planet Candidate Selection. In C. Afonso, D. Weldrake, and T. Henning, editors, *Transiting Extrapolar Planets Workshop*, volume 366 of *Astronomical Society of the Pacific Conference Series*, page 187, July 2007.

J. N. Winn. Transits and Occultations. *ArXiv e-prints*, January 2010.

J. N. Winn, J. A. Johnson, D. Fabrycky, A. W. Howard, G. W. Marcy, N. Narita, I. J. Crossfield, Y. Suto, et al. On the Spin-Orbit Misalignment of the XO-3 Exoplanetary System. *ApJ*, 700:302–308, July 2009.

R. A. Wittenmyer, J. Horner, M. Tuomi, G. S. Salter, C. G. Tinney, R. P. Butler, H. R. A. Jones, S. J. O'Toole, et al. The Anglo-Australian Planet Search. XXII. Two New Multi-planet Systems. *ApJ*, 753: 169, July 2012.

A. Wolszczan and D. A. Frail. A planetary system around the millisecond pulsar PSR1257 + 12. *Nature*, 355:145–147, January 1992.

J. T. Wright, G. W. Marcy, A. W. Howard, J. A. Johnson, T. D. Morton, and D. A. Fischer. The Frequency of Hot Jupiters Orbiting nearby Solar-type Stars. *ApJ*, 753:160, July 2012.